

Study on Heat Transfer to Supercritical Water in Application to SMRs

by

Nikita Dort-Goltz

A thesis submitted to the School of Graduate and Postdoctoral Studies in partial fulfillment of the requirements for the degree of

Master of Applied Science in Nuclear Engineering

The Faculty of Energy Systems and Nuclear Science

University of Ontario Institute of Technology (Ontario Tech University)

Oshawa, Ontario Canada

December, 2021

© Nikita Dort-Goltz, 2021

Thesis Examination Information

Submitted by: **Nikita Dort-Goltz**

Master of Applied Science in Nuclear Engineering

Thesis title: Study on Heat Transfer to Supercritical Water in Application to SMRs
--

An oral defense of this thesis took place on October 1, 2021 in front of the following examining committee:

Examining Committee:

Chair of Examining Committee	Dr. Daniel Hoornweg
Research Supervisor	Dr. Igor Pioro
Research Co-supervisor	Dr. Jennifer McKellar
Examining Committee Member	Dr. Rachid Machrafi
Thesis Examiner	Dr. Anatoli Chkrebtti

The above committee determined that the thesis is acceptable in form and content and that a satisfactory knowledge of the field covered by the thesis was demonstrated by the candidate during an oral examination. A signed copy of the Certificate of Approval is available from the School of Graduate and Postdoctoral Studies.

Abstract

The SuperSafe Reactor (SSR), a small modular reactor (SMR) concept with a supercritical water coolant, was subjected to a thermalhydraulic analysis and an economic analysis of its Levelized Unit of Energy Cost (*LUEC*).

Heat transfer data was examined for the onset of deteriorated heat transfer using three correlations that relied on NIST REFPROP v.10 for thermophysical property values. The experimental inside-wall temperature and heat transfer coefficient profiles were stable while the selected correlations generated poor predictions. NIST REFPROP v.10 was investigated at the critical point of water and the program was discovered to generate non-physical results.

G4ECONS calculated the SSR's *LUEC*, and when compared to other nuclear technologies, the SSR was among the least economically competitive. The application of several economic factors unique to SMRs helped reduce the SSR's *LUEC* and increase its economic value. Overall, the SSR would be a technologically viable SMR concept with potential long-term industry adoption.

Keywords: Small Modular Reactors; Supercritical Water-cooled Reactors; Economics; Levelized Unit Electricity Cost; Heat Transfer

Author's Declaration

I hereby declare that this thesis consists of original work of which I have authored. This is a true copy of the thesis, including any required final revisions, as accepted by my examiners.

I authorize the University of Ontario Institute of Technology (Ontario Tech University) to lend this thesis to other institutions or individuals for the purpose of scholarly research. I further authorize University of Ontario Institute of Technology (Ontario Tech University) to reproduce this thesis by photocopying or by other means, in total or in part, at the request of other institutions or individuals for the purpose of scholarly research. I understand that my thesis will be made electronically available to the public.

Nikita Dort-Goltz

Statement of Contributions

Part of the work described in Chapter 2 has been published as:

Pioro, I., Duffey, R.B., Kirillov, P.L., and Dort-Goltz, N., 2020. Current Status of Reactors Deployment and Small Modular Reactors Development in the World. *ASME J. NERS*, Vol. 6, No. 4, 24 pages. Free download from:

<https://asmedigitalcollection.asme.org/nuclearengineering/article/6/4/044001/1085654/Current-Status-of-Reactors-Deployment-and-Small>.

I collected the technical information on the small modular reactor concepts and created the tables organizing this data.

Part of the work described in Chapter 4 has been published as:

Dort-Goltz, N., Pioro, I., and McKellar, J., 2021c. Specifics of Calculating Thermophysical Properties of Water in Critical Point Using NIST REFPROP Program, Proceedings of the 10th International Symposium on SCWRs (ISSCWR-10), Prague, the Czech Republic, March 15-18, 10 pages.

I generated the thermophysical property values from NIST v.10 and then created the graphical representation of these values using the Sigmaplot graphing software.

Part of the work described in Chapter 4 has also been published/accepted-to-be-published as:

Dort-Goltz, N., Pioro, I., and McKellar, J., 2021a. Study on Deteriorated Heat Transfer in Upward Flow of Supercritical Water in a 1-M Vertical Bare Tube, Proceedings of 28th International Conference on Nuclear Engineering, Virtual Conference, August 4-6, 10 pages.

Dort-Goltz, N., Pioro, I., and McKellar, J., 2021b. Experimental Study on Heat Transfer to Upward Flow of Supercritical Water in a 1-M Vertical Bare Tube, Proceedings of 40th Annual Conference of the Canadian Nuclear Society and 45th Annual CNS/CNA Student Conference (virtual), June 6-9, 6 pages. Master's Level Submission.

I created the Python code to calculate the inside-wall temperatures and heat transfer coefficients using the three selected correlations and then graphed these calculated results alongside the experimental results using Sigmaplot.

Acknowledgements

First and foremost, I would like to thank my co-supervisors, Dr. Igor Pioro and Dr. Jennifer McKellar, for their tireless effort and support over these past two years. Your guidance, wisdom, and knowledge were invaluable towards the completion of this thesis. My deepest and sincerest appreciation to the both of you for taking me on as a graduate student and helping me grow both as a professional and as a person.

I would also like to thank my family, especially my mother and sister, for all of their love, reassurance, and encouragement. Whenever the down days appeared, I knew I could count on you to pull me out of my ruts and keep me going. This thesis I dedicate to you for helping me throughout my studies and life up to this point in time. Additionally, I would like to thank God for giving me the opportunities to succeed and learn and for blessing me with all of the people who have impacted me, positively or negatively, in my life.

Any acknowledgement section would not be complete without gratitude for all the work done by all the students and professionals from years past. I thank all of you, particularly Sarah Mokry and Sahil Gupta, for your hard work in the pursuit of knowledge.

Thank you also to the Ontario Tech University, the Faculty of Energy Systems and Nuclear Science, and the National Sciences and Engineering Research Council of Canada for all of the resources and funding you have provided me to succeed.

Table of Contents

Thesis Examination Information	ii
Abstract	iii
Author’s Declaration	iv
Statement of Contributions	v
Acknowledgements	vi
Table of Contents	vii
Nomenclature	xiv
Chapter 1: Introduction	1
1.1: Current Status of Electricity Generation	1
1.2: GIF and Generation IV Reactor Concepts	6
1.2.1: Gas-cooled Fast Reactor (High Temperature Reactor) (GFR/HTR)	7
1.2.2: Very High Temperature Reactor (VHTR)	8
1.2.3: Sodium-cooled Fast Reactor (SFR)	8
1.2.4: Lead-cooled Fast Reactor (LFR)	8
1.2.5: Molten Salt Reactor (MSR)	9
1.2.6: SuperCritical Water-cooled Reactor (SCWR)	9
1.3: SMRs	11
1.4: Heat Transfer and NIST REFPROP	13
1.5: Objectives	16
Chapter 2: Literature Review	18
2.1: General Overview of Heat Transfer in SCW	18
2.2: Heat Transfer Correlations Selected for Use	29
2.3: Overview of Nuclear Economics	35
2.4: Review of SMR Concepts	44
2.4.1: Overview of SuperSafe Reactor SMR	59
Chapter 3: Methodology	61
3.1: Investigational Procedure into NIST REFPROP v.10	61
3.1.1: Theoretical Calculations of Thermophysical Properties by NIST REFPROP v.10	61
3.1.2: Procedure for Investigating the Critical Properties of Water	68

3.2: Experimental Setup and Procedure for 1-m Supercritical Heat Transfer Analysis	70
3.2.1: Description of Experimental Setup	70
3.2.2: Verification of Python Code and Graphing of Results	74
3.3: Framework for the Economic Analysis of the SSR SMR	79
3.3.1: EMWG Model and G4ECONS Software	79
3.3.2: Estimation of Life Cycle Costs for the SSR	89
Chapter 4: Results and Discussion	94
4.1 Investigative Results for NIST REFPROP v.10	94
4.1.1 Conclusion	103
4.2 1-m Heat Transfer Dataset Analysis	104
4.2.1 Conclusion	120
4.3 LUEC Computation for SSR	121
4.3.1 Conclusion	128
Chapter 5: Conclusions	130
References	134
Appendix A: Collection of Global SMR Concepts	149
Appendix B: Full Formulations of REFPROP v.10 Theoretical Models	162
B.1: Dimensionless Helmholtz Energy	162
B.2: Thermal Conductivity	166
B.3: Dynamic Viscosity	168
Appendix C: Sample Python Code for Analysis of 1-m Supercritical Heat Transfer Dataset	171
Appendix D: Sensitivity Analysis for SSR LUEC Parameters	177
D.1: Plant Lifetime	177
D.2: Construction Time	178
D.3: Plant Capacity Factor	180
D.4: Natural Uranium Mining Prices	182
D.5: Fuel Enrichment Costs	184
Appendix E: N. Dort-Goltz Publications and Conferences Attended	188
Appendix F: Awards, Honours, and Accomplishments by N. Dort-Goltz	190
Appendix G: Copyright Permissions	192

List of Figures

Figure 1-1: Human Development Index scores compared to the electrical energy consumption per capita in various countries (data taken from UNDP (2020), Worldometer (2021), and IEA (2021)(courtesy of I. Pioro)).	1
Figure 1-2: Distribution of global electrical energy generation according to types of energy sources (Pioro, ..., Dort-Goltz, 2020) (courtesy and copyright of ASME).	2
Figure 1-3: Carbon footprint of different energy sources (courtesy of Dr. J. Roberts, University of Manchester, UK; based on data from http://researchbriefings.files.parliament.uk/documents/POST-PN-268/POST-PN-268.pdf).	3
Figure 1-4: Nuclear reactor generation roadmap (Nuclear Energy Today, 2012).	7
Figure 1-5: NIST REFPROP v.10 startup menu (NIST, 2018).	15
Figure 2-1: Pressure-Temperature diagram for water around its critical point (based on data from NIST (2018)).	20
Figure 2-2: Thermophysical properties of water at $P_{cr}=22.064$ MPa and $P=25$ MPa; (a)-Density; (b)-Specific Heat; (c)-Specific Enthalpy; (d)-Thermal Conductivity (based on data from NIST (2018)).	21
Figure 2-2: Thermophysical properties of water at $P_{cr}=22.064$ MPa and $P=25$ MPa; (e)-Dynamic Viscosity; (f)-Kinematic Viscosity; (g)-Prandtl Number; (h)-Volume Expansivity (based on data from NIST (2018)).	22
Figure 2-3: Specific Heat-Temperature graph for water at various pressures above $P_{cr}=22.064$ MPa (based on data from NIST (2018)).	23
Figure 2-4: Graph of selected thermophysical property variation for water at $P=25$ MPa (based on data from NIST (2018)).	25
Figure 2-5: Bulk-Fluid- and Inside-Wall-Temperatures, and HTC profiles along heated length of vertical-bare-circular tube with upward flow of SCW (data by Kirillov et al. (2003)): $D = 10$ mm; $L_h = 4$ m; and $q_{ave} > q_{dht}$. Points – experimental data; curves – calculated data; curve for HTC is calculated through Dittus-Boelter correlation (Equation 2-2). q_{dht} is based on Equation (2-9).	28
Figure 2-6: Comparison of different heat transfer correlations in calculating HTC and T_w of supercritical water in upward flow through a 4-m, vertical bare tube. Data obtained by Kirillov et al. D-B stands for Dittus-Boelter; (prepared using Kirillov et al. (2003) dataset).	32
Figure 2-7: $LUEC$ values for electricity-generating options in Ontario. Monetary values are in CAD. (Courtesy of I. Pioro and data obtained from Ontario's Ministry of Energy Long-Term Energy Plan (2013). *-Updated for 2014 Feed-In Tarriff prices.	41
Figure 2-8: Schematic layout of KLT-40S reactor and its safety systems (obtained from Pioro, ..., Dort-Goltz (2020)) (courtesy and copyright of ASME).	56
Figure 2-9: Russian SMRs. (a)-KLT-40S; (b)-RITM-200M (obtained from Pioro, ..., Dort-Goltz (2020)) (courtesy and copyright of ASME).	57

Figure 3-1: Fluid information window for water taken from REFPROP v.10 (NIST, 2018). Critical point and density are given along with the range of applicability for the “Equation of State”. The range of applicability will change for the “Viscosity” and “Thermal Conductivity” sections due to different theoretical models used for property calculation.	63
Figure 3-2: Steps for generating isoproperty table in REFPROP v.10 (NIST, 2018). (a)-Selection of properties to be held constant/varied; (b)-Specification of parameters	69
Figure 3-3: Schematic of SKD-1 Loop (Pioro et al., 2010; Kirillov et al., 2005); 1-circulating pump; 2-mechanical filter; 3-regulating valves; 4-electrical heater; 5-flow meter; 6-test section; 7-throttle valve; 8-mixer-cooler; 9-discharge tank; 10-heat exchanger; 11-feedwater tank; 12-volume compensator; 13-feedwater pump.	72
Figure 3-4: Verification graphs for Mokry et al. correlation; (a)- $L_h=4$ m, $G=1500$ kg/m ² ·s, $q_{ave}=884$ kW/m ² ; (b)- $L_h=4$ m, $G=1500$ kg/m ² ·s, $q_{ave}=874$ kW/m ² ; Green-NDG verification results, Red/Black-Original Mokry et al. results	75
Figure 3-5: Verification graphs for Gupta et al. correlation; (a)- $L_h=4$ m, $G=1495$ kg/m ² ·s, $q_{ave}=884$ kW/m ² ; (b)- $L_h=4$ m, $G=1000$ kg/m ² ·s, $q_{ave}=826$ kW/m ² ; Green-original Gupta et al. results, Blue-NDG verification results with entrance effect, Maroon- NDG verification without entrance effect.	77
Figure 3-6: INEEM developed by EMWG (EMWG, 2007).	80
Figure 3-7: Detailed Construction and Production Costs of the INEEM (EMWG, 2007).	83
Figure 3-8: Uranium-based fuel cycle structure used in the INEEM (EMWG, 2007).	85
Figure 3-9: User inputs for drop-down cells within “Case Operational Parameters” page of the G4ECONS software (EMWG, 2018).	91
Figure 4-1: (a)-Density (ρ) vs. Temperature, (b)-Enthalpy (h) vs. Temperature; Water, critical region (Dort-Goltz et al., 2021c).....	95
Figure 4-1: (c)-Specific Heat (c_p) vs. Temperature, (d)-Thermal Conductivity (k) vs. Temperature; Water, critical region (Dort-Goltz et al., 2021c).	96
Figure 4-1: (g)-Thermal diffusivity (α) vs. Temperature, (h)-Prandtl Number (Pr) vs. Temperature; Water, critical region (Dort-Goltz et al., 2021c).	100
Figure 4-1: (i)-Volume Expansivity (β) vs. Temperature; Water, critical region (Dort-Goltz et al., 2021c).	101
Figure 4-2: Error message that would appear in REFPROP v.10 if a temperature increment below 0.002 °C was chosen and contained the critical point. All liquid-phase ($T < 356$ °C) calculations would be discarded and only vapor-phase calculations ($T \geq 356$ °C) would appear in the isoproperty table.....	103
Figure 4-3: Collection of high G HTC and T_w profiles for the 1-m long bare tube dataset by Kirillov et al. (a)-(b) $P=24.6$ MPa, $G=991-993$ kg/m ² ·s, $q_{ave}=874-1028$ kW/m ² . Markers-experimental data, Curves-calculated data; (prepared, based on Kirillov et al. (2003) dataset).	111

Figure 4-3: Collection of high G HTC and T_w profiles for the 1-m long bare tube dataset by Kirillov et al. (c)-(d) $P=24.6$ MPa, $G=993-994$ kg/m²·s, $q_{ave}=874-979$ kW/m². Markers-experimental data, Curves-calculated data; (prepared, based on Kirillov et al. (2003) dataset). 112

Figure 4-3: Collection of high G HTC and T_w profiles for the 1-m long bare tube dataset by Kirillov et al. (e)-(f) $P=24.5-24.6$ MPa, $G=994-996$ kg/m²·s, $q_{ave}=581-970$ kW/m². Markers-experimental data, Curves-calculated data; (prepared, based on Kirillov et al. (2003) dataset). 113

Figure 4-4: Collection of medium G HTC and T_w profiles for the 1-m long bare tube dataset by Kirillov et al. (a)-(b) $P=24.9$ MPa, $G=497-498$ kg/m²·s, $q_{ave}=484-585$ kW/m². Markers-experimental data, Curves-calculated data; (prepared, based on Kirillov et al. (2003) dataset). 114

Figure 4-4: Collection of medium G HTC and T_w profiles for the 1-m long bare tube dataset by Kirillov et al. (c)-(d) $P=24.8-24.9$ MPa, $G=495$ kg/m²·s, $q_{ave}=389-390$ kW/m². Markers-experimental data, Curves-calculated data; (prepared, based on Kirillov et al. (2003) dataset). 115

Figure 4-4: Collection of medium G HTC and T_w profiles for the 1-m long bare tube dataset by Kirillov et al. (e)-(f) $P=24.9$ MPa, $G=496-498$ kg/m²·s, $q_{ave}=433-585$ kW/m². Markers-experimental data, Curves-calculated data; (prepared, based on Kirillov et al. (2003) dataset). 116

Figure 4-5: Collection of low G HTC and T_w profiles for the 1-m long bare tube dataset by Kirillov et al. (a)-(b) $P=24.8-25$ MPa, $G=198-199$ kg/m²·s, $q_{ave}=181-324$ kW/m². Markers-experimental data, Curves-calculated data; (prepared, based on Kirillov et al. (2003) dataset). 117

Figure 4-5: Collection of low G HTC and T_w profiles for the 1-m long bare tube dataset by Kirillov et al. (c)-(d) $P=24.9$ MPa, $G=200$ kg/m²·s, $q_{ave}=88-228$ kW/m². Markers-experimental data, Curves-calculated data; (prepared, based on Kirillov et al. (2003) dataset). 118

Figure 4-5: Collection of low G HTC and T_w profiles for the 1-m long bare tube dataset by Kirillov et al. (e)-(f) $P=24.7-24.9$ MPa, $G=201$ kg/m²·s, $q_{ave}=275-374$ kW/m². Markers-experimental data, Curves-calculated data; (prepared, based on Kirillov et al. (2003) dataset). 119

Figure 4-6: SSR LUEC breakdown at discount rates of 5%, 3%, and 10%. 126

List of Tables

Table 1-1: Average capacity factors of a selection of energy sources (Pioro and Kirillov, 2013).	4
Table 1-2: Quantity of nuclear-power reactors connected to electrical grids and any forthcoming units as of July 2020 (Pioro,...., Dort-Goltz, 2020) (courtesy and copyright of ASME). Updated using latest information from Pioro et al. (2021).....	4
Table 1-3: Overview of GFR Parameters.	7
Table 1-4: Overview of VHTR Parameters.	8
Table 1-5: Overview of SFR Parameters.	8
Table 1-6: Overview of LFR Parameters.....	8
Table 1-7: Overview of LFR Parameters.....	9
Table 1-8: Overview of SCWR Parameters.....	9
Table 2-1: Pseudocritical temperatures and peak specific heat values for water at select pressures (data from NIST (2018)).	23
Table 2-2: Summary of assessments performed on <i>HTC</i> accuracy of heat transfer correlations for SCW in vertical, upwards flow through a bare tube.	33
Table 2-3: Selection of empirical correlations used to predict minimal heat flux for DHT, q_{dht} ..	34
Table 2-4: Breakdown of capital costs associated with activities during construction (based off data from World Nuclear Association (2020b)).....	38
Table 2-5: Breakdown of capital costs associated with equipment during construction (based off data from World Nuclear Association (2020b)).....	38
Table 2-6: <i>LUEC</i> estimates for miscellaneous energy sources. Discount rate was set at 7%. Long Term Operation refers to the number of years a nuclear reactor operates beyond its assumed lifetime (set at 60 years). All data obtained from IEA and OECD (2020).	39
Table 2-7: Land-based water-cooled SMRs/S&MRs (33 in total) (obtained from Pioro,...., Dort-Goltz (2020)) (courtesy and copyright of ASME).....	45
Table 2-8: Marine-based water-cooled SMRs/S&MRs (7 in total) (obtained from Pioro,...., Dort-Goltz (2020)) (courtesy and copyright of ASME).....	47
Table 2-9: High-temperature gas-cooled SMRs/S&MRs (Generation IV concept) (21 in total) (obtained from Pioro,...., Dort-Goltz (2020)) (courtesy and copyright of ASME).....	48
Table 2-10: Fast-neutron spectrum SMRs/S&MRs (Generation IV concept) (26 in total) (obtained from Pioro,...., Dort-Goltz (2020)) (courtesy and copyright of ASME).....	50
Table 2-11: Molten salt SMRs/S&MRs (Generation IV concept) (17 in total) (obtained from Pioro,...., Dort-Goltz (2020)) (courtesy and copyright of ASME).....	52
Table 2-12: Other SMRs/S&MRs (4 in total) (obtained from Pioro,...., Dort-Goltz (2020)) (courtesy and copyright of ASME).....	54

Table 2-13: KLT-40S and RITM-200M parameters (obtained from Pioro, ..., Dort-Goltz (2020)) (courtesy and copyright of ASME). Production of desalinated water is in case of desalination complex. For refueling, the combined barge and SMR unit will be brought back to the manufacturing plant and completely overhauled every 12 years.....	57
Table 3-1: Estimated uncertainties in models used for the calculation of selected properties and ranges of applicability. These are provided mainly for clarity and did not have an impact on the analysis in Section 4.1. All values were taken from the source of the model used by NIST (2018) except for density, whose uncertainty was stated by NIST (2018).....	64
Table 3-2: Maximum uncertainties of measured and calculated parameters (Kirillov et al., 2005).	73
Table 3-3: Test matrix for 1-m long, vertical, upward flow bare tube dataset (data obtained by Kirillov et al. (2003)); Orange-high <i>G</i> tests; Blue-medium <i>G</i> tests; Green-low <i>G</i> tests.	73
Table 3-4: Error analysis of Mokry et al. and Gupta et al. correlation (Equations 2-3 -2-5)	77
Table 3-5: Economic factors and their values for use in calculating the <i>LUEC</i> of the SSR.	92
Table 4-1: Extrema values of two selected temperature difference curves for the nine thermophysical properties. In bold-three largest percent differences.	101
Table 4-2: Relative RMS of the three correlations used to analyze the data found in Figures 4-3–4-5. Bold indicates lowest RMS for that particular set of data.	106
Table 4-3: Parameters for the base case <i>LUEC</i> evaluation of the SSR.	121
Table 4-4: OCC breakdown for SSR and reference SCWR reactor.	121
Table 4-5: Breakdown of <i>LUEC</i> for the SSR. Monetary figures are in 2007 USD.....	121
Table 4-6: Implementation of SMR factors and the subsequent effect on the SSR <i>LUEC</i> and its components. Bold values represent figures of merit.....	122
Table 4-7: Comparison of <i>LUEC</i> for different reactor technologies in 2020 USD.	127

Nomenclature

Symbols

A	area, m ² ; overnight capital cost of FOAK unit, \$ (USD)
c_p	isobaric specific heat, J/kg · K
\bar{c}_p	averaged isobaric specific heat within the range of $(T_w - T_b)$; $\left(\frac{H_w - H_b}{T_w - T_b} \right)$, J/kg · K
C	overnight capital cost, \$ (USD)
D	inner diameter, m
D_{hy}	hydraulic diameter, m; $\frac{4A_{fl}}{p_{wet}}$
E	electrical energy generated, J
F	annual fuel cycle component cost, \$ (USD)
F_{IND}	proportion of indivisible cost factor, 0.34 (Carelli et al., 2010)
G	mass flux, $\frac{\text{kg}}{\text{m}^2\text{s}}$; $\left(\frac{\dot{m}}{A_{fl}} \right)$
HTC	heat transfer coefficient, W/m ² · K
H, h	specific enthalpy, J/kg
I	annual capital expenditures, \$ (USD)
IDC	interest during construction, \$ (USD)
i	discrete annual interest rate
k	thermal conductivity, W/m · K; industrial productivity coefficient
L	length, m
$LUEC$	levelized unit of energy cost, \$ (USD)/MW _{el} h
M	quantity of material/service flow through fuel cycle component
\dot{m}	mass flow rate, kg/s

n	total number of data points; economies of scale exponent; quantity of reactors used in Co-siting Factor
OCC_{small}	overnight capital cost of reactor with smaller electrical capacity, \$ (USD)
OCC_{large}	overnight capital cost of reactor with larger electrical capacity, \$ (USD)
P, p	pressure, Pa; unit price of material/service in fuel cycle component, \$ (USD)
p_{wet}	wetted perimeter, m
Pr	power, W
Q	heat-transfer rate, W
q	heat flux, W/m ²
R	specific gas constant (water), 0.46151805 kJ/kg·K; learning rate
R_a	arithmetic average surface roughness, μm
r	real discount rate; residual component
T	temperature, °C; construction period, years
\bar{T}	reduced temperature
V	volume, m ³
X	quantity of units needed to produce cumulative rated power
x	axial position, m
Y	capital cost of NOAK unit using Learning Curve, \$ (USD)
y	capital cost reduction factor for a pair of twin units
y_{actual}	original data point; most often determined by experimentation
$y_{calculated}$	new data point; most often calculated using a theoretical model, linear regression, etc.
z	capital cost reduction factor for two pairs of twin units, 0.74-0.85 (NEA/OECD, 2011)

Greek Letters

Δ	difference
α	thermal diffusivity, m^2/s
β	volume expansivity, $1/\text{K}$
δ	reduced density, $\frac{\rho}{\rho_{cr}}$
λ	thermal conductivity, $\text{W}/\text{m}\cdot\text{K}$
λ^*	reference thermal conductivity, $1.0 \times 10^{-3} \text{ W}/\text{m}\cdot\text{K}$
$\bar{\lambda}$	reduced thermal conductivity, $\frac{\lambda}{\lambda^*}$
μ	dynamic viscosity, $\text{Pa} \cdot \text{s}$
μ^*	reference dynamic viscosity, $1.0 \times 10^{-6} \text{ Pa}\cdot\text{s}$
$\bar{\mu}$	reduced dynamic viscosity, $\frac{\mu}{\mu^*}$
ν	kinematic viscosity, m^2/s
ρ	density, kg/m^3
ρ^*	critical density, $322 \text{ kg}/\text{m}^3$
$\bar{\rho}$	reduced density, $\frac{\rho}{\rho^*}$
τ	reduced temperature
ϕ	dimensionless Helmholtz free energy

Non-dimensional Numbers

Nu	Nusselt number $\left(\frac{HTC \cdot D}{k}\right)$
Pr	Prandtl number $\left(\frac{\mu \cdot c_p}{k}\right)$
$\bar{\text{Pr}}$	Averaged Prandtl number $\left(\frac{\mu \cdot \bar{c}_p}{k}\right)$
Re	Reynolds number $\left(\frac{G \cdot D}{\mu}\right)$

Subscripts

ave	average
b	bulk-fluid
cr	critical point
dht	deteriorated heat transfer
el	electrical
fl	flow
h	heated
i	index notation
in	inlet
out	outlet
pc	pseudocritical point
sat	saturated
t	time step position
th	thermal
U	uranium
w	wall
wet	wetted

Abbreviations and Acronyms

4S	Super Safe, Small and Simple
ABV	Nuclear Modular Water-cooled reactor (translation from Russian abbreviation)
ABWR	Advanced Boiling Water Reactor
AC	Alternating Current

Acct	Account
ACP	Advanced Chinese Pressurized-water reactor
ACPR	Advanced Chinese Pressurized-water Reactor
ACR	Advanced CANDU Reactor
AECL	Atomic Energy of Canada Limited
AFR	Advanced sodium-cooled Fast Reactor
AGR	Advanced Gas-cooled Reactor
A-HTR	Advanced High Temperature Reactor
AHTR	Advance High Temperature Reactor
AHWR	Advanced Heavy Water Reactor
ALFRED	Advanced Lead Fast Reactor European Demonstrator
ANTARES	Areva's New Technology and Advanced gas-cooled Reactor for Energy Supply
AP	Advanced Plant (Westinghouse Electric Company LLC, USA)
APWR	Advanced Pressurized Water Reactor
ARC	Advanced Reactor Concepts
ARIS	Advanced Reactors Information System (IAEA)
ASTRID	Advanced Sodium Technological Reactor for Industrial Demonstration
BARC	Bhabha Atomic Research Center (India)
BCC	Base Construction Cost
BN	Fast Sodium (translation from Russian abbreviations)
BREST-OD	Fast Reactor with Inherent safety Lead Coolant- Experimental Demonstration (translation from Russian abbreviation)
BWR	Boiling Water Reactor
CA	Copenhagen Atomics (Denmark)

CAD	Canadian Dollar
CANDU [®]	CANada Deuterium Uranium (reactor)
CAP	China Advanced Passive
CAREM	Central Argentina de Elementos Modulares (Argentina)
CCR	Compact Containment boiling-water Reactor
CEA	Atomic Energy Commission (translated from French abbreviation)
CFR	China Fast Reactor
CGNPC	China General Nuclear Power Corporation
CHF	Critical Heat Flux
CIAE	China Institute of Atomic Energy
CMSR	Compact Molten Salt Reactor
CNEA	National Atomic Energy Commission (translated from Spanish abbreviation)
CNNC	China National Nuclear Corporation
CNP	China Nuclear Power
COA	Code of Accounts
cor.	correlation
Corp.	Corporation
CPF	Coated-Particle Fuel
CRIEPI	Central Research Institute of Electric Power Industry (Japan)
CSF	Co-Siting Factor
D-B	Dittus-Boelter (correlation)
D&D	Decontamination and Decommissioning
DAS	Data Acquisition System

DCNS	Direction des Constructions Navales (France)
DHR	District Heating Reactor
DMS	Double MS (Modular Simplified and Medium Small)
EDF	Électricité de France
DHT	Deteriorated Heat Transfer
DoM	Degree of Modularization
ECS	Extended Corresponding State
EEC	Electrical Energy Consumption
Eff.	Efficiency
EFPD	Effective Full Power Days
EIA	Energy Information Administration
El.	Elements
ELFR	European Lead-cooled Fast Reactor
EM ²	Energy Multiplier Module
EMWG	Economic Modelling Working Group
ENHS	Encapsulated Nuclear Heat Source
Enrich.	Enrichment
EPC	Engineering, Procurement, and Construction
EPR	European Pressurized Reactor
Equip.	Equipment
ESBWR	Economic Simplified Boiling Water Reactor
EU	European Union
FBNR	Fixed Bed Nuclear Reactor

Fed.	Federal
FCF	Fuel Cycle Facility
FCM	Fully Ceramic Micro-encapsulated™ (fuel)
FOAK	First-Of-A-Kind
G4M	Gen4 Module
GE	General Electric (USA)
GIF	Generation IV International Forum
GFR	Gas-cooled Fast Reactor
GMFR	Gas-cooled Modular Fast Reactor
GT-MHR	Gas Turbine-Modular Helium Reactor
GTHTR	Gas Turbine High Temperature Reactor
HALEU	High-Assay Low-Enriched Uranium
HAPPY	Heating-reactor of Advanced low-Pressurized and Passive safety system
HEU	Highly Enriched Uranium
HDI	Human Development Index
HEC	High Efficiency Channel
HM	Heavy Metal
HLW	High-level waste
HPT	High Pressure Turbine
HT	Heat Transfer
HTMR	High Temperature Modular Reactor
HTR	High Temperature Reactor
HTR-PM	High Temperature Reactor Pebble-bed Modular

HWR	Heavy Water Reactor
IAEA	International Atomic Energy Agency
ID	Inner Diameter
IEA	International Energy Agency
IHT	Improved Heat-Transfer
ILW	Intermediate-level waste
IMR	Integrated Modular water Reactor
IMSR	Integral Molten Salt Reactor
Inc.	Incorporated
INEEM	Integrated Nuclear Energy Economic Model
INET	Institute of Nuclear Energy and Technology (China)
Int.	International
IPPE	Institute of Physics and Power Engineering (Obninsk, Russia)
IRIS	International Reactor Innovative and Secure
JAEA	Japan Atomic Energy Agency
JAERI	Japan Atomic Energy Research Institute
JSC	Joint Stock Company
KAERI	Korean Atomic Energy Research Institute (Korea S.)
KALIMER	Korea Advanced LIquid MEtal Reactor
KARAT	Boiling Nuclear Reactor of Autonomous Heat Supply (translation from Russian abbreviation)
KLT	Container-carrier cargo-Lighter Transport (translated from Russian abbreviation)
KP-FHR	Kairos Power-Fluoride-salt-cooled High-temperature Reactor
Lab.	Laboratory/Laboratories

LBE	Lead-Bismuth-Eutectic
LCOE	Levelized Cost of Electricity
LEADIR-PS	LEAD-cooled Integral Reactor- Passively Safe
LEU	Low-enriched uranium
LEU-Th	Low-enriched uranium and thorium
LF	Learning Factor
LFR	Lead-cooled Fast Reactor
LFR-AS/TL	Lead-cooled Fast Reactor-Amphora-Shaped/ Transportable Long-lived
LFTR	Liquid-Fluoride Thorium Reactor
LGR	Light-water-cooled, Graphite-moderated Reactor
LHR	Light water-cooled Heavy water-moderated Reactor
LLC	Limited Liability Company
LLW	Low-level waste
LMFBR	Liquid-Metal Fast Breeder Reactor
LMFR	Liquid-Metal-cooled Fast Reactor
LMR	Liquid-Metal-cooled Reactor
LNR	Large Nuclear Reactor
LSPR	LBE-Cooled Long-Life Safe Simple Small Portable Proliferation-Resistant Reactor
Ltd.	Limited
LUEC	Levelized Unit of Energy Cost
LUPC	Levelized unit product cost
LWR	Light Water Reactor

Max.	Maximum
MCFR	Molten Chloride Fast Reactor
MCSFR	Molten Chloride Salt Fast Reactor
MDF	Modular Design Factor
MF	Metallic Fuel
MHI	Mitsubishi Heavy Industries (Japan)
MHR	Modular Heat Tractor (translated from Russian abbreviation)
MHR-T	Modular Helium Reactor-high Temperature
Min.	Minimum
Mk1 PB-FHR	Mark 1 Pebble-Bed Fluoride-salt-cooled High-temperature Reactor
MMR	Micro Modular Reactor
MoveluX	Mobile-Very-small reactor for Local Utility in X-mark
MOX	Mixed OXide (fuel)
MRX	Marine Reactor
MSF	Molten Salt Fuel
MSFR	Molten Salt Fast neutron Reactor
MSK	Medvedev-Sponheuer-Karnik scale
MSR	Molten Salt Reactor
MSTW	Molten Salt Thermal Wasteburner reactor
N/A	Not Available/Not Applicable
Nat.	National
NDG	Nikita Dort-Goltz
NEA	Nuclear Energy Agency

NETL	National Energy Technology Laboratory (USA)
NHT	Normal Heat Transfer
NHR	Nuclear Heating Reactor
NIKIET	N.A Dollezhal Research and Development Institute of Power Engineering (translated from Russian abbreviation)
NIST	National Institute of Standards and Technology (USA)
No.	number
NOAK	N th -Of-A-Kind
NPCI	Nuclear Power Corporation of India
NPP	Nuclear Power Plant
NSSS	Nuclear Steam Supply System
NUWARD	NUclear forWARD
O&M	Operation and Maintenance
OCC	Overnight Capital Cost
OD	Outer Diameter
OECD	Organization for Economic Co-operation and Development
OKBM	Experimental Design Bureau of Mechanical-engineering (translated from Russian abbreviation)
OPG	Ontario Power Generation
PB-FHR	Pebble-Bed-Fluoride-salt High-temperature Reactor
PBMR	Pebble-Bed Modular Reactor
PBWFR	Pb-Bi-cooled direct contact Boiling Water Fast Reactor
PEACER	Proliferation-resistant Environment-friendly Accident-tolerant Continuable and Economical Reactor
PFBR	Prototype Fast Breeder Reactor

PGSFR	Prototype Gen-IV Sodium-cooled Fast Reactor
PHWR	Pressurized Heavy Water Reactor
PRISM	Power Reactor Innovative Small Module
PT	Pressure Tube
PV	Pressure Vessel
PWR	Pressurized Water Reactor
R&D	Research and Development
RAPID-L	Refueling by All Pins Integrated Design-Lunar-base
RDPE	Research and Development Institute of Power Engineering
REFPROP	REference fluid PROPERTIES
RITM	Reactor Integral Type Modular (translation from Russian abbreviation)
RMS	Root Mean Square
RMSE	Root Mean Square Error
RUTA	Reactor Plant for Heat Supply with Atmospheric pressure in the first circuit (translations from Russian abbreviation)
S.	South
S&MR	Small and Medium-sized Reactors
SC	SuperCritical
SC-HTGR	Steam Cycle-High Temperature Gas-cooled Reactor
SCW	SuperCritical Water
SCWR	SuperCritical Water-cooled Reactor
SEALER	Swedish Advanced Lead Reactor
SFR	Sodium-cooled Fast Reactor

SINAP	Shanghai Institute of Applied Physics (China)
SmAHTR	Small modular Advanced High-Temperature Reactor
SMART	System-integrated Modular Advanced Reactor
SMR	Small Modular Reactor
SNERDI	Shanghai Nuclear Engineering and Design Institute (China)
SNF	Spent Nuclear Fuel
SNP	State Nuclear Power (China)
SPIC	State Power Investment Corporation (China)
SSR	SuperSafe Reactor
SUPERSTAR	Sustainable Proliferation-resistance Enhanced Refined Secure Transportable Autonomous Reactor
SVBR	Lead-Bismuth Fast Reactor (translation from Russian abbreviation)
TCIC	Total Capital Investment Cost
Tech.	Technologies, Technology
Th.	Thermal
TRISO	TRi-structural ISOtropic
TRU	TransUranic
TMSR-LF	Thorium Molten Salt Reactor-Liquid Fuel
Tokyo Tech.	Tokyo Institute of Technology (Japan)
TVA	Tennessee Valley Authority
TWR-P	Travelling Wave Reactor-Prototype
UK	United Kingdom
UNITHERM	UNIversal THERMal reactor
Univ.	University

US	United States
USA	United State of America
USD	United States Dollar
USNC	Ultra Safe Nuclear Corporation
v.	version
VBER	Water Safe Power Reactor (translation from Russian abbreviation)
VHTR	Very High Temperature Reactor
VK	Water-cooled Boiling (translation from Russian abbreviation)
Vol.	Volume
VVER	Water Water Power Reactor (translation from Russian abbreviation)
W-SMR	Westinghouse Small Modular Reactor
WLFR	Westinghouse Lead-cooled Fast Reactor
WPu	Weapons-grade Plutonium

Chapter 1: Introduction

1.1: Current Status of Electricity Generation

Countries around the world continuously strive to economically develop and thereby improve the lives of their inhabitants. For both developed and developing nations, a steady source of energy is fundamental to sustaining these endeavors as there is a strong correlation between the Human Development Index (HDI) and electric energy consumption (EEC) per capita (see Figure 1-1). With the world population expected to continue to rise, the generation of electricity becomes all the more necessary to meet the needs of a larger populace. This can be achieved by using one of many renewable (solar, wind, geothermal, tidal, hydro, and biomass) and non-renewable (coal, oil, natural gas, and nuclear) energy sources.

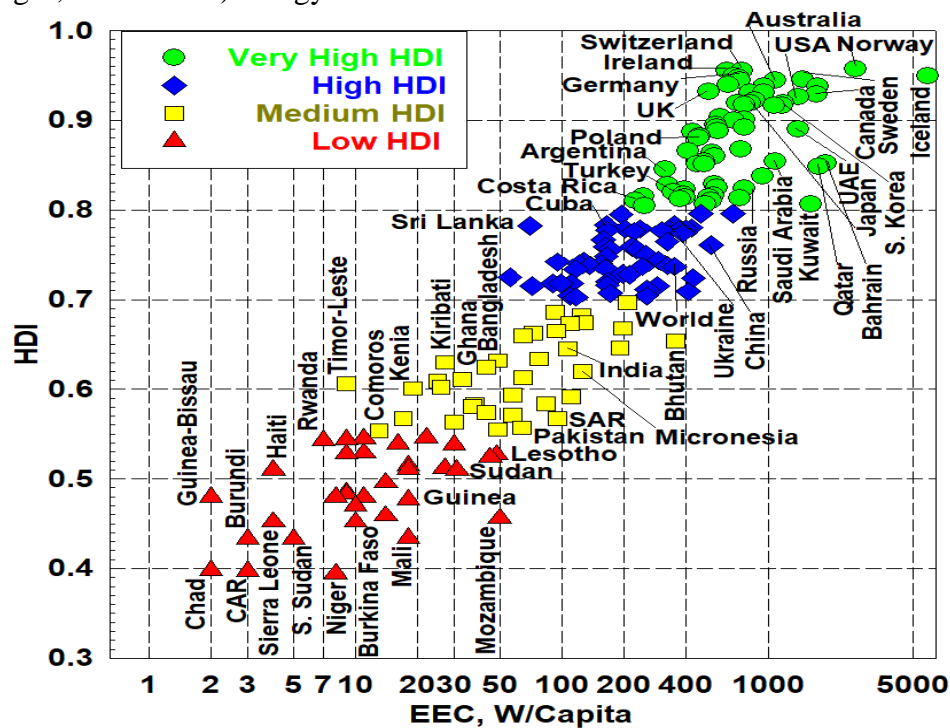


Figure 1-1: Human Development Index scores compared to the electrical energy consumption per capita in various countries (data taken from UNDP (2020), Worldometer (2021), and IEA (2021)(courtesy of I. Pioro)).

Globally, non-renewable energy sources account for 74.7% of all generated electrical energy (see Figure 1-2). Unfortunately, these, with the exception of nuclear, also have sizeable carbon footprints (see Figure 1-3) and given the international initiative to combat climate change, more

attractive avenues for electricity production need to be explored. On the other hand, renewable energy sources have low carbon footprints but are hampered by low capacity factors. The capacity factor of an electrical generating power plant is the ratio of the actual electrical energy generated in a year to the theoretical electrical energy generated in a year if the power plant was operating at full power without pause. A number of aspects impact a power plant's capacity factor including frequency/length of scheduled maintenance, any accidents/disruptions to electrical generation, and natural forces such as the amount of sunshine or wind in a given geographic region. Renewable energy sources rely on these natural forces to generate electricity meaning that during periods of time with reduced wind, solar, or tidal activity, electricity generation will stall. This prevents renewable energy sources from acting as baseloads to energy grids since their delivery of steady electricity is heavily dependent on natural conditions.

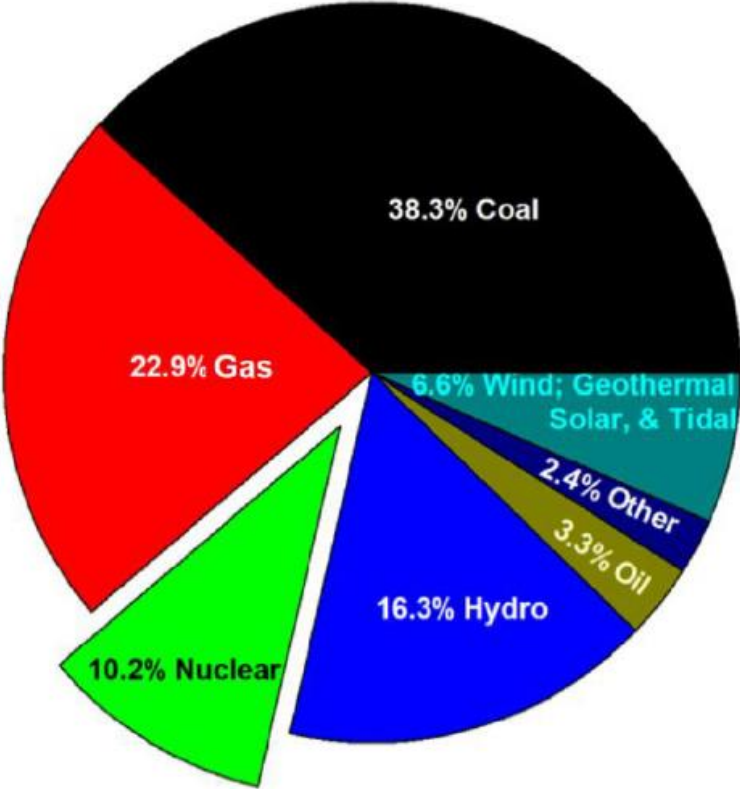


Figure 1-2: Distribution of global electrical energy generation according to types of energy sources (Pioro, ..., Dort-Goltz, 2020) (courtesy and copyright of ASME).

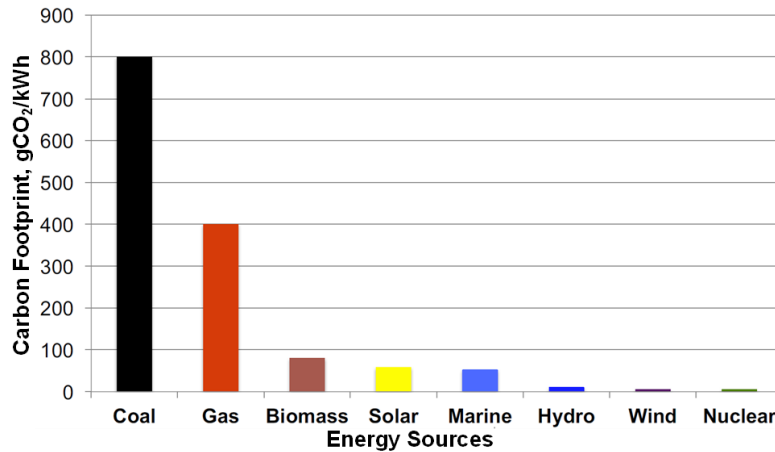


Figure 1-3: Carbon footprint of different energy sources (courtesy of Dr. J. Roberts, University of Manchester, UK; based on data from <http://researchbriefings.files.parliament.uk/documents/POST-PN-268/POST-PN-268.pdf>).

An amalgamation of the benefits presented by non-renewable fossil fuel energy sources (namely their dispatchability and ability to act as energy grid baseloads) and renewable energy sources exists in nuclear power. Nuclear power plants have very high capacity factors (see Table 1-1) and so are suited for ensuring a growing population meets its base energy demand. Additionally, the carbon footprint of nuclear power plants is significantly lower than fossil fuel power plants and is comparable to other renewable energy sources. Nuclear energy represents an effective solution to address the pressing energy and climate issues facing mankind in the coming decades. Unfortunately, there are obstacles facing the widespread adoption of nuclear power the most significant being public perception regarding the safety and reliability of nuclear power plants. Since the Fukushima-Daiichi accident in March of 2011, electricity generation from nuclear power dropped globally from around 14% to 10% currently with Japan, Germany, and the U.S.A shutting down 21, 11, and 9 nuclear reactors respectively (Pioro, ..., Dort-Goltz, 2020). Even with an influx of new reactors being built elsewhere in the world (with five non-nuclear nations working towards incorporating nuclear energy), the total quantity of reactors operating in the world has decreased since March 2011 (see Table 1-2). Much of this has been due to negative

public perception of nuclear power following the Fukushima-Daichii accident (Pioro et al., 2021).

Table 1-1: Average capacity factors of a selection of energy sources (Pioro and Kirillov, 2013).

No.	Power Plant Type	Location	Year	Capacity Factor, %
1	Nuclear	USA	2010	91
		UK	2011	66
2	Combined-cycle	UK	2011	48
			2007-2011	62
3	Coal-fired	UK	2011	42
4	Hydroelectric	UK	2011	39
		World (average)	-	44
		World (range)	-	10-99
5	Wind	UK	2011	30
		World	2008	20-40
6	Wave	Portugal	-	20
7	Concentrated-solar thermal	USA California	-	21
8	Photovoltaic solar	USA Arizona	2008	19
		USA Massachusetts	-	12-15
		UK	2011 2007-2011	5.5 8.3
9	Concentrated-solar photovoltaic	Spain	-	12

Table 1-2: Quantity of nuclear-power reactors connected to electrical grids and any forthcoming units as of July 2020 (Pioro, ..., Dort-Goltz, 2020) (courtesy and copyright of ASME). Updated using latest information from Pioro et al. (2021).

Rank by No	Reactor type (% total reactors / average installed capacity)	No. of units		Installed capacity, GW _{el}		Forthcoming units ¹	
		As of March 2021	Before Mar. 2011	As of March 2021	Before Mar. 2011	No. of units	GW _{el}
1	Pressurized Water Reactors (PWRs) (68% / 950 MW _{el})	302 ↑	268	288 ↑	248	39+35?	45+37?

¹ ?-indicates indefinite start date; *-forthcoming reactor is a Generation IV helium-cooled reactor

Rank by No	Reactor type (% total reactors / average installed capacity)	No. of units		Installed capacity, GW _{el}		Forthcoming units ¹	
		As of March 2021	Before Mar. 2011	As of March 2021	Before Mar. 2011	No. of units	GW _{el}
2	Boiling Water Reactors (BWRs) or Advanced BWRs (15% / 1025 MW _{el})	63 ↓	92	65 ↓	84	4?	5.3?
3	Pressurized Heavy Water Reactors (PHWRs) (11% / 500 MW _{el})	49 ↓	50	24 ↓	25	2+5?	1.3+3.3?
4	Advanced Gas-cooled Reactors (AGRs) (CO₂-cooled) (3% / 550 MW _{el})	14 ↓	18	8 ↓	9	1?*	0.2?*
5	Light-water-cooled, Graphite-moderated Reactors (LGRs) (3% / 715 MW _{el})	12 ↓	15	8 ↓	10	0	0
6	Liquid-Metal Fast-Breeder Reactors (LMFBRs – SFRs) (0.5% / 690 MW _{el})	2 ↑	1	1.4 ↑	0.6	2+1?	1.1+0.6?
In total		442 ↓	444	395 ↑	377	44+45?	48+46?

Another issue plaguing nuclear energy is the relatively low thermal efficiency of water-cooled nuclear power plants when compared to modern fossil-fuel-fired thermal power plants. Coal-fired power plants have been employing a supercritical water (SCW) Rankine cycle (pressures greater than 22.064 MPa) for their power generation since the 1950s (Pioro and Duffey, 2007). Such a transition from sub-critical conditions (pressures below 22.064 MPa; usually from 7-16 MPa) has allowed coal-fired power plants to reach thermal efficiencies up to 55% (Pioro, 2016). Additionally, combined cycle power plants that employ a dual power generation configuration (usually with a topping Brayton cycle and a bottoming Rankine cycle) have achieved thermal efficiencies up to 62% (Pioro, 2016). Comparatively, water-cooled land-based nuclear power

plants, which make up around 68% of all global nuclear reactors and use sub-critical Rankine power cycles (Pioro,..., Dort-Goltz, 2020), have achieved thermal efficiencies up to 38% with the latest Generation III+ designs such as the EPR developed by AREVA (IAEA, 2020a). In fact, the highest thermal efficiencies achieved by any nuclear power plant is the carbon-dioxide-cooled Advanced Gas-cooled Reactors (AGRs) with efficiencies around 42%. This is because of the higher outlet temperatures for the core coolant, especially compared to water-cooled reactors, even though the AGR also employs a sub-critical Rankine power cycle (Nonboel, 1996).

However, no new AGRs have been built in the last 32 years and there are no plans to construct any more.

To address these drawbacks, the Generation IV International Forum (GIF) was organized in 2001 by 10 countries with the goal of stimulating the development of revolutionary reactor designs that would be safer and more efficient than the current fleet of nuclear power plants.

1.2: GIF and Generation IV Reactor Concepts

In 2001, Canada along with nine other countries came together and created the Generation IV International Forum (GIF). The goal of this organization is to facilitate the research and development of a new generation of reactors that are safer, more efficient, and more economical than the current global fleet of nuclear reactors. These reactors will emphasize sustainable and efficient fuel systems that reduce the amount of waste generated by the nuclear fuel cycle, provide a clear economical advantage over their lifetime compared to other energy sources, further reduce the likelihood of core damage and meltdown by greater implementation of passive safety systems, and include more robust security systems to protect against proliferation and theft (GIF, 2002). Motivated by the above-stated guidelines, GIF conducted a review of hundreds of different reactor concepts and settled on six that they concluded were the most attractive options.

These are the Gas-cooled Fast Reactor/High Temperature Reactor (GFR/HTR), Very High Temperature Reactor (VHTR), Sodium-cooled Fast Reactor (SFR), Lead-cooled Fast Reactor (LFR), Molten Salt Reactor (MSR), and the SuperCritical Water-cooled Reactor (SCWR) (GIF, 2020). The roadmap for nuclear reactor development is given in Figure 1-4 with a hopeful Generation IV commercial start date sometime in the 2030s from the figure below.

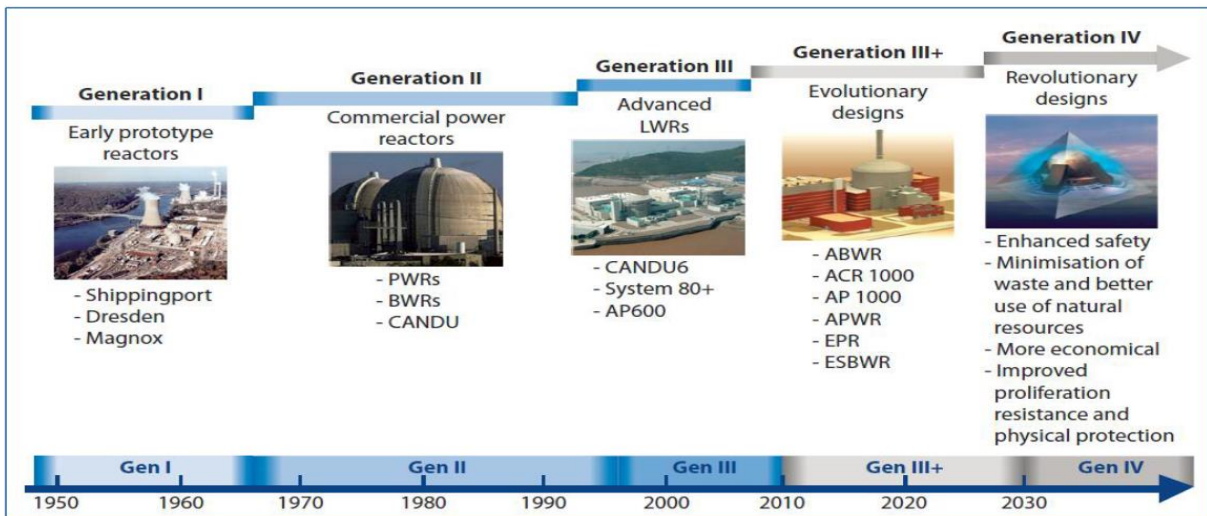


Figure 1-4: Nuclear reactor generation roadmap (Nuclear Energy Today, 2012).

An overview of each Generation-IV nuclear reactor system including reactor coolant type, power cycle approach, and thermal efficiency is given below. All information was taken from the *Handbook of Generation IV Nuclear Reactors* (Pioro, 2016).

1.2.1: Gas-cooled Fast Reactor (High Temperature Reactor) (GFR/HTR)

Table 1-3: Overview of GFR Parameters.

Reactor Parameters	
Reactor Design	PV
Neutron Spectrum	Fast
Reactor Coolant/Moderator	Helium/-
Outlet Reactor Pressure/Temperature	$P=9$ MPa, $T=850$ °C
Power Cycle	Brayton/ Combined (Primary Brayton; Backup Rankine)
Type of Nuclear Power Plant Cycle	Direct (Brayton)/Indirect (Combined)
Working Power Fluid	He (Brayton)/ He-N ₂ (Combined Brayton) + H ₂ O (Combine Rankine)

Reactor Parameters	
Thermal Efficiency	≥50%

1.2.2: Very High Temperature Reactor (VHTR)

Table 1-4: Overview of VHTR Parameters.

Reactor Parameters	
Reactor Design	PV
Neutron Spectrum	Thermal
Reactor Coolant/Moderator	Helium/Graphite
Outlet Reactor Pressure/Temperature	$P=7$ MPa, $T=1000$ °C
Power Cycle	Brayton/Combined (Primary Brayton; Backup Rankine)
Type of Nuclear Power Plant Cycle	Direct/Indirect (Combined)
Working Power Fluid	He (Brayton)/CO ₂ (Combined Brayton) + H ₂ O (Combine Rankine)
Thermal Efficiency	≥55%

1.2.3: Sodium-cooled Fast Reactor (SFR)

Table 1-5: Overview of SFR Parameters.

Reactor Parameters	
Reactor Design	Vessel
Neutron Spectrum	Fast
Reactor Coolant/Moderator	Sodium
Outlet Reactor Pressure/Temperature	$P=0.1$ MPa, $T\sim 550$ °C
Power Cycle	Brayton, Rankine
Type of Nuclear Power Plant Cycle	Indirect
Working Power Fluid	SC CO ₂ (Brayton), H ₂ O (Rankine)
Thermal Efficiency	~40%

1.2.4: Lead-cooled Fast Reactor (LFR)

Table 1-6: Overview of LFR Parameters.

Reactor Parameters	
Reactor Design	Vessel
Neutron Spectrum	Fast
Reactor Coolant/Moderator	Lead/-
Outlet Reactor Pressure/Temperature	$P=0.1$ MPa, $T=540$ °C
Power Cycle	Brayton, SC or Sub-critical Rankine
Type of Nuclear Power Plant Cycle	Indirect
Working Power Fluid	SC CO ₂ (Brayton), H ₂ O (Rankine)
Thermal Efficiency	~41-43%

1.2.5: Molten Salt Reactor (MSR)

Table 1-7: Overview of MSR Parameters.

Reactor Parameters	
Reactor Design	PV
Neutron Spectrum	Thermal or Fast
Reactor Coolant/Moderator	Molten Salt Mix/Graphite (if Thermal)
Outlet Reactor Pressure/Temperature	$P=0.1$ MPa, $T=700-800$ °C
Power Cycle	Brayton, Rankine
Type of Nuclear Power Plant Cycle	Indirect
Working Power Fluid	SC CO ₂ (Brayton), H ₂ O (Rankine)
Thermal Efficiency	~50%

1.2.6: SuperCritical Water-cooled Reactor (SCWR)

Table 1-8: Overview of SCWR Parameters.

Reactor Parameters	
Reactor Design	PV/PT
Neutron Spectrum	Thermal
Reactor Coolant/Moderator	SC H ₂ O/Heavy Water
Outlet Reactor Pressure/Temperature	$P=25$ MPa, $T=\text{up to } 625$ °C
Power Cycle	Rankine
Type of Nuclear Power Plant Cycle	Direct
Working Power Fluid	SC H ₂ O (Rankine)
Thermal Efficiency	45-50%

In addition to being used for electricity generation, many of these reactors have additional benefits that are in line with GIF guidelines (Pioro, 2016).

- The high outlet reactor temperatures of the GFR, VHTR, MSR, and SCWR are ideal for high-temperature electrolysis in the production of hydrogen or water de-salination in regions where fresh water is in short supply.
- The SFR and the LFR will be operating on closed fuel cycles with long refueling intervals characterized by actinide management and recycling, thereby reducing the overall amount of waste produced from the nuclear fuel.

- The VHTR, with the highest outlet reactor temperature of all Gen-IV reactors, is a prime candidate for industrial use in the chemical, oil, and iron industries where high temperatures are required for many of the involved processes.
- The different types of molten salt fuel mixture used in MSR's lend themselves to the burning of transuranic (TRU) waste, thus helping reduce waste from other reactors, in addition to rendering the MSR near immune against a core meltdown, greatly increasing the safety.
- The higher thermal efficiencies of Generation IV reactors ensure that fuel is utilized more thoroughly so that all of these reactors, regardless of fuel cycle, generate less waste heat, reducing the amount of thermal pollution in the water sources used for cooling.

The Generation IV reactors are all at different stages of development with some still in the conceptual phase and others already operational. Among these, the SCWR with two primary designs (pressure-vessel and pressure-tube), the MSR, with two main designs (Molten Salt Fast Neutron Reactor (MSFR) and Advanced High Temperature Reactor (AHTR)), and GFR are still purely conceptual with no plans of physical development for a demonstration reactor in the foreseeable future (World Nuclear Association, 2020a). Currently under construction in China is the high temperature reactor pebble-bed modular (HTR-PM) demonstration VHTR reactor that will be put into operation sometime in 2021 (Pioro, ..., Dort-Goltz, 2020). In Russia, a construction license has been issued for the BREST-OD-300 reactor and once built (scheduled for the end of 2026), it will be the first demonstration LFR in the world (World Nuclear News, 2021). Additionally, the BN-800 SFR was put into operation in 2016 in Russia (joining the BN-600) and another SFR, Kalpakkam PFBR of 500 MW_{el}, is currently under construction in India (World Nuclear Association, 2020a).

Once commercially available, Generation-IV reactors will supposedly resolve many of the issues plaguing past generation reactors and will be economically competitive against other energy sources, namely fossil fuels, while further reducing the environmental impact of nuclear energy. But the deployment of another fleet of large nuclear reactors (LNRs) does not address the problem of providing electricity to small and remote communities with no connection to a reliable energy grid. To resolve this, a new type of reactor called the small modular reactor (SMR) is required.

1.3: SMRs

The problems associated with supplying electricity to remote communities by LNRs are remedied with the existence of small nuclear reactors. As described in *Handbook of Small Modular Reactors* (2021), these typically have electrical power ratings of around 100 MW_{el} or smaller and in general are defined to be reactors with less than 300 MW_{el} power. These were the very first types of nuclear reactors constructed back in the 1950s and have found extensive deployment in naval propulsion namely icebreakers and submarines. However, they can also be used to supply small settlements such as military bases with electrical power. The drawback of these reactors for commercial usage is their economic cost. When compared to LNRs, small nuclear reactors are less expensive to make in absolute cost but they also generate less electricity and so building multiple units to match the production of a single LNR may end up costing more. For rural usage, diesel generators and other fossil fuel sources are cheaper to make than small nuclear reactors while also generating the same amount of electricity. As such, modifications to the design of small reactors are needed in order to make them more economically attractive. This can be achieved through adopting the technique of modularization when constructing the Nuclear Steam Supply System (NSSS) though this can be applied to other sections of the SMR power plant.

Further explained in *Handbook of Small Modular Reactors* (2021), modularization in itself is not a new phenomenon and various modular design techniques have been employed by different industries for decades beginning near the middle half of the 20th century. Applying this technique to a NSSS would mean mass producing key parts in factories and then assembling the NSSS from these parts at the construction site. Thus, a SMR is a nuclear reactor whose power rating is smaller than 300 MW_{el} and whose NSSS components were constructed using modular building techniques. The advantages of SMRs are their modularity and size. Using modularization can significantly reduce the cost of creating a small nuclear reactor making it an economically competitive option in both small and large energy grid settings (*Handbook of Small Modular Reactors*, 2021). Building multiple SMRs on a single power-generating site will therefore theoretically not cost any more than an LNR and the ability to put into operation the SMRs as the power-generating unit is being built means early revenue that can offload some of the project costs. For rural areas that need the electrical output of an SMR, SMRs would now have similar economic performance to fossil fuel sources but with a smaller environmental impact (*Handbook of Small Modular Reactors*, 2021). The economic argument for the development of SMRs has further been explored and supported by Boarin et al. (2012), Locatelli et al. (2014, 2017), and Lokhov et al. (2013),

Many countries with nuclear experience have begun developing SMR concepts that use established water-cooling technology in addition to designs that utilize Generation-IV technologies (Pioro,..., Dort-Goltz, 2020). A comprehensive list of these designs organized by country can be found in Appendix A. To note from Pioro,...,Dort-Goltz (2020), only one SMR concept, the KLT-40S based off reactors used in Russian nuclear icebreakers, has been put into operation in Port of Pevek, Russia in 2019. Four other SMRs are currently being constructed;

RITM-200M in Russia, CAREM in Argentina, and the CFR-600 and HTR-PM in China (Piro, ..., Dort-Goltz, 2020). The other designs are all in pre-construction development with different levels of design finalization (refer to Section 2.4). During this phase, the physical parameters of the reactor are determined and adjusted according to its specific performance objectives (electricity generation, de-salination etc.). One of the parameters that is investigated is the thermal performance of the reactor core namely the heat transfer characteristics between the fuel and coolant, a process that invokes the need of thermalhydraulics.

1.4: Heat Transfer and NIST REFPROP

Determination of the coolant heat transfer characteristics in a nuclear reactor usually begins using a simplified experimental setup, most often with vertical bare tubes that match the hydraulic diameter and length of the proposed coolant channels in the reactor (Dort-Goltz et al., 2021a). Once experimental data have been obtained, heat transfer correlations can be developed and then used to explore the different heat transfer regimes that may exist during reactor operation. Such a process is globally currently underway with supercritical fluids such as supercritical CO₂ and supercritical H₂O (Piro, 2019). This is motivated largely by their proposed use as coolants in Generation IV LNRs and SMRs and so the development of heat transfer correlations at supercritical conditions for CO₂ and H₂O is required. This thesis reports focuses exclusively on heat transfer through SCW in vertical bare tubes.

According to Piro and Duffey, (2007), development of heat transfer correlations for supercritical fluids began as early as the 1930s. It was only in the 1950s that supercritical fluids, namely water, were seriously considered for commercial use in fossil fuel plants that up until that point had been using sub-critical water in their power cycles. Supercritical fluids, unlike sub-critical fluids, do not have a distinct phase transition from the liquid to gas so the concept of

critical heat flux (CHF) and the possibility of dryout do not apply and thus make them an attractive option as both a coolant and power cycle fluid (Pioro and Duffey, 2003). Around this time during the 1950s and 1960s, the first designs of the SCWR were concocted though they were put on hold due to technological limitations. The coal industry did eventually make the switch to using SCW in coal-fired power plants and achieved significant increases in thermal efficiency. Indeed, this is another benefit of using SCW, or CO₂, in nuclear reactors and will help the nuclear industry match the fossil fuels industry in thermal efficiency (Pioro and Duffey, 2007).

Several correlations exist that can be used for heat transfer in SCW including Dittus-Boelter (1930), Bishop et al. (1964), Swenson et al. (1965), and Jackson (2002) (Pioro and Duffey, 2007). In recent years, correlations were developed by Mokry et al. (2009) and Gupta et al. (2011) that better predicted heat transfer coefficients (*HTCs*) and inside wall temperatures (T_w 's) of SCW in vertical bare tubes when compared to already established correlations. The data used in this thesis was experimentally obtained by Kirillov et al. (2003) in Russia at a SCW facility using vertical bare tube arrangements of 4 m and 1 m lengths. However, only the 4 m long dataset was considered when the Mokry et al. (2009) and Gupta et al. (2011) correlations were formulated due to the limited amount of data collected in the 1 m long dataset. Application of these correlations to the 1-m long dataset is still useful especially when analyzing the heat transfer characteristics of an SMR given the similarities in magnitude of the proposed fuel channels (Pioro, ..., Dort-Goltz, 2020). All these correlations are still limited in that they cannot accurately predict the onset of the deteriorated heat transfer (DHT) regime in SCW in the 4 m long dataset (Pioro, 2019). This regime is characterized by lower-than-expected *HTCs* and thus higher-than-expected T_w 's that, although not as destructive as a CHF regime, can still damage the

fuel rods and shorten their lifetime. The development of a heat transfer correlation that can predict DHT was not covered in this thesis work and instead the focus was put on analyzing the 1-m long dataset with the Mokry et al. (2009) and Gupta et al. (2011) correlations.

These correlations, as any other, depend on the thermophysical properties of the target fluid including specific heat capacity, specific enthalpy, Prandtl number, dynamic viscosity, and so forth. Numerical values of these properties can be obtained by using thermophysical reference programs such as NIST REFPROP. The term REFPROP is an acronym for REFERENCE fluid PROPERTIES and the program itself accurately calculates the thermophysical properties of up to 147 pure fluids, 5 pseudo-pure fluids, and mixtures with up to 20 components (NIST, 2018). A screenshot of the REFPROP user interface is included in Figure 1-5 for illustration.

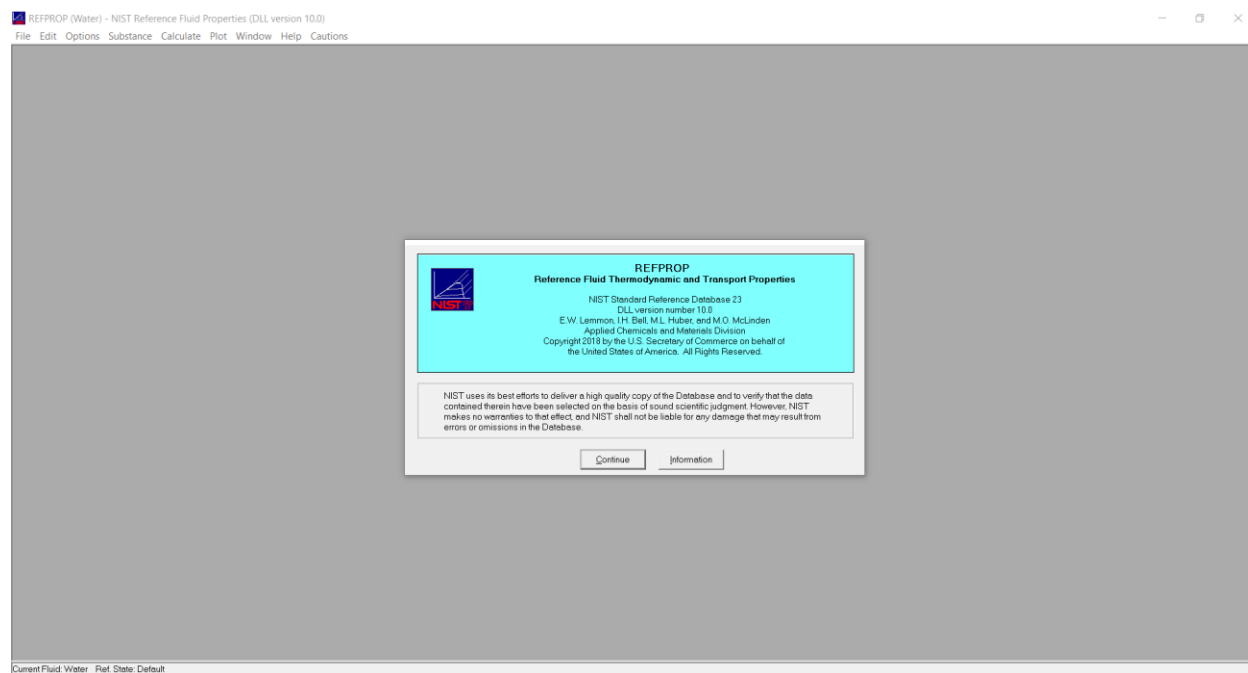


Figure 1-5: NIST REFPROP v.10 startup menu (NIST, 2018).

The software itself is not open source and a license must be purchased in order to use it. Once obtained, the main source code is available to the user but modification/alteration of these files must be acceptable under the licensing agreement. When implemented into a computer program,

REFPROP can be used to calculate the required thermophysical properties to calculate the $HTCs$ and T_w 's using the heat transfer correlations. The version of REFPROP used in this analysis is version 10 (v.10) and it was released in 2018. Like the other versions of REFPROP, this current iteration continues to use a theoretical approach to calculating the values of these thermophysical properties across a wide range of pressures and temperatures for water. Near the critical point of water, stated by REFPROP to be 22.064 MPa and 373.94 °C, a number of these primary thermophysical properties, such as specific heat capacity and thermal conductivity, begin to attain values approaching infinity. Caution must be taken when performing a heat transfer analysis near the critical point of water due to this non-physical behavior.

1.5: Objectives

The objectives for this thesis are as follows,

- Investigate NIST REFPROP v.10's handling of the primary thermophysical properties near the critical point of water by analyzing the effect a change in temperature increment and range will have on the values of said thermophysical properties.
- Investigate NIST REFPROP v.10's calculation of secondary thermophysical properties by calculating these in Excel using their given formulae and then comparing to the values generated by REFPROP v.10.
- Apply the Dittus-Boelter (1930), Mokry et al. (2009), and Gupta et al. (2011) heat transfer correlations using Python to the 1 m long dataset of experimental $HTCs$ and T_w 's of SCW.
- Explore whether the 1 m long dataset exhibits an onset of the DHT regime and whether or not the aforementioned correlations can predict this behavior.

- Perform a levelized unit of energy cost analysis of the SuperSafe Reactor (SSR), a SCWR-type SMR, and analyze whether this reactor is economically competitive when compared to other energy sources.

The overall goal of this thesis is to perform a preliminary analysis on the thermalhydraulic and economic performance of the SSR and inspect the viability of putting into operation an SCWR-type SMR.

Chapter 2: Literature Review

2.1: General Overview of Heat Transfer in SCW

Discussions regarding the heat transfer of SCW necessitates the definition of several key terms.

These are listed below (Pioro and Duffey, 2007):

- **Compressed Fluid**- a fluid with a pressure above its critical pressure but with a temperature below its critical temperature
- **Critical Point**-(also called the critical state) is a thermodynamic point where the distinction between liquid and vapour no longer exists. The fluid is now a single-phase entity characterized by phase-state parameters such as T_{cr} (critical temperature), P_{cr} (critical pressure), and V_{cr} (critical volume) that are unique to each pure substance
- **Deteriorated Heat Transfer (DHT)**-a heat transfer regime characterized by lower values of the wall HTC compared to those in the normal heat transfer regime. Thus, higher T_w 's are reached within some, or all, of the test section.
- **Improved Heat Transfer (IHT)**-a heat transfer regime characterized by higher values of the wall HTC compare to those in the normal heat transfer regime. Thus, lower T_w 's are reached within some, or all, of the test section.
- **Near-critical point**-a narrow region around the critical point where all the thermophysical properties of a pure fluid exhibit rapid variations.
- **Normal Heat Transfer (NHT)**- a heat transfer regime characterized by wall HTC similar to those appearing in subcritical, convective heat transfer far from the critical/pseudocritical regions. These can be calculated according to conventional, single-phase Dittus-Boelter-type correlations.
- **Pseudo-boiling**- a physical phenomenon, similar to subcritical pressure nucleate boiling, that may appear at supercritical pressures. This occurs due to the heating of a

supercritical fluid with a bulk-fluid temperature below the pseudocritical temperature (i.e liquid-like), causing some layers near a heating surface to attain temperatures above the pseudocritical temperature (i.e gas-like). The low-density, gas-like fluid leaves the heating surface in the form of variable density (bubble) volumes. During pseudo-boiling, the wall HTC usually increases i.e IHT regime.

- **Pseudocritical line**-a line consisting of pseudocritical points
- **Pseudocritical point**-a point at a pressure above the critical pressure and at a temperature (above the critical temperature) corresponding to the maximum value of the specific heat for this particular pressure. This state is characterized by the parameters P_{pc} and T_{pc} .
- **Pseudo-film boiling**-a physical phenomenon similar to subcritical pressure film boiling that may appear at supercritical pressures. During this process, a low-density fluid (temperature above the pseudocritical temperature i.e gas-like) prevents a high-density fluid (temperature below the pseudocritical temperature i.e liquid-like) from contacting (“rewetting”) a heated surface. Pseudo-film boiling leads to the DHT regime.
- **Supercritical fluid**-a fluid whose pressure and temperature are higher than its critical pressure and temperature.
- **Supercritical steam**-a term widely used in literature when referring to supercritical steam generators and turbines. This is not a unique entity and is instead just SCW due to the single-phase nature of supercritical fluids.
- **Superheated steam**-steam that exists at pressures below the critical pressure but at temperatures above the critical temperature. Also referred to as overheated steam.

A graphical representation of the different types of phases for a fluid near its critical point can be seen in Figure 2-1 below:

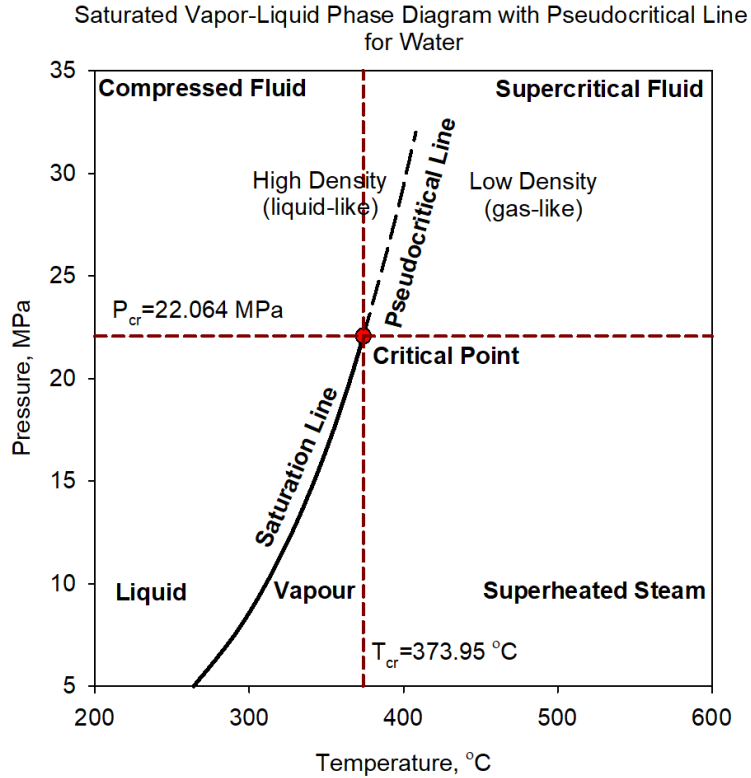


Figure 2-1: Pressure-Temperature diagram for water around its critical point (based on data from NIST (2018)).

The critical point of water is officially given to be $T_{cr}=373.95\text{ °C}$, $P_{cr}=22.064\text{ MPa}$ (NIST, 2018).

In this state, water does not undergo the usual transition from a saturated liquid to a saturated vapour that is characteristic at subcritical pressures. Instead, the water now exists in a single phase and so the concerns associated with critical heat flux and dryout are no longer relevant (Piro and Duffey, 2003). However, the thermophysical properties of water as a supercritical fluid change dramatically near the critical point and around the pseudocritical temperatures. A comparison of the properties for water at critical ($P_{cr}=22.064\text{ MPa}$) and supercritical ($P=25\text{ MPa}$) conditions are given in Figure 2-2. Some pseudocritical temperatures and their corresponding specific heat values between 23 to 50 MPa are given in Table 2-1. In general, the specific heat value peak that determines the pseudocritical temperature flattens at higher pressures and becomes less and less defined as illustrated in Figure 2-3.

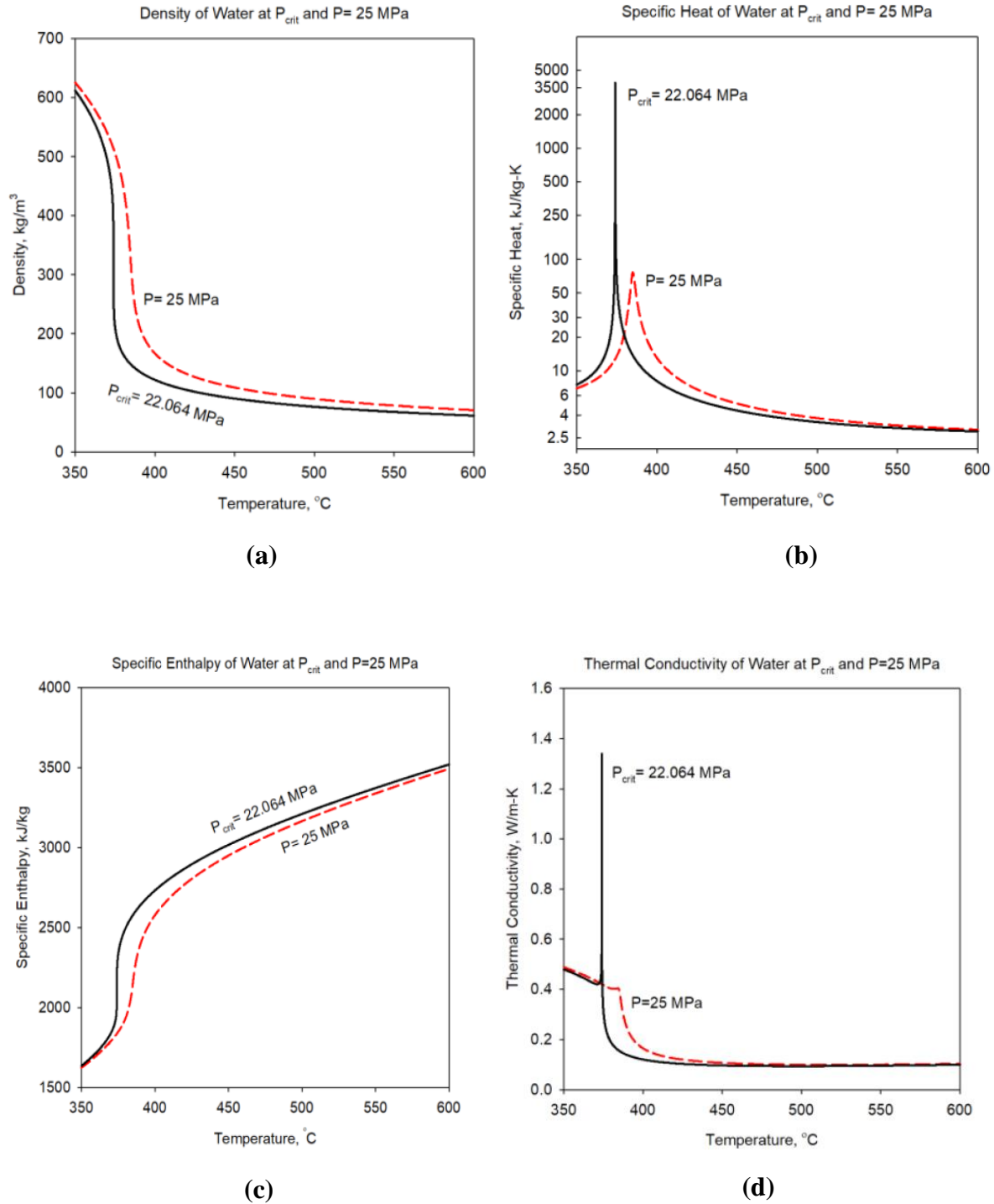
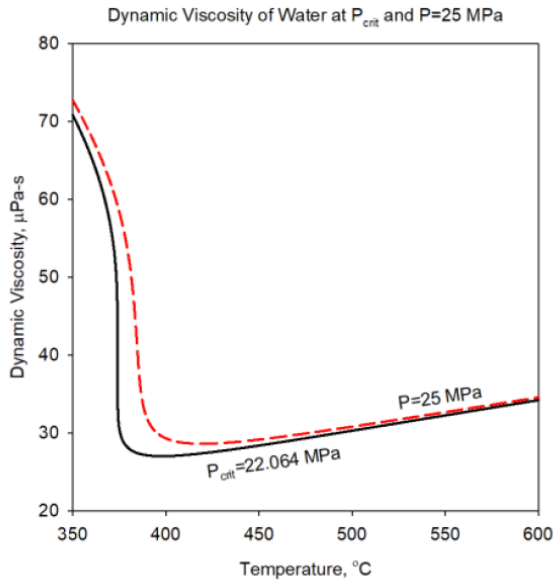
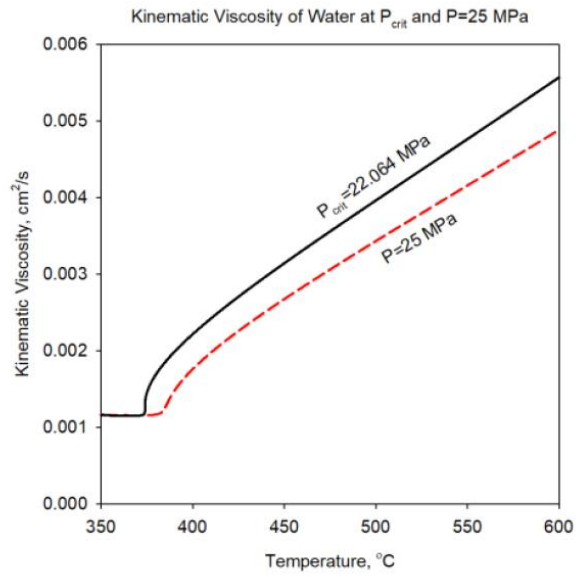


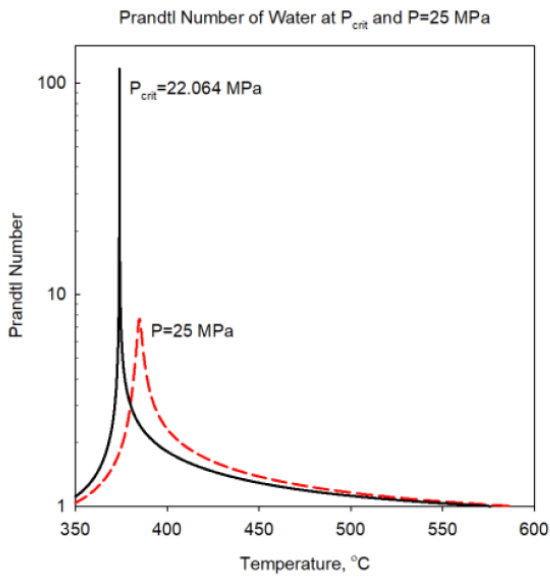
Figure 2-2: Thermophysical properties of water at $P_{cr}=22.064$ MPa and $P=25$ MPa; (a)-Density; (b)-Specific Heat; (c)-Specific Enthalpy; (d)-Thermal Conductivity (based on data from NIST (2018)).



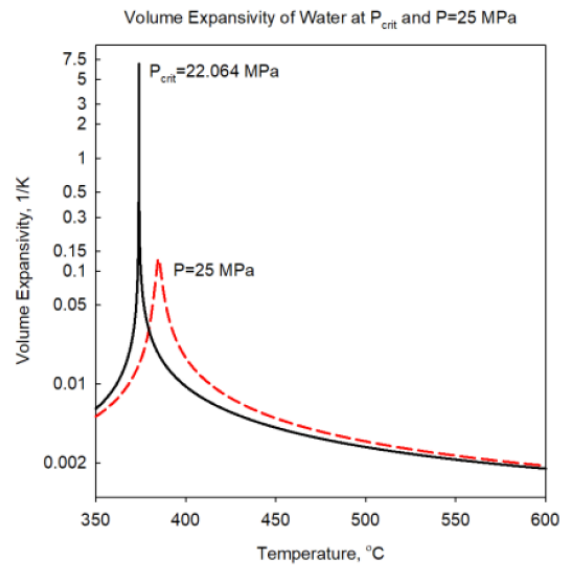
(e)



(f)



(g)



(h)

Figure 2-2: Thermophysical properties of water at $P_{cr}=22.064$ MPa and $P=25$ MPa; (e)-Dynamic Viscosity; (f)-Kinematic Viscosity; (g)-Prandtl Number; (h)-Volume Expansivity (based on data from NIST (2018)).

Table 2-1: Pseudocritical temperatures and peak specific heat values for water at select pressures (data from NIST (2018)).

Pressure, MPa	Pseudocritical Temperature, °C	Peak Value of Specific Heat, kJ/kg·K
23	377.5	284.3
24	381.2	121.9
25	384.9	76.4
30	401.9	27.0
35	416.7	17.2
40	430.3	13.2
45	443.1	11.0
48	450.2	10.1
49	452.5	9.9
50	454.8	9.6

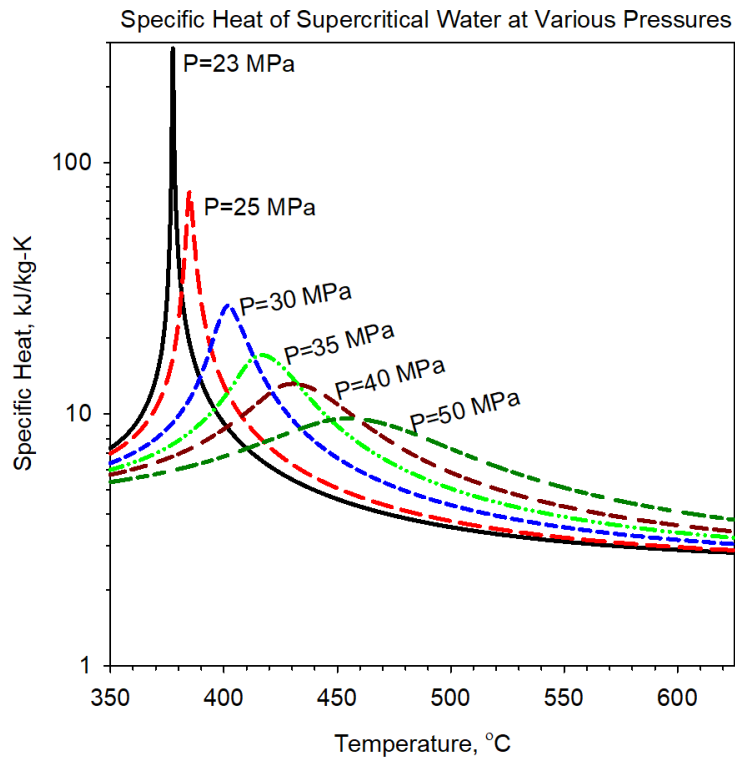


Figure 2-3: Specific Heat-Temperature graph for water at various pressures above $P_{cr}=22.064$ MPa (based on data from NIST (2018)).

SCWRs and SMRs based off the larger SCWRs, will mainly operate at pressures around 25 MPa. This is to provide a safety buffer during operation so that the SCW coolant does not experience pressure drops below P_{cr} in certain parts of the fluid. If the operating pressure were to

be set closer to P_{cr} , there is a chance that part of the coolant would drop below P_{cr} and so become a two-phase fluid. The resultant vaporization could cause significant damage to the fuel channel in the reactor core and lead to an extensive disruption to operation (Peiman, 2011). As a result of the chosen operating pressure, physical phenomena (such as pseudo-boiling) associated with the greatly varying properties of SCW may be present during reactor operation. The peaks of some of the thermophysical properties do not necessarily occur at the pseudocritical temperature as does the specific heat (Piro and Duffey, 2007). However, these extremum values do appear within close proximity to the pseudocritical temperature. As evidenced in Figure 2-2, the thermophysical properties of SCW experience the most rapid amount of change roughly around the pseudocritical temperature, a range of about 25 degrees on either side of the pseudocritical temperature. This is better exemplified in Figure 2-4 where several thermophysical properties at a supercritical pressure are projected together across the SCWR operating temperature range.

This process is what causes the onset of pseudo-boiling and pseudo-film boiling in SCW.

Around the pseudocritical temperature, the density of the fluid will change dramatically causing it to go from a high-density, liquid-like thermodynamic state to the low-density, gas-like thermodynamic state. Since the bulk-fluid temperature (T_b) of a fluid is often taken to be its mean temperature, there will be sections of SCW whose temperature is at or above the pseudocritical temperature. Thus, a mix of low-density and high-density SCW will ensue. As the bulk-fluid temperature approaches the pseudocritical temperature, a greater proportion of the SCW will achieve temperatures above the pseudocritical temperature and become gas-like.

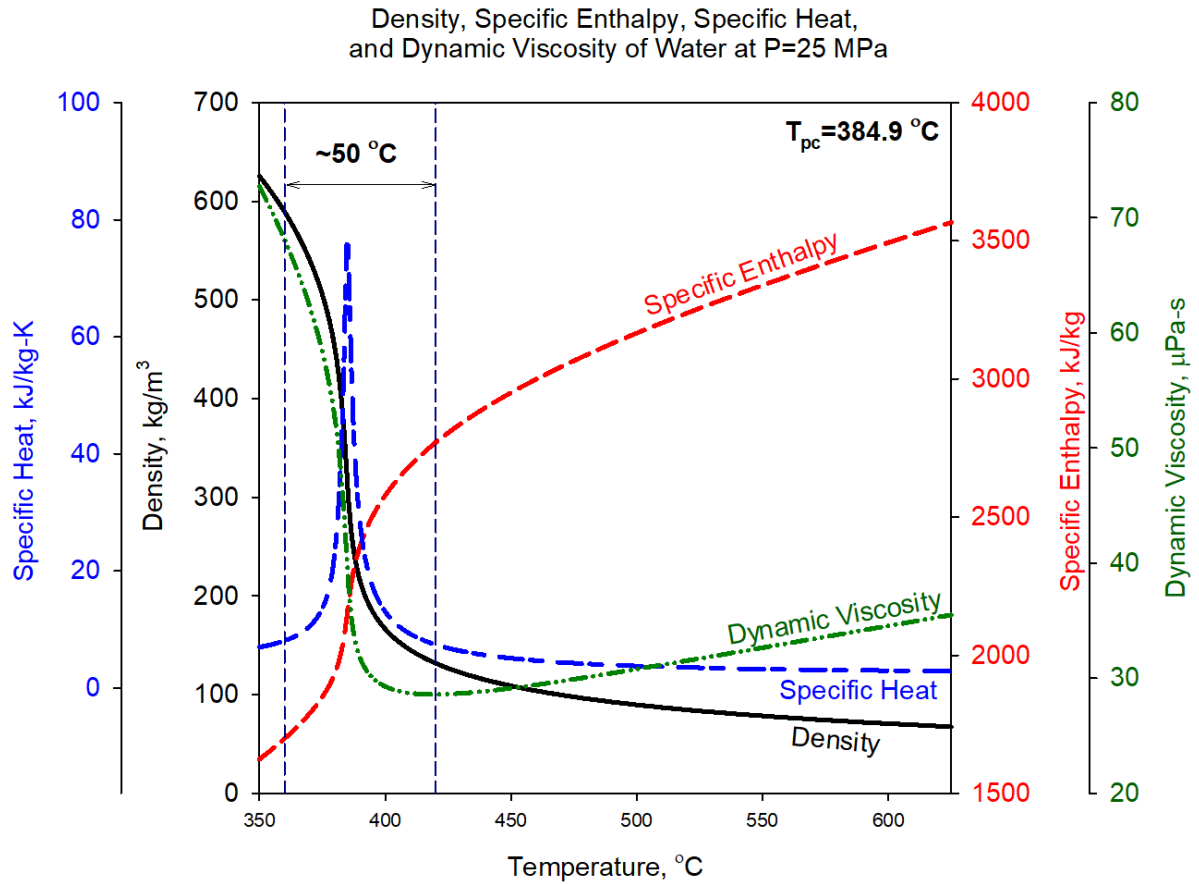


Figure 2-4: Graph of selected thermophysical property variation for water at $P=25$ MPa (based on data from NIST (2018)).

If enough SCW has entered the gas-like thermodynamic state, pseudo-film boiling may occur and the resultant heat transfer deteriorates. Alternatively, if a smaller proportion of the SCW has become gas-like, pseudo-boiling may occur instead, improving the resultant heat transfer.

Indeed, the three different heat transfer regimes (NHT, IHT, and DHT) are borne from the significant property changes that occur in SCW around the pseudocritical point (Gupta, 2014).

Of special interest to SCWR operation is the formulation of the DHT regime and the conditions that make such a situation possible. In the context of SCW flow through bare tubes, and referring to the definitions outlined earlier, the DHT regime is the phenomena where the inside tube wall HTC of SCW becomes much lower than what would be expected during NHT. A drop in the

HTC correspondingly leads to a higher T_w . As was mentioned, dryout does not occur in supercritical fluids since there are no distinct liquid or vapor phases. Thus, runaway fuel cladding temperatures due to poor heat transfer will not occur and the fuel rods will not melt. But, higher T_w 's (i.e higher fuel rod temperatures) due to DHT may still have a long-term effect in the form of physical degradation such as thermal fatigue (IAEA, 2020b). Therefore, understanding the conditions that lead to the onset of DHT is important to help prolong the operating lifetime of SCWR-type reactors.

The work done by Shiralkar and Griffith (1968) with supercritical fluid flow through bare tubes provides some insight into the development of DHT in supercritical fluids. Their model postulates that when $T_b < T_{pc} < T_w$, the fluid near the wall is low-density (gas-like) but the rest of the fluid behaves like a high-density (liquid-like) substance. Referring to Figure 2-4, such a difference means that there is a significant decrease in the dynamic viscosity (internal resistance of a fluid) and density of the overall bulk fluid as it goes from a liquid-like to gas-like state because of the change in temperature. Consequently, the shear stress between fluid layers decreases as well since the overall bulk fluid velocity remains relatively unchanged even with the changes in dynamic viscosity and density. Therefore, the flow becomes less turbulent near the wall and heat transfer is reduced. At low heat fluxes, this reduction in heat transfer is not as stark since T_b and T_w are closer in value. With higher heat fluxes, the difference between T_b and T_w widens considerably and so DHT is much more noticeable. For significant DHT to occur, it was observed that two conditions had to be met (Shiralkar and Griffith, 1968):

1. $T_b < T_{pc} < T_w$
2. Heat flux must be above a given value that is dependent on flow rate and pressure

Additionally, a number of factors facilitate the degree of severity in DHT, among which include:

- **Heat-to-Mass flux ratio:** Higher values of the heat-to-mass flux ratio typically leads to an earlier and more severe onset of DHT.
- **Inlet Enthalpy:** Lower inlet enthalpies result in worse heat transfer deterioration.
- **Entrance Regions:** Better mixed fluids have shown to have reduced deterioration.
- **Flow Geometry:** Turbulence-enhancing designs that promote heat transfer reduce the degree of DHT.
- **Pressure:** Deterioration is much harsher in pressures closer to the critical pressure due to even more abrupt changes in thermophysical properties.
- **Flow Orientation:** It has been observed that DHT is more profound in upward flow than in horizontal flow. Further investigation is needed into this phenomenon.

The onset of DHT is dependent upon the fluid pressure, mass flux (G), inner tube diameter, and orientation of flow but this is often a smooth and gradual occurrence (Cheng and Schulenberg, 2001). Since there is no distinct, identifiable point where DHT begins, it is difficult to determine whether the given flow and heat flux conditions in a reactor will lead to DHT so caution must be employed when defining the operating conditions. An example of the different heat transfer regimes is given in Figure 2-5 below (Dort-Goltz et al., 2021).

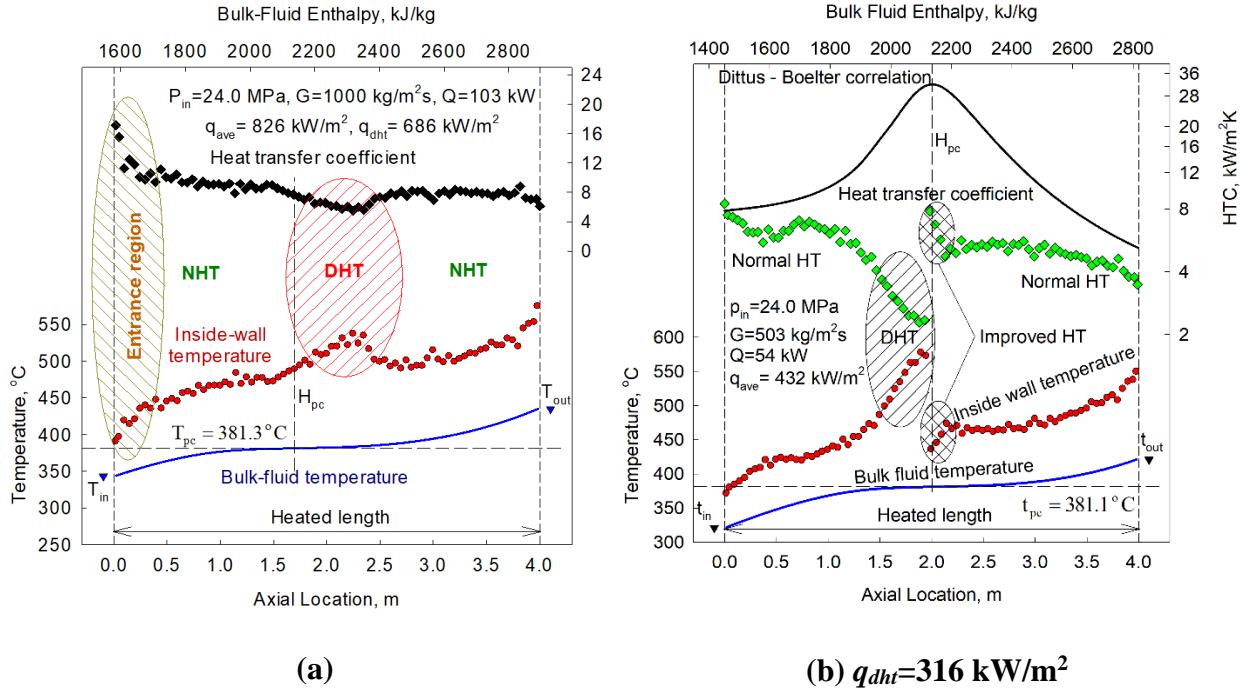


Figure 2-5: Bulk-Fluid- and Inside-Wall-Temperatures, and HTC profiles along heated length of vertical-bare-circular tube with upward flow of SCW (data by Kirillov et al. (2003)): $D = 10 \text{ mm}$; $L_h = 4 \text{ m}$; and $q_{ave} > q_{dht}$. Points – experimental data; curves – calculated data; curve for HTC is calculated through Dittus-Boelter correlation (Equation 2-2). q_{dht} is based on Equation (2-9).

As evidenced with the data in Figure 2-5 (a)(b), the appearance of DHT is marked by a steady decline in the value of the HTC . This lasts for a section of the bare tube and then ends once the thermophysical properties of SCW stabilize away from the pseudocritical region. The regions labelled as DHT are done so because they represent sections with significant departures from the $HTCs$ and T_w 's expected in the NHT regime. Therefore, these DHT regions do not encompass the sections with only minor reductions in HTC that then stabilize afterwards. There are no existing heat transfer correlations that can accurately predict the HTC during DHT but there do exist simple correlations that predict the minimum heat flux required for DHT to begin (this is the q_{dht} value shown in Figure 2-5 (b). See Section 2.2 for a further explanation.

2.2: Heat Transfer Correlations Selected for Use

For the heat transfer work done in this thesis, three correlations were selected for use when analyzing the 1-m long dataset:

1. Dittus-Boelter (1930)
2. Mokry et al. (2009)
3. Gupta et al. (2011)

The Dittus-Boelter correlation is the most widely used heat transfer correlation for forced convection at subcritical pressures. A version of this correlation, proposed by McAdams (1942), can be used to calculate *HTCs* in turbulent flows at subcritical pressures during forced convection,

$$\mathbf{Nu_b = 0.0243 Re_b^{0.8} Pr_b^{0.4}} \quad \mathbf{(2-1)}$$

The Dittus-Boelter correlation was originally developed for application in car radiators and was not planned for use with nuclear reactors (Dittus and Boelter, 1930). However, Equation 2-1 was used in supercritical conditions and, according to Schnurr et al. (1976), showed good agreement for SCW at low heat fluxes, with a pressure of 31 MPa, and flowing inside of a circular tube. Unrealistic results may be drawn with the use of Equation 2-1 during certain flow conditions especially around the critical and pseudocritical temperatures. This is largely due to its sensitivity to property variations. Nevertheless, this correlation was used as the base for many different supercritical heat transfer correlations. A more widely used form of the Dittus-Boelter correlation is shown in Equation 2-2 (Incorpera et al., 2007),

$$\mathbf{Nu_b = 0.023 Re_b^{0.8} Pr_b^{0.4}} \quad \mathbf{(2-2)}$$

This version was chosen for use here, as opposed to Equation 2-1, because it is a more popular version of the Dittus-Boelter correlation (refer to Incropera et al. (2007)) and has been used in the work of Mokry (2009) though using either would not have a significant impact on the results achieved in this work. Its inclusion in the analysis was primarily for reference purposes to examine the efficacy of the other correlations when predicting the HTC and T_w . In general, the Dittus-Boelter correlation, as either Equation 2-1 or Equation 2-2, over-predicts the HTC and T_w in SCW around the pseudocritical and critical point (Pioro and Duffey, 2007) thus limiting its use in the thermalhydraulic development of SCWR-type reactors. On the other hand, the Mokry et al. (2009) and Gupta et al. (2011) correlations do a much better job at predicting the HTC and T_w in SCW in all three HT regimes (though the error increases when applied in the DHT regime). Many of the other experimental correlations, such as Swenson et al. (1965) and Bishop et al. (1964), that were proposed for use in forced convection at supercritical pressures, were developed during the 1960s and 1970s using less advanced experimental techniques and outdated thermophysical properties. In essence, many of these correlations are not very accurate when predicting the HTC in SCW and often produce predictions that wildly deviate from experimental data (Pioro, 2019).

A need for an updated correlation for forced convective heat transfer at supercritical pressures was the motivation for the development of the Mokry et al. (2009) correlation. Whereas, the established heat transfer correlations used experimental results obtained in the 1960s and 1970s, the data used for the formulation of the Mokry et al. (2009) correlation was obtained by Kirillov et al. (2003) at the IPPE SuperCritical-Water Test Facility in Russia in a 4-m long, bare tube with vertical upward flow of SCW. This was new heat transfer data that was attained using more advanced experimental techniques and so better represented the heat transfer that would occur in

the operational parameters of an SCWR-type reactor. Additionally, the thermophysical properties of water had been updated during the nineties (Pioro and Duffey, 2007), so a new correlation developed on these properties would more accurately predict the HTC and T_w in SCW at SCWR operating conditions. Incorporating these two advancements, the Mokry et al. (2009) correlation takes on the form given in Equation 2-3,

$$\mathbf{Nu}_b = 0.0061 \mathbf{Re}_b^{0.904} \overline{\mathbf{Pr}}_b^{0.684} \left(\frac{\rho_w}{\rho_b} \right)^{0.564} \quad (2-3)$$

This correlation uses an averaged Prandtl number and a bulk-fluid temperature approach when calculating the non-dimensional entries of Equation 2-3. For calculations using bare-tubes with vertical, upward SCW flow, the Mokry et al. (2009) correlation has an accuracy of $\pm 25\%$ for calculating the HTC and $\pm 15\%$ for calculating T_w of the 4-m long Kirillov et al. dataset. The Gupta et al. (2011) correlation used the same dataset for development except the non-dimensional entries were calculated using thermophysical properties taken at T_w , instead of T_b . Two forms of the correlation are given by Equation 2-4 and Equation 2-5,

$$\mathbf{Nu}_w = 0.0033 \mathbf{Re}_w^{0.941} \overline{\mathbf{Pr}}_w^{0.764} \left(\frac{\mu_w}{\mu_b} \right)^{0.398} \left(\frac{\rho_w}{\rho_b} \right)^{0.156} \quad (2-4)$$

$$\mathbf{Nu}_w = 0.0033 \mathbf{Re}_w^{0.941} \overline{\mathbf{Pr}}_w^{0.764} \left(\frac{\mu_w}{\mu_b} \right)^{0.398} \left(\frac{\rho_w}{\rho_b} \right)^{0.156} \left[1 + \exp\left(-\frac{x}{24D}\right) \right]^{0.3} \quad (2-5)$$

Equation 2-5 includes a corrective term for entrance effects within the bare tube. However, Equation 2-4 was used in the analysis of this thesis due to Equation 2-5 not significantly improving the HTC , T_w predictions given by Equation 2-4, as the error estimates for both were $\pm 25\%$ for HTC calculations with $\pm 15\%$ for T_w predictions (Equation 2-4) and $\pm 10\%$ for T_w predictions (Equation 2-5) with the 4-m long Kirillov et al. dataset (Gupta, 2014). A comparison

of these three correlations, plus the Bishop et al. and Swenson et al. correlations, is given in Figure 2-6.

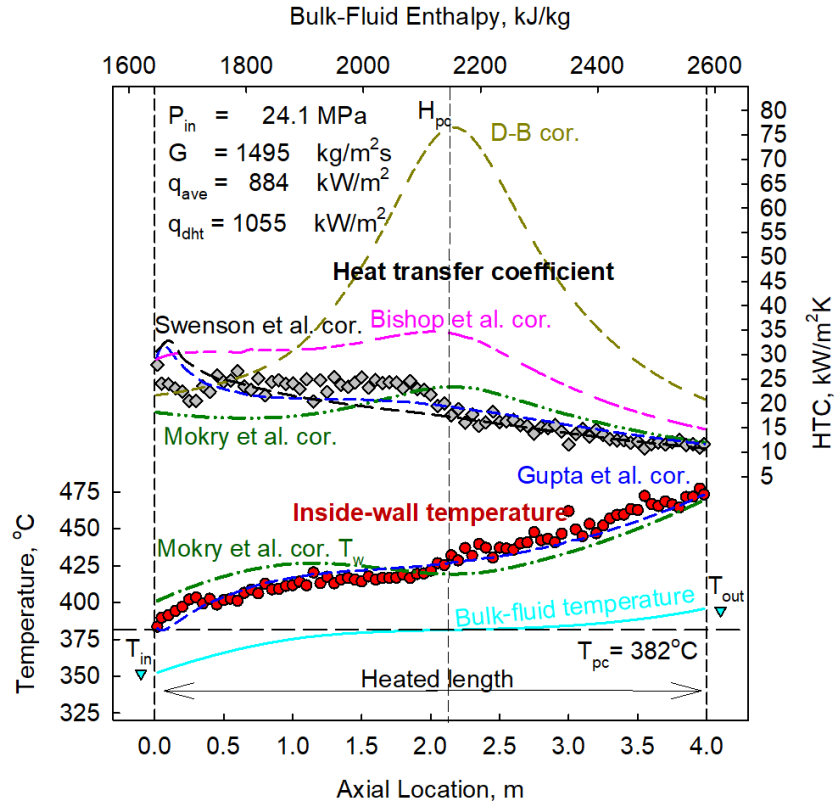


Figure 2-6: Comparison of different heat transfer correlations in calculating HTC and T_w of supercritical water in upward flow through a 4-m, vertical bare tube. Data obtained by Kirillov et al. D-B stands for Dittus-Boelter; (prepared using Kirillov et al. (2003) dataset).

Assessments regarding the accuracy of established heat transfer correlations at supercritical conditions have been done by a variety of authors. The Mokry et al. (2009) and Gupta et al. (2011) correlations were consistently found to either be the most accurate or one of the most accurate, by Root Mean Square (RMS) benchmarks, when calculating the HTC of water in supercritical conditions for upward flow in a vertical bare tube. Among these include an assessment by Zahlan et al. (2011, 2010) that reviewed sixteen correlations across three regions (gas-like, liquid-like, critical/pseudocritical) and concluded that the Mokry et al. (2009)

correlation was the most accurate predictor of the *HTC*, according to RMS, in all three regions. Another assessment done by Gschnaidtner et al. (2018) analyzed eleven different correlations and concluded that the Swenson et al. (1965) and Gupta et al. (2011) correlations were most accurate when predicting the *HTC* for SCW in vertical, upward flow. A compilation of the assessments done for correlation accuracy in vertical, upward flow through a bare tube is given in Table 2-2.

Table 2-2: Summary of assessments performed on *HTC* accuracy of heat transfer correlations for SCW in vertical, upwards flow through a bare tube.

Assessment	Operating Parameters (<i>P</i> ,MPa/ <i>G</i> ,kg/m ² s/ <i>q_{ave}</i> , kW/m ² / <i>T_b</i> , °C/ Inner diameter (ID), mm)	No. of Correlations	Inclusion of Gupta et al./Mokry et al.	Most Accurate Correlation	Means of Comparison
Zahlan et al. (2011,2010)	22.3-34.5/90- 5000/72- 5457/17- 564/2-38	16	Both	Mokry et al. (2009)	RMS
Wang and Li (2014)	/	16	Neither	Swenson et al. (1965)/ Hu (2001)	Mean Average Error (MEA)
Chen et al. (2015)	22-41/200- 2500/0- 1800/50- 576/7.5-26	26	Both	Mokry et al. (2009)	RMS
Gschnaidtner et al. (2018)	22-34.4/55- 3700/37- 4522/20- 554/1.57-38	11	Both	Swenson et al. (1965)/Gupta et al. (2011)	RMS
Lei et al. (2019)	22.5-41/100- 2150/100- 1800/-/1.5-26	22	Neither	Lei et al. (2019)	RMS

Even with the Mokry et al. (2009) and Gupta et al. (2011) correlations being among the most accurate to date for *HTC* calculations in vertical bare tubes with upwards flow for SCW, Gschnaidtner et al. (2018) noted that none of the correlations they analyzed were able to predict more than 51% of their results to within 20% accuracy. Evidently, there are still limitations to Equations 2-3 and 2-4 regarding both accuracy and use. As with other correlations, Equations 2-3 and 2-4 were developed for calculating *HTCs* in the NHT and IHT regimes. Neither was developed for predicting the *HTC* and T_w of SCW in the DHT regime. Indeed, no heat transfer correlation currently exists that can be used effectively within the DHT regime of supercritical heat transfer.

There do exist simple correlations that can be used to predict the minimum heat flux (q_{dht}) at which DHT will begin to appear. These correlations do not serve the same function as those mentioned previously in that they do not calculate the *HTC* or T_w of SCW. Instead, they are empirical and semi-empirical correlations that, as mentioned, only calculate q_{dht} to give an indication as to the heat fluxes that will create conditions for the formation of a DHT regime. A collection of empirical q_{dht} correlations (ones that only depend on G) are given in Table 2-3.

Table 2-3: Selection of empirical correlations used to predict minimal heat flux for DHT, q_{dht} .

Author	Equation
Styrikovich et al. (1967)	$q_{dht}=580G$ (2-6)
Yamagata et al. (1972)	$q_{dht}=0.2G^{1.2}$ (2-7)
Kitoh et al. (2001)	$q_{dht}=200G^{1.2}$ (2-8)
Mokry et al. (2011)	$q_{dht}=-58.97 +0.745G$ (2-9)

For calculations of q_{dht} , Equation 2-9 was used in this thesis as an assessment done by Wang et al. (2018) concluded that Equation 2-9 could be used for preliminary estimations. This was concluded after it was found that of all the empirical q_{dht} correlations, Equation 2-9 was one of two that gave predictions closer to the middle between the two boundary calculations. Thus,

Equations 2-2, 2-3, 2-4, and 2-9 were selected for analysis of the 1-m long heat transfer dataset obtained by Kirillov et al. (2003).

2.3: Overview of Nuclear Economics

For nuclear reactors to be built, there must be economic incentive for parties to invest their funds into the construction of a new nuclear power plant. Many factors affect this decision such as the cost of electricity in the energy market, competition from other energy sources, and government regulations. These are reviewed when exploring the profitability of an already built nuclear power plant. To reach this stage, a nuclear power plant must first be put into operation, entailing the procurement of the necessary capital to cover all material and labour costs for the completion of the project. The cost of constructing a nuclear power plant is a very important factor considered by potential investors as it is often quite large and can become even larger during construction.

A basic metric for assessing the economic competitiveness of a power generating station (including a nuclear power plant) is the levelized unit of energy cost (*LUEC*) or, as it is also referred to, the levelized cost of electricity (LCOE). This is the ratio of the total cost to build and operate a plant over its entire lifetime to the total energy generated during that period. Its units are often given in \$/MW_{el}h or \$/kW_{el}h. Equation 2-10 is a mathematical representation of the *LUEC* with *I* the annual capital expenditures, FUEL the annual total fuel cycle cost, O&M the annual operations and maintenance cost, *E* the annual electrical energy generated, and *r* the real discount rate (IEA and NEA,1998),

$$LUEC = \frac{\sum_{t=1}^n \frac{I_t + FUEL_t + O\&M_t}{(1+r)^t}}{\sum_{t=1}^n \frac{E_t}{(1+r)^t}} \quad (2-10)$$

At its core, the *LUEC* is the price of electricity needed for the project to break even over its lifetime. Effects such as inflation, opportunity cost of capital, and escalation are all covered within the framework of Equation 2-10. Caution must be taken during comparisons as the *LUEC* does not consider the system cost of integrating output into an energy grid to meet demand (World Nuclear Association, 2020b). Thus, dispatchable sources such as nuclear or fossil fuels cannot be directly compared with non-dispatchable sources such as solar and wind with dispatchability being the ability of an energy source to have its load adjusted by an operator to meet energy grid demands. It is also dependent on the location and time of when the calculation is computed since different countries will have different figures for parts, salaries, interest rates, and so forth in addition to these costs changing over time as well. Nevertheless, the *LUEC* is a very useful tool in performing a preliminary evaluation of the economic competitiveness of a project.

The total cost of a nuclear power plant is divided into several categories (World Nuclear Association, 2020b):

- **Capital Costs:** These are all the costs that are incurred while the power plants are under construction and include expenditures on necessary equipment, engineering and labour, and cost of financing the investment.
 - **Overnight Capital Cost (OCC):** These are capital costs exclusive of financing charges. Examples include engineering, procurement and construction (EPC); Owner's costs (land, cooling, infrastructure, site works, first core etc.); and various contingencies.
 - **Financing Costs:** These are also referred to as Interest During Construction (*IDC*) and are the financing charges associated with any

loans taken to finance the project. Construction period and applicable interest charged on debt are the two biggest contributors to this cost.

Extended delays during the construction schedule may cause the financing costs to rapidly grow and thus inflate the total capital costs

- **Total Capital Investment Cost (TCIC):** This is defined as the summation of the OCC and financing cost.
- **Plant Operating Costs:** This is the total cost to operate the power plant and is often broken down into the costs of the fuel cycle, operation and maintenance (O&M), and decommissioning and decontamination (D&D).
 - **Fuel Cost:** This category refers to the “front-end” and “back-end” of the fuel cycle. “Front-end” activities include mining, processing, enriching, and fabricating the nuclear fuel. “Back-end” activities include used fuel storage, waste disposal, and any reprocessing activities. Overall, these represent a small fraction of the overall cost of a nuclear power plant.
 - **Operation and Maintenance (O&M):** These represent the costs of actually running the power plant and can be categorized by either fixed costs (for example, employee salaries) that exist whether or not the power plant is working and variable costs (such as materials and parts) that depend on plant output.
 - **Decontamination and Decommissioning (D&D):** This is the cost of shutting down a nuclear power plant. It often represents about 9-15% of the initial TCIC but is spread out over the lifetime of the power plant.

Around 60% of the *LUEC* of a nuclear power plant is made up of the TCIC (World Nuclear Association, 2020b). A further breakdown of the OCC by the World Nuclear Association shows that ~80% of it is related to EPC costs, ~70% of which are direct costs (physical plant equipment with labour and materials to assemble them) with the other 30% related to indirect costs such as supervisory engineering. The other ~20% of the OCC is for project contingencies/owner’s costs. Some capital costs breakdowns are given in Tables 2-4 and 2-5 to illustrate activity cost and equipment cost distribution.

Table 2-4: Breakdown of capital costs associated with activities during construction (based off data from World Nuclear Association (2020b)).

Category	Proportion
Design, Architecture, Engineering, and Licensing	5%
Project Engineering, Procurement, and Construction Management	7%
Construction/Installation Works:	
Nuclear Island	28%
Conventional Island	15%
Balance of Plant	18%
Site Development/ Civil Works	20%
Transportation	2%
Commissioning/Fuel Loading	5%
Total	100%

Table 2-5: Breakdown of capital costs associated with equipment during construction (based off data from World Nuclear Association (2020b)).

Category	Proportion
Nuclear Steam Supply System	12%
Electricity and Generating Equipment	12%
Mechanical Equipment	16%
Instrumentation and Control System (including software)	8%
Construction Materials	12%
Labor Onsite	25%
Project Management Services	10%
Other Services	2%
First Fuel Load	3%
Total	100%

In addition to the *LUEC*, another concept important to the economic evaluation of a nuclear power plant is that of the discount rate. There are multiple definitions for the discount rate and the one that applies depends heavily on the context in which it is being employed. Within a financial analysis, the discount rate refers to the internal rate of return for a project or the rate of return that sets the net present value of the nuclear power plant equal to zero (Mignacca and Locatelli, 2020). Within an economic analysis, the discount rate refers to a parameter that takes the time value of money into account and is a measure of the risk of investment into a new nuclear power plant (IAEA, 2014). The latter interpretation is the one adopted by the Economic Modelling Working Group (EMWG) of GIF and so will be used in this thesis. Commonly used values of the discount rate are 3%, 5%, and 10% with lower values representing more government regulation of electricity markets (less risky investment with a more guaranteed chance for return of investment) while higher values represent less regulated, more mercantile electricity markets where the chance for return of investment is not as ensured (IAEA, 2014). For capital cost heavy investments such as nuclear power plants, lower discount rates result in significantly lower *LUECs* (World Nuclear Association, 2020b). Estimates for the *LUEC* of different energy sources have been made or compiled by various authors. A new set of estimates has recently been published by the IEA and OECD (2020) and a selection of these are included in Table 2-6.

Table 2-6: *LUEC* estimates for miscellaneous energy sources. Discount rate was set at 7%. Long Term Operation refers to the number of years a nuclear reactor operates beyond its assumed lifetime (set at 60 years). All data obtained from IEA and OECD (2020).

Energy Source	LUEC (Min.), USD/MW _{el} h	LUEC (Max.), USD/ MW _{el} h	LUEC (Average), USD/ MW _{el} h	Average Capacity Factor, %
CCGT (85% capacity factor)	40.32	106.79	69.49 (16 units)	/

Ultra-supercritical coal (85% capacity factor)	70.53	117.27	89.69 (6 units)	/
Nuclear-New build (85% capacity factor)	42.02	101.84	69.78 (8 units)	/
Nuclear-Long Term Operation, 10 years (85% capacity factor)	32.65	37.18	35.49 (4 units)	/
Nuclear-Long Term Operation, 20 years (85% capacity factor)	28.17	33.24	28.57 (4 units)	/
Solar- Utility scale	33.94	172.05	60.61 (20 units)	22
Onshore wind- ≥ 1 MW _{el}	29.18	154.78	61.45 (33 units)	35
Offshore wind	45.09	200.18	85.21 (23 units)	43
Hydropower (run of river)- ≥ 5 MW _{el}	46.12	103.82	79.38 (7 units)	58
Hydropower (reservoir)- ≥ 5 MW _{el}	38.65	142.40	81.14 (4 units)	49
Biomass	53.50	288.83	134.03 (4 units)	73
Geothermal	61.80	151.80	102.47 (6 units)	84
Combined Heat and Power	52.47	195.65	100.66 (12 units)	64
Fuel cells	158.07	237.03	195.66 (4 units)	85

Additional *LUEC* estimates were also generated by Ontario's Ministry of Energy in their 2013 Long-Term Energy Plan for some of the common energy sources found in the province (see Figure 2-7).

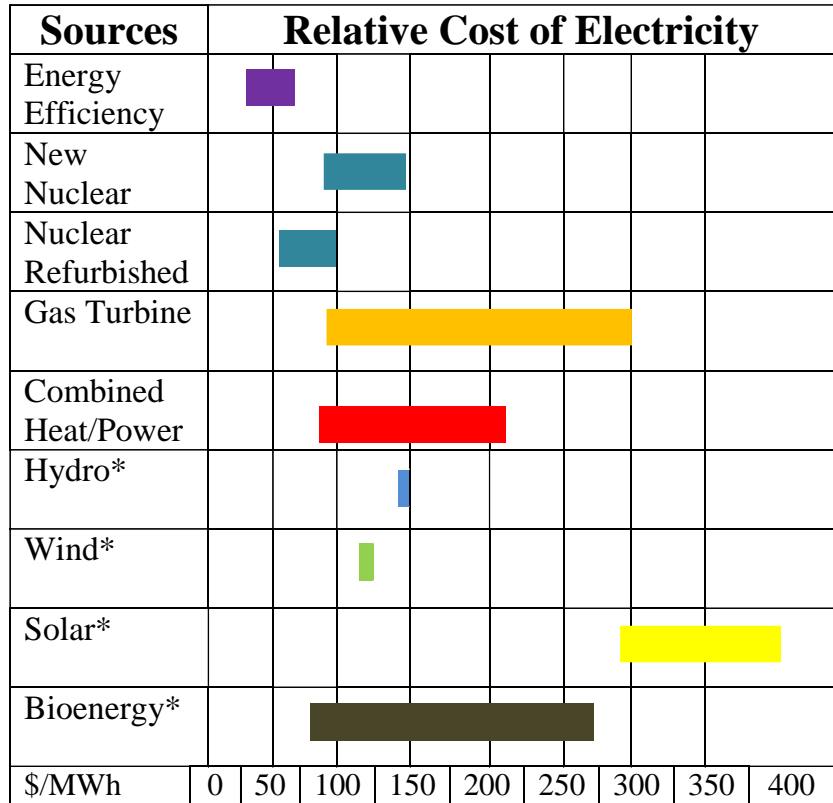


Figure 2-7: LUEC values for electricity-generating options in Ontario. Monetary values are in CAD. (Courtesy of I. Piore and data obtained from Ontario's Ministry of Energy Long-Term Energy Plan (2013). *-Updated for 2014 Feed-In Tariff prices.

As is evident from Table 2-6 and Figure 2-7, *LUEC* estimates vary considerably between the authors and sources of energy (though it must be noted the currencies used in Table 2-6 and Figure 2-7 differ as well). This is apparent for renewables as the minimum *LUEC* estimates for these energy sources in Table 2-6 were generally equivalent to the minimum *LUEC* estimates of non-renewables. However, Figure 2-7 indicates that renewables are for the greater part more expensive, with the exception of bioenergy, than non-renewables with little overlap between their respective lower bound estimates. As has been noted, the *LUEC* figures for dispatchable and non-dispatchable energy sources cannot be directly compared so the discrepancy between the *LUEC* estimates for renewables in Table 2-6 and Figure 2-7 is not a serious issue if a comparison is made to the *LUEC* estimates of non-renewables since such a comparison is null in

the first place. For the most part, the *LUEC* will not be the sole factor that determines the feasibility of an energy project as there are other considerations to be made by a potential investor.

Investigating the economics of SMRs introduces several new economic concepts that uniquely impact the attractiveness of investing in new SMR projects. These are factors that reduce the capital costs of an SMR and arise from the modular nature of these types of reactors:

- **Modularization/Modularity:** Conventional LNRs typically employ a stick-built construction strategy that entails bringing all necessary material and components to the reactor site and building all power plant systems from the ground-up. SMRs would have a variable amount of these parts standardized and factory made before being shipped to the construction site, ready to be put together upon arrival. This has the potential effects of reducing construction schedules; increasing efficiency of construction, operation, and decommissioning; reduction of maintenance costs; and a safer construction process (Mignacca and Locatelli, 2020). The downside to this type of construction process is the need for new supply chains and the associated costs of transportation, both of which are expected to be high (Mignacca and Locatelli, 2020).
- **Modularity Factor:** This factor represents the magnitude of capital cost reduction dependent on the degree to which an SMR is made modular. Increasing the amount of reactor parts (referred to as modules) that are factory made leads to a greater proportion of on-site costs being shifted to the factories. There are diminishing returns with this factor as capital cost savings eventually reach a maximum and further modularization yields no further effect. The degree of modularization (DoM) ranges from 0.0 (no

components are modularized) to 1.0 (all components are modularized) (Lloyd et al., 2018).

- **Co-siting Reduction Factor:** This factor represents the reduction in capital costs associated with building multiple SMR units on a single site. A proportion of the capital costs are indivisible and only apply to the first unit. These can then be distributed among the other units and the overall capital cost per unit is reduced (Boldon and Sabharwell, 2014).
- **Learning Reduction Factors:** These are represented by two categories. The first category deals with the learning factor associated with building multiple units on the same site. By fabricating, constructing, and sharing facilities and systems, the building process may be optimized and overall construction costs reduced. The second category deals with technological maturity. As more and more units incorporating a certain technology are made, that technology matures and so the cost of production is reduced. This typically continues until a certain critical threshold is reached and the technology is deemed mature. Any units past that point will be considered Nth-Of-A-Kind (NOAK) models and will have the maximum amount of cost reduction. For Generation IV reactors, the EMWG defines the threshold for NOAK units to be a cumulative power rating of 8 GW_{el}. Both of these categories have the effect of reducing the OCC of an SMR (Boldon and Sabharwell, 2014).
- **Modular Design Reduction Factor:** This has the effect of reducing the OCC of an SMR as a result of design simplifications to allow modularization and standardization to occur. The degree of reduction is dependent on the rated power of the SMR since smaller reactors will typically have a greater degree of simplification than larger reactors. This

factor becomes equal to 0.6 for SMRs with capacities equal to or below 35 MW_{el} and reaches a maximum of 1 (indicating no cost saving) for SMRs rated at 600 MW_{el} or greater (Boldon and Sabharwell, 2014).

The factors introduced above are important when calculating the economic costs of SMRs as they enable SMRs to be more competitive when compared to LNRs. A straightforward economies of scale approach to calculating the capital costs of an SMR is not appropriate since all this does is scale the capital costs of an LNR at a particular capacity to an SMR at another capacity. This method assumes that the designs of the LNR and SMR are very similar when in actuality there are differences and so an economies of scale approach does not work. A more detailed and in-depth explanation of *LUEC* estimating techniques is given in Section 3.3.

2.4: Review of SMR Concepts

Before choosing the reference reactor to be used in the economic analysis of this work, a survey was performed of all the SMR concepts in different stages of development from across the globe (Piro, ..., Dort-Goltz, 2020). A distinction was established between SMRs – given the definition in Section 1 – and small and medium-sized reactors (S&MRs) that have installed capacities of <300 MW_{el}, if small-sized, and 300-700 MW_{el}, if medium-sized. Many S&MRs claimed features of modularity in design, production, and/or construction since there was no restraint regarding the degree, extent, or type of modularity for a specified module. Thus, an entire reactor core could be defined as a module and the vendor could label the reactor design as modular. To avoid any complications, the acronym S&MR was adopted as an overarching term to refer to any reactor designs with electrical capacities <700 MW_{el} and with claims of modularity. The reactor designs were initially organized by reactor technology namely:

- Land-based water-cooled

- Marine-based water-cooled
- High-temperature gas-cooled
- Fast-neutron spectrum
- Molten salt
- Other

There are 33 land-based water-cooled, 7 marine-based water-cooled, 21 high-temperature gas-cooled, 26 fast-neutron spectrum, 17 molten salt, and 4 other SMRs and S&MRs for a total of 106 concepts. An explanation of status terms and organization by country is included in Appendix B with all data obtained from Pioro, Dort-Goltz, and McKellar (2020). The SMR/S&MR tables from Pioro, ..., Dort-Goltz (2020) are provided in this section from Tables 2-7 to 2-12.

Table 2-7: Land-based water-cooled SMRs/S&MRs (33 in total) (obtained from Pioro, ..., Dort-Goltz (2020)) (courtesy and copyright of ASME).

Country	Design	Output MW _{el} /th =Th.Ef f., %	Type	Designers	Phase	Fuel Enrich ./ Cycle, years	Fuel Type
Argentina	CAREM	30/100 =30	PWR	CNEA	Construction	3.1%/1 .2	UO ₂
Brazil	FBNR	70/134 =52.2	PWR	Fed. University of Rio Grande do Sul	Conceptual	N/A/N/ A	TRISO
Canada (1)	CANDU SMR	300/960 =31.25	PHWR	Candu Energy Inc.	Conceptual	-/On- line	UO ₂
Canada (2)	SSR	300/667 =45	SCWR	AECL	Conceptual	Enrich ed	U or Th
China (1)	ACP100	125/385 =33	PWR	CNNC	Basic	<5%/2	UO ₂
China (2)	DHR400	-/400= N/A	LWR	CNNC	Basic	<5.0%/ 0.8	UO ₂

Country	Design	Output MW _{el} /th =Th.Ef f., %	Type	Designers	Phase	Fuel Enrich ./ Cycle, years	Fuel Type
China (3)	CAP200	>200/6 00=>30	PWR	CGNPC	Conceptual	4.2%/2	UO ₂
China (4)	CNP-300	300-340 /1000= 30-34	PWR	CNNC	Operational in China/Pakistan	<5%/1. 25	UO ₂
China (5)	SNP350	350/103 5=33.8	PWR	SNERDI	Conceptual	<5%/N /A	UO ₂
China (6)	NHR-200II	-/200= N/A	PWR	INET	Final	<5%/N /A	UO ₂
China (7)	HAPPY200	-/200= N/A	PWR	SPIC	Final	N/A/N/ A	N/A/N/ A
Czech Republic	TEPLATOR	- /50=N/ A	HWR	UWB Pilsen & CIIRC CTU	Conceptual	<1.2%/ 0.83	Spent VVER- 400 fuel
# of Countries	IRIS	335/100 0=34	PWR	IRIS Consortium	Conceptual	5%/4	UO ₂ /M OX
France	NUWARD	300-400 /-=N/A	PWR	CEA, EDF, Naval Gr., TechnicAtome	Preliminary	N/A/N/ A	N/A
India (1)	AHWR-300- LEU	304/920 =33	LHR (HWR)	BARC	Conceptual	<5% (MOX) /Cont.	Th-U or Th-Pu, MOX
India (2)	PHWR-220	235/755 =31.2	PHWR	NPCI Ltd.	16 Units Operational	<5%/C ont.	UO ₂
Japan (1)	DMS	300/840 =36	BWR	Hitachi-GE	Basic	<5%/2	UO ₂
Japan (2)	IMR	350/100 0=35	PWR	MHI	Conceptual	4.8%/2 .2	UO ₂
Japan (3)	CCR	423/126 8=33.4	BWR	Toshiba Corp.	Conceptual	N/A/2	N/A
Japan (4)	MRX	33.3/10 0=33.3	PWR	JAERI	Final	4.3%/3 .5	UO ₂
Korea S.	SMART	100/330 =30	PWR	KAERI	Certified	<5%/3	UO ₂
Russia (1)	ELENA	0.068/3. 3=2	PWR	Kurchatov Institute	Conceptual	15.2%/ 25	UO ₂ (MOX)
Russia (2)	UNITHERM	6.6/30= 22	PWR	NIKIET	Conceptual	19.8%/ 16.7	UO ₂

Country	Design	Output MW _{el} /th =Th.Ef f., %	Type	Designers	Phase	Fuel Enrich ./ Cycle, years	Fuel Type
Russia (3)	RUTA-70	-/70=N/ A	PWR	NIKIET	Conceptual	3%/3	Cermet
Russia (4)	KARAT-45	45- 50/180 =25-28	BWR	NIKIET	Conceptual	4.5%/7	UO ₂
Russia (5)	KARAT-100	100/360 =28	BWR	NIKIET	Conceptual	4%/7.5	UO ₂
Russia (6)	VK-300	250/750 =33	BWR	NIKIET	Final	4%/6	UO ₂
UK	UK-SMR	443/127 6=26	PWR	Rolls-Royce	Final	<5%/1. 5-2	UO ₂
USA (1)	NuScale	50/160 =31	PWR	NuScale Power	Preliminary	<5%/2	UO ₂
USA (2)	SMR-160	160/525 =31	PWR	Holtec Int.	Preliminary	5%/1.5 -2	UO ₂
USA (3)	mPower	195/575 =34	PWR	BWX Tech.	Developmental	<5%/2	UO ₂
USA (4)	W-SMR	>225/8 00=>28	PWR	Westinghouse	Conceptual	<5%/2	UO ₂
USA (5)	BWRX-300	300/- =N/A	BWR	GE-Hitachi	Final	3.4-4.9 5%/N/ A	UO ₂

Table 2-8: Marine-based water-cooled SMRs/S&MRs (7 in total) (obtained from Piroo,...., Dort-Goltz (2020)) (courtesy and copyright of ASME).

Country	Design	Output MW _{el} /th =Th.Eff., %	Type	Designers	Phase	Fuel Enrich. / Cycle, years	Fuel Type
China	ACPR50S	50/200=25	PWR	CGNPC	Preliminary	<5%/2. 5	UO ₂
France	Flexblue	160/600=2 6.7	PWR	DCNS	Preliminary	<5%/3	UO ₂
Russia (1)	SHELF	6.6/28.4=2 3	Immersed NPP	NIKIET	Preliminary	19.7%/ 6	UO ₂
Russia (2)	ABV-6E	6-9/38=16 -24	Floating PWR	OKBM Afrikantov	Final	<20%/1 0-12	UO ₂
Russia (3)	KLT-40S	35/150=23	Floating PWR	OKBM Afrikantov	Operating	18.6%/ 2.5-3	UO ₂

Country	Design	Output MW _{el} /th =Th.Eff., %	Type	Designers	Phase	Fuel Enrich. / Cycle, years	Fuel Type
Russia (4)	RITM- 200M	50/175=29	Floating PWR	OKBM Afrikantov	Manufactured	<20%/1 0	UO ₂
Russia (5)	VBER- 300	325/917=3 5	Floating NPP	OKBM Afrikantov	Final	4.95%/ 6	UO ₂

Table 2-9: High-temperature gas-cooled SMRs/S&MRs (Generation IV concept) (21 in total) (obtained from Pioro,...., Dort-Goltz (2020)) (courtesy and copyright of ASME).

Country	Design	Output MW _{el} /th =Th.Eff., %	Designers	Phase	Fuel Enrichment / Cycle, years	Fuel Type
Africa S. (1)	HTMR-100	35/100=3 5	Steenkampskraal Thorium Ltd.	Conceptual	10%- 93%/Online refueling	LEU, Th/LEU, Th/HEU, Th/Pu
Africa S. (2)	A-HTR-100	50/100=5 0	Eskom Holdings SOC Ltd.	Conceptual	LEU or WPu/N/A	CPF
Africa S. (3)	PBMR-400	165/400= 41.3	PBMR SOC Ltd.	Preliminary	9.6% LEU or WPu/N/A	CPF
Africa S. (4)	PBMR-100	100/250= 40	PBMR SOC Ltd.	Preliminary	N/A/Online	TRISO- coated UP ₂
Canada	Starcore SMR	20/36=55 .6	Starcore	Preliminary	N/A/5	TRISO
China (1)	HTR-10	2.5/10=2 5	Tsinghua University/INET	Operational	17%/On-line	Spherical El. with TRISO particles fuel
China (2)	HTR-PM	210/2×25 0=42	INET, Tsinghua University	Construction	8.5%/On-line refueling	Spherical El. with CPF
France (1)	Allegro	-/50-100 =N/A	CEA	Conceptual	N/A/N/A	MOX
France (2)	ANTARES	-/≥600=N /A	AREVA	Conceptual	N/A/N/A	N/A
Indonesia	RDE/Micro- PeLUIt	3/10=30	BATAN	Preliminary	17%/On-line	Spherical El. with

Country	Design	Output MW _{el} /th =Th.Eff., %	Designers	Phase	Fuel Enrichment / Cycle, years	Fuel Type
						coated particle fuel
Japan (1)	GTHTTR300	100- 300/<600 =>17-50	JAEA	Basic	14%/4	UO ₂
Japan (2)	HTTR	-/30=N/A	JAEA	Operational	3-10 (6 avg)%/ 660 EFPD	UO ₂ TRISO ceramic coated particle
Russia (1)	MHR-100	25-87/21 5=12-41	OKBM Afrikantov	Conceptual	LEU<20%/N /A	CPF
Russia (2)	GT-MHR	288/600= 48	OKBM Afrikantov	Preliminary	LEU or WPU/2.08	CPF
Russia (3)	MHR-T	4×206/4× 600=34	OKBM Afrikantov	Conceptual	20%/2.5	CPF
UK (1)	U-Battery	4/10=40	URENCO	Preliminary	17-20%/5	TRISO
USA (1)	Xe-100	75/200=3 7.5	X-energy LLC	Conceptual	15.5%/Onlin e refueling	UCO TRISO
USA (2)	SC-HTGR	272/625= 43.5	FRAMATOME Inc.	Conceptual	<20%/½ core replaced every 1.5 years	UCO TRISO particle fuel
USA (3)	Prismatic HTR	150/350= 42.8	General Atomics	Development al	15.5%/1.5	TRISO- coated UCO
USA (4)	MMR	5/15=33. 3	USNC	Preliminary	N/A/Never	FCM
USA (5)	HOLOS	3-13/22= 13.6-59.0	HolosGen	Preliminary	15%/3.5-8	TRISO

Table 2-10: Fast-neutron spectrum SMRs/S&MRs (Generation IV concept) (26 in total) (obtained from Pioro,...., Dort-Goltz (2020)) (courtesy and copyright of ASME).

Country	Design	Output MW _{el} /th =Th.Ef f., %	Type	Designers	Phase	Fuel Enrich ment / Cycle, years	Fuel Type
China	CFR-600	600/15 00=40	SFR	CIAE	Construction	N/A/N /A	UO ₂ /M OX
France	ASTRID	600/15 00=40	SFR	CEA	Preliminary	N/A/N /A	MOX
Italy (1)	ALFRED	125/30 0=41.7	LFR	Ansaldo	Preliminary	N/A/5	MOX
Italy / EU (2)	ELFR	630/15 00=42	LFR	Ansaldo	Conceptual	N/A/2. 5	MOX
Japan (1)	4S	10/30= 33	LMFR	Toshiba Corp.	Developmental	<20%/ N/A	MF (U- Zr)
Japan (2)	LSPR	53/150 =35.3	SFR	Tokyo Tech.	Developmental	10- 12.5%/ 12	U-Pu- N/U-Pu- Zr
Japan (3)	PBWFR-150	150/45 0=33.3	LMFR	Tokyo Tech.	Developmental	N/A/1 0	U-Pu nitride
Japan (4)	RAPID-L	0.2/5=4	LMFR	CRIEPI	Operating	40%/1 0	UN
Korea S. (1)	KALIMER- 600	600/15 23.4=3 9.4	LMFR	KAERI	Preliminary	N/A/1	U-TRU- Zr
Korea S. (2)	PGSFR	150/40 0=37.5	SFR	KAERI	Preliminary	N/A/~ 1	U-TRU- Zr
Korea S. (3)	PEACER	300/85 0=35	LMFR	Seoul Nat. Univ.	Conceptual	N/A/1	U-TRU- Zr
Korea S. (4)	MicroURAN US	20/60= 33.3	LMFR	UNIST	Pre- Conceptual	8,10,1 2%/N/ A	UO ₂
Luxembo urg (1)	LFR-TL-X	5/15=3 3 10/30= 33 20/60= 33	LFR	Hydromine Nuclear Energy	Conceptual	19.8%/ ≥8.33	LEU
Luxembo urg (2)	LFR-AS-200	200/48 0=42	LFR	Hydromine Nuclear Energy	Preliminary	14.6%- 20.4%- 23.2%	MOX

Country	Design	Output MW _{el} /th =Th.Ef f., %	Type	Designers	Phase	Fuel Enrich ment / Cycle, years	Fuel Type
						in Pu/6.7 years for 5 batche s	
Russia (1)	SVBR-100	100/28 0=37	LFR	JSC AKME Engineering	Final	<19.3 %/0.58 -0.67	UO ₂
Russia (2)	BREST-OD- 300	300/70 0=43	LFR	NIKIET (RDIPE)	Final	13.5%/ 2.46-4. 1	Mixed U-Pu-N
Sweden	SEALER	3/8=38	Lead Cooled	LeadCold	Conceptual	19.75 %/27 full power years	UO ₂
USA (1)	SUPERSTAR	120/30 0=40	LMFR	Argonne National Lab.	Conceptual	<12%/ 15	Particul ate- based U-Pu-Zr MF with weapon s Pu
USA (2)	EM ²	265/50 0=53	GMFR	General Atomics	Conceptual	14.5% LEU/3 0	UC
USA (3)	WLFR	>450(N et)/950 =>47	LFR	Westinghouse	Conceptual	≤19.75 %/≥2	Oxide
USA (4)	AFR-100	100/25 0=40	LMFR	Argonne National Lab.	Conceptual	13.5%/ N/A	U-Zr
USA (5)	ARC-100	100/26 0=38.5	LMFR	ARC	Final	N/A/2 0	LEU
USA (6)	G4M (HYPERION)	25/70= 35.7	LMFR	Gen4 Energy Inc.	Conceptual	19.75 %/10	UN
USA (7)	PRISM	311/50 0=62	LMFR	GE-Hitachi	Preliminary	N/A/1. 33	U-Pu-Zr metal

Country	Design	Output MW _{el/th} =Th.Eff f., %	Type	Designers	Phase	Fuel Enrich ment / Cycle, years	Fuel Type
USA (8)	ENHS	50/125 =40	LFR	UC Berkeley	Conceptual	13% (U-Zr)/ N/A	Pu-U/U- Zr
USA (9)	TWR-P	600/14 75=41 %	SFR	TerraPower	Conceptual	N/A/1. 5-2	U- Zr10% MF

Table 2-11: Molten salt SMRs/S&MRs (Generation IV concept) (17 in total) (obtained from Piroo,...., Dort-Goltz (2020)) (courtesy and copyright of ASME).

Country	Design	Output MW _{el/th} =Th.Eff., %	Designers	Phase	Fuel Enrichment / Cycle, years	Fuel Type
Canada (1)	IMSR	190/400= 48	Terrestrial Energy	Basic	<5%/7 years before core- unit replacement	MSF
China (1)	smTMSR-400	168/400= 42	SINAP, CAS	Pre- Conceptual	19.75%/10 years	LiF-BeF ₂ - UF ₄ -ThF ₄ fuel salt
China (2)	TMSR-LF	168/373= 45	SINAP	Conceptual	19.75%/Onli ne	LiF-BeF ₂ - UF ₄ -ThF ₄ , LiF-BeF ₂ - PuF ₃ -ThF ₄
Czech Republic	Energy Well	8/20=40	Centrum vyzkumu Rez	Pre- Conceptual	<20%/7	TRISO
Denmark (1)	CA Waste Burner	20/50=40	Copenhagen Atomics	Conceptual	N/A/N/A	LiF-ThF ₄
Denmark (2)	CA Waste Burner 0.2.5	- /100=N/A	Copenhagen Atomics	Conceptual	N/A/Continu ous	LiF-ThF ₄
Denmark (3)	CMSR (MSTW)	100- 115/250= 40-46 115/270= 42.6	Seaborg Technologies	Conceptual	Pre- processed SNF (U 1.1% fissile, Pu 69% fissile)/6	Na- actinide fluoride (93% Th,

Country	Design	Output MW _{el} /th =Th.Eff., %	Designers	Phase	Fuel Enrichment / Cycle, years	Fuel Type
						3.5% U, 3.5% Pu)
Int. Consortium	ThorCon	250 (per module) /557=45	Martingale	Basic	19.7%/8	12% HM in NaBe salt
Japan	FUJI	200/450=44	Int. Thorium Molten-Salt Forum	Pre conceptual	2.0% Pu or LEU (continuous operation is possible)	MSF with Th & U
UK (1)	Stable Salt Reactor-Wasteburner	300 (continuous as baseload) /750=40	Moltex Energy	Conceptual	Reactor grade Pu/12.5	MSF
UK (2)	Stable Salt Reactor - Th. Spectrum	300 (baseload) /750=40	Moltex Energy	Pre-Conceptual	5%/2	MSF
USA (1) & Canada (2)	MCSFR	50/100=50	Elysium Industries	Conceptual	10%-20%/online refueling	MSF
USA (2)	Mk1 PB-FHR	100/236=42	University of CA, Berkeley	Pre-Conceptual	19.9%/2.1 months for fuel core residence time	TRISO particles
USA (3)	LFTR	250/600=42	Flibe Energy	Conceptual	N/A /continuous refueling	LiF-BeF ₂ -UF ₄
USA (4)	KP-FHR	140/311=45	Kairos Power	Developmental	19.75%/Online	TRISO particles
USA (5)	MCFR	N/A/N/A=N/A	TerraPower	Developmental	N/A/Online	N/A
USA (6)	SmAHTR	50/125=40	Oak Ridge National Lab.	Conceptual	19.75%/N/A	TRISO particles

Table 2-12: Other SMRs/S&MRs (4 in total) (obtained from Pioro,...., Dort-Goltz (2020)) (courtesy and copyright of ASME).

Country	Design	Output MW _{el/th} =Th.Eff., %	Type	Designers	Phase	Fuel Enrich. / Cycle, years	Fuel Type
Canada	Leadir- PS100	36/100=3 6	LMR	Northern Nuclear Industries	Conceptual	N/A/N/ A	TRISO
Japan	MoveluX	N/A/10= N/A	Heat Pipes	Toshiba	Preliminary	4.99/N/ A	LEU
USA (1)	Aurora	1.5/N/A= N/A	Heat Pipes	Oklo	Preliminary	<20%/N/ /A	HALE U-U-Zr
USA (2)	eVinci	0.2-15/0. 6-40=33. 3-37.5	Heat Pipes	Westingho use	Developme ntal	19.5%/1 0	UO ₂ or UN

Regarding the fast-neutron spectrum SMR/S&MR concepts, these are categorized by designs that would employ a fast spectrum of neutrons instead of the typical thermal spectrum. The coolants used in the reactors of this category are generally liquid metals though one gas-cooled concept is included. All the designs in Table 2-9, high-temperature gas-cooled reactors, are thermal spectrum reactors with gas coolants, namely helium. In Table 2-11, there is a mixture of fast and thermal spectrum reactors but all employ molten salt as either a coolant or fuel source in the reactor core. The reactors in Table 2-7 and 2-8 are all water-cooled – no distinction as to whether the coolant is light, heavy, or SCW – but the designs included in Table 2-8 are planned for offshore use, whether underwater or on a barge/platform. All reactor designs that did not fit into any of these tables were put into Table 2-12 and designated as “Other” SMRs/S&MRs. As noted in Pioro,....,Dort-Goltz (2020), many of the Generation IV concepts and SMRs/S&MRs of small electrical capacity rely on higher levels of enrichment than what are currently used in conventional nuclear reactors. This is due to the proposed locations of these reactors and the type of technology under consideration. Those designs that are considered for use in remote, off-grid

communities such as mining operations, will be put into geographical regions that are hard to access, placing restrictions on the frequency of fuel resupply. To extend refueling intervals, higher levels of enrichment could be used to allow prolonged operation. In addition, fast-neutron spectrum reactors are envisioned as breeder reactors and for proper functionality, higher levels of enrichment are required compared to thermal spectrum reactors (World Nuclear Association, 2021a).

From Section 1, only one SMR concept, the KLT-40S, has been put into operation. Two KLT-40S units were connected to grid in December of 2019 and currently reside on a barge outside of the port of Pevek, Russia's northernmost city. This SMR was developed by using proven marine reactor technology from Russia's Arctic icebreakers, and adjusting it for electricity generation and heat supply. A schematic layout of the KLT-40S reactor and its systems is included in Figure 2-8 that shows:

1. Passive system of containment emergency pressure decrease (condensing system).
2. Active emergency cooling system.
3. Passive emergency core cooling system (hydraulic accumulators).
4. Active emergency core cooling system from feedwater pumps.
5. Active system for injecting liquid absorber.
6. Active emergency core cooling system from feedwater pumps.
7. Active emergency core cooling system through recirculation pumps.
8. System of reactor caisson filling with water.
9. Containment passive emergency pressure decrease system (bubbling).
10. Active emergency shutdown cooling system (through process condensers).
11. Passive emergency shutdown cooling system

12. Opening to atmosphere.

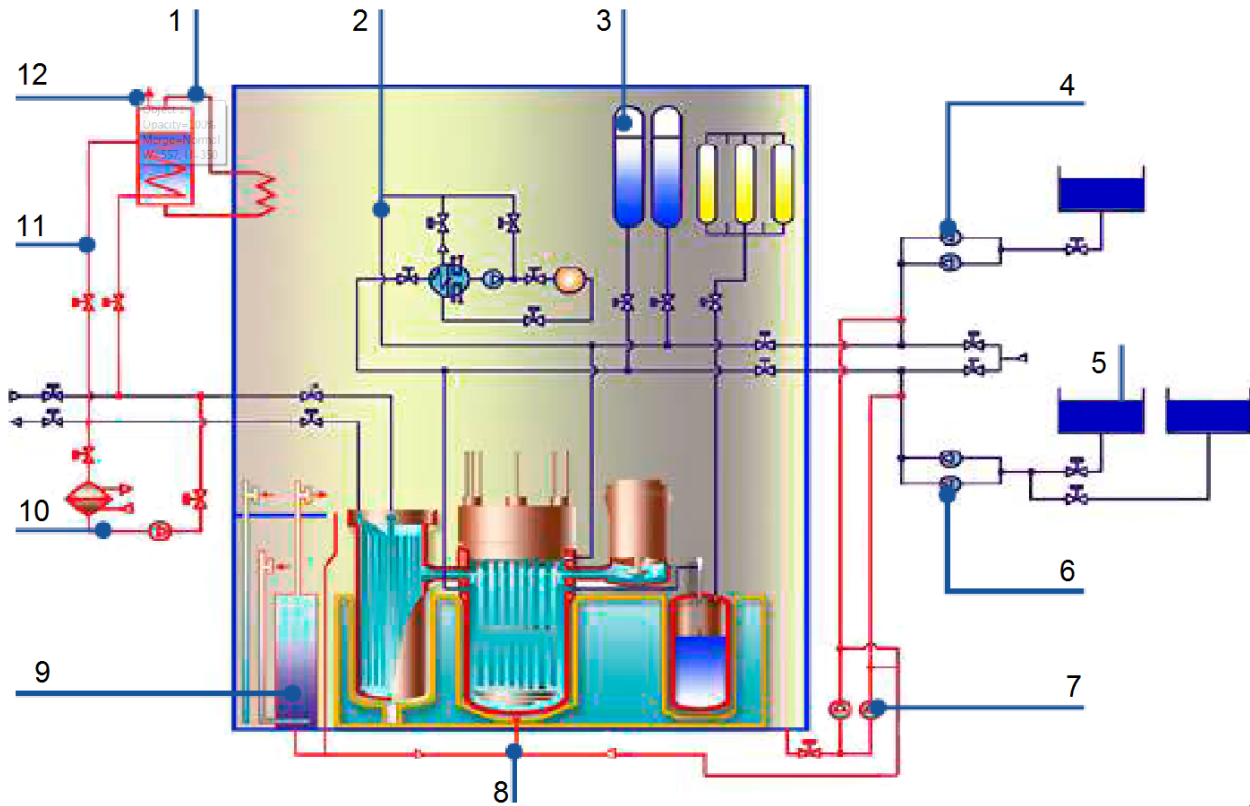


Figure 2-8: Schematic layout of KLT-40S reactor and its safety systems (obtained from Piro, ..., Dort-Goltz (2020)) (courtesy and copyright of ASME).

A more advanced SMR, RITM-200M, is also currently being tested by Russia for commercial electricity and heat generation operations in remote communities by 2028 with several reactors already incorporated into new icebreakers still under construction (Rosatom, 2020). The RITM-200M SMR is an integral PWR – its heat exchangers are integrated into the reactor pressure vessel – with similar projected thermal and electrical outputs as the KLT-40S but with higher thermal efficiency. Pictures of both the KLT-40S and RITM-200M are included in Figure 2-9 with a comparison of physical and operational parameters presented in Table 2-13.



(a)



(b)

Figure 2-9: Russian SMRs. (a)-KLT-40S; (b)-RITM-200M (obtained from Pioro, ..., Dort-Goltz (2020)) (courtesy and copyright of ASME).

Table 2-13: KLT-40S and RITM-200M parameters (obtained from Pioro, ..., Dort-Goltz (2020)) (courtesy and copyright of ASME). Production of desalinated water is in case of desalination complex. For refueling, the combined barge and SMR unit will be brought back to the manufacturing plant and completely overhauled every 12 years.

Parameters	KLT-40S	RITM-200M
Reactor type	PWR	Integral PWR
Generation of SMRs	III	III ⁺
Reactor coolant / moderator	Light water	
Thermal power, MW _{th}	150	175
Electric power, gross / net, MW _{el}	38.5 / 35	55 / 50
Thermal efficiency, %	~26	~31
Expected capacity factor, %	60 – 70	65
Maximum output thermal power, GJ/h (Gcal/h); MW	305.6 (73); 84.9	- ²
Production of desalinated water, m ³ /day	40,000 – 100,000*	-
Operating range of power, %	10 – 100	-
Normal-mode power variation, % / s	0.1	-
Primary circuit pressure, MPa	12.7	15.7
Primary circuit T_{in}/T_{out} , °C	280 / 316	277 / 313
Reactor coolant mass-flow rate, t/h	680	3250
Primary circuit circulation mode	Forced	

² '-': unavailable

Parameters	KLT-40S	RITM-200M
Power cycle	Indirect Rankine cycle	
P_{steam} at steam-generator outlet, MPa	3.72	3.82
T_{sat} at P_{steam} , °C	246.1	247.4
Overheated T_{steam} at steam-generator outlet, °C	290	295
Steam mass-flow rate, t/h	240	261
T feedwater in – out, °C	70 – 130	-
RPV height / diameter, m	4.8 / 2.0	9.2 / 3.5
Maximum mass of reactor pressure vessel, t	46.5	-
Fuel type / Assembly array	UO ₂ pellets in silumin matrix	UO ₂ pellet / hexagonal
Fuel assembly active length, m	1.2	2.0
Number of fuel assemblies	121	241
Core service life, h	21,000	75,000
Refueling interval, years	~3**	Up to 10
Refueling outage, days	30 – 36	-
Fuel enrichment, %	18.6	Up to 20
Fuel burnup, GWd/t	45.4	-
Predicted core-damage frequency, event / reactor year	$0.5 \cdot 10^{-7}$	-
Seismic design	9 point on MSK scale	0.3g

In addition to these, three other SMR concepts are also under construction though these are just demonstration units; CAREM, HTR-PM, and CFR-600. Of the near 100+ concepts presented in this section, only a handful are currently either operating or under construction. The overwhelming majority of SMR and S&MR concepts are still in the early phases of development and so reliable data regarding key operational parameters is lacking and subject to constant change. Since many of these designs also tout new and improved safety systems, licensing will be an obstacle for any vendor wishing to put into operation a new SMR/S&MR concept in addition to financial and intellectual restraints. It is most likely the case that very few of the presented SMR/S&MR concepts will make it to the final design phase regardless of the enthusiasm surrounding these types of nuclear reactors (Pioro, ..., Dort-Goltz, 2020).

2.4.1: Overview of SuperSafe Reactor SMR

The SMR selected for the economic analysis of this thesis is called the SuperSafe Reactor (SSR).

Outlined in Yetisir et al. (2012), the SSR is a scaled down version of the SCWR LNR rated at 300 MW_{el} with a thermal rating of roughly 667 MW_{th}. This represents an assumed thermal efficiency of around 45%, achieved by using SCW as a reactor coolant at a pressure of 25 MPa and an outlet temperature of 625 °C. The core of the SSR will contain 120 fuel channels arranged in a 25 cm square lattice pitch with an overall core diameter of 400 cm. The top of the core is characterized by an inlet plenum containing light water coolant while the bottom has an attached low-pressure calandria vessel that contains heavy water moderator. Pressure tubes oriented vertically contain the full-length fuel assemblies and are connected to a tube sheet that separates the coolant from the moderator. Light water coolant is injected into the plenum and then forced vertically downwards into the fuel channels through a central flow channel. Due to the double flow pass configuration, the coolant exits the central flow channel and begins to flow upwards over the fuel elements. Initially, the coolant is at a pressure of 26 MPa and a temperature of 350 °C when in the plenum but it exits the fuel channel at an average pressure of 25 MPa and 625 °C. A direct cycle will be employed for power generation so the exit coolant will then be directed towards high pressure turbines (HPTs) and eventually make its way to the condenser where the cycle will begin anew.

The fuel assemblies and channels for the SCWR and SSR are identical. The fuel channel is based on the high efficiency channel (HEC) concept (Chow and Khartabil, 2008). The outermost component of the HEC is a zirconium-based alloy, Excel, pressure tube that is in direct contact with the moderator. Directly inside the pressure tube is a porous zirconia insulator that insulates it from the high temperatures of the coolant. On the inner surface of the insulator is a perforated liner tube used for structural support. For fuel, several options are being considered including

low-enriched uranium (LEU) and low-enriched uranium and thorium (LEU-Th). A LEU once-through cycle would use 6% enriched uranium and would have a cycle length of 720 effective full power days (EFPD). The advantage of using this in the short-term, compared to other options, would be the longer cycle length resulting in a 10% higher capacity factor (Yetisir et al., 2012). This could have potential economic benefit. The reactor is still being developed so many parameters are still being investigated and finalized. A discussion of the estimated reactor parameters is given in Section 3.3.2

Chapter 3: Methodology

3.1: Investigational Procedure into NIST REFPROP v.10

3.1.1: Theoretical Calculations of Thermophysical Properties by NIST REFPROP v.10

The National Institute of Standards and Technology (NIST) is the developer of a program called REFPROP (REFerence fluid PROPERTIES) that calculates the thermophysical properties of pure fluids and mixtures. As of the most current release, v.10, REFPROP has a library of 147 pure fluids, 5 pseudo-pure fluids (for example air), and mixtures with up to twenty components (NIST, 2018). To do this, three models, stated by NIST (2018) to be the most accurate available, are used to calculate the thermophysical properties of pure fluids. These are:

- Equations of state explicit in Helmholtz energy
- The modified Benedict-Rubin equation of state
- An extended corresponding state (ECS) model

For mixtures, a model that applies mixing rules to the Helmholtz energy of the components is employed along with a departure function to account for the departure from ideal mixing. For the viscosity and thermal conductivity of the fluids and mixtures, fluid-specific correlations, an ECS method, or in some cases the friction theory method will be used. As to the method used for a specified pure fluid, REFPROP provides a “Fluid Information” window located in the “Substance” tab of the user interface. Within this window, standard information about the fluid is given, such as its critical point, along with a range of applicability for the model used to calculate a specific thermophysical property. An example of this is given in Figure 3-1 where the “Fluid Information” for water is shown.

Water was the fluid used in the supercritical heat transfer experiments by Kirillov et al. (2003), hence for the investigation into REFPROP’s handling of thermophysical properties, water was

chosen as the main subject. The properties whose behaviors were explored around the critical point of water were selected to be:

1. Density, ρ
2. Specific Enthalpy, h
3. Specific Heat, c_p
4. Thermal Conductivity, k
5. Dynamic Viscosity, μ
6. Kinematic Viscosity, ν
7. Thermal Diffusivity, α
8. Prandtl Number, **Pr**
9. Volume Expansivity, β

Properties 1-3 are categorized as “Thermodynamic” properties in REFPROP, with properties 4-8 categorized as “Transport” properties, and property 9 categorized as a “Derivative” property. The enthalpy, and specific heat of water are calculated in REFPROP using the dimensionless Helmholtz free energy formulation found in Wagner and Pruss (2002). The thermal conductivity is by calculated by the correlation found in Huber et al. (2012) while the dynamic viscosity is calculated using the correlation from Huber et al. (2009). Alternative models are available for the calculation of these thermophysical properties however, the ones listed above are recommended by NIST for use in REFPROP (NIST, 2018). These nine properties were selected because they are some of the more common thermophysical properties encountered in heat transfer correlations commonly cited in academic textbooks such as Incorpera et al. (2007).

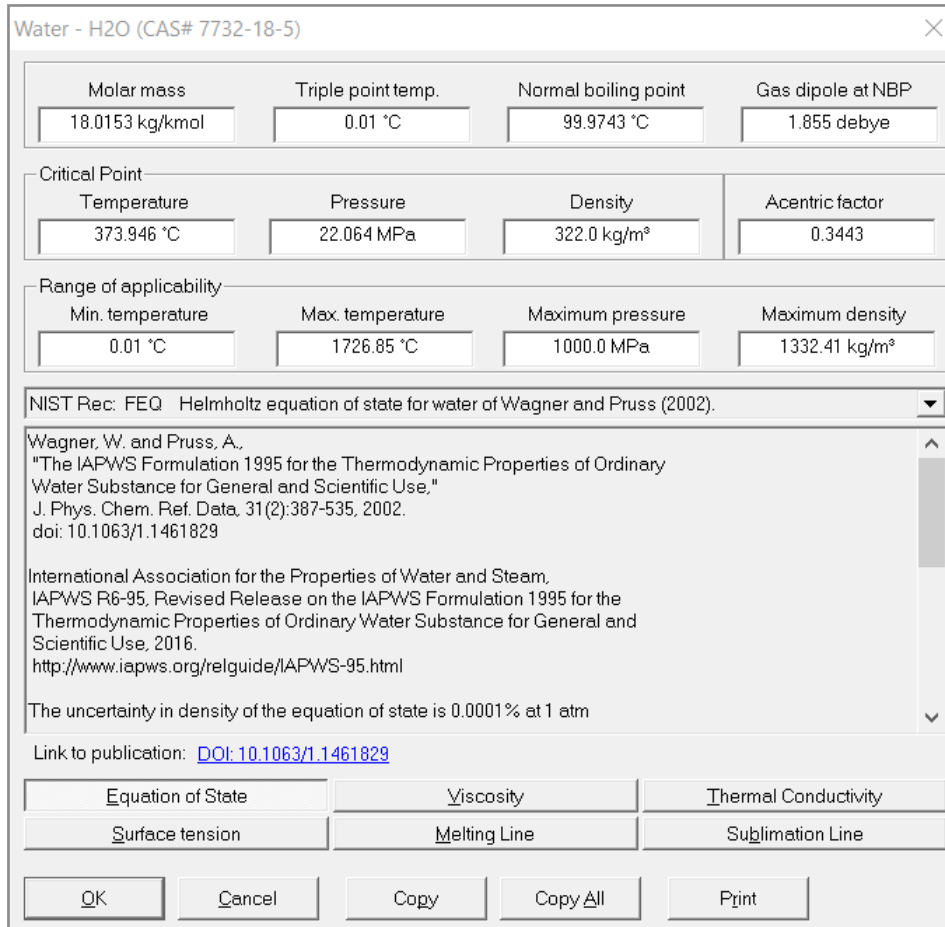


Figure 3-1: Fluid information window for water taken from REFPROP v.10 (NIST, 2018). Critical point and density are given along with the range of applicability for the “Equation of State”. The range of applicability will change for the “Viscosity” and “Thermal Conductivity” sections due to different theoretical models used for property calculation.

As such, these models were used in the generation of all thermophysical properties used in this thesis. The kinematic viscosity, thermal diffusivity, Prandtl number, and volume expansivity were all calculated using derived equations dependent on other thermophysical properties (see Equations 3-1–3-4).

$$v = \frac{\mu}{\rho} \quad (3-1)$$

$$\alpha = \frac{k}{\rho c_p} \quad (3-2)$$

$$\mathbf{Pr} = \frac{\mu C_p}{k} \quad (3-3)$$

$$\beta = \frac{1}{V} \frac{\partial V}{\partial T} \Big|_P = - \frac{1}{\rho} \frac{\partial \rho}{\partial T} \Big|_P \quad (3-4)$$

Regarding the error associated with the value of the density, pressure, isobaric specific heat capacity, dynamic viscosity, and thermal conductivity as well as ranges of applicability, please see Table 3-1.

Table 3-1: Estimated uncertainties in models used for the calculation of selected properties and ranges of applicability. These are provided mainly for clarity and did not have an impact on the analysis in Section 4.1. All values were taken from the source of the model used by NIST (2018) except for density, whose uncertainty was stated by NIST (2018).

Property	Model	Estimated Uncertainties	Range of Applicability for Model
Density	N/A	<ul style="list-style-type: none"> ±0.001% @ 1 atm (liquid phase); ±0.001% at pressures/temperatures up to 10 MPa/ T=423 K (liquid state) ±0.05% (vapor state) Noted that uncertainties increase at higher temperatures/pressures but generally less than ±0.1% except for extreme conditions 	<ul style="list-style-type: none"> Min. temperature: 0.01 °C Max. Temperature: 1726.85 °C Max. Pressure: 1000.0 MPa Max. Density: 1332.41 kg/m³
Pressure	Dimensionless Helmholtz free energy ³ (Wagner and Pruss, 2002)	<ul style="list-style-type: none"> ±0.1% in critical region 	
Isobaric Specific Heat Capacity		<ul style="list-style-type: none"> ±0.2% (vapor phase) ±0.1% (liquid phase) Noted that these increase in the critical region and at high temperatures/pressures 	

³ The thermodynamic property, enthalpy, is also calculated using this model. However, an error estimate was not provided by Wagner and Pruss (2002).

Property	Model	Estimated Uncertainties	Range of Applicability for Model
Dynamic Viscosity	Huber et al. (2009) correlation	<ul style="list-style-type: none"> • $\pm 1\text{-}3\%$ (liquid phase; supercritical conditions) • $\pm 2\%$ (vapor phase) • $\pm 7\%$ @ $P \geq 100$ MPa and $373 \text{ K} \leq T \leq 1173 \text{ K}$ 	<ul style="list-style-type: none"> • Min. temperature: $-21.985 \text{ }^\circ\text{C}$ • Max. Temperature: $1076.85 \text{ }^\circ\text{C}$ • Max. Pressure: 1000.0 MPa • Max. Density: 1332.41 kg/m^3
Thermal Conductivity	Huber et al. (2012) correlation	<ul style="list-style-type: none"> • $\pm 1.5\%$ @ $P \leq 50$ MPa and $273.15 \text{ K} \leq T \leq 523 \text{ K}$ • $\pm 2\%$ (vapor phase) • Error increase with increasing pressure and temperature • Max estimated error ($\pm 6\%$) @ $T \geq 824 \text{ K}$ 	<ul style="list-style-type: none"> • Min. temperature: $-21.985 \text{ }^\circ\text{C}$ • Max. Temperature: $1076.85 \text{ }^\circ\text{C}$ • Max. Pressure: 1000.0 MPa • Max. Density: 1332.41 kg/m^3

All three models rely on dimensionless terms that use some reference properties of water. These are the critical temperature, $T_{cr}=647.096 \text{ K}$ or $373.946 \text{ }^\circ\text{C}$; critical pressure, $P_{cr}=22.064 \text{ MPa}$; critical density, $\rho_{cr}=322 \text{ kg/m}^3$; reference dynamic viscosity, $\mu^*=1.00 \times 10^{-6} \text{ Pa}\cdot\text{s}$; and reference thermal conductivity⁴, $\lambda^*=1.00 \times 10^{-3} \text{ W/m}\cdot\text{K}$. For the dimensionless Helmholtz free energy from Wagner and Pruss (2002), the forms of the reduced (dimensionless) quantities are given in

⁴ The notation used by Huber et al. (2011) for thermal conductivity is representing it by the Greek symbol, λ , as k is used instead in index notation.

Equations 3-6 and 3-7 with the general dimensionless Helmholtz free energy given in Equation 3-5,

$$\frac{f(\rho, T)}{RT} = \phi(\delta, \tau) = \phi^o(\delta, \tau) + \phi^r(\delta, \tau) \quad (3-5)$$

$$\delta = \frac{\rho}{\rho_{cr}} \quad (3-6)$$

$$\tau = \frac{T_{cr}}{T} \quad (3-7)$$

Equation 3-6 is referred to as the reduced density and Equation 3-7 is referred to as the inverted reduced temperature. In Equation 3-5, $f(\rho, T)$ is referred to as the specific Helmholtz free energy, with $\phi(\delta, \tau)$ the dimensionless Helmholtz free energy, $\phi^o(\delta, \tau)$ the ideal-gas part obtained from an equation for the specific isobaric heat capacity in the ideal-gas state developed by Cooper (1982), $\phi^r(\delta, \tau)$ the residual part, and R is the specific gas constant ($R=0.46151805$ kJ/kg·K). The thermophysical properties that REFPROP calculates with this model are done so using appropriate combinations of the ideal-gas and residual parts along with their derivatives. Variations of the dimensionless Helmholtz free energy used to calculate the enthalpy (Equation 3-8) and isobaric specific heat (Equation 3-9) of water are given below⁵,

$$\frac{h(\delta, \tau)}{RT} = 1 + \tau(\phi_\tau^o + \phi_\tau^r) + \delta\phi_\delta^r \quad (3-8)$$

⁵ Dimensionless variable subscripts represent partial derivatives with respect to the dimensionless variable.

$$\frac{c_p(\delta, \tau)}{R} = -\tau^2(\phi_{\tau\tau}^o + \phi_{\tau\tau}^r) + \frac{(1 + \delta\phi_{\delta}^r - \delta\tau\phi_{\delta\tau}^r)^2}{1 + 2\delta\phi_{\delta}^r + \delta^2\phi_{\delta\delta}^r} \quad (3-9)$$

For calculations of the dynamic viscosity and thermal conductivity, REFPROP makes use of the correlations developed by Huber et al. (2009, 2012). These correlations have very similar forms, being composed of a term representing the thermophysical property at the dilute-gas limit, a term representing the contribution to the thermophysical property due to finite density, and a third term representing a critical enhancement term that is only applicable within a small region around the critical point of water. For dynamic viscosity, this region is defined as $645.91 \text{ K} < T < 650.77 \text{ K}$ and $245.8 \text{ kg/m}^3 < \rho < 405.3 \text{ kg/m}^3$. Given below, in Equations 3-10 and 3-11, are the Huber et al. correlation (2009) for dynamic viscosity and the Huber et al. correlation (2012) for thermal conductivity along with the definitions of any present dimensionless quantities⁶.

$$\bar{\mu} = \bar{\mu}_0(\bar{T}) \times \bar{\mu}_1(\bar{T}, \bar{\rho}) \times \bar{\mu}_2(\bar{T}, \bar{\rho}) \quad (3-10)$$

$$\bar{\lambda} = \bar{\lambda}_0(\bar{T}) \times \bar{\lambda}_1(\bar{T}, \bar{\rho}) + \bar{\lambda}_2(\bar{T}, \bar{\rho}) \quad (3-11)$$

$$\bar{\mu} = \frac{\mu}{\mu^*} \quad (3-12)$$

$$\bar{\lambda} = \frac{\lambda}{\lambda^*} \quad (3-13)$$

$$\bar{T} = \frac{T}{T^*} \quad (3-14)$$

$$\bar{\rho} = \frac{\rho}{\rho^*} \quad (3-15)$$

In Equations 3-10 and 3-11, the dimensionless quantities that have the subscript “0” are the dilute-gas limit terms, ones with the subscript “1” are the finite density contribution terms, and ones with the subscript “2” are the critical enhancement terms. Their full representation, along

⁶ The quantities T^* and ρ^* are just the critical temperature and density of water respectively and their roles are analogous to the ones played by T_{cr} and ρ_{cr} in the dimensionless Helmholtz energy model.

with the full representation of the terms in Equations 3-5, 3-8, and 3-9, may be found in Appendix B as they are quite lengthy and are not of immediate value. In all three models used by NIST (2018), caution is given by the authors to their use near the critical point of water.

With Wagner and Pruss (2002), the form of the dimensionless Helmholtz free energy used to calculate the isobaric specific heat capacity of water depends on higher derivatives. Around the critical point, these terms begin to rapidly increase in value and so the values generated by Equation 3-9 become unphysical. For the Huber et al. correlations (2009, 2012), the critical enhancement terms include an isotherm partial derivative of density with respect to pressure that does not converge at the critical point. This causes the critical enhancement terms in Equations 3-10 and 3-11 to exhibit unphysical behaviour close to the critical point of water. Consequently, several other thermophysical properties, such as kinematic viscosity or the Prandtl number, begin exhibiting unphysical behaviour around the critical point as well due to their dependence on either the isobaric heat capacity, dynamic viscosity, or thermal conductivity. As a result, any calculations involving the thermophysical properties of water and their generation by NIST REFPROP v.10 around the critical point must be handled with extreme care.

3.1.2: Procedure for Investigating the Critical Properties of Water

A relatively simple procedure was formulated to investigate the critical property values of water generated by REFPROP v.10. First, the values of the thermophysical properties listed in Section 3.1.1 were organized and compiled into a single table. To do so, isoproperty tables were constructed within REFPROP v.10 using the “Calculate >>Isoproperty Table” feature. Prompts for setting up the table are given in Figure 3-2. Four different temperature increments were analyzed:

- $\Delta T_I = 1 \text{ }^\circ\text{C}$

- $\Delta T_2=0.1$ °C
- $\Delta T_3=0.01$ °C
- $\Delta T_4=0.002$ °C

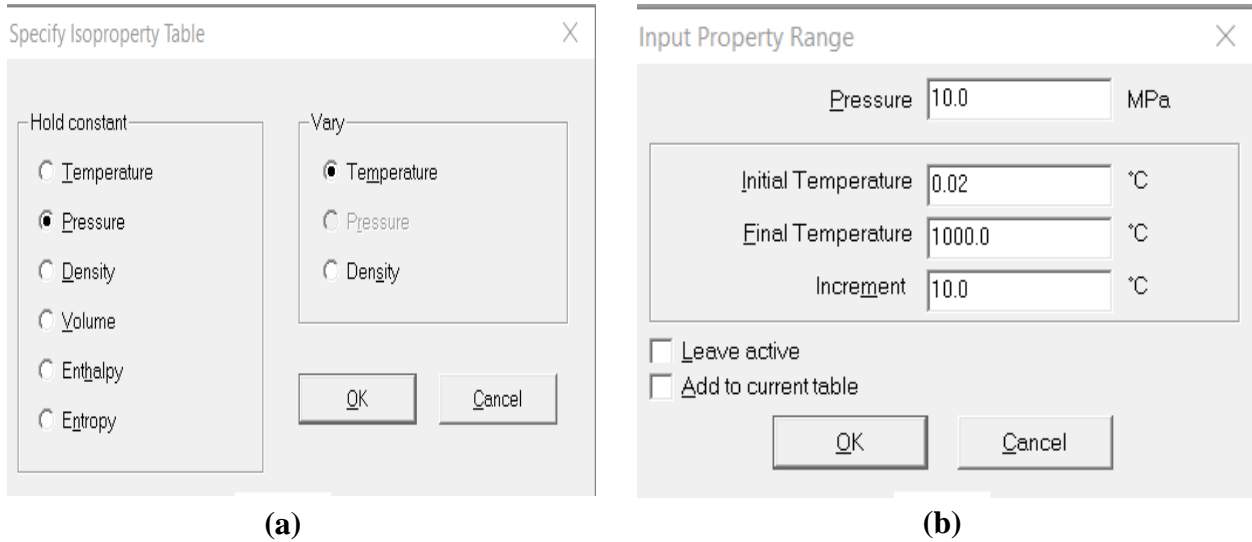


Figure 3-2: Steps for generating isoproperty table in REFPROP v.10 (NIST, 2018). (a)- Selection of properties to be held constant/varied; (b)-Specification of parameters

For the first temperature increment, a temperature range of 370 °C to 386 °C was chosen. The second temperature increment was used with a temperature range of 370 °C to 384 °C while the third and fourth temperature increments were used with temperature ranges of 370 °C to 382 °C and 370 °C to 380 °C respectively. Unique temperature ranges were assigned to every temperature increment in order to separate the curves from each other, thus allowing a clearer view of the critical properties, while also allowing a sufficient amount of data points to be created for a more satisfactory curve. It was also done to prevent computational strain while calculating the thermophysical properties as, for example, using ΔT_4 with a temperature range of 370 °C to 386 °C would result in 8000 data points and it was feared this may lead to slower performance by REFPROP v.10. Pressure was selected as the constant property for the isoproperty table with a value of 22.064 MPa, or the critical pressure.

Once the property values were generated, they were copied and pasted into an Excel worksheet, organized by their respective temperature increments. From there, the pages from the Excel worksheet were imported into Sigmaplot, a graphing software, and the graphs for each set of thermophysical properties were formed. In each graph, four different x-axes were introduced for the four temperature increment curves. To differentiate, each x-axis was colour-coded to match its respective curve and vertical reference lines were added (with matching colour) to indicate the location of the critical temperature on a particular curve. A single horizontal reference line was added to mark the critical value of the specified property. For the specific heat, thermal conductivity, Prandtl number, and thermal expansivity graphs, common log scales were used for the vertical y-axis due to the extremely large values encountered. The x-axis scales were kept as linear for all graphs and the limits set as the boundaries of the temperature ranges for each temperature increment.

To verify that Equations 3-1 to 3-4 were the ones used by REFPROP v.10 to calculate their specific thermophysical properties, another Excel worksheet was created and used for the verification process. Using the values generated by REFPROP v.10 for the non-dependent properties (such as specific heat and thermal conductivity), the dependent properties were re-calculated using Equations 3-1 to 3-4. The relative errors between the re-calculated values and the generated values for all dependent thermophysical properties were explored, with an acceptable result defined as $\pm 1\%$ of the generated value.

3.2: Experimental Setup and Procedure for 1-m Supercritical Heat Transfer Analysis

3.2.1: Description of Experimental Setup

The experimental, SCW data used in this thesis was obtained by Kirillov et al. (2003) at the State Scientific Center of Russian Federation - Institute for Physics and Power Engineering Supercritical-Test Facility (Obninsk, Russia). It was taken at operating conditions close to those

of an SCWR-type reactor (Mokry et al., 2009). The apparatus used was the SKD-1 loop (Kirillov et al., 2005), a high-temperature and high-pressured pumped loop with the ability to operate at pressures up to 28 MPa, outlet water temperatures up to 500 °C, and electrical power up to 600 kW and a diameter close in magnitude to the hydraulic-equivalent diameter (D_{hy}) of the fuel bundle proposed for the SCWR (Mokry et al., 2009). The test section was a bare tube of heated length of 1-m with a vertical orientation and upward flow of SCW. The tube was circular with an ID of 10 mm, and an outer diameter (OD) of 12 mm. It was made of stainless-steel (12Cr18Ni10Ti) with an internal arithmetic averaged surface roughness (R_a) of 0.63-0.8 μm . Heating was achieved by a 600 kW (AC) power supply running through the walls of the tube. To minimize the environmental heat loss during the flow of SCW, the tube was wrapped in thermal insulation (Pioro and Duffey, 2007). After comparison of the electrical heat input to the actual heat transfer to the water, it was shown that the heat-loss from the test section was small and was within 3% of the electrical heat input (Kirillov et al., 2005; Pioro and Duffey, 2007).

The water used as a coolant was distilled and de-ionized and passed through a pump to a flowmeter, a preheater, the test section, and then the mixing cooler before going through the main loop heat exchangers (site of the largest portion of heat removal) and then back to the pump. Pressurization was achieved with the use of high-pressure nitrogen gas (N_2). A schematic of the SKD-1 loop is included in Figure 3-3. During the experimental runs, the following test-section parameters were measured or calculated (Mokry, 2009):

- Test-section current and voltage to calculate the power
- Pressure at test-section inlet
- Temperatures at the test-section inlet and outlet. These were measured using ungrounded sheathed thermocouples (K-type) inserted into the fluid stream and calibrated *in situ*. The

thermocouples were installed just downstream of the mixing chambers (3 and 8 in Figure 3-3) that were used to minimize any non-uniformity in the cross-sectional temperature distribution

- Outside wall temperatures at equal intervals of 50 mm along the 1-m long test section. Twenty-one thermocouples were contact welded to the outside wall surface, isolated by glass cord, and calibrated *in situ*
- Water mass-flow rate was calculated based on the measured pressure drop over a small orifice plate that was monitored with differential-pressure cell
- Ambient temperature

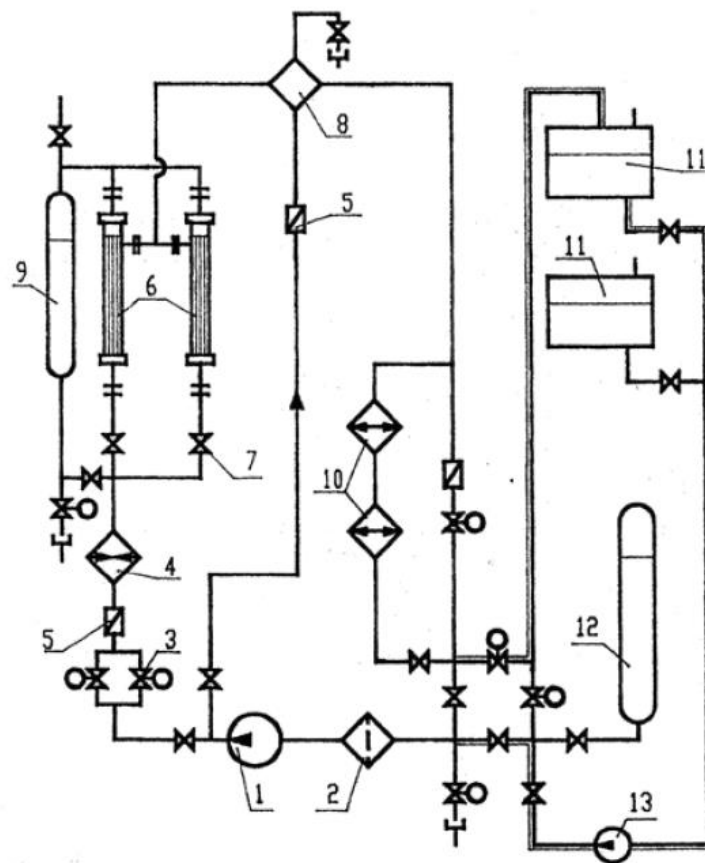


Figure 3-3: Schematic of SKD-1 Loop (Pioro et al., 2010; Kirillov et al., 2005); 1-circulating pump; 2-mechanical filter; 3-regulating valves; 4-electrical heater; 5-flow meter; 6-test section; 7-throttle valve; 8-mixer-cooler; 9-discharge tank; 10-heat exchanger; 11-feedwater tank; 12-volume compensator; 13-feedwater pump.

The uncertainty of the measured and calculated parameters, arising due to instrumentation limitations, is given in Table 3-2. These parameters were then used to calculate the local T_w 's and $HTCs$ at the specific test condition. This process was repeated for each new test condition.

Table 3-2: Maximum uncertainties of measured and calculated parameters (Kirillov et al., 2005).

Parameters		Max. Uncertainty
Measured Parameters	Test-Section power	$\pm 1.0\%$
	Inlet Pressure	$\pm 0.25\%$
	Wall Temperatures ⁷	$\pm 3.0^\circ\text{C}$
Calculated Parameters	Mass-flow rate	$\pm 1.5\%$
	Heat loss	$\leq 3\%$

The experimental dataset was recorded by a Data Acquisition System (DAS) when the desired flow and power conditions had been reached and stabilized. Once all data had been obtained, a new power level and/or a set of flow conditions was set. For the 1-m long dataset, three different flow regimes were recognized as being either low G , $\sim 200 \text{ kg/m}^2 \cdot \text{s}$; medium G , $\sim 500 \text{ kg/m}^2 \cdot \text{s}$; or high G , $\sim 1000 \text{ kg/m}^2 \cdot \text{s}$ in Kirillov et al. (2003). The test matrix with all experimental parameters, such as q_{ave} , is given in Table 3-3.

Table 3-3: Test matrix for 1-m long, vertical, upward flow bare tube dataset (data obtained by Kirillov et al. (2003)); Orange-high G tests; Blue-medium G tests; Green-low G tests.

No.	Test #	P_{in}	G	T_{in}	T_{out}	T_{pc}	q_{ave}	Q
–	–	MPa	$\text{kg/m}^2 \cdot \text{s}$	$^\circ\text{C}$	$^\circ\text{C}$	$^\circ\text{C}$	kW/m^2	kW
1	21/40	24.6	996	300	337	383	581	18
2	21/44	24.6	993	300	362	383	979	31
3	21/63	24.5	994	349	381	383	970	30
4	21/81	24.6	994	359	382	383	874	27
5	21/98	24.6	993	370	382	383	874	27
6	22/19	24.6	991	380	387	383	1028	32
7	25/61	24.8	495	350	378	384	390	12
8	25/70	24.9	495	359	381	385	389	12
9	25/72	24.9	498	359	384	385	585	18

⁷ Note: These wall temperatures refer to outside wall temperatures and not T_w , or the inside wall temperatures.

No.	Test #	P_{in}	G	T_{in}	T_{out}	T_{pc}	q_{ave}	Q
–	–	MPa	kg/m ² ·s	°C	°C	°C	kW/m ²	kW
10	25/83	24.9	497	368	384	385	484	15
11	25/98	24.9	498	381	389	385	585	18
12	26/24	24.9	496	350	380	385	433	14
13	27/22	24.9	200	301	362	385	228	7
14	27/53	24.9	200	349	360	385	88	3
15	27/86	24.7	201	358	383	384	275	9
16	27/88	24.9	201	358	387	385	374	12
17	27/98	25	198	370	383	385	181	6
18	28/01	24.8	199	371	387	384	324	10

With the 1-m dataset, a computer code was created using Python to analyze the data with the Dittus-Boelter (Equation 2-2), Mokry et al. (Equation 2-3), and Gupta et al. (Equation 2-4) correlations to calculate the predicted $HTCs$ and T_w 's.

3.2.2: Verification of Python Code and Graphing of Results

A Python code, referred to as the Nikita Dort-Goltz (NDG) code, was constructed to calculate the $HTCs$ and T_w 's of the 1-m long dataset using Equations 2-2, 2-3, and 2-4. To verify the correct implementation of the Mokry et al. (2009) and Gupta et al. (2011) correlations, the code was first used to re-calculate the predicted $HTCs$ and T_w 's of the 4-m long Kirillov et al dataset (2003). This was the dataset used by Mokry et al. (2009) and Gupta et al. (2011) to develop their correlations. A sample of the Python code used for analysis are included in Appendix C. The predicted $HTCs$ and T_w 's for the 4-m long dataset that were calculated by the Mokry et al. (2009) and Gupta et al. (2011) correlations were kept in separate Sigmaplot files. These files also contained the experimental $HTCs$ and T_w 's along with the T_b 's from the 4-m long dataset. The predicted $HTCs$, T_w 's were transferred into “.txt” files and imported into an intermediate Python program with the purpose of reverse-calculating the local heat flux, q , along the heated length of the 4-m bare tube using Equation 3-16,

$$q=HTC*(T_w-T_b) \quad (3-16)$$

The bulk fluid temperature used in Equation 3-16 was also transferred from the Sigmaplot files as preliminary calculations of the bulk fluid temperature revealed little to no difference between the bulk fluid temperatures calculated from scratch and the ones found in the Sigmaplot files. After the local heat fluxes were calculated, they were exported as “.txt” files and then imported into the main Python code. Four verifications were performed with two involving the Mokry et al. (2009) correlation at different inlet temperatures but identical G 's and two involving the Gupta et al. (2011) correlation at different G 's. The Python code was then put into operation to output a new set of predicted $HTCs$ and T_w 's which were then compared to the original Mokry et al. (2009) and Gupta et al. (2011) correlations. Results are given in Figures 3-4 and 3-5.

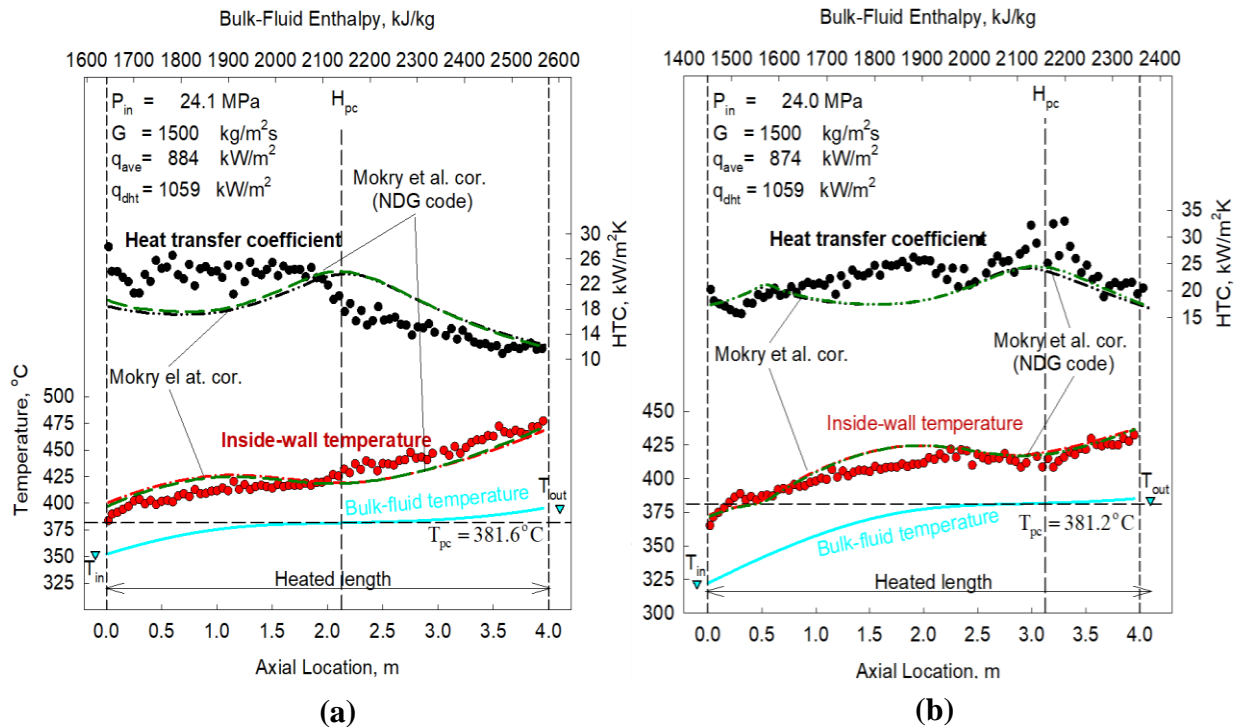


Figure 3-4: Verification graphs for Mokry et al. correlation; (a)- $L_h=4 \text{ m}$, $G=1500 \text{ kg/m}^2\text{s}$, $q_{ave}=884 \text{ kW/m}^2$; (b)- $L_h=4 \text{ m}$, $G=1500 \text{ kg/m}^2\text{s}$, $q_{ave}=874 \text{ kW/m}^2$; Green-NDG verification results, Red/Black-Original Mokry et al. results

Originally, the non-entrance-effect Gupta et al. (2011) correlation, Equation 2-4, was used in the verification of the results. However, there was an unsatisfying fit within the entrance region of the data and so the entrance-effect Gupta et al. (2011) correlation, Equation 2-5, was used as well. This resulted in a better fit of the results calculated from the original MATLAB code. Verification of the Gupta et al. (2011) correlation with both Equation 2-4 and Equation 2-5 is given in Figure 3-5. Additionally, a root-mean square (RMS), or root-mean square error (RMSE), analysis along with a computation of the max percent error was performed for all four verification cases in Microsoft Excel. The results are listed in Table 3-4 and for computing the root mean square error and percent errors, the following forms were used,

$$RMS = \sqrt{\frac{\sum_{i=1}^n (y_{actual,i} - y_{calculated,i})^2}{n}} \quad (3-17)$$

$$Percent\ Error = \left(\frac{y_{calculated} - y_{actual}}{y_{actual}} \right) \times 100\% \quad (3-18)$$

Equation 3-17 uses errors, instead of relative errors, in its formulation hence the final quantity will have the same unit as the parameter being analyzed. Regardless of whether error or relative error is employed, a lower RMS value indicates a better fit of the model to the observed data. As shown in Table 3-4, the correlations were correctly implemented in the Python code as evidenced by the fairly low RMS scores for all correlations (for comparison, an RMS of 0 represents an ideal fit). The maximum percent errors that were calculated corresponded to the largest percent error encountered in the entire verification cycle. Thus, the large percent errors associated with the *HTC* calculation by Equation 2-4 in both verification cycles was the result of comparing the values calculated by Equation 2-4 to those of Equation 2-5

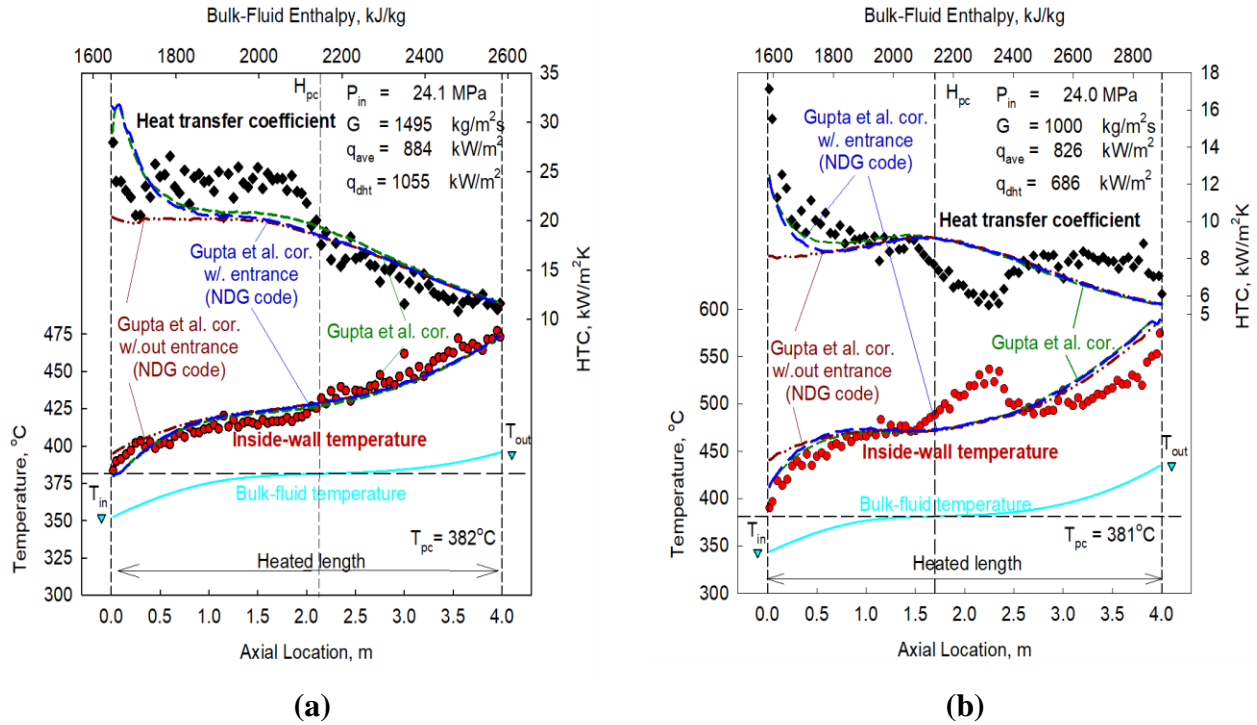


Figure 3-5: Verification graphs for Gupta et al. correlation; (a)- $L_h=4$ m, $G=1495$ kg/m²·s, $q_{ave}=884$ kW/m²; (b)- $L_h=4$ m, $G=1000$ kg/m²·s, $q_{ave}=826$ kW/m²; Green-original Gupta et al. results, Blue-NDG verification results with entrance effect, Maroon- NDG verification without entrance effect.

Table 3-4: Error analysis of Mokry et al. and Gupta et al. correlation (Equations 2-3 -2-5)

Correlation/ Equation No.	Key Parameters	RMS, (T_w , °C/ HTC , kW/m ² ·K)	Maximum Percent Error, (T_w , %/ HTC , %)
Mokry et al./Equation 2-3	$G=1500$ kg/m ² ·s; $q_{ave}=884$ kW/m ²	1.7/0.5	0.9/5.5
Mokry et al./Equation 2-3	$G=1500$ kg/m ² ·s; $q_{ave}=874$ kW/m ²	1.0/0.5	0.7/5.1
Gupta et al./ Equation 2-4	$G=1495$ kg/m ² ·s; $q_{ave}=884$ kW/m ²	4.0/2.5	4.1/36.1
Gupta et al./ Equation 2-5	$G=1495$ kg/m ² ·s; $q_{ave}=884$ kW/m ²	1.2/0.5	0.5/4.5
Gupta et al./ Equation 2-4	$G=1000$ kg/m ² ·s; $q_{ave}=826$ kW/m ²	5.8/0.6	5.2/26.8
Gupta et al./ Equation 2-5	$G=1000$ kg/m ² ·s; $q_{ave}=826$ kW/m ²	2.6/0.2	1.3/5.8

The original data obtained from the Sigmaplot files seemed to have been calculated using Equation 2-5 and so a comparison of the maximum percent errors for Equation 2-5 was more appropriate for gauging the implementation of the Gupta et al. (2011) correlation in Python. When done, the RMS and maximum percent errors decrease significantly once more indicating that the correlations were correctly implemented in the Python code. The biggest discrepancy between Equations 2-4 and 2-5 for both $HTCs$ and T_w 's, based off the results in Figure 3-5, seemed to have been in the entrance region of the test section. Otherwise, there was significant overlap along the rest of the test section indicating that aside from the entrance region, both Equations 2-4 and 2-5 produced similar values. Thus, the use of Equation 2-4 in the heat transfer analysis for this work would probably not generate dissimilar predictions if Equation 2-5 were employed instead.

Once the verification process was completed, a code was built to analyze the HTC and T_w data obtained by Kirillov et al. (2003) in the 1-m long bare tube. This used the correlations forms implemented in the verification Python code and accepted as input, data arrays, in the form of “.txt” files, for the bulk-fluid temperatures, local heat fluxes, and bulk-fluid enthalpies from the Sigmaplot files containing the experimental data. Within the code, the calculation of the thermophysical properties was handled by a C++ library called CoolProp (Bell et al., 2014). A Python wrapper of this library was installed and imported into the main Python code to calculate the thermophysical properties of water. CoolProp was chosen because of its simple to understand interface and ability to interact with REFPROP's thermophysical property library namely through the use of REFPROP's “.dll” files. In essence, CoolProp simply extracted the thermophysical property values from REFPROP database into the Python code and made them available for use in the correlation calculations. The output of the Python code was six data

arrays, in the form of “.txt” files, containing the predicted HTC 's and T_w 's of the Dittus-Boelter, Mokry et al., and Gupta et al. correlations for the 1-m long bare tube dataset.

These data arrays were then imported into the Sigmaplot files containing the experimental results and curves were generated to represent the predicted results. This was done for all 18 test runs considered in this thesis. After all graphs were created, an error analysis was performed using Equations 3-17 and 3-18 to calculate the RMS of the percent error and analyze how well the correlations matched the given experimental data.

3.3: Framework for the Economic Analysis of the SSR SMR

3.3.1: EMWG Model and G4ECONS Software

The EMWG was established in 2003 by GIF with the goal of creating economic models and guidelines to facilitate future evaluations of Generation IV nuclear reactors (EMWG, 2007).

These would help Generation IV reactors reach the economic goals set by GIF namely to have a life cycle cost advantage over other energy sources and to reach a comparable level of financial risk (EMWG, 2007). As a result, an Integrated Nuclear Energy Economic Model (INEEM) was developed by EMWG to economically evaluate Generation IV reactors and it is this model that is used by the G4ECONS software (EMWG, 2018). The structure of this model is given in Figure 3-6 and begins with a pre-defined Code of Accounts (COA) that serve as the guidelines for the economic evaluation and concludes with a *LUEC* estimation of the nuclear power plant. Non-nuclear energy sources, such as fossil-fuels or renewables, are not included in this model as it was designed for application to the development process of nuclear reactors (EMWG, 2007). The methodology used by EMWG for the economic cost-estimation of a nuclear technology is fairly general and can be applied to any nuclear energy system at different stages of development and technical maturity (GIF, 2019). For Generation IV nuclear systems, several assumptions are fixed for all concepts as stated by the EMWG (2007):

- Site characteristics for international “generic” sites.
- Design, construction, and operation labor rates/productivity within a country.
- The methodology to determine economic figures of merit (“\$/kW installed” and “\$/MWh of power generated”).
- Cost-estimating categories such as the GIF COA.
- Financial parameters such as discount rates and amortization periods.
- Use of cost-scaling relationships when insufficient detail is available

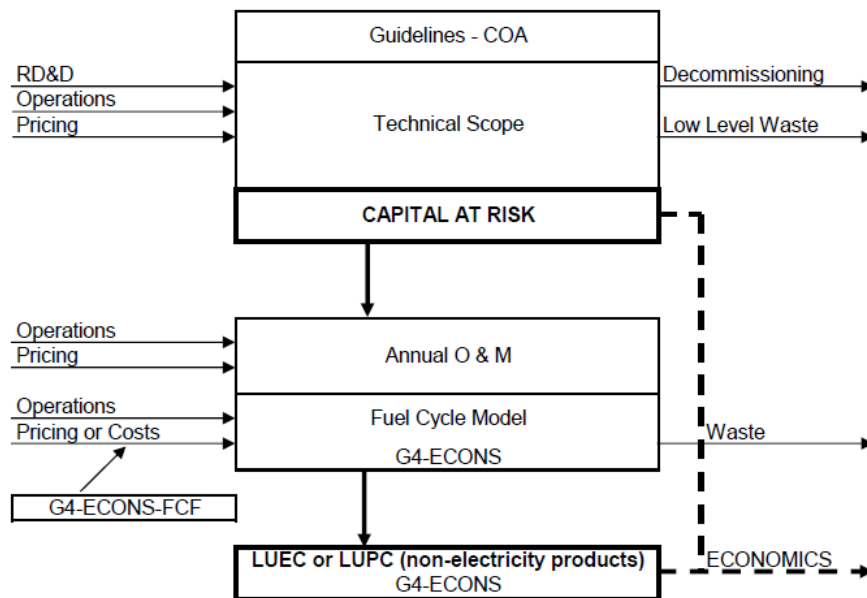


Figure 3-6: INEEM developed by EMWG (EMWG, 2007).

Due to the early stage of development for many Generation IV nuclear reactors, there exists a considerable amount of uncertainty in the cost estimates for development, design, construction, and operation. To manage this, several assumptions are further made by EMWG (2007) regarding cost estimates for nuclear power plants including:

- Systems at deployment stage are assumed to be pre-licensed in their country of origin

- A pre-approved -licensed- site is assumed to exist for plant construction.
- The finance and business model assumes that project financing is available for all phases of the final engineering design, site development, plant layout, owner's cost, construction, and commissioning of a plant.
- No provision is made for *force majeure*, war, labor strikes, or future changes in regulatory requirements.

The model itself can be used in two different ways, called the top-down and bottom-up approaches (EMWG, 2007). A top-down approach to cost estimation is usually done in the early stages of development where precise physical descriptions of the nuclear power plant are unavailable. Instead, only a general overview exists of the nuclear power plant and cost estimating relies on the use of reference models to estimate economic costs. This entails choosing an already established nuclear power plant, similar in design and operational output to the one being analyzed, whose cost information is already known and scaling that to the parameters of the new NPP. Contrastingly, a bottom-up approach is adopted later in the development cycle once detailed designs exist of the target NPP. Individual, base component costs are estimated using reference data and the overall economic cost of the total project is calculated by summing over these estimates. Depending on the stage of development, either approach can be utilized by the EMWG cost-estimating model.

To organize the efforts of developers in estimating the economic cost of potential nuclear power plants, GIF constructed the aforementioned COA to assist in evaluating the component-by-component cost. The COA is divided into two categories; two-digit high level categories (of the format XX) and three/four-digit sub-categories (of the format XXX/XXXX) that physically divide the nuclear power plant into separate cost accounts. This assists developers in identifying

all direct and indirect costs associated with the project that must be accounted when performing an economic evaluation. At the two-digit level, the COA may be applied to both a top-down and bottom-up approach whereas the three/four-digit level is most appropriate for a bottom-up estimate as it divides all two-digit categories into smaller, more detailed parts. For the two-digit categories, the COA takes on the following form (EMWG, 2007),

Accounts 1X – Capitalized Pre-Construction Costs

Accounts 2X – Capitalized Direct Costs

Direct Cost

Accounts 31-34 – Field Indirect Costs

Total Field Cost

Accounts 35-39 – Capitalized Field Management Costs

Base Construction Cost (BCC)

Accounts 4X – Capitalized Owner Operations

Accounts 5X – Capitalized Supplementary Costs

Overnight Construction Cost

Accounts 6X – Capitalized Financial Costs

TCIC

Each of the higher-level categories can be divided into the more detailed three- and-four-digit accounts. For example, Account Number 55, Initial Fuel Core Load, can be expanded into the three-digit Account Number 551, Fuel Assembly Supply, First Core, which itself gives way to Account Number 5512, First Core Conversion. Using such a COA eliminates the need for separate systems of categorization in addition being used as filing, drawing and document control, and numbering and coding of equipment (EMWG, 2007). Annualized O&M costs are covered by Account Numbers 7X with Account Numbers 8X reserved for Fuel Cycle costs and Account Numbers 9X for Annualized Financial Costs. A more detailed expansion of the INEEM

is provided in Figure 3-7 where the GIF COA is incorporated into the construction and production cost parts of the model.

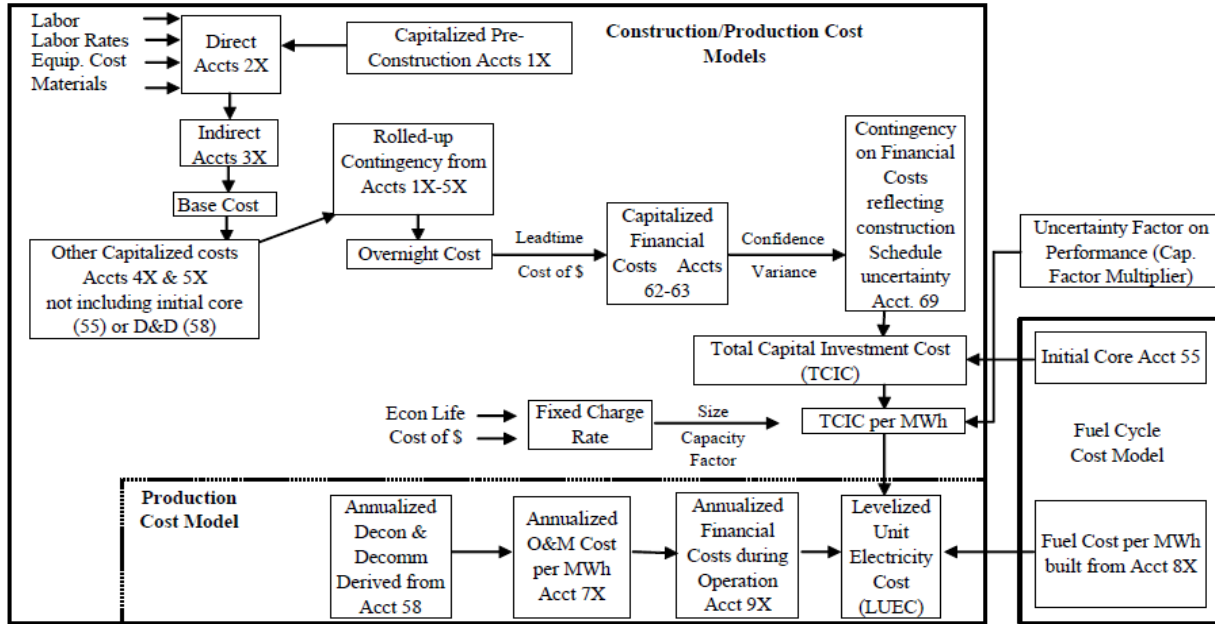


Figure 3-7: Detailed Construction and Production Costs of the INEEM (EMWG, 2007).

The primary figure of merit to be calculated by the INEEM is the *LUEC* for the nuclear powerplant. In its calculation, the TCIC, O&M costs, fuel cycle costs, and D&D cost are included, while all research and development (R&D) and demonstration costs are excluded from consideration since these phases of development do not commercially produce electricity for the project. Additionally, three types of contingencies are considered by the model with the first applied to the base cost to cover construction cost uncertainty; second applied to the *IDC* to cover construction schedule uncertainty; and third applied to the capacity factor to cover uncertainty in plant performance.

The INEEM uses a standard levelized cost calculation method when calculating the contribution of the fuel cycle to the *LUEC* (EMWG, 2007). This method entails identifying all the components of the specified fuel cycle and the appropriate point in time when they occur.

Additionally, the mass flow of material through these components must also be identified using the fuel requirements and specifications of the reactor. Then, the component cost can be calculated by multiplying the quantity of material/service flowing through that component (M_i) by the unit price of the material/service ($P_i(t)$). Assuming that the reactor is working at equilibrium along with the assumption that material losses between the components are negligible and can be ignored, summing over the annual component costs gives the annual fuel cycle cost. The contribution to the *LUEC* is then determined by dividing the annual fuel cycle cost with the kilowatt (or megawatt) hours generated per year. The component cost and annual fuel cycle cost are given in Equations 3-19 and 3-20 respectively.

$$F_i(t) = M_i \times P_i(t) \quad (3-19)$$

$$\text{Annual Fuel Cycle Cost (FUEL}(t)) = \sum_i F_i(t) \quad (3-20)$$

First core load is not included in the annual fuel cost and is instead grouped with the other owner's costs. There are three fuel cycle options available for analysis in the INEEM, those being the open or "once-through" option, partial-recycle, or fully closed (EMWG, 2007). Most commercially available fuel sources are included for use in the INEEM however, the fuel cycle cost methodology can only be applied to a single reactor at a time and cannot be used to analyze multiple reactors in a symbiotic system. The fuel cycle is split by the INEEM into a front-end section and a back-end section with separate annual costs calculated for both (see Figure 3-8)

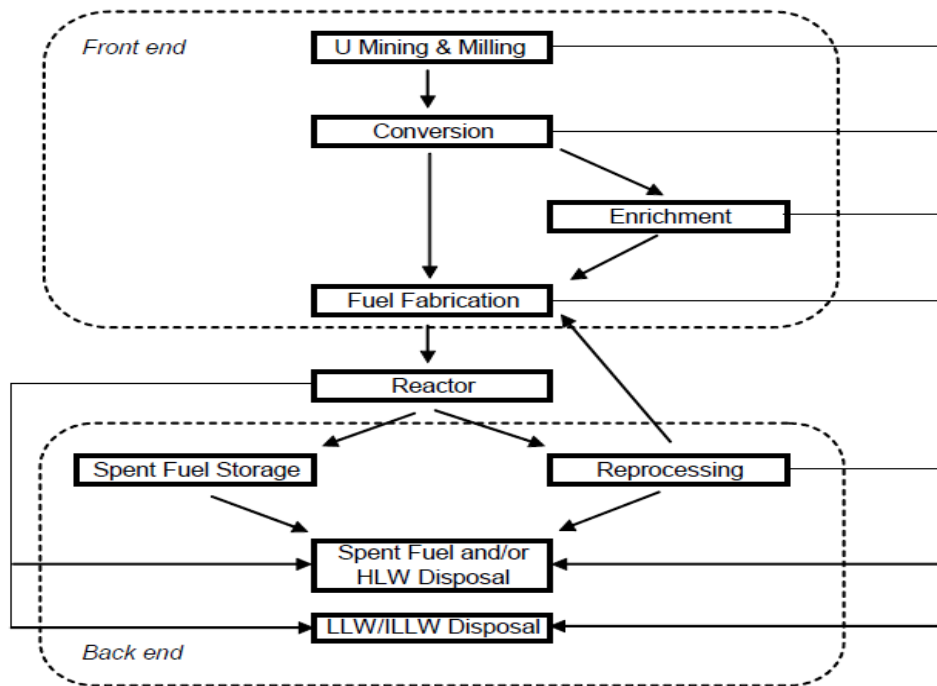


Figure 3-8: Uranium-based fuel cycle structure used in the INEEM (EMWG, 2007).

To assist developers in implementing the INEEM and calculating the NPP’s *LUEC* (using Equation 2-10), the EMWG developed an Excel-based program called G4ECONS that incorporates the GIF COA and other aspects from the INEEM (EMWG, 2018). The program is divided into several sections stated below:

1. **List Page:** This tab contains all of the possible dropdown menu options found in the second tab, **Case Operational Parameters**, and requires little to no alteration by the user.
2. **Case Operational Parameters:** General information about the reactor, such as thermal capacity, capacity factor, fuel burnup and so forth, is entered here along with the user choices for the dropdown menus specifying options such as the fuel source, used fuel disposition, D&D cost option along with whether “Detailed” or “Lumped” sum estimates

will be used in the summation of the TCIC and *LUEC*. The interest rate parameters (*IDC*, operation, D&D fund) are also set here.

3. **Levelized Cost Results:** All the final levelized costs for the parameters considered in the *LUEC*, and the *LUEC* itself, are displayed here. No user input is required.
4. **Operational Output:** All operational outputs of the reactor (plant electrical power, core fuel loading, refueling interval etc.) are displayed here and are dependent on the parameters set in **Case Operational Parameters**. No user input is required on this page.
5. **Mass Flows:** The annual mass flow by material into and out of the reactor core is displayed here. Specifically, only fuel material is tracked going into and out of the core, not the full range of materials found in the mass flow. No user input is required.
6. **Fuel Cycle Parameters:** In this tab, the user will enter information regarding initial core composition, equilibrium core composition, used fuel composition, and reprocessed material composition (if required). This takes the form of defining uranium enrichment, feed/tailings assay, and fuel compositions with mass fractions. Several assumptions are stated by EMWG (2018) when using the fuel cycle model in G4ECONS,
 - Only two types of fresh fuel can be defined: the initial core fuel and the reload fuel. Reloads are assumed to be identical over the operating life of the reactor.
 - The unit cost of fuel cycle services/materials remain unchanged (in constant currency) over the lifetime of the reactor.
 - No material losses between steps.
 - Timing (lag and lead times) of fuel cycle service purchasing is not treated in this model. This avoids any complexities associated with time-dependent variables.
 - Fuel cycle material flows/costs are adjusted to annual average values.

- Quantity of fuel data utilized in the reactor model should be consistent with the fuel description and desired power level of the reactor.

7. **Capital/O&M Costs COA (pages 7-13):** Starting from the seventh tab and extending to the thirteenth tab, the GIF COA is used to organize the estimated capital and O&M costs associated with the NPP. Each page is divided into a section containing cells for a cost estimate of the two-digit COA categories and another section for a lumped sum estimate. Depending on the user choice in **Case Operational Parameters**, either the detailed sum of all two-digit COA categories or the lumped sum figure will be used when calculating the TCIC and by extension the *LUEC*. Regarding the calculation of the *IDC*, the discrete annual interest rate (defined in **Case Operational Parameters**) is converted into a continuous rate and integrated over the assumed S-curve construction period (the length of the construction period given in **Case Operational Parameters**). The formula used for calculating the *IDC* is given in Equation 3-21 with *C*, the OCC, *i*, the discrete annual interest rate, and *T*, the construction period in years (EMWG, 2018).

$$IDC = C \left(\frac{\pi^2((1+i)^T + 1)}{2(\pi^2 + (\ln(1+i))^2 T^2)} - 1 \right) \quad (3-21)$$

14. **Capital and D&D Rollup:** This page calculates the TCIC of the NPP using the information provided from pages 7-13. Also present is the calculation of the total D&D cost of the reactor and the annualized D&D sinking fund contribution. Depending on the choices made in **Case Operational Parameters**, user input may or may not be required here.

15. Per-unit Cost Information: The unit prices of all materials/services used in the model fuel cycle are listed here. Users can input relevant cost data applicable to the fuel cycle being modeled.

There are several further assumptions and simplifications used in the INEEM adopted for the G4ECONS program (EMWG, 2018):

- All cost, material data, and operational parameters are entered as point-estimate values representative of full-life operations when calculating the *LUEC*. As such, the amortization life is equal to the operational life of the NPP.
- There are no flags within the model to prevent physically nonsensical scenarios so it assumes a basic knowledge of nuclear power plant engineering.
- All data are input, manipulated, and generated in constant currency units so there is no need for escalation tables.
- No reactor physics calculations are built in so data must be obtained separately to provide equilibrium fuel cycle data.
- The same real (inflation-free) r is used for construction financing, capital amortization, and D&D escrow fund accumulation.

The G4ECONS software is not designed for market, supply chain, dynamic system, financial, or business modeling. As such, it cannot be used for detailed analyses supporting business planning. Further, the program does not track discrete activities such as operations, fuel cycle material balances, annual cash flows, capital upgrades, or life extension beyond the amortization period. Instead, it can be used to preliminarily compare the economic value of immature nuclear technology concepts across the globe for general comparisons regardless of the level of maturity.

3.3.2: Estimation of Life Cycle Costs for the SSR

For the analysis of the life cycle costs for the SSR, and the estimation of its *LUEC* using G4ECONS, a “bottom-up” approach was ruled out due to the conceptual nature of the reactor. There were no detailed schematics of the NPP and so conducting a three/four-digit COA cost estimation would be very difficult. Instead, an altered “top-down” approach was adopted where a reference SCWR plant, whose life cycle costs were estimated by Moore et al. (2016), was chosen and its capital costs were scaled to the scope of the SSR using the economy of scale. Performing an economy of scale between an LNR and an SMR is not applicable because such an approach assumes the designs of the LNR and SMR are more or less identical with the exception of size (Mignacca and Locatelli, 2020). In most cases, the designs of the reference LNR and specified SMR will greatly differ such as, for example, using the cost data from a PWR, like the AP1000, to estimate the cost for an HTGR SMR. The economy of scale principle ends up inflating the specific cost, or cost per electrical capacity, of the SMR as evidenced in the work by Carelli et al. (2008), Boarin et al. (2012), and Playbell (2017). This approach was applicable to the *LUEC* estimate of the SSR because the SSR was stated as being a scaled-down version of the SCWR (Yetisir et al., 2012) and so many of the systems in the LNR SCWR would be found in the SSR. Hence, the OCC calculated by Moore et al. (2016) for the Canadian SCWR could be scaled to the SSR using the economy of scale. The general form of this relationship is given in Equation 3-22 below,

$$OCC_{small} = OCC_{large} \times \left(\frac{Pr_{small}}{Pr_{large}} \right)^n \quad (3-22)$$

The exponent n in Equation 3-22 has been reported to range from 0.4-0.7 depending on the SMR project (NEA and OECD, 2011). The value used was 0.51, or the average value of n as determined by the Nuclear Energy Agency (NEA and OECD, 2011). After the OCC of the SSR

was estimated, the cost was divided into the different capital cost categories of G4ECONS using the breakdowns of the World Nuclear Association (2020b) and the NETL (2011). Thus, 80% of the OCC was dedicated to EPC costs (with 70% being direct costs and 30% being indirect costs) and the other 20% reserved for contingencies and owner's costs. An overall contingency rate of 15% was used, with owner's costs representing 5% of the OCC. This seemed to be reasonable given the cost distributions for nuclear reactors as reported by the EIA (2020) and the contingency rate estimates for SMRs by the NEA and OECD (2011). A D&D cost rate of 33% was chosen in line with the EMWG Guidelines (EMWG, 2007). For O&M costs, a conservative parametric cost of \$135/kW_e-year was chosen for fixed costs, given estimates by SMR Start (2017), and a variable cost of \$3/MW_eh was chosen given the estimates by EIA (2020).

For the G4ECONS software, user inputs for the drop-down menus are given in Figure 3-9 and specify the framework for the SSR fuel-cycle and the treatment of cost data as either detailed or lumped sum figures. The base case of the *LUEC* estimate assumes an operational lifetime of 60 years, a construction period of 4 years, and a discount rate of 5%. Given the proposed purpose (energy generation for remote or small communities) of SMRs, many have extended fuel cycles with years between refueling (Pioro,..., Dort-Goltz, 2020). A refueling interval of roughly 2 years was assumed for the SSR which was in-line with the refueling intervals of other SMRs with similar electrical capacities given the trends in Pioro,...,Dort-Goltz (2020). A capacity factor of 95% was assumed for the SSR, a decision motivated by the reported longer refueling intervals, remote locations, and higher enrichment levels of fuel for SMRs. An average burnup of 66.65 GW_{th}-d/Mt_U was calculated for the SSR given the 7% enrichment level of U-235 from Section 2.4.1, and 2 years of uninterrupted reactor operation. Application of the SMR economic factors from Section 2 was done after the base *LUEC* was calculated for the SSR with the purpose of

illustrating the impact these factors would have on the *LUEC* of the SSR compared to only applying the economy of scale. This does not mean that the SSR will be deployed in such a way that all of these factors would be applicable. Instead, a “best case” scenario is established for the sake of highlighting the potential effect these factors will have on the economic competitiveness of SMRs.

Fuel Source (Choose)		Mined Material
Used Fuel Disposition (Choose)		Geologic Repository
Geological Disposition Cost Basis (Choose)		Mass
Back-end Separations (Choose)		None
D&D Cost Option (Choose)		Calculated as Fraction
Operations Cost Option (Choose)		Parametric Cost
Total Capitalized Costs Option (Choose)		Detailed Sum
Pre-Construction Cost Option (Choose)		Lumped Sum
Capitalized Direct Cost Option (Choose)		Lumped Sum
Capitalized Support Service Cost Option (Choose)		Lumped Sum
Capitalized Operation Cost Option (Choose)		Detailed Sum
Capitalized Supplementary Cost Option (Choose)		Lumped Sum
Other Financial Cost Option (Choose)		Detailed Sum

Figure 3-9: User inputs for drop-down cells within “Case Operational Parameters” page of the G4ECONS software (EMWG, 2018).

The SMR economic factors were applied to the OCC cell in G4ECONS on the “Capital and D&D Rollup” since these factors only apply to the capital costs of an SMR. It was assumed when applying these factors that the SSR was on a site with three other identical reactors (for four total SSRs) and that each SSR was an NOAK unit as opposed to the First-Of-A-Kind (FOAK) status of the base case. This was done to maximize the per-unit capital cost reduction by the SMR factors and to investigate the effect this would have on the *LUEC* of the SSR once it had reach NOAK status. A list of the equations used for calculating the SMR factors is given in Table 3-5.

Table 3-5: Economic factors and their values for use in calculating the LUEC of the SSR.

Factor	Mathematical Expression	Value of Variables/Constants	Final Result
Co-siting Factor	$\frac{1 + (n - 1)(1 - F_{IND})}{n} \quad (3-23)$	$n=4$ $F_{IND}=0.34$	0.745
Learning Factor (Site)	$\frac{1}{4} \left(1 + y + \frac{z}{1+k} + \frac{y}{(1+k)^2} \right) \quad (3-24)$	$y=0.795$ $z=0.885$ $k=0.01$	0.863
Modular Design Factor	$4 \times 10^{-10}(Pr)^3 - 10^{-6}(Pr)^2 + 0.0012(Pr) + 0.581 \quad (3-25)$	$Pr=300 \text{ MW}_{el}$	0.8618
Learning Curve (NOAK)	$Y = AX^{\frac{\log(1-R)}{\log 2}} \quad (3-26)$	$A=1.93$ $X=26$ $R=0.045$	1.55 (Y/A=0.805)
Modularization	N/A	N/A	~0.7

Note: NOAK- Nth-of-a-kind, LUEC- Levelized Unit of Energy Cost, F_{IND} -proportion of indivisible cost factor, Pr -Power, MW_{el} .

The form for the co-siting factor was developed by Wilton (2012) while the value for F_{IND} was calculated by Carelli et al. (2010). Wilton (2012) also developed the form for the Modular Design Factor. For the Learning Factor (Site), the form used was developed for the cost reduction of a multi-unit site with values for the variables given by NEA and OECD (2011). The Learning Curve factor was reported by NETL (2013) and represents the capital cost reduction of maturing technology. The variable R represents the learning rate of the curve and is indicative of the maturity of the technology. A value of 0.045 was chosen since it represents a nuclear plant that will contain a mixture of mature and immature technologies (Boldon and Sabharwall, 2014). The variable X represents the number of units needed to produce a cumulative rated power. A value of 8 GW_{el} was chosen as the cumulative rated power since GIF defines a reactor to be NOAK once 8 GW_{el} of cumulative power had been produced (EMWG, 2007). At an electrical capacity of 300 MW_{el} , approximately 26 SSRs would need to be developed to achieve NOAK status. The variable A is the OCC of the FOAK unit so the value of the Learning Curve factor (when applied to the OCC) was calculated by taking the ratio of Y to A . Applying this factor to

the OCC of the SSR is, like the other factors, meant to be illustrative of an effect. In this case, this effect shows the outcome on the OCC when the SSR transforms from an FOAK to an NOAK technology. The ratio of Y to A in Equation 3-26 is representative of this effect. Therefore, the source of the OCC estimate for the SSR in Equation 3-22, whether it is the estimated OCC from a NOAK or FOAK LNR SCWR, is irrelevant to analyzing this effect. The Modularization Factor was taken from Lloyd et al. (2018) by analyzing the OCC cost reductions when the modularization factors were applied to different test SMRs.

Once the SMR factors were applied, a sensitivity analysis was done by varying the different parameters of the SSR and analyzing their impacts on the calculated *LUEC*. These can be found in Appendix D with the exception of the discount rate analysis, which is presented in Section 4. In all calculation of the *LUEC*, taxes were not applied and all monetary figures were given in 2007 USD. A discussion regarding the specific capital cost, $\$/kW_{el}$, of the SSR (with the SMR factors applied) was also included in Section 4.

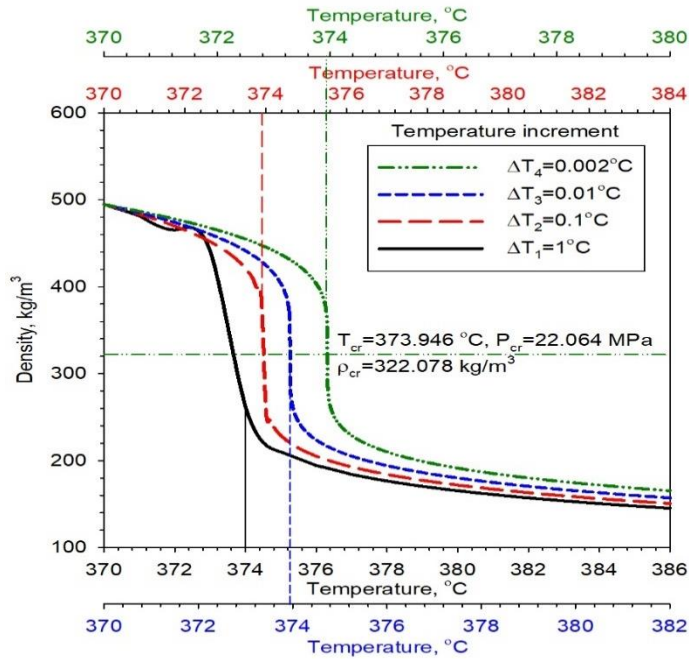
Chapter 4: Results and Discussion

4.1 Investigative Results for NIST REFPROP v.10

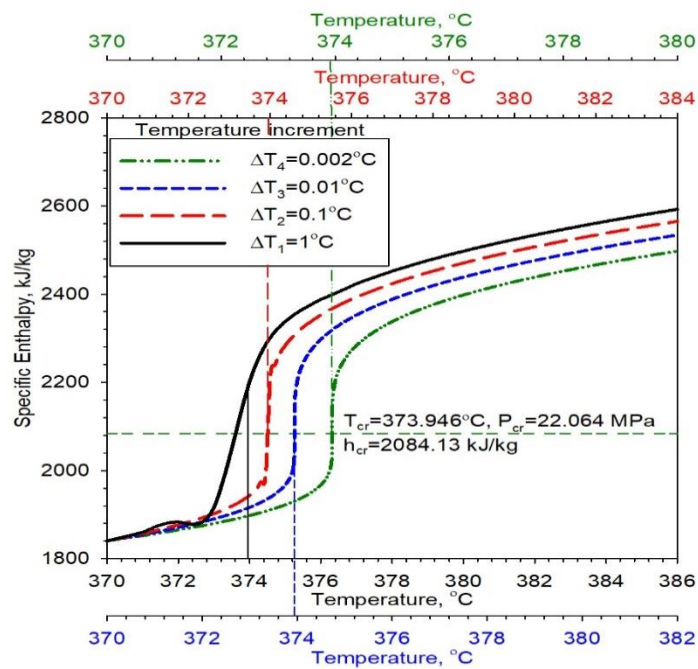
A total of nine graphs were put together using the thermophysical property values generated by NIST REFPROP v.10. These are given in Figures 4-1 (a)-(i) following the same order presented in Section 3.1.1. The density and specific enthalpy values for critical water (see Figures 4-1a,b), as determined by REFPROP v.10, remain bounded and do not show significant numerical deviation. Around the critical point, rapid change is experienced due to the transition from compressed to supercritical fluid but no infinities are approached. This indicates that the dimensionless Helmholtz free energy model, by Wagner and Pruss (2002), used by REFPROP v.10 is stable in the critical region when calculating the specific enthalpy of water. However, this is not the case for the isobaric specific heat capacity of water in the critical region (see Figure 4-1c). The form of the dimensionless Helmholtz free energy used to calculate the isobaric specific heat capacity approaches a singularity around the critical point of water. In fact, at the critical point in the ΔT_4 curve, the calculated specific heat capacity was 2.42×10^9 kJ/kg·K and represents an energy well of sorts. This is in direct contrast with the calculated values of the specific enthalpy that indicate the energy content of water at the critical point remains finite. Therefore, the behavior displayed by the specific heat capacity is non-physical since it evidently cannot store a near-infinite amount of energy.

Both of these thermophysical properties are calculated using the same model so even though the specific enthalpy remains bounded, it may not be representative of actual physical values.

Comparison was made by Wagner and Pruss (2002) between the results of the dimensionless Helmholtz free energy model and experimental data on the enthalpy of water. However, the experimental data used was for enthalpy differences at a range of pressures (temperatures) from

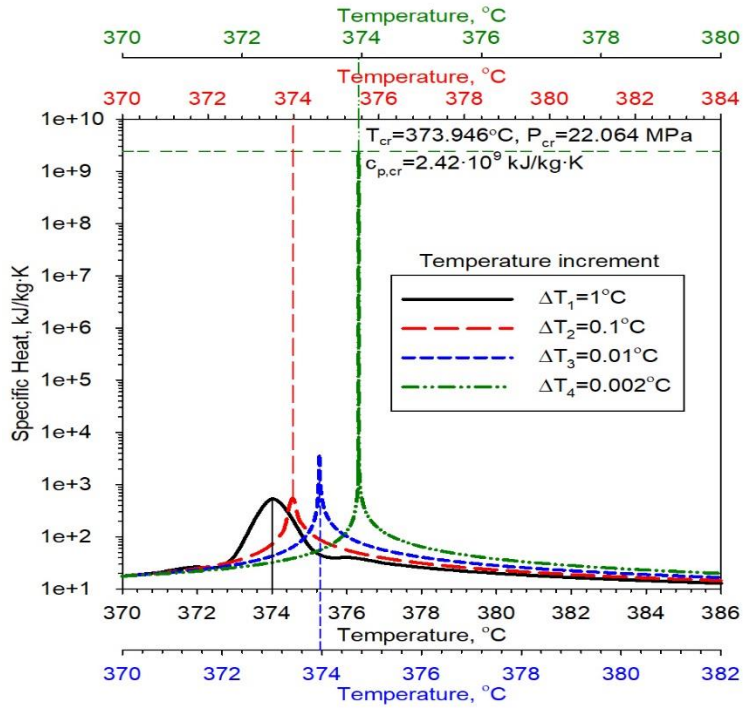


(a)

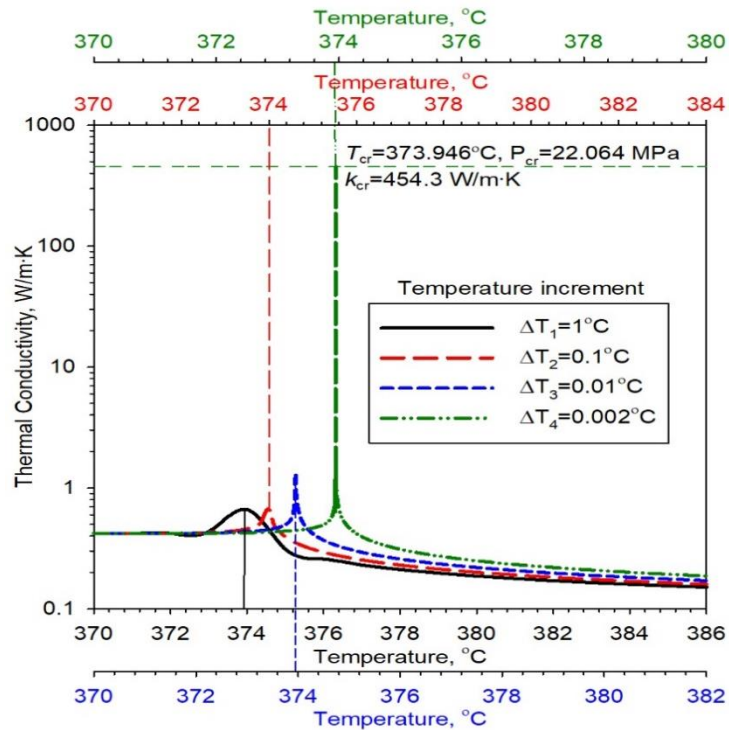


(b)

Figure 4-1: (a)-Density (ρ) vs. Temperature, (b)-Enthalpy (h) vs. Temperature; Water, critical region (Dort-Goltz et al., 2021c)



(c)

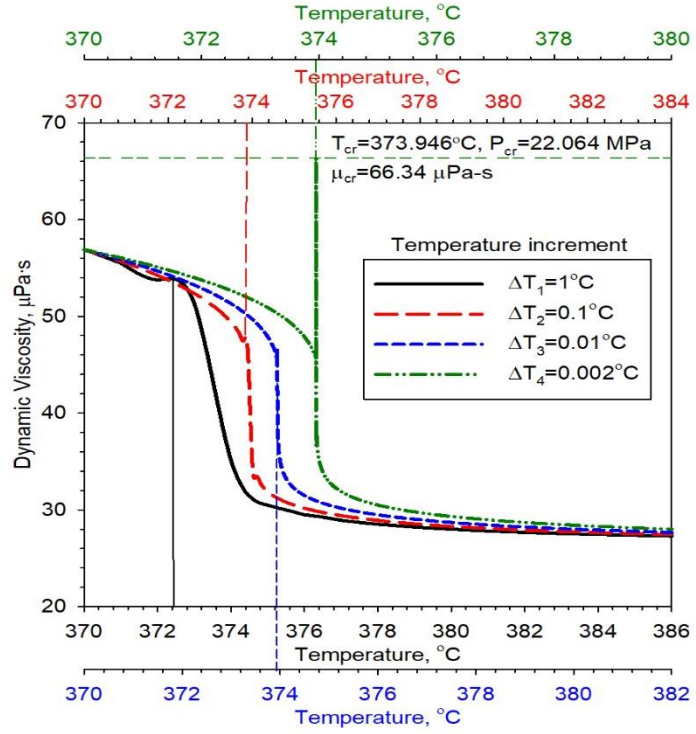


(d)

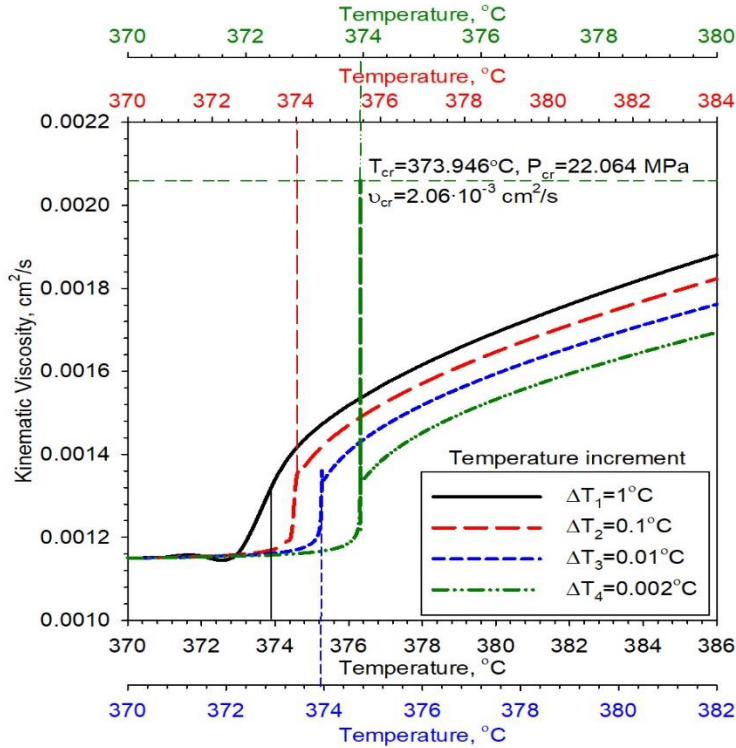
Figure 4-1: (c)-Specific Heat (c_p) vs. Temperature, (d)-Thermal Conductivity (k) vs. Temperature; Water, critical region (Dort-Goltz et al., 2021c).

0.7 MPa-11.9 MPa (328-455 K) and 20-50 MPa (300-670 K) taken from 1990 and 1987 respectively, since experimental enthalpy difference data prior to 1987 was deemed to not meet the required quality standards (Wagner and Pruss, 2002). Further, no direct experimental enthalpy difference data was taken at the critical point of water with the closest pressure of a datum being 22.9756 MPa. Within this region of 22.5 MPa and 24.1 MPa, referred to as the critical region, the error between the enthalpy difference calculated by the model and the collected experimental data reached up to 35% (Wagner and Pruss, 2002). But, from Sato et al. (1988), with respect to single-phase water, enthalpy results from equations of state are perhaps more reliable than experimental results. This is largely due to a larger quantity of accurate experimental data existing for water's isobaric specific heat and specific volume, the basis for the development of equations of state, compared to the quantity of experimental data for enthalpy (Sato et al, 1988). As such, the dimensionless Helmholtz free energy model may produce better enthalpy results at the critical point of water than experiment though there is little new experimental critical enthalpy data available for evaluation. Use of the dimensionless Helmholtz free energy to generate critical enthalpy values for heat transfer calculations will not generate severely inflated results but with questionable accuracy.

The models used for the thermal conductivity (Huber et al., 2011) and dynamic viscosity (Huber et al., 2009) also generate deviating values for water at the critical point. This is more noticeable for the thermal conductivity profile (see Figure 4-1d) than for the dynamic viscosity (see Figure 4-1e) as the thermal conductivity experiences around a 34,000% increase in the peak values of the ΔT_3 and ΔT_4 curves. In comparison, the dynamic viscosity experiences an approximate 70% increase between the peak values of the ΔT_3 and ΔT_4 curves. Thus, amongst the thermophysical



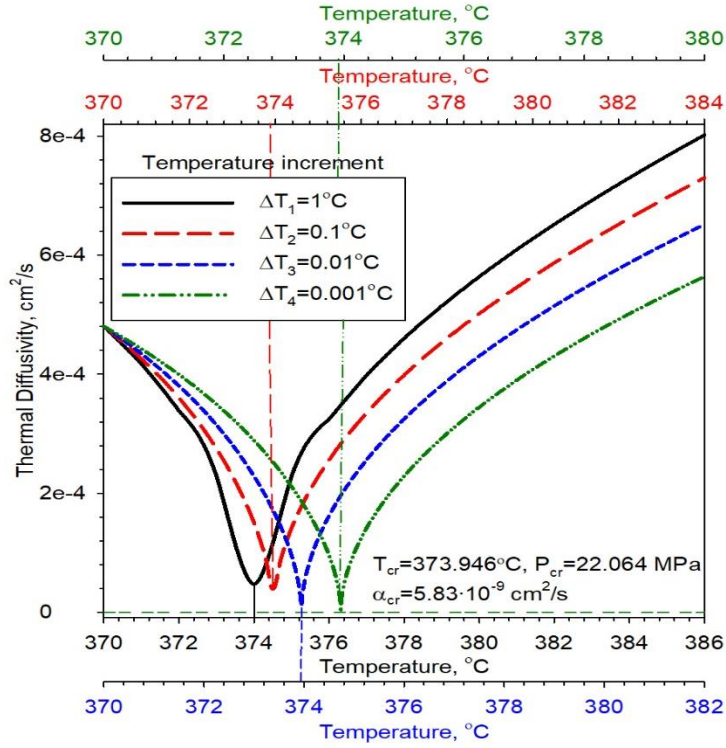
(e)



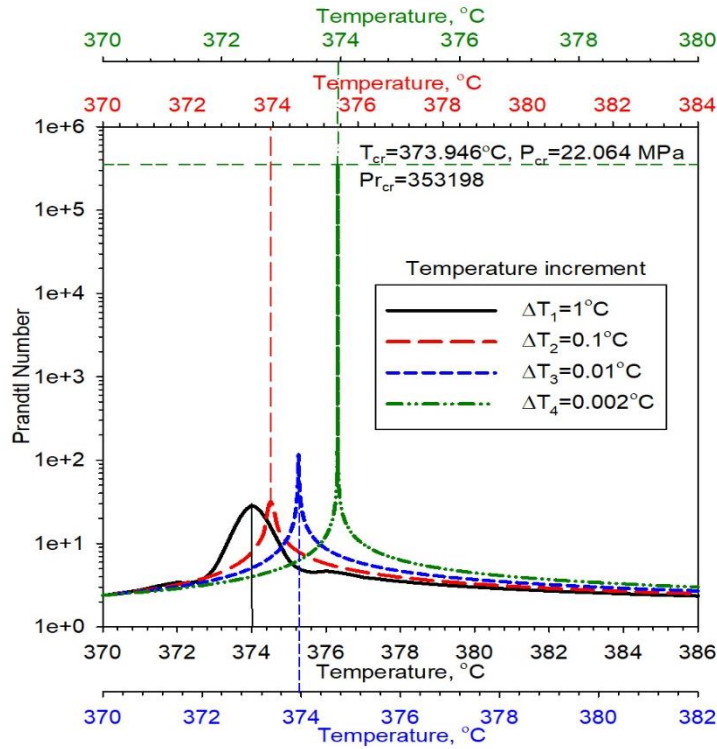
(f)

Figure 4-1: (e)-Dynamic Viscosity (μ) vs. Temperature, (f)-Kinematic Viscosity (ν) vs. Temperature; Water, critical region (Dort-Goltz et al., 2021c).

properties calculated by the three theoretical models described in Section 3.1.1, the specific heat capacity of water is the most unstable at the critical point and specific enthalpy the most stable. This is reflected in the derived properties that rely on any combination of the specific heat capacity, thermal conductivity, and dynamic viscosity such as the kinematic viscosity, Prandtl number, and thermal diffusivity. Referring to Figures 4-1f-h, the curves for these derived properties also exhibit significant variations in values at or near the critical point, though the Prandtl number experiences the largest amount of deviation. As for the volume expansivity (Figure 4-1i), the asymptotic behavior occurs due to the density-dependent partial derivative term in Equation 3-4. In the region close to the critical point, approximately 0.1 °C on either side of the critical temperature, the density experiences a near-infinite rate of change. For small incremental changes in the temperature, the density changes significantly so the partial derivative term in Equation 3-4 approaches increasingly larger values as the critical point is reached. Consequently, the volume expansivity also approaches very large values close to and at the critical point. A collection of the peak values for the nine thermophysical properties is given in Table 4-1, categorized by the values encountered in the ΔT_3 and ΔT_4 curves. The percent difference column in Table 4-1 (which illustrates the percent difference between the extrema of the ΔT_3 and ΔT_4 curves) further illustrates the non-physical values generated by REFPROP v.10 for certain properties, such as specific heat and volume expansivity. Such substantial percent differences between the extrema values arise from the mathematical processes used to create the thermophysical property profiles. They are not representative of any actual physical phenomena and are an indication of the limitation in using theoretical models, such as the dimensionless Helmholtz free energy, to predict physical behavior. These extrema values and the

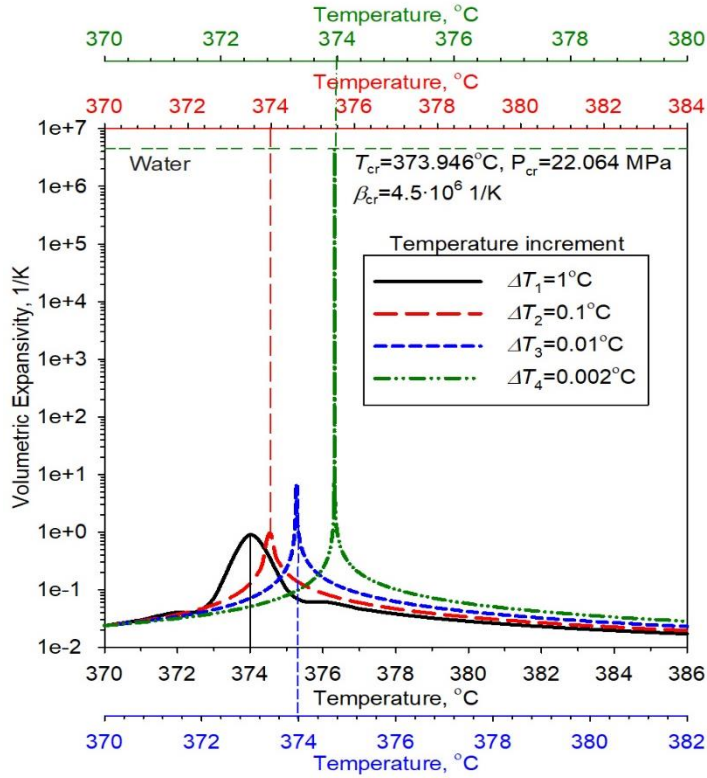


(g)



(h)

Figure 4-1: (g)-Thermal diffusivity (α) vs. Temperature, (h)-Prandtl Number (Pr) vs. Temperature; Water, critical region (Dort-Goltz et al., 2021c).



(i)

Figure 4-1: (i)-Volume Expansivity (β) vs. Temperature; Water, critical region (Dort-Goltz et al., 2021c).

Table 4-1: Extrema values of two selected temperature difference curves for the nine thermophysical properties. In bold-three largest percent differences.

No.	Property	Value at T_{cr}		Unit	Difference, %
		373.95 °C ($\Delta T_3=0.01$ °C)	373.946 °C ($\Delta T_4=0.002$ °C)		
1	Density	287.9	322.1	kg/m ³	+11.9
2	Specific Enthalpy	2146.6	2084.1	kJ/kg	-2.9
3	Specific heat capacity (max. or peak value)	3.86×10^3	2.42×10^9	kJ/kg·K	+6.3 × 10⁷
4	Thermal conductivity (max. or peak value)	1.34	454.3	W/m·K	+3.4 × 10 ⁴
5	Dynamic viscosity (max. or peak value)	39.06	66.34	μPa·s	+69.8
6	Kinematic viscosity (max. or peak value)	1.36×10^{-3}	2.06×10^{-3}	cm ² /s	+51.5
7	Thermal diffusivity (min. value)	1.21×10^{-8}	5.83×10^{-9}	cm ² /s	-51.8
8	Prandtl number (max. or peak value)	112.58	3.53×10^5	-	+3.1 × 10⁵

No.	Property	Value at T_{cr}		Unit	Difference, %
		373.95 °C ($\Delta T_3=0.01$ °C)	373.946 °C ($\Delta T_4=0.002$ °C)		
9	Volume expansivity (max. or peak value)	6.74	4.5×10^6	1/K	$+6.7 \times 10^7$

thermophysical property curves presented in this section agree with the results of Li et al. (2020) in their own preliminary study of NIST REFPROP v.10. This section expands on simply generating the thermophysical properties by identifying the reason the theoretical models used by NIST REFPROP v.10 for the most part produce non-physical results for the critical properties of water.

During the analysis, it was also confirmed that the smallest possible temperature increment to be used in REFPROP v.10 for the critical point to be calculated from the Isoproperty Table was $\Delta T_4=0.002$ °C. Using a smaller temperature increment, for example 0.001 °C, resulted in a failure-to-converge error message in the compressed liquid phase of the calculations (see Figure 4-2). This error was encountered with any temperature increments below ΔT_4 in temperature ranges where the critical point would be reached. However, at non-critical pressures (either sub-critical or supercritical) this error message disappeared. Additionally, it was noted that REFPROP v.10 would shut down if the quantity of temperature points within a specified range exceeded 10,000. Significant reductions in calculation speed were encountered while generating thermophysical properties in temperature ranges with roughly 3000-5000 temperature points. These would become more and more substantial with increasing quantities of temperature points until REFPROP v.10 shut down. However, it was unclear whether this was due to program or computer limitations.

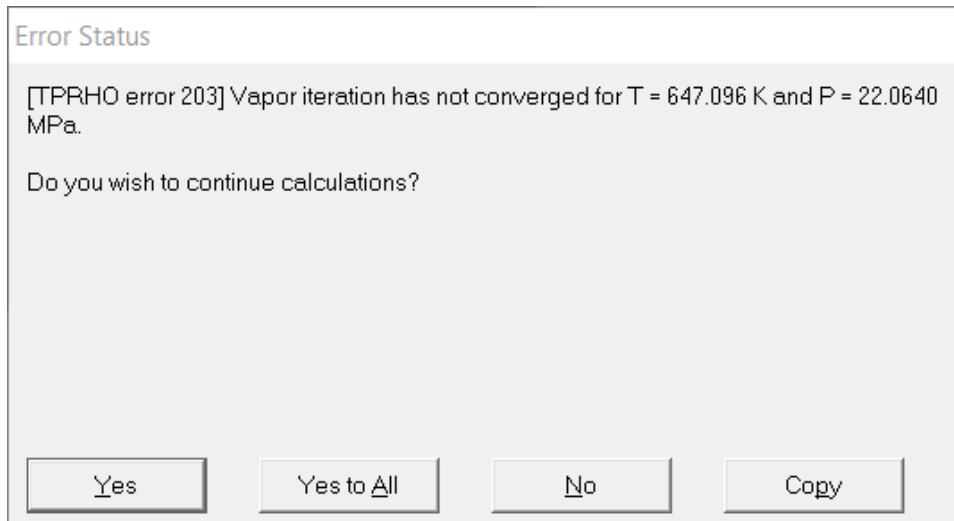


Figure 4-2: Error message that would appear in REFPROP v.10 if a temperature increment below 0.002 °C was chosen and contained the critical point. All liquid-phase ($T < 356$ °C) calculations would be discarded and only vapor-phase calculations ($T \geq 356$ °C) would appear in the isoproperty table.

In the error calculations performed for the derived temperature properties – kinematic viscosity, thermal diffusivity, Prandtl number, and volume expansivity – it was concluded that Equations 3-1–3-4 were used by REFPROP v.10 to calculate these thermophysical properties. The maximum percent errors encountered with each thermophysical property were below 0.5%, indicating excellent agreement between the values generated by REFPROP v.10 and the values calculated directly using Equations 3-1–3-4 across all analyzed temperatures and pressures.

4.1.1 Conclusion

Nine thermophysical properties of water were chosen to be analyzed in the v.10 of the reference program, REFPROP. The values for these properties were generated at the critical pressure and for four different temperature increments around the critical temperature. It was discovered that the theoretical models used by REFPROP v.10 to calculate the specific heat capacity, thermal conductivity, and dynamic viscosity of water were unstable around the critical point and generated non-physical data. This in turn led to other thermophysical properties also displaying

non-physical behavior. As such, using REFPROP v.10 to perform technical calculations around the critical point of water is not acceptable as enormous errors will be encountered in the results. It is recommended that an experimental approach be used instead to provide the critical values of the selected thermophysical properties (Dort-Goltz et al., 2021c). This was done by Le Neindre et al. (1984) regarding the critical properties of various gases and adopting this methodology would eliminate much of the non-physical behavior introduced by theoretical models. These experimental findings would then be updated every so often to reflect advancements in laboratory technology and experimental technique thereby providing more accurate results.

4.2 1-m Heat Transfer Dataset Analysis

The Sigmaplot graphs containing the predicted $HTCs$ and T_w 's for the 1-m long dataset, along with the experimentally determined $HTCs$ and T_w 's, are presented in Figures 4-3 – 4-5. Results from Section 4.1 and the uncertainties given in the descriptions of the models in Section 3.1 indicate that using the NIST REFPROP v.10 database (through CoolProp) for the heat transfer calculations at supercritical conditions using Equations 2-2 – 2-4 is relatively safe. It is only at the critical point of water that NIST REFPROP v.10 produces non-physical thermophysical property values. Otherwise, the estimated errors were under a $\pm 7\%$ margin, well within the stated error ranges for the Mokry et al. (2009) and Gupta et al. (2011) correlations. Regarding the experimental data presented in Figures 4-3 – 4-5, the T_w 's were calculated locally at the position of the thermocouples using the measured parameters from Section 3.2 and the experimental $HTCs$ were then determined using Equation 3-16 (Kirillov et al., 2005). The predicted $HTCs$ and T_w 's then refer to those calculated using Equations 2-2 – 2-4. High G results are represented in Figure 4-3, medium G in Figure 4-4, and low G in Figure 4-5.

In Figures 4-3–4-5, the colored curves represent Equations 2-2–2-4 with maroon representing Equation 2-2 (Dittus-Boelter correlation), dark green representing Equation 2-3 (Mokry et al. correlation), and dark blue representing Equation 2-4 (Gupta et al. correlation without the entrance term). The q_{dht} term was also calculated using Equation 2-9 and included within the parameter summary located at the top of each individual figure. In all test conditions above, with the exception of Figure 4-3f and Figure 4-5c, it was calculated that $q_{ave} > q_{dht}$ indicating that DHT was expected to occur in all or parts of the heated length (Dort-Goltz et al., 2021a,b). The onset of DHT was often gradual but could also be abrupt as in Figures 4-4c-e where a sharp decline in the HTC coincided with a sharp rise in T_w . The location of DHT was fairly consistent across all experimental conditions namely where the bulk-fluid temperature was within a region close to the pseudocritical temperature. Even with DHT, the experimental HTC and T_w data remained stable along the greater portion of the heated length. With the exception of a few instances where the HTC suddenly decreased (most often in the entrance region), the HTC and T_w profiles remained consistent and did not experience any exponential growth or decline.

Of interest as well was the existence of entrance region effects within the test section. In the entrance region, $HTCs$ decreased to some minimum value, once again coinciding with an increase in T_w , before the HTC and T_w profiles stabilized for the remainder of the heated length. Examples of significant entrance region effects may be seen in Figures 4-4a-b and 4-5a,e whereas more muted entrance region effects appear in Figures 4-5b,d-f. However, in other experimental conditions, entrance region effects did not seem to be present such as in Figures 4-3b-d,f and 4-4f. It is unclear whether the appearance and severity of these entrance region effects coincide to the abrupt appearance of DHT or the development of the turbulent flow thermodynamic boundary layer inside of the bare tube (Incorpera et al., 2007). Overall, it seemed

as if the high mass-flux results were the most stable out of the three groups. There were little to no entrance region effects at high mass-fluxes and the HTC and T_w profiles did not experience any abrupt changes in value. At medium mass-fluxes, the HTC and T_w profiles were most erratic with strong entrance region effects and much more pronounced appearances of DHT. At low mass-fluxes, depending on the experimental conditions, the HTC and T_w profiles could either be stable or rapidly changing.

All the correlations used in the analysis struggled to accurately predict the HTC and T_w profiles, in particular the Dittus-Boelter correlation (1930), as shown in Table 4-2.

Table 4-2: Relative RMS of the three correlations used to analyze the data found in Figures 4-3–4-5. Bold indicates lowest RMS for that particular set of data.

Correlation	Relative RMS, %					
	$(G \sim 200 \text{ kg/m}^2 \cdot \text{s})$		$(G \sim 500 \text{ kg/m}^2 \cdot \text{s})$		$(G \sim 1000 \text{ kg/m}^2 \cdot \text{s})$	
	T_w	HTC	T_w	HTC	T_w	HTC
Dittus-Boelter (1930)	17.3	299..2	17.5	288.0	13.4	230.7
Mokry et al. (2009)	37.05	49.9	9.5	31.7	13.6	34.6
Gupta et al. (2011)	18.9	40.8	6.9	32.1	7.7	25.3

This is to be expected as this correlation was developed for sub-critical conditions and would not be able to consistently and accurately predict HTC and T_w profiles near the critical and pseudocritical point (Dort-Goltz et al., 2021a,b). In the dataset, the bulk-fluid temperature was often close to the pseudocritical temperature and since the Dittus-Boelter correlation (1930) relies on thermophysical properties evaluated at the bulk-fluid temperature, the resultant HTC and T_w values were often over-predicted. Especially evident is the Dittus-Boelter (1930) correlation's over-estimation of the HTC in all three mass-flux regimes whereas the estimation of the T_w was not as poor. This could very well be due to the way the HTC and T_w were calculated by the correlations.

The correlations themselves calculated the HTC and these depend on the thermophysical properties of water. However, as was reviewed in Section 2.1, these properties undergo significant variations around the pseudocritical temperature of water. Many of the T_b 's in Figures 4-3 – 4-5 included the pseudocritical temperature (such as Figures 4-3b and 4-5e) and others, such as Figure 4-4d, were in close proximity to the pseudocritical temperature. Since the correlations relied, in one way or another, on thermophysical properties evaluated at T_b , the HTC calculation would be sensitive to this variation, thereby achieving high RMS values. The T_w was determined using Equation 3-16 for all three correlations. It was rearranged to solve for T_w and one of the terms from this rearrangement would be the ratio of q to HTC . In Figures 4-3 – 4-5, the magnitude of the $HTCs$ was smaller than that of q , usually by a factor between 10 and 100. So, the ratio of q to HTC was more resistant to the same property variations that surrounded the calculation of the HTC . With the property variation effect muted in Equation 3-16, this is probably the reason for the predicted T_w 's to be closer to the experimental T_w 's. This trend is displayed by all three correlations, especially the Dittus-Boelter correlation (1930) in Table 4-2.

The Mokry et al. correlation (2009) and Gupta et al. correlation (2011) did much better in predicting the HTC and T_w profiles compared to the Dittus-Boelter correlation (1930) near the pseudocritical temperature. This agreed with the findings for the 4-m long dataset analyzed by Mokry (2009) and Gupta (2014). Unfortunately, both correlations still had significant deviations near the entrance and exit regions of the test section. In particular, the Mokry et al. correlation (2009) significantly over-estimated the T_w profile of the data at low G (see Figure 4-5). Three possible factors for this could be the variation in thermophysical properties that are exacerbated by entrance-region effects and proximity to the pseudocritical temperature (often the location of DHT), the low G values, and computational convergence.

Like the Dittus-Boelter correlation (1930), the Mokry et al. correlation (2009) primarily relies on terms dependent on thermophysical properties evaluated at T_b . However, unlike the Dittus-Boelter correlation (1930), the Mokry et al. correlation (2009) includes a corrective term, the ratio between ρ_w and ρ_b . This could very well be the reason for the Mokry et al. correlation (2009) to have lower HTC RMS values than the Dittus-Boelter correlation (1930). The corrective term, much like the ratio of q to HTC , probably acted as a balancing force and prevented the significantly varying properties evaluated at T_b from causing too much of a discrepancy especially in areas where entrance-region effects or DHT could have possibly occurred. The Gupta et al. correlation (2011) contained two of these corrective terms and evaluated \mathbf{Re} and $\overline{\mathbf{Pr}}$ at T_w , which was generally well above the pseudocritical temperature. Thus, it was possibly more resistant to property variation than the Mokry et al. correlation (2009) and Dittus-Boelter (1930) correlation and as such achieve a lower HTC RMS than the Mokry et al. correlation (2009). However, this is not the sole factor since the Mokry et al. correlation (2009) achieved a lower HTC RMS than the Gupta et al. correlation (2011) for medium G conditions.

In the calculation of the HTC , all three correlations rely on \mathbf{Re} with the Mokry et al. (2009) and Dittus-Boelter (1930) correlations evaluating \mathbf{Re} at T_b and the Gupta et al. correlation (2011) evaluating it at T_w . This term depends on G , D , and μ , with μ the only variable depending on evaluation at T_b or T_w . Larger values of G could potentially have mitigated the fluctuation in the magnitude of μ , especially when evaluated at T_b , and reduced the overall volatility in the predicted HTC . This appears to be somewhat plausible because the HTC RMS values decreased as G increased, though this is not the case for the high G section for the Mokry et al. correlation so further calculation at intermediate G would better illustrate this potential relationship.

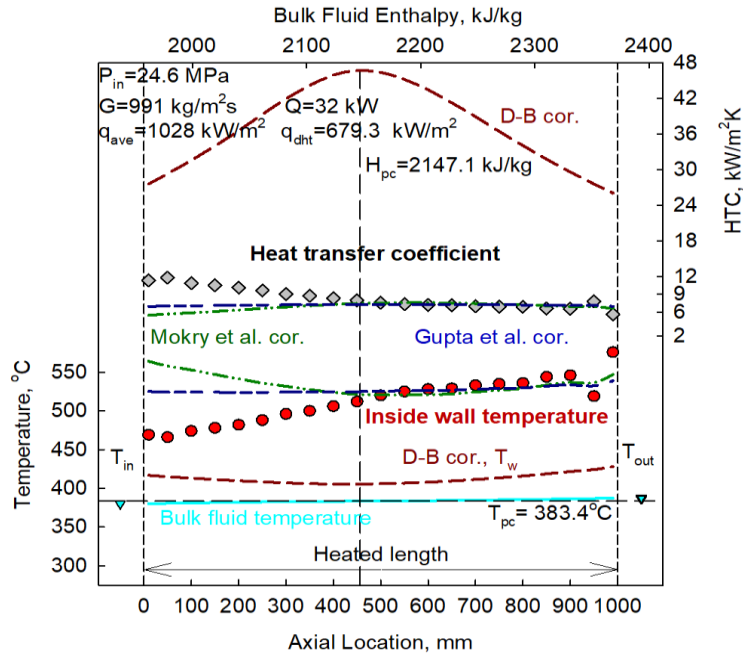
There is also the factor of computational convergence and its potential effect on the calculation on T_w by all three correlations. None of the terms in the Dittus-Boelter correlation (1930) rely on thermophysical properties evaluated at T_w and are instead evaluated at T_b . But, T_b was already determined for the entire heated length and so no iteration was needed to calculate T_w using Equation 3-16 since all the thermophysical properties were known beforehand and HTC could be calculated without issue. This was not the case for the Mokry et al. (2009) and Gupta et al. (2011) correlations since both included terms that relied on T_w . In order to calculate the properties evaluated at T_w , an initial guess of T_w was given at the beginning of the algorithm to calculate the HTC and T_w with the correlation (refer to Appendix C). Once the initial guess was made, the properties and terms dependent on T_w would be evaluated, an HTC produced, and a new T_w calculated. This was then compared to the initial guess and if the error was above the tolerance threshold, another iteration would begin with the new T_w used as the initial guess. Once the error tolerance had been reached, whatever final HTC and T_w produced by the correlation achieved this tolerance would be saved in the final output data array for the specified correlation, and the next T_w calculation along the heated length would commence.

With the Mokry et al. correlation (2009), only the corrective term relied on T_w and the iterative cycle concluded fairly quickly. The Gupta et al. correlation (2011) had more terms that relied on T_w so the iterative cycle was longer. In the initial stages of the code development, the error tolerance was not dynamically adjusted for either the Mokry et al. (2009) or Gupta et al. (2011) correlations. Computation of the HTC and T_w using the Mokry et al. correlation (2009) converged without problem but the Gupta et al. correlation (2011) failed to converge. Investigation found that the T_w 's generated by the Gupta et al. correlation (2011) oscillated between two possible values, one higher and another lower. This is what prompted the error

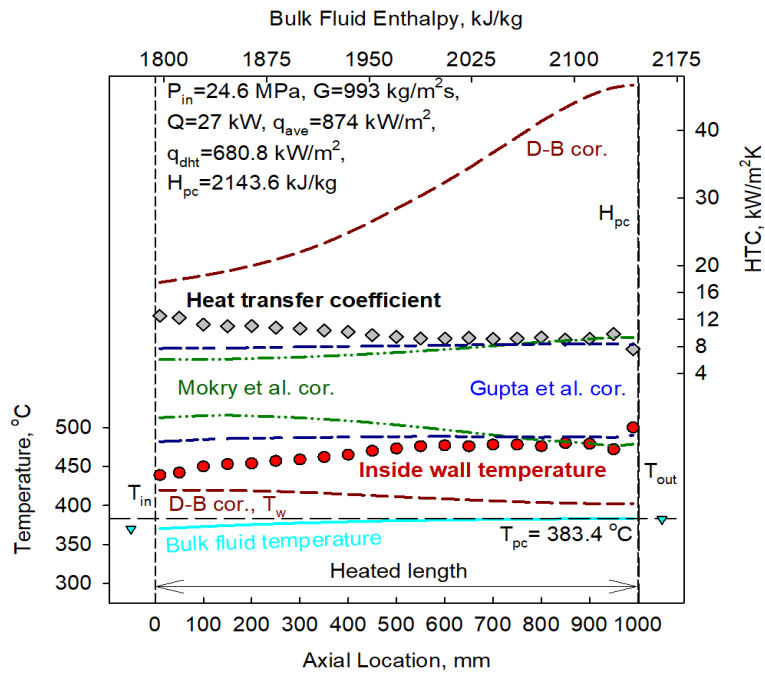
tolerance to become dynamic for the Gupta et al. correlation (2011) and adjust as the iterative cycle went on so that convergence could eventually be achieved.

Essentially, the Gupta et al. correlation (2011) would only settle on a final HTC and T_w value because the error tolerance would increase until the lower of the two fluctuating temperatures was saved, along with the corresponding HTC , in the final output data array. In contrast, the Mokry et al. correlation (2009) would settle on one set of HTC and T_w values without the need for its error tolerance to be increased. Such a difference in the computational convergence could possibly be why the T_w RMS for the Mokry et al. correlation (2009) is so much higher than corresponding RMS for the Dittus-Boelter (1930) and Gupta et al. (2011) correlations at low G . More likely, it is a combination of all three factors described but further investigation is warranted.

As it stands, the Mokry et al. (2009) and Gupta et al. (2011) correlations are appropriate for use around the pseudo-critical temperature in NHT and IHT regimes (Pioro, 2019). Use of all three correlations in the DHT regime will result in erroneous results that fail to predict the HTC and T_w profiles of the experimental data. Amongst the three mass-flux groups of data, the best-predicted data was in the high mass-flux group. This was to be expected as the data from that group displayed little-to-no entrance region effects and also did not show sudden changes in the HTC and T_w because of DHT. The worst-predicted was the low mass-flux group with large relative RMS values for all three correlations in both the T_w and HTC categories.

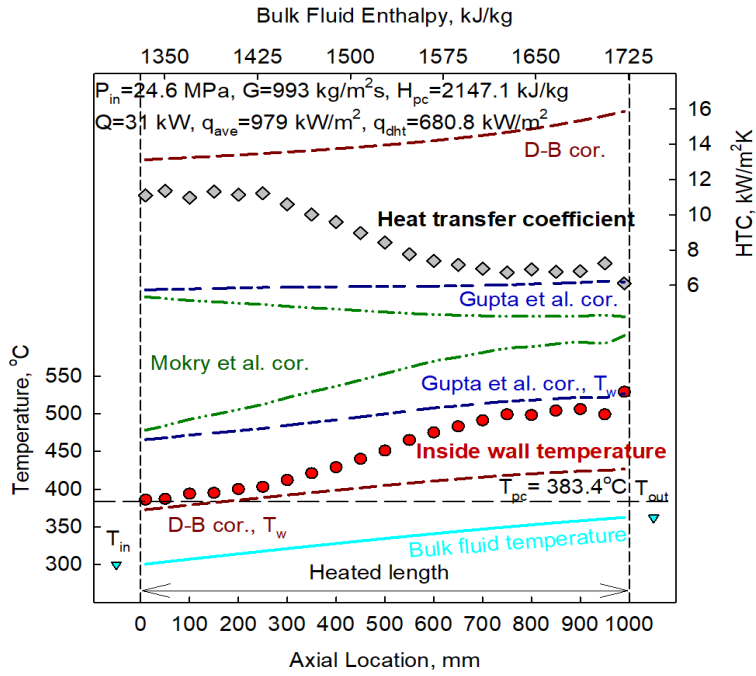


(a)

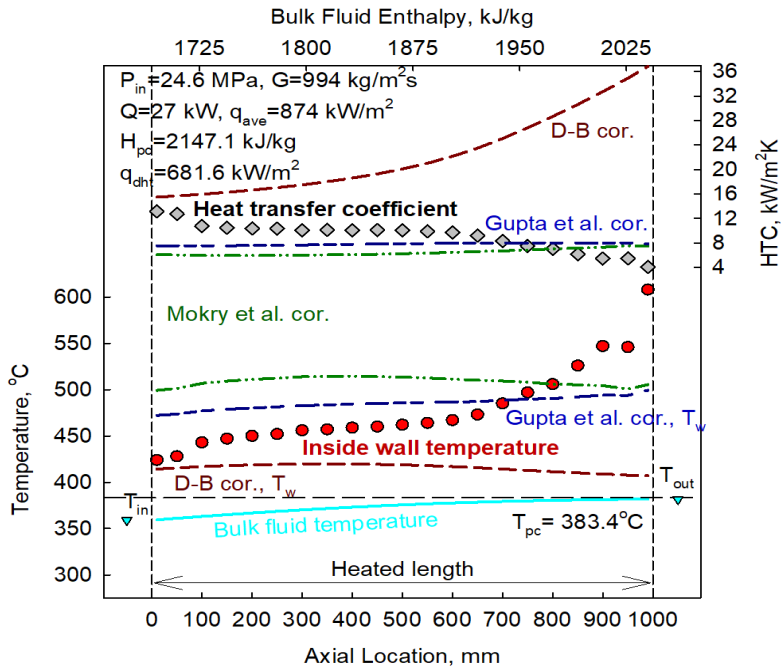


(b)

Figure 4-3: Collection of high G HTC and T_w profiles for the 1-m long bare tube dataset by Kirillov et al. (a)-(b) $P=24.6$ MPa, $G=991-993$ kg/m²·s, $q_{ave}=874-1028$ kW/m². Markers-experimental data, Curves-calculated data; (prepared, based on Kirillov et al. (2003) dataset).

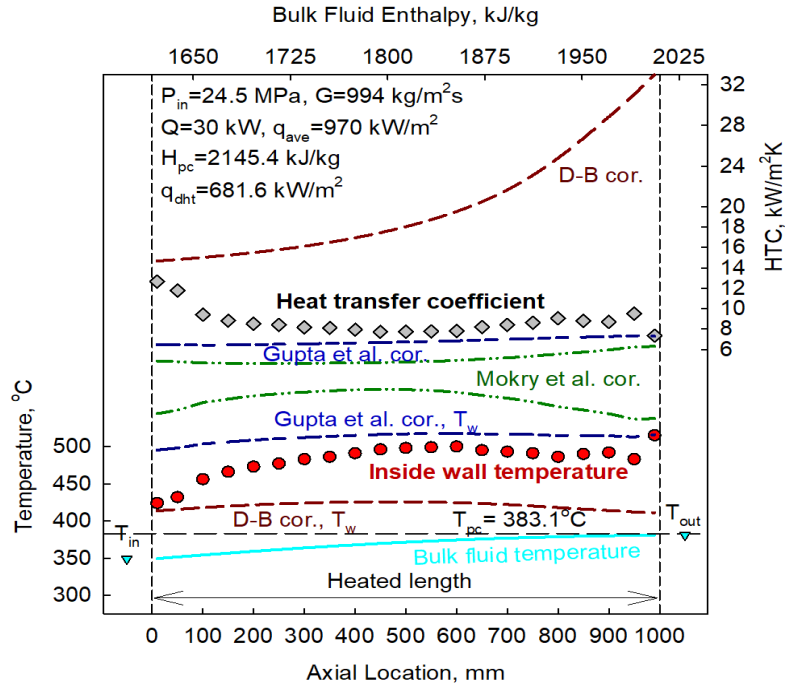


(c)

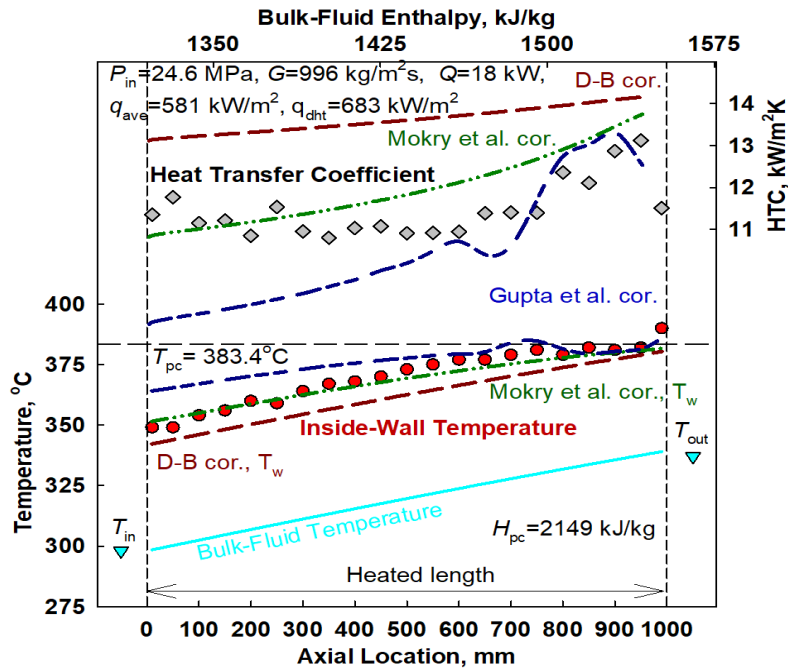


(d)

Figure 4-3: Collection of high G HTC and T_w profiles for the 1-m long bare tube dataset by Kirillov et al. (c)-(d) $P=24.6$ MPa, $G=993-994$ kg/m²·s, $q_{ave}=874-979$ kW/m². Markers-experimental data, Curves-calculated data; (prepared, based on Kirillov et al. (2003) dataset).

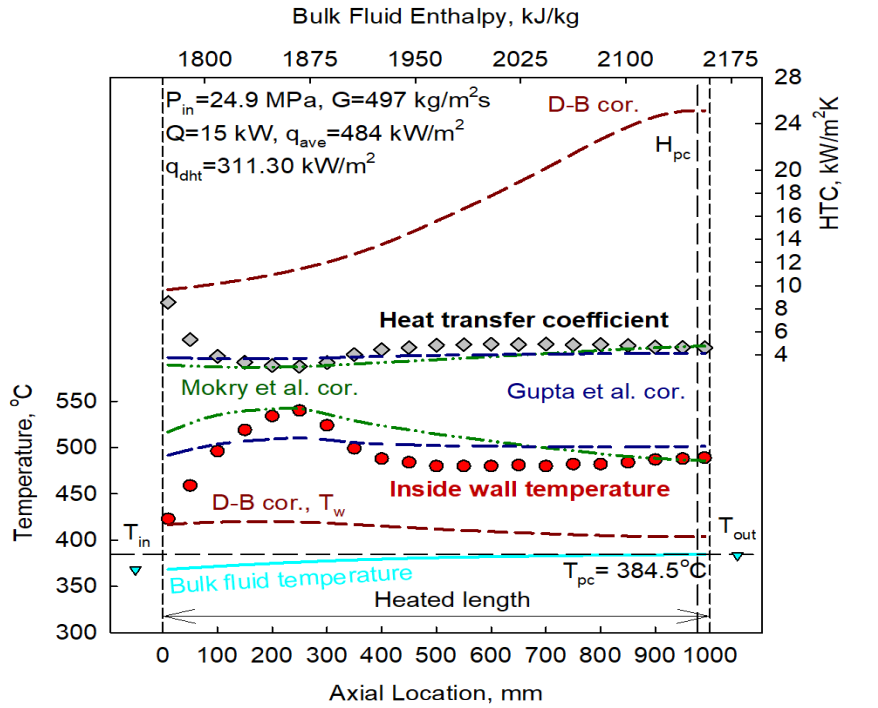


(e)

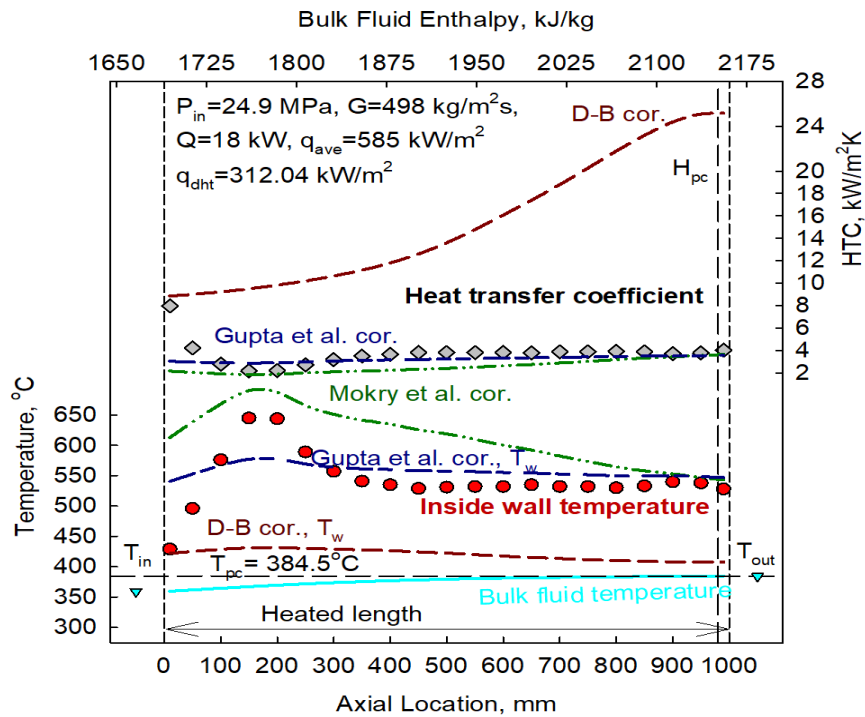


(f)

Figure 4-3: Collection of high G HTC and T_w profiles for the 1-m long bare tube dataset by Kirillov et al. (e)-(f) $P=24.5-24.6$ MPa, $G=994-996$ kg/m²·s, $q_{ave}=581-970$ kW/m². Markers-experimental data, Curves-calculated data; (prepared, based on Kirillov et al. (2003) dataset).

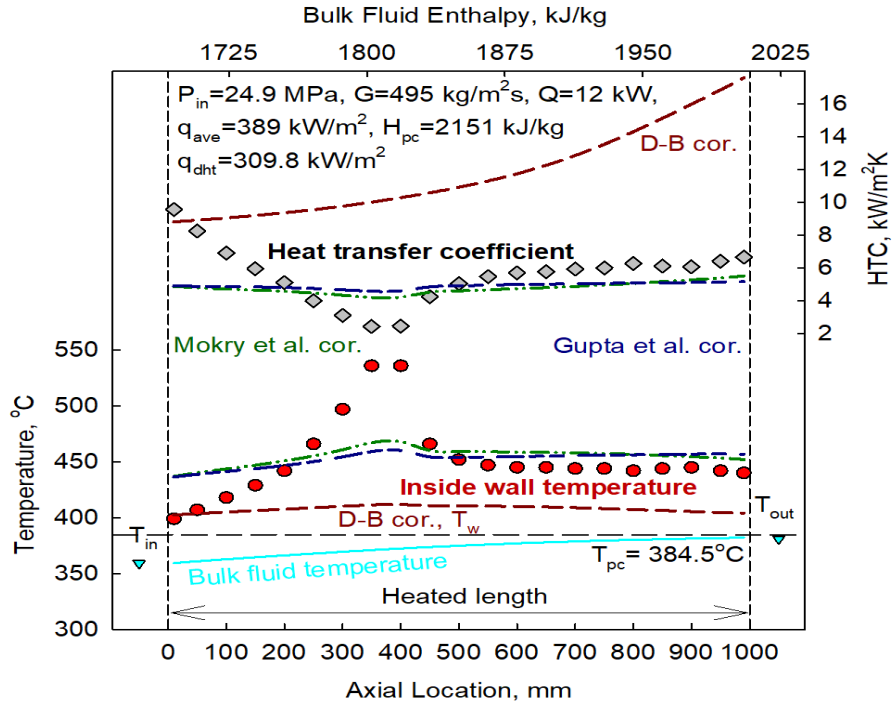


(a)

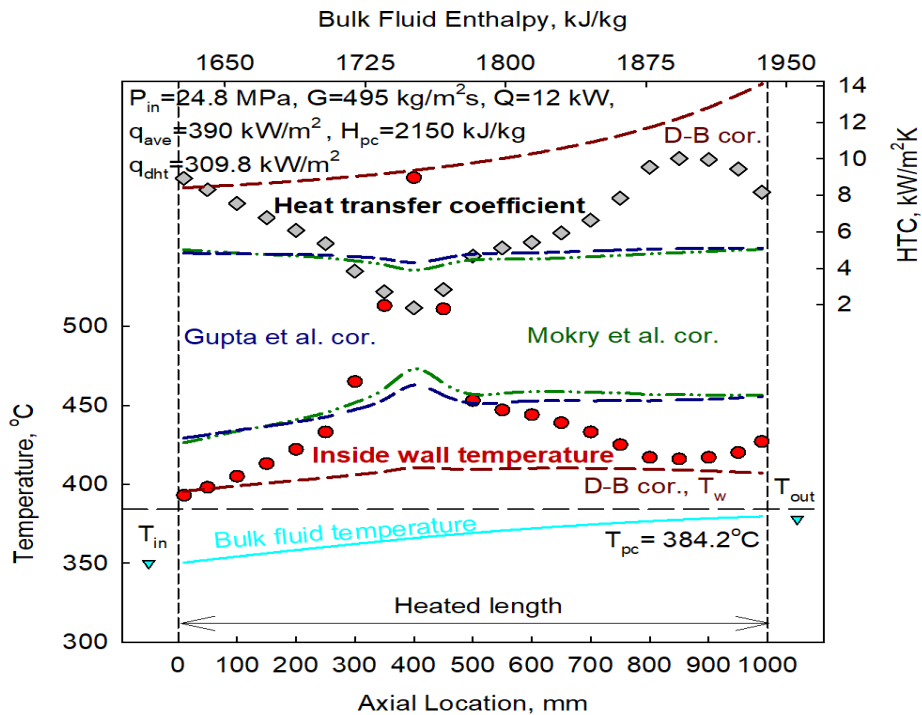


(b)

Figure 4-4: Collection of medium G HTC and T_w profiles for the 1-m long bare tube dataset by Kirillov et al. (a)-(b) $P=24.9$ MPa, $G=497-498$ kg/m²·s, $q_{ave}=484-585$ kW/m². Markers-experimental data, Curves-calculated data; (prepared, based on Kirillov et al. (2003) dataset).

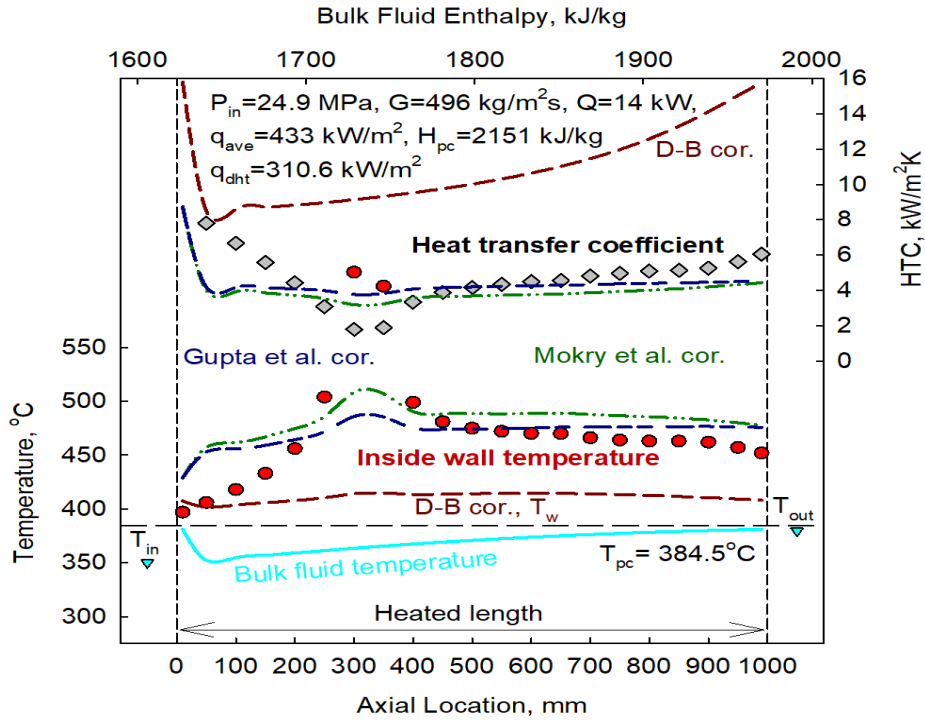


(c)

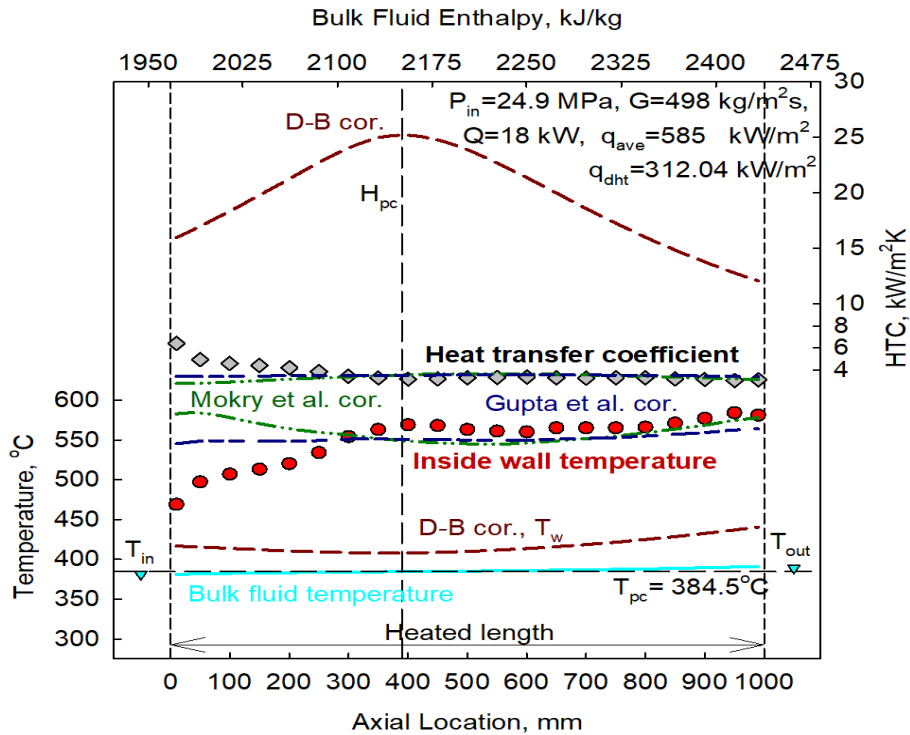


(d)

Figure 4-4: Collection of medium G HTC and T_w profiles for the 1-m long bare tube dataset by Kirillov et al. (c)-(d) $P=24.8-24.9$ MPa, $G=495$ kg/m²·s, $q_{ave}=389-390$ kW/m². Markers-experimental data, Curves-calculated data; (prepared, based on Kirillov et al. (2003) dataset).

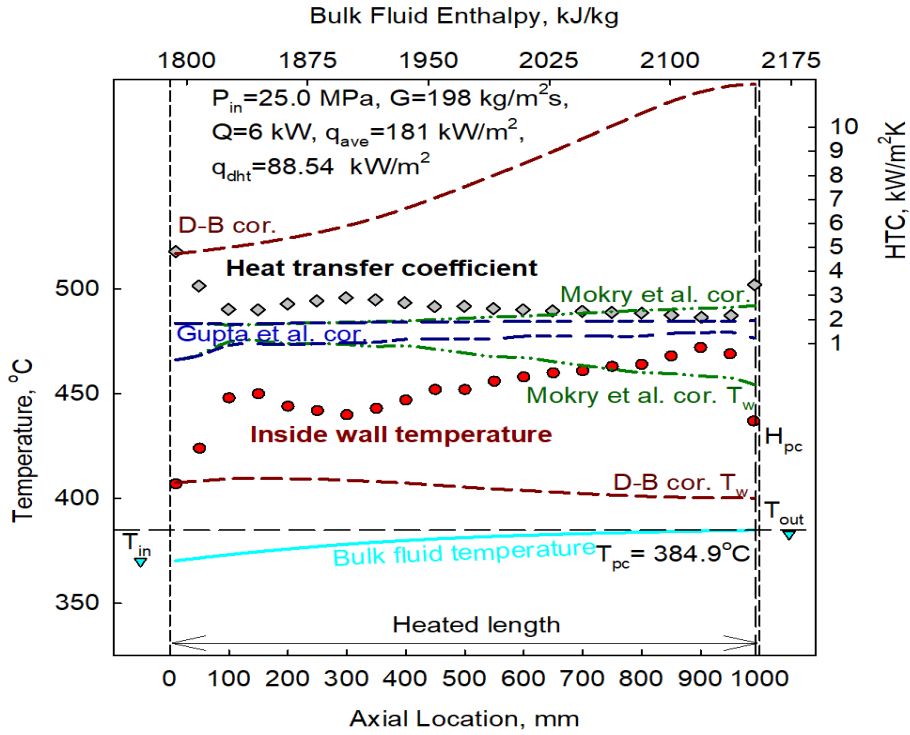


(e)

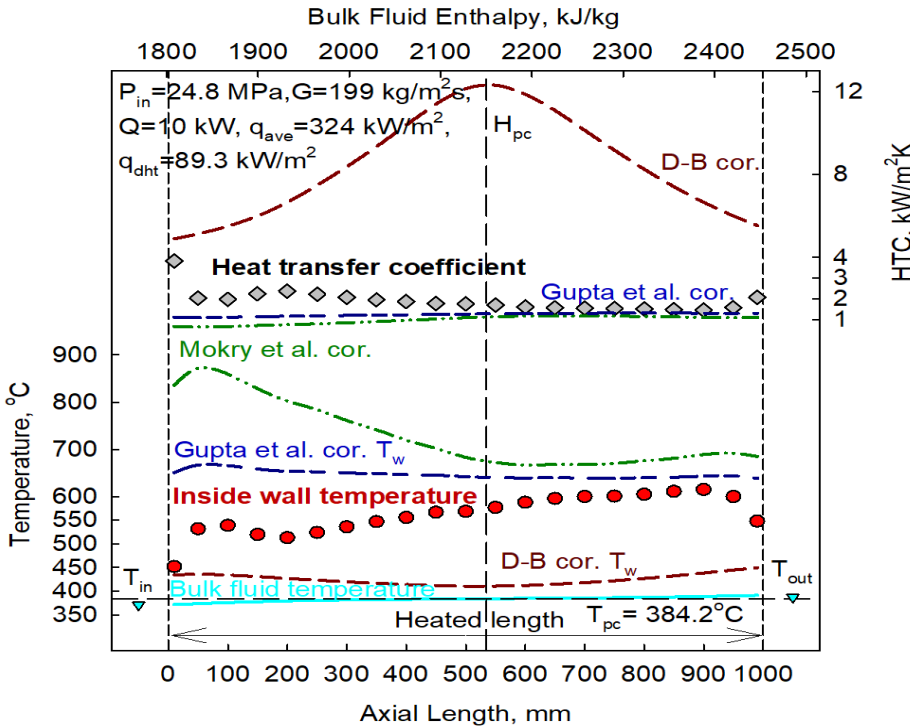


(f)

Figure 4-4: Collection of medium G HTC and T_w profiles for the 1-m long bare tube dataset by Kirillov et al. (e)-(f) $P=24.9 \text{ MPa}$, $G=496\text{-}498 \text{ kg/m}^2\text{s}$, $q_{ave}=433\text{-}585 \text{ kW/m}^2$. Markers-experimental data, Curves-calculated data; (prepared, based on Kirillov et al. (2003) dataset).

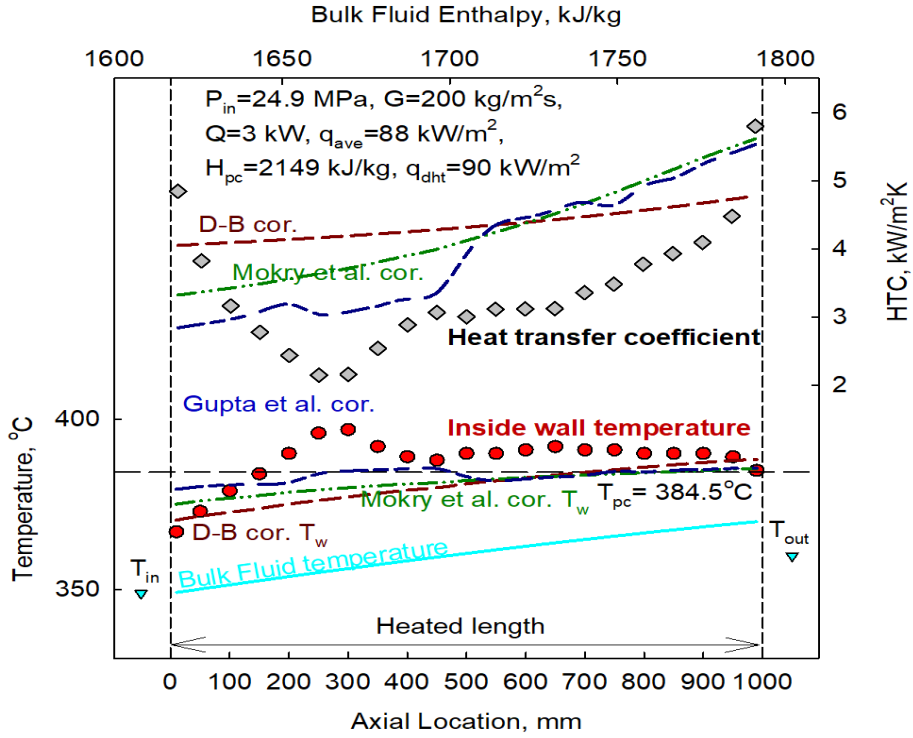


(a)

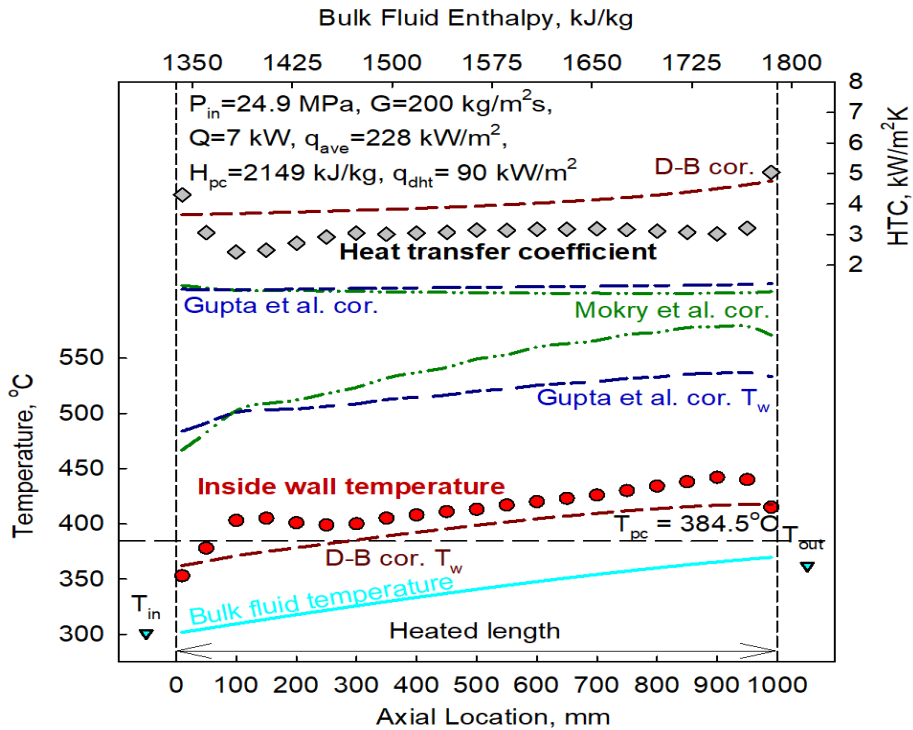


(b)

Figure 4-5: Collection of low G HTC and T_w profiles for the 1-m long bare tube dataset by Kirillov et al. (a)-(b) $P=24.8-25$ MPa, $G=198-199$ kg/m²·s, $q_{ave}=181-324$ kW/m². Markers-experimental data, Curves-calculated data; (prepared, based on Kirillov et al. (2003) dataset).

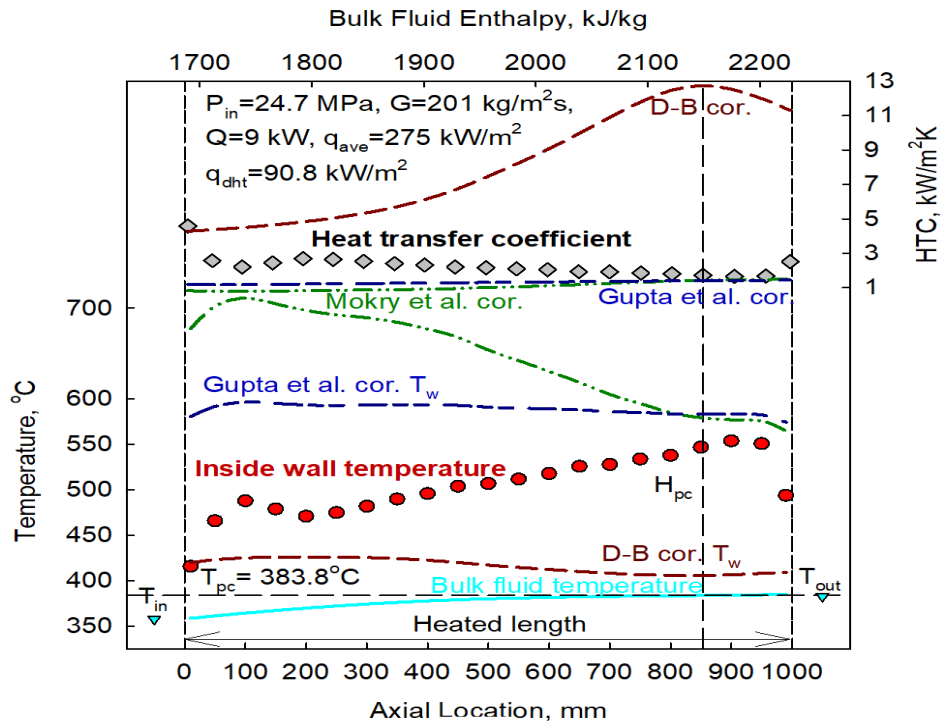


(c)

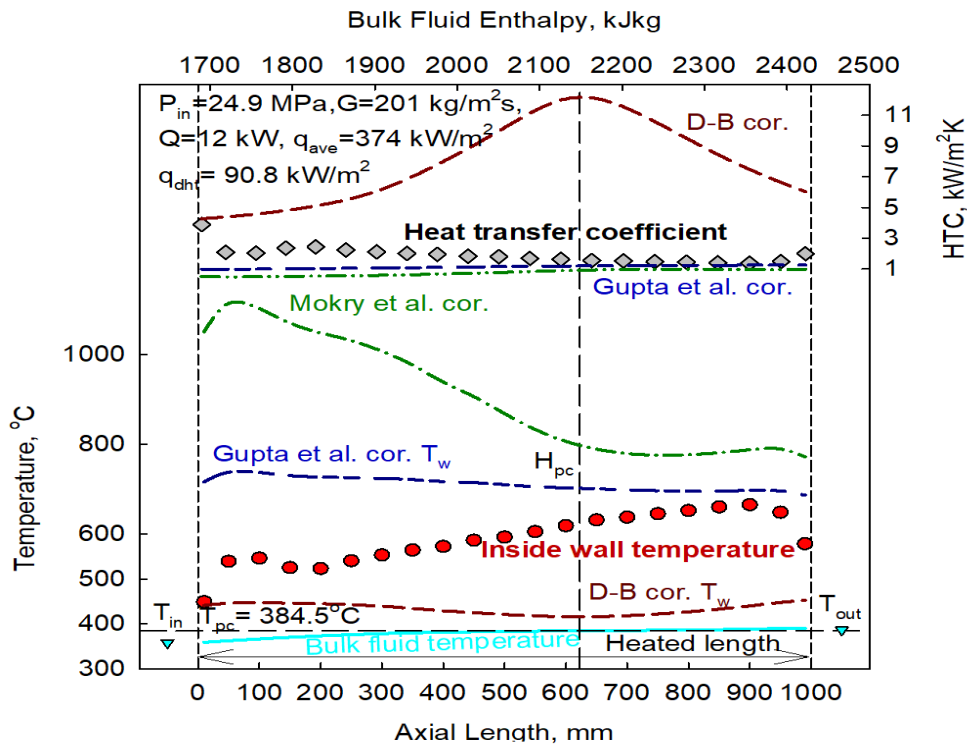


(d)

Figure 4-5: Collection of low G HTC and T_w profiles for the 1-m long bare tube dataset by Kirillov et al. (c)-(d) $P=24.9 \text{ MPa}$, $G=200 \text{ kg/m}^2\text{s}$, $q_{ave}=88\text{-}228 \text{ kW/m}^2$. Markers-experimental data, Curves-calculated data; (prepared, based on Kirillov et al. (2003) dataset).



(e)



(f)

Figure 4-5: Collection of low G HTC and T_w profiles for the 1-m long bare tube dataset by Kirillov et al. (e)-(f) $P = 24.7\text{-}24.9 \text{ MPa}, G = 201 \text{ kg/m}^2\text{s}, q_{ave} = 275\text{-}374 \text{ kW/m}^2$. Markers-experimental data, Curves-calculated data; (prepared, based on Kirillov et al. (2003) dataset).

4.2.1 Conclusion

Experimental data was obtained by Kirillov et al. (2003) at the IPPE Facility in Russia using the SKD-1 loop. The test section was a 1-m long, vertical, stainless steel bare tube with upward flow of SCW. Data was taken at three different G regimes – low, medium, and high – with varying pressures and average heat fluxes. It was found, using Equation 2-9, that nearly all the data was above the minimum heat flux, q_{dht} , necessary for the onset of DHT and the appearance of DHT was found in nearly all the data. This was characterized by a decline in the HTC and a subsequent increase in the T_w that could either be gradual or sharp. In all instances, the DHT regime was stable and there were no uncontrolled growths/reductions in either the HTC or T_w . Entrance region effects were also found to exist in some of the data and much like DHT onset, were characterized by lower $HTCs$ and higher T_w 's. These effects could either have a minimal or radical presence before the HTC and T_w profiles stabilized. To aid in the analysis, three correlations (Dittus-Boelter, Mokry et al., and Gupta et al.) were chosen to predict the HTC and T_w data. The Dittus-Boelter correlation over-predicted both the HTC and T_w profiles however, the error in the HTC was considerably larger. The Mokry et al. (2009) and Gupta et al. (2011) correlations did much better in predicting the HTC and T_w of the data but still failed to accurately predict both in the DHT regime. The relative performance of the three correlations in predicting $HTCs$ and T_w for the 1-m dataset followed the same trend in the analysis of the 4-m dataset by Mokry (2009) and Gupta (2014). Further development of HTC correlations that can predict the onset of DHT is needed along with more data from experiments using bundle geometry proposed for use in SCWR-type reactors (Dort-Goltz et al., 2021a,b).

4.3 LUEC Computation for SSR

The base case parameters for the *LUEC* calculation of the SSR are presented in Table 4-3 for ease of access. The reference data obtained from Moore et al. (2016) regarding the OCC of the large-scale Canadian SCWR is given in Table 4-4 along with the OCC breakdown of the SSR.

Table 4-3: Parameters for the base case *LUEC* evaluation of the SSR.

Parameter	Value
Technological maturity	FOAK
Plant capacity factor	95%
Fuel burnup	66.65 GW _{th-d} /Mt _U
Fuel enrichment	7%
Refueling interval	2.08 years
Plant lifetime	60 years
Construction period	4 years
Discount rate	5%

Table 4-4: OCC breakdown for SSR and reference SCWR reactor.

OCC Parameter	Canadian SCWR Concept, US\$ Millions (2007) (Moore et al., 2016)	SSR, US\$ Millions (2007)
Direct capital costs	2852	1091
Indirect capital costs	910	468
Supporting capital costs ⁸	190	390
Total	3952	1949

All pertinent data was input into G4ECONS and the base case *LUEC* was calculated for the SSR. A breakdown of this *LUEC* by capital, O&M, front-end and back-end fuel cycle, and D&D costs is given below in Table 4-5.

Table 4-5: Breakdown of *LUEC* for the SSR. Monetary figures are in 2007 USD.

G4ECONS Parameter	Levelized Annual Costs of Reactor	<i>LUEC</i> (\$/MW _{el} h)	Contribution to <i>LUEC</i> (%)
N/A	Capital (First Core and IDC Inclusive)	45	61
	Operations	19	26
	Fuel Cycle-Front	7	9

⁸ In the cost breakdown presented by the World Nuclear Association (2020b), the supporting capital costs are inclusive of project contingencies. However, this was not reflected in Moore et al. (2016) and their calculation of the supporting capital costs.

G4ECONS Parameter	Levelized Annual Costs of Reactor	<i>LUEC</i> (\$/MWh)	Contribution to <i>LUEC</i> (%)
	Fuel Cycle-Back End	2	3
	D&D Sinking Fund	1	1
	Total:	74	100

The estimated base case *LUEC* for the SSR was calculated to be roughly \$74/MWh with approximately 61% of that value reflected in the levelized annual capital costs of the reactor. The contributions towards the *LUEC* from the fuel cycle and D&D sinking fund are very small, making up just under 15% of the total *LUEC*. The *LUEC* is a very early estimate and is subject to considerable change especially since design of the SSR is still in a conceptual stage and will likely undergo alteration if it progresses towards construction (Pioro, ..., Dort-Goltz, 2020). Given the assumptions used in the G4ECONS model, factors such as price escalation and taxes are not included in the *LUEC* above and as such it is not directly comparable to the *LUECs* of established energy systems that do include these parameters. Furthermore, the capital, O&M, fuel cycle, and D&D costs that were utilized in the G4ECONS calculation were conservative estimates and could very well end up being greater or smaller if the SSR were to ever be built. The effects of the SMR economic factors on the preliminary *LUEC* estimate for the SSR are given in Table 4-6.

Table 4-6: Implementation of SMR factors and the subsequent effect on the SSR *LUEC* and its components. Bold values represent figures of merit.

G4ECONS Parameter	Levelized Annual Costs of Reactor	<i>LUEC</i> (\$/MWh)	Relative Change to Base Case (%)	Contribution to <i>LUEC</i> (%)
Co-Siting Factor (CSF)=0.745	Capital (First Core and IDC Inclusive)	34	-24	54
	Operations	19	0	30
	Fuel Cycle-Front	7	0	11

G4ECONS Parameter	Levelized Annual Costs of Reactor	<i>LUEC</i> (\$/MWh)	Relative Change to Base Case (%)	Contribution to <i>LUEC</i> (%)
	Fuel Cycle- Back End	2	0	3
	D&D Sinking Fund	1	0	2
	Total:	63	-15	100
Learning Factor (LF)=0.863 + CSF	Capital (First Core and <i>IDC</i> Inclusive)	29	-36	50
	Operations	19	0	33
	Fuel Cycle- Front	7	0	12
	Fuel Cycle- Back End	2	0	3
	D&D Sinking Fund	1	0	2
Total:	58	-22	100	
Modular Design Factor (MDF)=0.862 +LF+CSF	Capital (First Core and <i>IDC</i> Inclusive)	25	-44	46
	Operations	19	0	35
	Fuel Cycle- Front	7	0	13
	Fuel Cycle- Back End	2	0	4
	D&D Sinking Fund	1	0	2
Total:	54	-27	100	
NOAK=0.805 + CSF+LF+MDF	Capital (First Core and <i>IDC</i> Inclusive)	20	-56	41
	Operations	19	0	39
	Fuel Cycle- Front	7	0	14
	Fuel Cycle- Back End	2	0	4
	D&D Sinking Fund	1	0	2
Total:	49	-34	100	
Modularization=0.70 + CSF+LF+MDF +NOAK	Capital (First Core and <i>IDC</i> Inclusive)	14	-69	33
	Operations	19	0	44

G4ECONS Parameter	Levelized Annual Costs of Reactor	<i>LUEC</i> (\$/MW_eh)	Relative Change to Base Case (%)	Contribution to <i>LUEC</i> (%)
	Fuel Cycle- Front	7	0	16
	Fuel Cycle- Back End	2	0	5
	D&D Sinking Fund	1	0	2
	Total:	43	-42	100

Unique SMR economic factors were stated to only affect capital costs so it was expected that the sole *LUEC* component to change with the application of these factors was the capital cost.

Applying all five factors to the capital cost estimate of the SSR resulted in just over a 40% reduction in the *LUEC* with the capital cost making up a smaller portion of the *LUEC* than the O&M in that scenario. Even with only a single SMR factor, the *LUEC* of the SSR experienced around a 15% reduction and applying a second factor enhanced this reduction to roughly 20%.

Thus, any combination of these factors would contribute to the reduction of an SMR's *LUEC* and thereby increasing its economic competitiveness. The realization of these cost benefits however remains to be seen.

For the base case cost, a sensitivity analysis was performed (refer to Appendix D) where several parameters such as the assumed lifetime, capacity factor, and uranium prices, were varied and their effect on the *LUEC* was noted. With exception of the lifetime and capacity factor, most parameters did little to significantly affect the *LUEC* of the SSR and most of them achieved *LUECs* between \$70/MW_eh and \$80/MW_eh. A capacity factor of 85% resulted in a *LUEC* around \$86/MW_eh and a 10-year and 20-years lifetime assumptions resulted in *LUECs* of ~\$160/MW_eh and ~\$100/MW_eh respectively. But, the lifetime of nuclear reactors is now expected to exceed 20 years (World Nuclear Association, 2021b), so the realized lifetime of the

SSR would likely be over 20 years meaning the 10- and 20-years *LUECs* can be ignored. Therefore, the upper bound for the base case *LUEC* (or the highest *LUEC* achieved in the sensitivity analysis for the base case) would be $\sim \$86/\text{MW}_{\text{e}}\text{h}$ while the lower bound for the base case, taken from Table 4-6, would be $\sim \$43/\text{MW}_{\text{e}}\text{h}$. To quantify the error in the *LUEC*, a “worst-case” and “best-case” scenario were constructed where the parameter values that resulted in the highest *LUEC* (with the exception of the assumed lifetime) within the sensitivity analysis from Appendix D were used to generate a “worst-case” *LUEC*. The “best-case” scenario *LUEC* followed the same steps except the parameter values that minimized the *LUEC* in the sensitivity analysis were used in addition to the application of all five SMR economic factors. Doing so resulted in a “worst-case” *LUEC* of $\sim \$103/\text{MW}_{\text{e}}\text{h}$, around 40% higher than the base case *LUEC*, and a “best-case” *LUEC* of $\sim \$36/\text{MW}_{\text{e}}\text{h}$, around 50% lower than the base case *LUEC*. Producing a concrete error for the *LUEC* of the SSR is difficult to do given the amount of uncertainty and assumptions made to even arrive at the base case *LUEC*. As was mentioned, the SSR design is still in a conceptual stage so design parameters are subject to change and it is unclear whether any of the SMR economic factors will actually be used. Therefore, to account for all of these sources of uncertainty, an error of $\pm 50\%$ was adopted so that for the base case, the *LUEC* would be equal to $\$74/\text{MW}_{\text{e}}\text{h} \pm \$37/\text{MW}_{\text{e}}\text{h}$. The error applies to the *LUEC* at different discount rates as well since, from the sensitivity analysis, the curves for the *LUEC* at discount rates of 3% and 10% take on the same general shape as the curve for the 5% *LUEC*, indicating that the parameter variation impacted the *LUEC* similarly across the discount rates.

In addition to variations of the parameters in the base case *LUEC*, a sensitivity analysis was done regarding the discount rate. The base case adopted a standard 5% discount rate to represent a mix of a regulated and free market environment. This was changed to 3%, representative of a

heavily-regulated market with greater government funding, and 10%, representative of a free market with greater private investment (IAEA, 2014). A *LUEC* breakdown for all three discount rates is given in Figure 4-6.

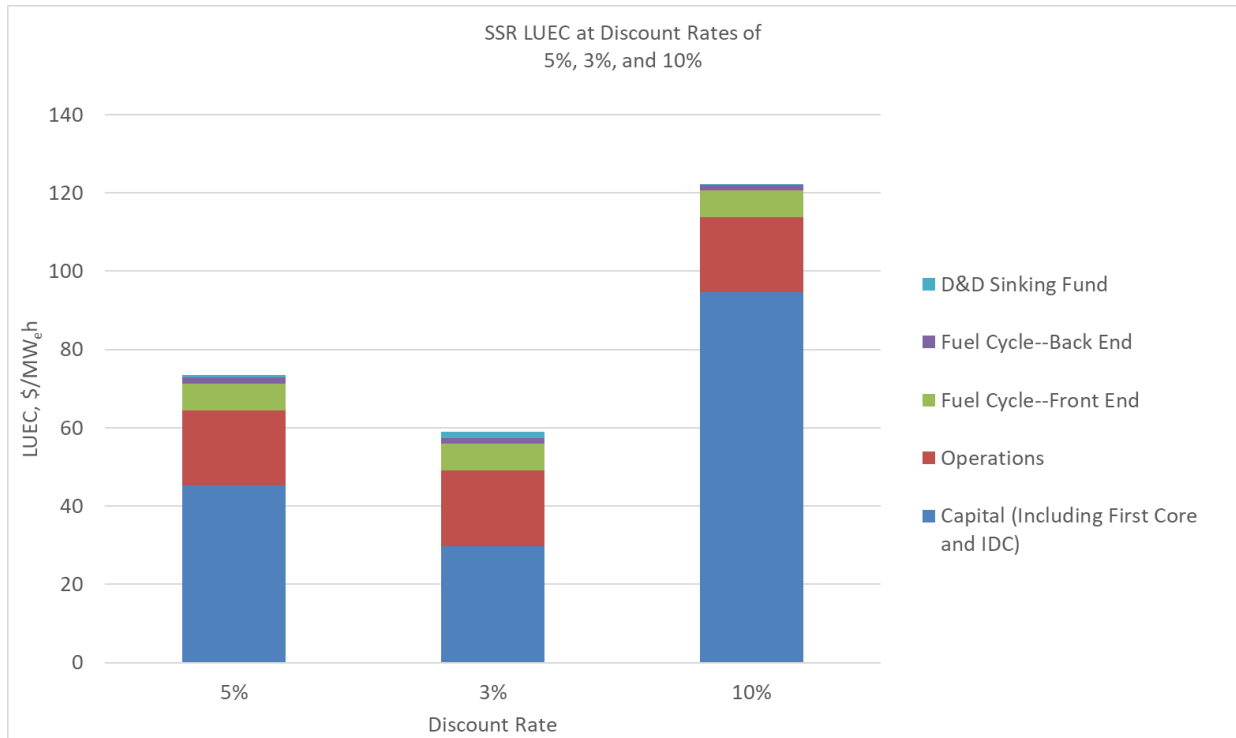


Figure 4-6: SSR LUEC breakdown at discount rates of 5%, 3%, and 10%.

Adjusting the discount rate to 3% resulted in a *LUEC* of approximately \$60/MW_eh with a capital cost reduction of around 33% and an overall *LUEC* reduction of ~20% compared to the base case. On the other hand, a 10% discount rate dramatically increased the *LUEC* to \$122/MW_eh representing a 66% increase over the base case. In this situation, the capital costs grew by ~109% compared to the base case. The D&D sinking fund also experienced some changes but they were minimal and did not impact the *LUEC* in any meaningful manner. The change arose in the capital costs and D&D sinking fund, and by extension the *LUEC*, from the variation in discount rate because of the G4ECONS assumption that the discount rate, interest rate during construction, and D&D fund interest rate were all the same. Adjusting these parameters to

separate amounts may result in either a more muted or aggressive change in the *LUEC*.

Regardless, the results above indicate the potential risk involved with investing in an SMR without large government involvement. SMRs are still capital-intensive projects and operating in a free market seems to diminish their economic competitiveness. But, as has been mentioned, these *LUEC* figures are preliminary estimates and further, detailed analyses are still needed. A tentative comparison of the base case *LUEC* calculated in this section for the SSR to other nuclear projects is given in Table 4-7, with *LUEC* figures in both the specified currency and 2020 USD.

Table 4-7: Comparison of *LUEC* for different reactor technologies in 2020 USD.

Reactor Technology	<i>LUEC</i> (\$/MWh)	Currency	In 2020 USD⁹
SSR	74	2007 USD	92
Canadian SCWR concept (Moore et al., 2016)	51.4	2007 USD	64.16
Reference ABWR (TVA, 2005)	38.78	2007 USD	48.41
Darlington (post-refurbishment) (OPG, 2013)	79	2013 CAD	85.22
IMSR600 (Samalova, 2017)	44.13	2015 USD	48.19
Boldon and Sabharwell (2014)	66-84	2014 USD	70-92
SMR Start (2017)	78-105	2017 USD	83-111
NEA and OECD (2011)	47-203	2011 USD	55-235

The adjusted base case *LUEC* for the SSR in 2020 USD is on the higher end of the *LUEC* estimates in Table 4-8. Among the data, the most economically competitive options are the ABWR and the IMSR600 while the least economically competitive are the SSR and the model

⁹ Escalation based on average annual consumer price index (U.S Bureau of Labor Statistics, 2021) since this was the method used by Moore et al. (2016) for their own price escalation.

SMRs used by Boldon and Sabharwell. It should be noted that the SMR and SCWR estimates were conducted using a top-down approach so the reference data and assumptions vary across cases. As it stands, the SSR would need to incorporate some of the economic SMR factors to become competitive with the other technologies considered above. Of the SMR estimates above, Samalova et al. (2017) and Boldon and Sabharwell (2014), along with SMR Start (2017) and NEA and OECD (2011), only Samalova (2017) did not apply SMR economic factors to their *LUEC* estimate.

An additional figure of merit is the specific capital cost of the reactor, in this case having units of 2007 USD/kW_{el}. For the base case SSR, this value becomes ~\$6500/kW_{el}, while applying all five SMR factors reduces this to ~\$2200/kW_{el}. In 2020 USD, these become ~\$8100/kW_{el} and ~\$2700/kW_{el} respectively. For reference (all monetary figures are 2020 USD and taken from EIA (2020)), SCP coal-fired power plants have specific capital costs generally between \$3500-\$6000/kW_{el}, combined-cycle plants are between ~\$1000-\$2500/kW_{el}, while solar photovoltaic plants range between ~\$1300-1800/kW_{el}. The SSR then becomes an attractive energy source if it fully utilizes the SMR economic factors whereas no incorporation leads it to being a relatively poor financial investment. However, the specific capital cost of an energy source does not fully encapsulate its worth, as factors such as power density, reliability, and operating life are not included in the calculation. Therefore, a collection of these metrics should be examined to better gauge the economic competitiveness of an energy source.

4.3.1 Conclusion

The OCC, O&M, fuel cycle, and D&D costs were estimated for the SSR using a reference large SCWR unit. These were implemented into the G4ECONS software and preliminary *LUEC* figures were calculated for the SSR. The base case preliminary *LUEC* estimate was found to be

around \$74/MW_eh with application of SMR economic factors lowering this value down to \$43/MW_eh. Depending on the discount rate, the *LUEC* of the SSR was estimated to be around \$60/MW_eh at 3% and around \$122/MW_eh at 10%. A comparison was also made in 2020 USD to other nuclear technologies and it was observed that the SSR was on the higher end of *LUEC* estimates. However, the figure calculated in this section is an early first estimate and does not include many other factors that could potentially affect its magnitude in addition to being subject to change based off any future SSR design alterations. The reactor costs were also based off of a reference SCWR unit whose costs were themselves based off of a reference ABWR reactor. Therefore, a considerable amount of uncertainty is associated with the *LUEC* estimate given in this section. Though, the efficacy of the SMR economic factors in increasing the economic competitiveness of SMRs was illustrated in this section. Adoption of these SMR-specific design choices would help make SMRs a more attractive option for investors, whether private or public. Based on comparisons to other nuclear technologies in Table 4-7 and Table 2-6, the SSR *LUEC* is within an economically feasible range for adoption as its magnitude, even in a “worst-case” scenario, is not much bigger than the larger end of *LUECs*.

Chapter 5: Conclusions

A preliminary thermalhydraulic and economic assessment was performed on a SCWR-type SMR named the SSR. Within this assessment:

1. It was found that the theoretical models used by reference property program called NIST REFPROP v.10 to calculate the values of nine thermophysical properties gave non-physical values around the critical point of water. Considerable deviations in property values between the four different temperature increments were also noted along with the occurrence of a failure-to-converge message that appeared in temperature increments below 0.002 °C and in temperature ranges that included the critical point.
2. To resolve the issues associated with the theoretical calculations of the selected thermophysical properties of water, it was suggested that experimental data be used in the database at the critical point so the values generated would be within physical possibilities, thus reducing the possibility for unacceptable errors in technical calculations.
3. To predict the heat transfer behavior of an SCWR-type reactor, experimental data was obtained by Kirillov et al. (2003) from upward flow of SCW in a 1-m long, bare tube. This was a conservative approach to analyzing the heat transfer characteristics of SCW as experiments with SCWR-specific bundle geometries are expensive (Dort-Goltz et al., 2021a). The data was organized into three groups according to the magnitude of G ; high, medium, and low and analyzed using three different correlations those being the Dittus-Boelter (1930), Mokry et al. (2009) and Gupta et al. (2011) correlations. Amongst the experimental data, it was found that the DHT regime existed in almost all test cases and the onset was either gradual or abrupt. In either situation, the HTC decreased while the T_w

increased during DHT. Entrance region effects were also found in some of the test cases with varying levels of severity as some test cases displayed rapid decreases/increases in the HTC/T_w values and others were more muted. In most occurrences of DHT, it was found the HTC and T_w profiles remained stable along the heated length of the bare tube. In all occurrences of DHT, uncontrolled change of either the HTC or T_w were not encountered which is a positive sign for future reactor operation.

4. Amongst the calculated data provided by the three correlations, it was confirmed that the use of the Dittus-Boelter correlation as a predictive tool of heat transfer is inappropriate near the pseudocritical temperature. It continuously over-estimated the HTC in all test cases and would introduce large errors in any possible analyses. The Mokry et al. (2009) and Gupta et al. (2011) correlations did a better job at predicting the HTC and T_w values, following the same trend found in the analysis of the 4-m dataset by Mokry (2009) and Gupta (2014), but they were also inaccurate within the DHT regime. From the relative RMS analysis, it was found that the high mass-flux test cases displayed the most stable heat transfer behavior whereas the medium and low mass-flux cases were much more erratic. Further development of heat transfer correlations in the DHT regime is necessitated.
5. The economic competitiveness of the SSR was examined through calculation of its $LUEC$ using the G4ECONS software provided by the EMWG. A reference SCWR reactor was used to estimate the cost breakdown of the SSR and this was input into the G4ECONS. The base case $LUEC$ of the SSR was calculated to be \$74/MW_eh (2007 USD).
6. Unique SMR economic factors were applied to the OCC of the SSR and their effect on its $LUEC$ was studied. It was found that incorporating all five factors resulted in a $LUEC$

reduction of 42% with at least one factor reducing the *LUEC* between 10-15%. Discount rate variation was also explored by changing the discount rate from 5% to 3% and 10%. The *LUEC* of the SSR became more competitive in the 3% case but became much less competitive in the 10% case, illustrating the risk of constructing a capital-intensive project like an SMR in a free market.

7. Other nuclear technologies and their *LUEC* estimates were compared to the base case *LUEC* of the SSR in 2020 USD. The SSR was determined to be the least economically competitive of all the options though assumptions and estimation techniques varied between the considered technologies. A more detailed study is needed to attain a more accurate *LUEC* estimate and to better gauge the economic competitiveness of the SSR. Though, it was concluded that incorporating SMR-specific features in the design process does result in positive economic performance and could very well become a widely-adopted strategy to help SMRs remain economically competitive.

Overall, the SSR is a SMR concept that can be used for long-term operation for electrical generation given the indicated thermalhydraulic stability of its proposed coolant, calculated using relatively accurate thermophysical property values generated by NIST REFPROP v.10, and becomes economically viable with the adoption of SMR-specific economic factors. Future work will primarily be centered around a heat transfer correlation that can better predict *HTCs* and *T_w*'s in the DHT regime along with a further investigation into the current computational capabilities of the three correlations used in this work. In addition, more accurate SSR *LUEC* estimates, that incorporate factors such as taxes and price escalation, are also warranted. Ultimately, commercial adoption of SSRs, or really any SCWR-type of reactor, is a long-term prospect especially given the need to further understand the thermalhydraulics of a SCW-cooled

reactor. Resolving the uncertainties associated with DHT, along with other challenges, is crucial to transforming the SSR from a conceptual reactor into an operating one that provides many benefits to its community.

References

“Charter of the Generation IV International Forum”, 2002. Generation IV International Forum Document (www.gen-4.org/PDFs/GIFcharter.pdf), February.

Bell, I., Wronski, J., Quoilin, S., and Lemort, V., 2014. Pure and Pseudo-pure Fluid Thermophysical Property Evaluation and the Open-Source Thermophysical Property Library CoolProp. *Industrial & Engineering Chemistry Research*, Vol. 53, No. 6, pp. 2498-2508.

Bishop, A.A., Sandberg, R.O., and Tong, L.S., 1964. High Temperature Supercritical Pressure Water Loop: Part IV, “Forced Convection Heat Transfer to Water at Near-Critical Temperatures and Super-Critical Pressures,” Westinghouse Electric Corporation WCAP 2056, Pittsburgh, Pennsylvania.

Boarin, S., Locatelli, G., Mancini, M., and Ricotti, M. E., 2012. Financial Case Studies on Small- and Medium-Size Modular Reactors. *Nuclear Technology*, Vol. 178, pp. 218-232.

Boldon, L.M, and Sabharwall, P., 2014. Small Modular Reactor: First-of-a-Kind (FOAK) and Nth-of-a-kind (NOAK) Economic Analysis. Idaho National Laboratory Report No. INL/EXT-14-32616.

Carelli, M., Garrone, P., Locatelli, G., Mancini, M., Mycoff, M. and Trucco, P., 2010. Economic features of integral, modular, small-to-medium size reactors. *Progress in Nuclear Energy*, Vol. 52, pp. 403-414.

Carelli, M. et al., 2008. Competitiveness of Small-Medium, New Generation Reactors: A Comparative Study on Capital and O&M Costs, Proceedings of 16th International Conference on Nuclear Engineering, Orlando, Florida, USA, May 11-15, 8 pages.

Chen, W., Fang, X., Xu, Y. & Su, X., 2015. An Assessment of Correlations of Forced Convection Heat Transfer to Water at Supercritical Pressure. *Annals of Nuclear Energy*, Vol. 76. pp. 451-460.

Cheng, X., Schulenberg, T., 2001. Heat Transfer at Supercritical Pressures Literature Review and Application to an HPLWR, 47 pages.

Chow, C.K., and Khartabil, H.F., 2008. Conceptual Fuel Channel Designs for CANDU-SCWR. *Nuclear Engineering and Technology*, Vol. 40, No. 2, pp. 139-146.

Cooper, J. R., 1982. Representation of the Ideal-Gas Thermodynamic Properties of Water. *Int. J. Thermophys.*, Vol. 3, pp. 35-43.

Dittus, F.W. and Boelter, L.M.K., 1930. Heat Transfer in Automobile Radiators of the Tubular Type, University of California, Berkeley, Publications on Engineering, Vol. 2(13), pp. 443-461.

Dort-Goltz, N., Pioro, I., and McKellar, J., 2021a. Study on Deteriorated Heat Transfer in Upward Flow of Supercritical Water in a 1-M Vertical Bare Tube, Proceedings of 28th International Conference on Nuclear Engineering, Virtual Conference, August 4-6, 10 pages.

Dort-Goltz, N., Pioro, I., and McKellar, J., 2021b. Experimental Study on Heat Transfer to Upward Flow of Supercritical Water in a 1-M Vertical Bare Tube, Proceedings of 40th Annual Conference of the Canadian Nuclear Society and 45th Annual CNS/CNA Student Conference (virtual), June 6-9, 6 pages. Master's Level Submission.

Dort-Goltz, N., Pioro, I., and McKellar, J., 2021c. Specifics of Calculating Thermophysical Properties of Water in Critical Point Using NIST REFPROP Program, Proceedings of the 10th

International Symposium on SCWRs (ISSCWR-10), Prague, the Czech Republic, March 15-18, 10 pages.

Economic Modelling Working Group (EMWG), 2007. Cost Estimating Guidelines for Generation IV Nuclear Energy Sources – Revision 4.2. Report No. GIF/EMWG/2007/004, OECD Nuclear Energy Agency, Paris, France.

Economic Modelling Working Group (EMWG), 2018. G4-ECONS Model —Version 3.0. OECD Nuclear Energy Agency, Paris, France.

EIA, 2020. Capital Cost and Performance Characteristic Estimates for Utility Scale Electric Power Generating Technologies. U.S Department of Energy Sargent and Lundy Report No. SL-014940. Available from:

https://www.eia.gov/analysis/studies/powerplants/capitalcost/pdf/capital_cost_AEO2020.pdf.

Generation IV International Forum (GIF), 2019. “FAQ on Economic Modelling Working Group.” https://www.gen-4.org/gif/jcms/c_110588/faq-on-economic-modelling-working-group-emwg#c_110603. Accessed: December 12, 2020.

Generation IV International Forum (GIF), 2020. “Generation IV Systems.” https://www.gen-4.org/gif/jcms/c_59461/generation-iv-systems. Accessed: January 13, 2021.

Gschnaidtner, T., Schatte, G., Kohlhepp, A., Wang, Y., Wieland, C. & Spliethoff, H., 2018. A New Assessment Method for the Evaluation of Supercritical Heat Transfer Correlations, Particularly with regard to the "Multiple/No Solutions" problem. *Thermal Science and Engineering Progress*, Vol. 7. pp. 267-278.

Gupta, S., 2014. Developing 1-D Heat Transfer Correlations for Supercritical Water and Carbon Dioxide in Vertical Tubes, *Master's Dissertation, University of Ontario Institute of Technology, Oshawa, Canada.*

Gupta, S., Mokry, S. and Pioro, I., 2011. Developing A Heat-Transfer Correlation for Supercritical-Water Flow in Vertical Bare Tubes and Its Application in SCWRS, Proceedings of the 19th International Conference On Nuclear Engineering (ICONE-19), Osaka, Japan, October 24-25, Paper# 43503, 11 pages.

Handbook of Generation IV Nuclear Reactors, 2016. Editor: I.L. Pioro, Elsevier – Woodhead Publishing (WP), Duxford, UK, 940 pages.

Handbook of Small Modular Nuclear Reactors, 2021. Editors: Carelli, M.D. and Ingersoll, D.T., 2nd edition, Elsevier – Woodhead Publishing (WP), Duxford, UK, 609 pages.

Hu, Z. H., 2001. Heat Transfer Characteristics of Vertical Up Flow and Inclined Tube in the Supercritical Pressure and Near-Critical Pressure Region. *Ph.D. Dissertation. Xi'an Jiaotong University, Xi'an, China.*

Huber, M.L., Perkins, R.A., Laesecke, A., Friend, D.G., Sengers, J.V., Assael, M.J., Metaxa, I.M., Vogel, E., Mares, R., and Miyagawa, K., 2009. New International Formulation for the Viscosity of Water. *J. Phys. Chem. Ref. Data, Vol.38, Issue 2*, pp.101-125.

Huber, M.L., Perkins, R.A., Friend, D.G., Sengers, J.V., Assael, M.J., Metaxa, I.N., Miyagawa, K., Hellmann, R., and Vogel, E., 2012. New International Formulation for the Thermal Conductivity of H₂O. *J. Phys. Chem. Ref. Data, Vol.41, Issue 3*, Article #033102.

IAEA, 2014. “INPRO Methodology for Sustainability Assessment of Nuclear Energy Systems: Economics. INPRO Manual”, IAEA Nuclear Energy Series No. NG-T-4.4, International Atomic Energy Agency, Vienna, Austria. Free download from: https://www-pub.iaea.org/MTCD/Publications/PDF/Pub1653_web.pdf.

IAEA, 2020a. “Advanced Large Water Cooled Reactors. A Supplement to: IAEA Advanced Reactors Information System (ARIS) 2020 Edition”, 36 pages. Free download from: https://aris.iaea.org/Publications/20-02619E_ALWCR_ARIS_Booklet_WEB.pdf.

IAEA, 2020b. Understanding and Prediction of Thermohydraulic Phenomena Relevant to Supercritical Water-Cooled Reactors (SCWRs), Final Report of a Coordinated Research Project, IAEA TECDOC Series, Vienna, Austria, 544 pages. Free download from: <https://www.iaea.org/publications/13636/understanding-and-prediction-of-thermohydraulic-phenomena-relevant-to-supercritical-water-cooled-reactors-scwrs>.

International Association for the Properties of Water and Steam (IAPWS), 2008. Release on the IAPWS Formulation 2008 for the Viscosity of Ordinary Water Substance. IAPWS R12-08. Available from: <http://www.iapws.org/relguide/viscosity.html>.

International Association for the Properties of Water and Steam (IAPWS), 2011. Release on the IAPWS Formulation 2011 for the Thermal Conductivity of Ordinary Water Substance. IAPWS R15-11. Available from: <http://www.iapws.org/relguide/ThCond.html>.

International Association for the Properties of Water and Steam (IAPWS), 2018. Revised Release on the IAPWS Formulation 1995 for the Thermodynamic Properties of Ordinary Water

Substance for General and Scientific Use. IAPWS R6-95. Available from:

<http://www.iapws.org/relguide/IAPWS-95.html>.

IEA, 2021. "Data and Publications," International Energy Agency, Paris, France.

<https://www.iea.org/data-and-statistics/data-products?filter=electricity>. Accessed June 5, 2021.

IEA and NEA, 1998. *Projected Costs of Generating Electricity: Update 1998*, Organisation for Economic Cooperation and Development, Paris, France.

IEA and OECD, 2020. *Projected Costs of Generating Electricity- 2020 Edition*, Available from:

<https://www.iea.org/reports/projected-costs-of-generating-electricity-2020>

Incropera, F.P, DeWitt D.P, Bergman T.L, and Lavine, A.S, 2007. *Fundamentals of Heat and Mass Transfer*. 6th Edition. John Wiley and Sons, Inc, New York, NY, USA.

Jackson, J.D., 2002. Consideration of the Heat Transfer Properties of Supercritical Pressure Water in Connection with the Cooling of Advanced Nuclear Reactors, Proceedings of the 13th Pacific Basin Nuclear Conference, Shenzhen City, China, October 21-25.

Kirillov, P.L., Lozhkin, V.V., and Smirnov, A.M., 2003. Investigation of Borders of Deteriorated Regimes of a Channel at Supercritical Pressures, (In Russian), State Scientific Center of Russian Federation Institute of Physics and Power Engineering by the name of A.I. Leypunskiy, FEI-2988, Obninsk, Russia, 20 pages.

Kirillov, P., Pometko, R., Smirnov, A., Grabezhaia, V., Pioro, I., Duffey, R., and Khartabil, H., 2005. Experimental study on heat transfer to supercritical water flowing in 1- and 4-m-long vertical tubes, Proceedings of GLOBAL 2005 International Conference, Nuclear Energy Systems for Future Generation and Global Sustainability (GLOBAL'05), Tsukuba, Japan, Oct. 9-13, Paper No. 518, 8 pages.

Kitoh, K., Koshizuka, S. & Oka, Y., 2001. Refinement of Transient Criteria and Safety Analysis for a High Temperature Reactor Cooled by Supercritical Water. *Nuclear Technology Vol. 135, No. 3*, pp. 252–264.

Ko, W.I, and Gao, F., 2012. Economic Analysis of Different Nuclear Fuel Cycle Options. *Science and Technology of Nuclear Installations, Vol. 2012*, Article ID 293467, 10 pages.

Le Neindre, B., Garrabos, Y., and Tufeu, R., 1984. Thermal Conductivity in Supercritical Fluids. *Berichte der Bunsengesellschaft für physikalische Chemie, Vol. 88, Issue 9*, pp 916-920.

Lei, X., Guo, Y., Zhang, W., Li, H. & Li, L., 2019. Development of Heat Transfer Correlation for Supercritical Water in Vertical Upward Tubes. *Heat Transfer Engineering, Vol. 40, No. 8*, pp. 652-666.

Li, Zh., Malik, H., Piro, I., and Machrafi, R., 2020. Specifics of Using NIST REFPROP Program for Calculating Thermophysical Properties of Water in Critical Point, Proceedings of 40th Annual Conference of the Canadian Nuclear Society and 44th Annual CNS/CNA Student Conference (virtual), May 31-June 3, 5 pages.

Lloyd, C.A, Roulstone, A.R.M., Middleton, C., 2018. The Impact of Modularisation Strategies on Small Modular Reactor Cost. Proceedings of the 2018 International Congress on Advances in Nuclear Power Plants (ICAPP 2018), Charlotte, NC, USA, April 8-April 11, 8 pages.

Locatelli, G., Bingham, C., and Mancini, M., 2014. Small modular reactors: A comprehensive overview of their economics and strategic aspects. *Progress in Nuclear Energy, Vol. 73*, pp. 75-85.

Locatelli, G., Pecoraro, M., Meroni, G., and Mancini, M., 2017. Appraisal of small modular nuclear reactors with ‘real options’ valuation. *Proceedings of the Institution of Civil Engineers: Energy*, Vol. 170, Issue EN2, pp. 51-66.

Lokhov, A., Cameron, R., and Sozoniuk, V., OECD/NEA Study on the Economics and Market of Small Reactors. *Nuclear Engineering and Technology*, Vol. 45, Issue 6, pp. 701-706.

Mignacca, B., and Locatelli, G., 2020. Economics and finance of Small Modular Reactors: A systematic review and research agenda. *Renewable and Sustainable Energy Reviews*, Vol. 118, Paper #109519.

McAdams, W., 1942. *Heat Transmission*, 2nd ed., McGraw-Hill, New York, NY, USA, 459 pages.

Mokry, S., 2009. Development of a Heat-Transfer Correlation for Supercritical Water in Supercritical Water-cooled Reactor Applications. *Master’s Dissertation, University of Ontario Institute of Technology, Oshawa, Canada*.

Mokry, S., Gospodinov, Y., Pioro, I. and Kirillov, P.L., 2009. Supercritical Water Heat-Transfer Correlation for Vertical Bare Tubes, Proceedings of the International Conference On Nuclear Engineering (ICONE-17), July 12-16, Brussels, Belgium, Paper #76010, 8 pages.

Moore, M., Leung, L., and Sadhankar, R., 2016. An Economic Analysis of the Canadian SCWR Concept using G4ECONS. *CNL Nuclear Review*, Vol. 5, No. 2, pp. 363-372.

NEA and OECD, 2011. Current Status, Technical Feasibility and Economics of Small Nuclear Reactors. Available from: <https://www.oecd-nea.org/ndd/reports/2011/current-status-small-reactors.pdf>.

National Energy Technology Laboratory (NETL), 2011. Cost Estimation Methodology for NETL Assessments of Power Plant Performance. Quality Guidelines for Energy System Studies. Report No. DOE/NETL-2011/1455. Available from: <https://www.osti.gov/biblio/1489510-quality-guideline-energy-system-studies-cost-estimation-methodology-netl-assessments-power-plant-performance>.

National Energy Technology Laboratory (NETL), 2013. Technology Learning Curve (FOAK to NOAK). Quality Guidelines for Energy System Studies. Report No. DOE/NETL-341/081213. Available from: <http://citeseerx.ist.psu.edu/viewdoc/download;jsessionid=2215E76B047081C1EF98E855F731153A?doi=10.1.1.385.8547&rep=rep1&type=pdf>.

NIST REFPROP, 2018. Reference Fluid Thermodynamic and Transport Properties, NIST Standard Reference Database 23, Version 10.0, Developers: E.W. Lemmon, I.H. Bell, M.L. Huber, and M.O. McLinden, Applied Chemicals and Materials Division, National Institute of Standards and Technology (NIST), Boulder, CO, USA.

Nonboel, E., 1996. Description of the Advanced Gas Cooled Type of Reactor (AGR). Riso National Laboratory, Report No. NKS/RAK2(96)TR-C2. Available from: <https://www.osti.gov/etdweb/servlets/purl/448871>.

Ontario Power Generation (OPG), 2013. Darlington Refurbishment Business Case Summary, November 14, 2013, Revision 1. Ontario Power Generation File No. N-REP-00120.3-10000-R001.

Ontario's Ministry of Energy, 2013. Achieving Balance: Ontario's Long-Term Energy Plan. Available from: https://files.ontario.ca/books/ltep_2013_english_web.pdf.

Parliamentary Office of Science and Technology, 2006. Carbon Footprint of Electricity Generation, postnote, October 2006, No. 268, 4 pages. Available from:

<http://researchbriefings.files.parliament.uk/documents/POST-PN-268/POST-PN-268.pdf>.

Peiman, W., 2011. Thermal Aspects of High Efficiency Channel with Conventional and Alternative Fuels in SuperCritical Water-cooled Reactor (SCWR) Applications. *Master's Dissertation, University of Ontario Institute of Technology, Oshawa, Canada.*

Pioro, I. and Duffey, R., 2007. Heat Transfer and Hydraulic Resistance at Supercritical Pressures in Power Engineering Applications, ASME Press, New York, NY, USA, 334 pages.

Pioro, I. and Kirillov, P., 2013. Current Status of Electricity Generation in the World, Chapter in the book: Materials and Processes for Energy: Communicating Current Research and Technological Developments, Energy Book Series #1, Editor: A. Méndez-Vilas, Publisher: Formatex Research Center, Spain, pp. 783-795. Free download from:

<http://www.formatex.info/energymaterialsbook/book/783-795.pdf>.

Pioro, I., Duffey, R.B., Kirillov, P.L., and Dort-Goltz, N., 2020. Current Status of Reactors Deployment and Small Modular Reactors Development in the World. *ASME J. NERS, Vol. 6, No. 4*, 24 pages. Free download from:

<https://asmedigitalcollection.asme.org/nuclearengineering/article/6/4/044001/1085654/Current-Status-of-Reactors-Deployment-and-Small>.

Pioro, I., Dort-Goltz, N., and McKellar, J., 2020. Current Status of Nuclear Power in the World Including Latest Developments on SMRs, Proc. NENE-2020, Portorož, Slovenia, Sept. 7-10, Paper 409, 10 pages. Free download from:

http://www.rcp.ijs.si/bojan/NENE2020USB/pdf/NENE2020_0409.pdf.

Pioro, I., Duffey, R.B., Kirillov, P.L., Pioro, R., 2021. Pros and Cons of Commercial Reactor Designs: Part 2- Current Status and Future Trends in the World Nuclear-Power Industry and Technical Considerations of Nuclear-Power Reactors. In: Greenspan, E. (Ed.), *Encyclopedia of Nuclear Energy Vol. 1*. Elsevier, pp. 288-303.

Pioro, I.L. and Duffey, R.B., 2003. Literature Survey of the Heat Transfer and Hydraulic Resistance of Water, Carbon Dioxide, Helium and Other Fluids at Supercritical and Near-Critical Pressures, Report AECL-12137/FFC-FCT-409, CRL AECL, April, ISSN 0067-0367, 182 pages.

Pioro, I.L., 2019. Current status of research on heat transfer in forced convection of fluids at supercritical pressures. *Nuclear Engineering and Design, Vol. 354, Article #110207*, 14 pages.

Pioro, I.L., Kirillov, P.L., Mokry, S.J. and Gospodinov, Y.K., 2010. Supercritical Water Heat Transfer in a Vertical Bare Tube: Normal, Improved and Deteriorated Regimes. *Nuclear Technology, Vol. 172, Issue 1*, 10 pages.

Playbell, I., 2017. Economy, safety, and applicability of small modular reactors. *Proceedings of the Institution of Civil Engineers-Energy, Vol. 170, Issue 2*, pp. 67-79.

Rosatom, 2020. "SMR Nuclear Power Plant To Be Built In Yakutia By 2028". <https://rusatom-overseas.com/media/news/smr-nuclear-power-plant-to-be-built-in-yakutia-by-2028.html>.

Accessed: April 3rd, 2021.

Samalova, L., Chvala, O., and Maldonado, I., 2017. Comparative economic analysis of the Integral Molten Salt Reactor and an advanced PWR using the G4-ECONS methodology. *Annals of Nuclear Engineering, Vol. 99*, pp. 258-265.

Sato, H., Uematsu, M., and Watanabe, K., 1988. New International Skeleton Tables for the Thermodynamic Properties of Ordinary Water Substance. *J. Phys. Chem. Ref. Data*, Vol. 17, Issue 4, pp. 1439-1540.

Schnurr, N.M., Sastry, V.S., and Shapiro, A.B., 1976. A Numerical Analysis of Heat Transfer to Fluids near the Thermodynamic Critical Point Including the Thermal Entrance Region, *Journal of Heat Transfer*, Transactions of the ASME, 98 (4), pp. 609-615.

Shiralkar, B.S, and Griffith, P., 1968. The Deterioration in Heat Transfer to Fluids at Super-Critical Pressure and High Heat Fluxes, Department of Mechanical Engineering, Massachusetts Institute of Technology, Report No. 70332-51, March 1, 67 pages.

SMR Start, 2017. The Economics of Small Modular Reactors. Available from:

<http://smrstart.org/wp-content/uploads/2017/09/SMR-Start-Economic-Analysis-APPROVED-2017-09-14.pdf>.

Styrikovich, M.A., Margulova, T.K., and Miropolskii, Z.L., 1967. Problems in the development of designs of supercritical boilers. *Teploenergetika*, Vol. 14, No. 6, 1967, pp. 4-7.

Swenson, H.S., Carver, J.R., and Kakarala, C.R, 1965. Heat Transfer to Supercritical Water in Smooth-Bore Tubes, *J. of Heat Transfer*, Trans. ASME Series C, 87 (4), pp. 477-484.

Tennessee Valley Authority (TVA), 2005. ABWR Cost/Schedule/COL Project at TVA's Bellefonte Site. TVA, Knoxville, TN, Document no. DE-AI07-04ID-14620.

UNDP, 2020. Human Development Report 2020. United Nations Development Programme.

Available from: <http://hdr.undp.org/en/2020-report/download>.

U.S Bureau of Labor Statistics, 2021. “CPI Inflation Calculator”

https://www.bls.gov/data/inflation_calculator.htm. Accessed: January 15, 2021.

Wagner, W. and Pruss, A., 2002. The IAPWS Formulation 1995 for the Thermodynamic Properties of Ordinary Water Substance for General and Scientific Use. *J. Phys. Chem. Ref. Data, Vol. 31, Issue 2*, pp. 387-535.

Wang, C. & Li, H., 2014. Evaluation of the Heat Transfer Correlations for Supercritical Pressure Water in Vertical Tubes. *Heat Transfer Engineering, 35:6-8*. Taylor and Francis Group, LLC. pp. 685-692.

Wang, H., Leung, L.K.H., Wang, W., Bi, Q., 2018. A review on recent heat transfer studies to supercritical pressure water in channels. *Appl. Therm. Eng.* 142, 573–596.

Wilton, E., 2012. A Conceptual Framework for the Comparison of Small Modular Reactors based on Passive Safety Features, Proliferation Resistance, and Economic Potential, *Master’s Dissertation, Utrecht University, Utrecht, Netherlands*.

World Nuclear Association, 2020a. “Generation IV Nuclear Reactors”. <https://world-nuclear.org/information-library/nuclear-fuel-cycle/nuclear-power-reactors/generation-iv-nuclear-reactors.aspx>. Accessed January 15, 2021.

World Nuclear Association, 2020b. “Economics of Nuclear Power”. <https://world-nuclear.org/information-library/nuclear-fuel-cycle/nuclear-power-reactors/generation-iv-nuclear-reactors.aspx>. Accessed January 25, 2021.

World Nuclear Association, 2020c. “Uranium Markets”. <https://www.world-nuclear.org/information-library/nuclear-fuel-cycle/uranium-resources/uranium-markets.aspx>.

Accessed January 30, 2021.

World Nuclear Association, 2021a. “Fast Neutron Reactors”. <https://world-nuclear.org/information-library/current-and-future-generation/fast-neutron-reactors.aspx>.

Accessed January 17, 2021.

World Nuclear Association, 2021b. “Plans for New Reactors Worldwide”. <https://www.world-nuclear.org/information-library/current-and-future-generation/plans-for-new-reactors-worldwide.aspx> Accessed January 17, 2021.

World Nuclear News, 2021. Construction license issued for Russia’s BREST reactor. *World Nuclear News*. <https://www.world-nuclear-news.org/Articles/Construction-licence-issued-for-Russias-BREST-react>. Accessed March 1, 2021.

Worldometer, 2021. “Countries in the world by population (2021)”. <https://www.worldometers.info/world-population/population-by-country/>. Accessed June 5, 2021.

Yamagata, K., Nishikawa, K., Hasegawa, S., Fugii, T., Yoshida, S., 1972. Forced convection heat transfer to supercritical water flowing in tubes. *Int. J. Heat and Mass Transfer*, Vol. 15, pp. 2575-2593.

Yetisir, M., et al. ,2012. “The Supersafe© Reactor: A Small Modular Pressure Tube SCWR”. *AECL Nuclear Review* , Vol. 1, No. 2, pp. 13-18.

Zahlan, H., Groeneveld, D., Tavoularis, S., 2010. Look-up table for trans-critical heat transfer. Proc. 2nd Canada-China Joint Workshop on Supercritical Water-Cooled Reactors (CCSC-2010). Canadian Nuclear Society (CNS), Toronto, Ontario, Canada.

Zahlan, H., Groeneveld, D., Tavoularis, S., Mokry, S. & Pioro, I. L., 2011. Assessment of Supercritical Heat Transfer Prediction Methods. *The 5th International Symposium, SCWR (ISSCWR-5), Vancouver, B.C., Canada, March 13-16*. pp. 1-20.

Appendix A: Collection of Global SMR Concepts

Included here is an extensive list of SMR concepts organized by country of origin presented at the NENE 2020 Conference (Pioro, Dort-Goltz, and McKellar, 2020). An explanation of the terminology used for SMR status is also provided and was developed by Pioro, . . . , Dort-Goltz (2020) based off the IAEA system (2020). A few notes regarding the definitions of the design status terms:

- Much design data is considered or labeled “proprietary” and, hence, not in the public domain. For the status of the designs, reliance on published statements and claims was needed and was subject to some interpretation. Classification was done according to the typical phases in the normal design and development evolution process. This assisted in characterizing the relative “maturity” or potential technical “feasibility”. It was recognized that some designs may have had prior development, a pause or hiatus between phases, and not all aspects in a phase may be at the same stage at the same time.
- No judgment was passed regarding the viability, development potential, and probability of demonstration success of these alternatives, which will be ultimately determined in and by the evolving national and international marketplaces and any related enabling governmental policies.
- The phases may not totally be distinct in that they continually merge, transition and may overlap as the design progresses. *A priori* it was not known if all developers even use the same terminology so this was an attempt to standardize and define the design status as far as possible to allow or enable inter-comparison.
- The degree and extent of independent reviews, safety and risk-analysis requirements, and national licensing processes will vary. The terminology and status may vary according to

whether the design is in the commercial or governmental domain, or directly or indirectly subsidized, and whether the schedule and/or demonstration cost is known or even revealed.

- The actual timing of the phases may also vary according to the market conditions, funding revenue, budget and incurred expenses, and R&D and licensing schedules.

Listed below are the design statuses used in the SMR lists and the SMRs themselves:

1. **Pre-conceptual** - Basic ideas, sketches, preliminary or scoping calculations, and possible parameter ranges, free-wheeling options in performance and costs, continual changes, objective evolution, evaluation of acceptable items or targets, competitive analyses, concept scrubbing.
2. **Conceptual** - Firm outline, optional layouts, R&D needs, design “cartoons”, range limits, performance goals and design targets set, initial physics and safety feasibility, economic and size requirements established, ‘show stoppers’ identified, outline costing, project scope defined.
3. **Basic** - Main layout, thermal limits and fuel requirements, commercial risk assessment, safety argument defined, R&D program initiated, initial CAD/CAE diagrams, system requirements specified, plant performance, and safety-analysis models, initial investment secured, documentation underway, initial independent reviews undertaken, preliminary business case made.
4. **Developmental** - Design and layout in computer or CAD/CAE format, physics and core design semi-complete, engineering analyses underway, scoping costing, potential project schedule, safety analysis underway, confirmatory R&D in progress, performance and

safety margins defined, fuel cycle and components definition, and refining of design optimization(s), commitments to proceed, milestones established.

5. **Preliminary** - Transition to formal project management, design review, uncertainties defined, layout fixed, formal change control initiated, reference parameters established, costing re-evaluated, fuel cycle, physics and thermal performance optimized, design changes subject to controls, R&D results incorporated, BOP and systems layout fixed, modules and manufacturing defined, supply chain established, bid estimate uncertainties defined, formal licensing basis established, desired build schedule established, project management structure and business controls, external independent review(s).
6. **Final/Certified** - “Frozen” design, final safety analyses completed, R&D finished, engineering work nearly complete, final documentation of design, licensing basis, and/or “certification” review underway, commercial contracts and suppliers in place, systems for QA / QC / change controls, all major construction tasks and sequence established and proven, advanced or long-lead components and manufacturing, interface agreements and integrated customer schedule in place, business model and financing established.
7. **Construction** - Authorization to proceed, site preparation completed, project management assures product delivery, overall schedule and costs known, final work breakdown schedule, on-site work underway, prototype, FOAK or “demonstration” unit, manufacturing and component delivery in progress, interface agreements refined, building and system installation, staff training and assignments, licensing finalized or only subject to final review / verification, customer acceptance criteria, commissioning and operation planned, contingency refined.

Table A-1: SMRs and S&MRs from USA (In total - 27).

Design	Output MW_{el}/th =Th.Eff., %	Type	Designers	Status	Fuel Enrichment / Cycle, years	Fuel Type
Land-based Water-cooled Reactors (In total - 5)						
NuScale	50/160=31	PWR	NuScale Power	Preliminary	<4.95% / 2	UO ₂
SMR-160	160/525=31	PWR	Holtec Int.	Preliminary	4.95% / 1.5-2	UO ₂
mPower	195/575=34	PWR	BWX Tech.	Developmental	<5% / 2	UO ₂
W-SMR	>225/800=>28	PWR	Westinghouse	Conceptual	<5% / 2	UO ₂
BWRX-300	300/-=N/A	BWR	GEH	Final	N/A / N/A	N/A
High-Temperature Gas-cooled Reactors (HTGRs) (In total - 5) (Generation-IV concepts)						
Xe-100	75/200=38	HTGR	X-energy LLC	Conceptual	15.5% / Online refueling	UCO TRISO
SC-HTGR	272/625=44	HTGR	Framatome Inc.	Conceptual	<20% / ½ core replaced every 1.5 years	UCO TRISO particle fuel
Prismatic HTR	150/350=42.8	HTGR	General Atomics	Developmental	15.5% / 1.5	TRISO-coated UCO
MMR	5/15=33.3	HTGR	USNC	Preliminary	N/A / Never	FCM
HOLOS	3-13/22=13.6-59.0	HTGR	HolosGen	Preliminary	15% / 3.5-8	TRISO
Fast-Neutron-Spectrum Reactors (In total - 9) (Generation-IV concepts)						
SUPERSTAR	120/300=40	LMFR	ANL	Conceptual	<12% / 15	Particle fuel U-Pu-Zr
EM ²	265/500=53	GMFR	General Atomics	Conceptual	14.5% LEU / 30	UC
WLFR	>450(Net)/950=>47	LFR	Westinghouse	Conceptual	≤19.75% / ≥2	Oxide
AFR-100	100/250=40	LMFR	ANL	Conceptual	13.5% / N/A	U-Zr
ARC-100	100/260=38.5	LMFR	ARC	Final	N/A / 20	LEU
Gen4 Module	25/70=35.7	LMFR	Gen4 Energy Inc.	Conceptual	19.75% / 10	UN
PRISM	311/500=62	LMFR	GE-Hitachi	Preliminary	N/A / 1.33	U-Pu_Zr metal

Design	Output MW _{el/th} =Th.Eff., %	Type	Designers	Status	Fuel Enrichment / Cycle, years	Fuel Type
ENHS	50/125=40	LFR	UC Berkeley	Conceptual	13% (U-Zr) / N/A	Pu-U/ U-Zr
TWR-P	600/1475=41	SFR	TerraPower	Conceptual	N/A / 1.5-2	U-Zr10% MF
Molten Salt Reactors (In total - 6) (Generation-IV concepts)						
MCSFR	50/100=50	MSR	Elysium Industries	Conceptual	10%-20% / online refuel.	Molten salt fuel
Mk1 PB-FHR	100/236=42	MSR	University of CA, Berkeley	Pre-Conceptual	19.9% / 2.1 months for fuel core residence time	TRISO particles
LFTR	250/600=42	MSR	Flibe Energy	Conceptual	N/A / cont. refueling	LiF-BeF ₂ -UF ₄
KP-FHR	140/311=45	MSR	Kairos Power	Developmental	19.75% / Online	TRISO particles
MCFR	N/A/N/A=N/A	MSR	TerraPower	Developmental	N/A / Online	N/A
SmAHTR	50/125=40	MSR	ORNL	Conceptual	19.75% / N/A	TRISO particles
Heat Pipes (HPs) Reactors (In total - 2)						
Aurora	1.5/N/A=N/A	HPs	Oklo	Preliminary	<20% / N/A	HALEU -U-Zr
eVinci	0.2-15/0.6-40=33-38	HPs	Westinghouse	Developmental	19.5% / 10	UO ₂ or UN

Table A-2: SMRs and S&MRs from Russia (In total - 16).

Design	Output MW _{el/th} =Th.Eff., %	Type	Designers	Status	Fuel Enrich. / Cycle, years	Fuel Type
Land-based Water-cooled Reactors (In total - 6)						
ELENA	0.068/3.3=2	PWR	Kurchatov Inst.	Conceptual	15.2% / 25	UO ₂ (MOX)
UNITERM	6.6/30=22	PWR	NIKIET	Conceptual	19.75% / 16.7	UO ₂
RUTA-70	-/70=N/A	PWR	NIKIET	Conceptual	3% / 3	Cermet
KARAT-45	45-50/180=25-28	BWR	NIKIET	Conceptual	4.5% / 7	UO ₂
KARAT-100	100/360=28	BWR	NIKIET	Conceptual	4% / 7.5	UO ₂

Design	Output MW _{el/th} =Th.Eff., %	Type	Designers	Status	Fuel Enrich. / Cycle, years	Fuel Type
VK-300	250/750=33	BWR	NIKIET	Final	4% / 6	UO ₂
Marine-based Water-cooled Reactors (In total - 5)						
SHELF	6.6/28.4=23	Immersed NPP	NIKIET	Preliminary	19.7% / 6	UO ₂
ABV-6E	6-9/38=16-24	Floating PWR	OKBM Afrikantov	Final	<20% / 10-12	UO ₂
KLT-40S	35/150=23	Floating PWR	OKBM Afrikantov	Operating	18.6% / 2.5-3	UO ₂
RITM-200M	50/175=29	Floating PWR	OKBM Afrikantov	Construction	<20% / 10	UO ₂
VBER-300	325/917=35	Floating NPP	OKBM Afrikantov	Final	4.95% / 6	UO ₂
High-Temperature Gas-cooled Reactors (HTGRs) (In total - 3) (Generation-IV concepts)						
MHR-100	25-87/215=12-41	HTGR	OKBM Afrikantov	Conceptual	LEU<20% / N/A	Coated particle fuel
MHR-T	4×205.5/4×600=34	HTGR	OKBM Afrikantov	Conceptual	20% / 2.5	Coated particle fuel
GT-MHR	288/600=48	HTGR	OKBM Afrikantov	Preliminary	LEU or WPu / 2.1	Coated particle fuel
Fast-Neutron-Spectrum Reactors (In total - 2) (Generation-IV concepts)						
SVBR-100	100/280=36	LMFR	JSC AKME Eng.	Final	<19.3% / 0.58-0.67	UO ₂
BREST-OD-300	300/700=43	LMFR	NIKIET	Final	13.5% / 2.46-4.1	U-Pu-N

Table A-3: SMRs and S&MRs from China (In total - 13).

Design	Output MW _{el/th} =Th.Eff., %	Type	Designers	Status	Fuel Enrich./ Cycle, years	Fuel Type
Land-based Water-cooled Reactors (7 SMRs)						
ACP100	125/385=33	PWR	CNNC	Basic	<4.95% / 2	UO ₂
DHR400	-/400=N/A	LWR	CNNC	Basic	<5.0% / 0.8	UO ₂
CAP200	>200/600=>30.3	PWR	CGNPC	Conceptual	4.2% / 2	UO ₂

Design	Output MW _{el/th} =Th.Eff., %	Type	Designers	Status	Fuel Enrich./ Cycle, years	Fuel Type
CNP-300	300- 340/1000=30-34	PWR	CNNC	Conceptual	<5% / N/A	UO ₂
SNP350	350/1035=33.8	PWR	SNERDI	Preliminary	N/A / N/A	N/A
NHR-200II	-/200=N/A	PWR	INET	Final	<5% / N/A	UO ₂
HAPPY200	-/200=N/A	PWR	SPIC	Final	N/A / N/A	N/A
Marine-based Water-cooled Reactor (In total - 1)						
ACPR50S	50/200=25	PWR	CGNPC	Preliminary	<5% / 2.5	UO ₂
High-Temperature Gas-cooled Reactor (HTGR) (In total - 2) (Generation-IV concept)						
HTR-10	2.5/10=25	HTGR	Tsinghua University/INET	Operational	17%/On- line	Spherical El. With TRISO particles fuel
HTR-PM	210/2×250=42	HTGR	INET, Tsinghua University	Construction	8.5% / On-line refueling	Spherical El. with coated particle fuel
Fast-Neutron-Spectrum Reactor (In total - 1) (Generation-IV concepts)						
CFR-600	600/1500=40	LMFR	CNNC	Construction	N/A / N/A	UO ₂ /MOX
Molten Salt Reactor (In total - 2) (Generation-IV concept)						
smTMSR- 400	168/400=42	MSR	SINAP, CAS	Pre- conceptual	19.75%/10 years	LiF-BeF ₂ - UF ₄ -ThF ₄ fuel salt
TMSR-LF	168/373=45	MSR	SINAP	Conceptual	19.75% / Online	LiF-BeF ₂ - UF ₄ -ThF ₄ , LiF-BeF ₂ - PuF ₃ -ThF ₄

Table A-4: SMRs and S&MRs from Japan (In total - 12).

Design	Output MW _{el/th} =Th.Eff., %	Type	Designers	Status	Fuel Enrichment/ Cycle, years	Fuel Type
Land-based Water-cooled Reactors (In total - 4)						
DMS	300/840=36	BWR	Hitachi- GE	Basic	<5% / 2	UO ₂
IMR	350/1000=35	PWR	MHI	Conceptual	4.8% / 2.2	UO ₂
CCR	423/1268=33.4	BWR	Toshiba Corp.	Conceptual	N/A / 2	N/A
MRX	33.3/100=33.3	PWR	JAERI	Final	4.3% / 3.5	UO ₂

Design	Output MW _{el/th} =Th.Eff., %	Type	Designers	Status	Fuel Enrichment/ Cycle, years	Fuel Type
High-Temperature Gas-cooled Reactor (HTGR) (In total - 2) (Generation-IV concept)						
GTHTR300	100- 300/<600=17- 50	HTGR	JAEA	Basic	14% / 4	UO ₂
HTTR	-/30=N/A	HTGR	JAEA	Operational	3-10 (6 avg)%/660 EFPD	UO ₂ TRISO ceramic coated particle
Fast-Neutron-Spectrum Reactors (In total - 4) (Generation-IV concept)						
4S	10/30=33	LMFR	Toshiba Corp.	Developmental	<20% / N/A	Metal fuel (U- Zr)
LSPR	53/150=35.3	LMFR	Tokyo Tech.	Developmental	10-12.5% / 12	U-Pu- N/U-Pu- Zr
PBWFR- 150	150/450=33.3	LMFR	Tokyo Tech.	Developmental	N/A / 10	U-Pu itride
Rapid-L	0.2/5=4	LMFR	CRIEPI	Operating	40% / 10	UN
Molten Salt Reactor (In total - 1) (Generation-IV concept)						
FUJI	200/450=44	MSR	Int. Thorium Molten- Salt Forum	Pre-conceptual	2.0% Pu or LEU (continuous operation is possible) / N/A	Molten salt with Th & U
Heat Pipe Reactor (In total - 1)						
MoveluX	N/A/10=N/A	Heat Pipes	Toshiba	Preliminary	4.99% / N/A	LEU

Table A-5: SMRs and S&MRs from Canada (In total - 6)

Design	Output MW _{el/th} =Th.Eff., %	Type	Designers	Status	Fuel Enrichment/ Cycle, years	Fuel Type
Land-based Water-cooled Reactor (In total - 2) (Generation-IV concept)						
CANDU SMR	300/960= 31.25	PHWR	Candu Energy Inc.	Conceptual	-/On-line	UO ₂
SSR	300/667= 45	SCWR	AECL	Conceptual	Enriched / N/A	U or Th
High-Temperature Gas-cooled Reactor (HTGRs) (In total - 1) (Generation-IV concept)						
Starcore SMR	20/36=55. 6	HTGR	Starcore	Preliminary	N/A / 5	TRI SO

Design	Output MW _{el/th} =Th.Eff., %	Type	Designers	Status	Fuel Enrichment/ Cycle, years	Fuel Type
Molten Salt Reactors (In total - 2) (Generation-IV concept)						
IMSR	190/400= 48	MSR	Terrestrial Energy	Basic	<5% / 7 years before core-unit replacement	MSF
MCSFR	50/100=5 0	MSR	Elysium Industries	Conceptual	10%-20% / online refueling	MSF
Other Reactor (In total - 1)						
Leadir- PS100	36/100=3 6	LMR	Northern Nuclear Industries	Conceptual	N/A/N/A	TRI SO

Table A-6: SMRs and S&MRs from France (5 designs).

Design	Output MW _{el/th} =Th.Eff., %	Type	Designers	Status	Fuel Enrichment/ Cycle, years	Fuel Type
Land-based Water-cooled Reactor (In total - 1)						
Nuward	300-400/- =N/A	PWR	CEA, EDF, Naval Group, TechnicAtome	Preliminary	N/A / N/A	N/A
Marine-based Water-cooled Reactor (In total - 1)						
Flexblue	160/600=26.7	PWR	DCNS	Preliminary	<5% / 3	UO ₂
High-Temperature Gas-cooled Reactors (HTGRs) (In total - 2) (Generation-IV concept)						
Allegro	-/50- 100=N/A	HTGR	CEA	Conceptual	N/A / N/A	MOX
ANTARES	-/≥600=N/A	HTGR	Areva	Conceptual	N/A / N/A	N/A
Fast-Neutron-Spectrum Reactor (In total - 1) (Generation-IV concept)						
ASTRID	600/1500=40	SFR	CEA	Preliminary	N/A / N/A	MOX

Table A-7: SMRs and S&MRs from Korea S. (In total - 5).

Design	Output MW _{el/th} =Th.Eff., %	Type	Designers	Status	Fuel Enrich. / Cycle, years	Fuel Type
Land-based Water-cooled Reactor (In total - 1)						
SMART	100/330=30	PWR	KAERI	Certified	<5% / 3	UO ₂
Fast-Neutron-Spectrum Reactors (In total - 4) (Generation-IV concept)						
KALIMER-600	600/1523.4= 39.4	LMFR	KAERI	Preliminary	N/A / 1	U- TRU -Zr
PGSFR	150/400=37. 5	SFR	KAERI	Preliminary	N/A / ~1	U- TRU -Zr

Design	Output MW _{el/th} =Th.Eff., %	Type	Designers	Status	Fuel Enrich. / Cycle, years	Fuel Type
PEACER	300/850=35	LMFR	Seoul National University	Conceptual	N/A / 1	U- TRU -Zr
MicroURANUS	20/60=33.3	LMFR	UNIST	Pre- Conceptual	8,10,12%/N /A	UO ₂

Table A-8: SMRs and S&MRs from Africa S. (In total - 4)

Design	Output MW _{el/th} =Th.Eff., %	Type	Designers	Status	Fuel Enrich./ Cycle, years	Fuel Type
High-Temperature Gas-cooled Reactors (HTGRs) (In total - 4) (Generation-IV concept)						
HTMR-100	35/100=35	HTGR	Steenkampskraal Thorium Ltd.	Conceptual	10%-93% / Online refueling	LEU, Th/LEU, Th/HEU, Th/Pu
A-HTR-100	50/100=50	HTGR	Eskom Holdings SOC Ltd.	Conceptual	LEU or WPu / N/A	Coated particle fuel
PBMR-400	165/400=41.3	HTGR	PBMR SOC Ltd.	Preliminary	9.6% LEU or WPu / N/A	Coated particle fuel
PBMR-100	100/250=40	HTGR	PBMR SOC Ltd.	Preliminary	N/A / Online	TRISO- coated UP ₂

Table A-9: SMRs and S&MRs from UK (In total - 4)

Design	Output MW _{el/th} =Th.Eff., %	Type	Designers	Status	Fuel Enrichment/ Cycle, years	Fuel Type
Land-based Water-cooled Reactor (In total - 1)						
UK-SMR	443/1276=26	PWR	Rolls-Royce	Final	<5% / 1.5-2	UO ₂
High-Temperature Gas-cooled Reactor (HTGR) (In total - 1) (Generation-IV concept)						
U-Battery	4/10=40	HTGR	URENCO	Preliminary	17-20% / 5	TRISO
Molten Salt Reactors (In total - 2) (Generation-IV concept)						
Stable Salt Reactor-Wasteburner	300 (continuous as baseload)/750 =40	MSR	Moltex Energy	Conceptual	Reactor grade Pu / 12.5	MSF
Stable Salt Reactor - Th. Spectrum	300 (baseload)/750 =40	MSR	Moltex Energy	Pre-Conceptual	5% / 2	MSF

Table A-10: SMRs and S&MRs from Denmark (In total - 3).

Design	Output MW _{el/th} =Th.Eff., %	Type	Designers	Status	Fuel Enrich. / Cycle, years	Fuel Type
Molten Salt Reactors (In total - 3) (Generation-IV concept)						
CA Waste Burner	20/50=40	MSR	Copenhagen Atomics	Conceptual	N/A / N/A	LiF-ThF ₄
CA Waste Burner	-/100=N/A	MSR	Copenhagen Atomics	Conceptual	N/A/ Continuous	LiF-ThF ₄
CMSR	100-115/250 =40-46	MSR	Seaborg Technologies	Conceptual	Pre-processed SNF (U 1.1% fissile, Pu 69% fissile) / 60	Na-actinide fluoride (93% Th, 3.5% U, 3.5% Pu)

Table A-11: SMRs and S&MRs from Czech Republic (In total -2).

Design	Output $MW_{el/th}$ =Th.Eff., %	Type	Designers	Status	Fuel Enrichment/ Cycle, years	Fuel Type
Land-based Water-cooled Reactors (In total - 2)						
TEPLATOR	- /50=N/A	HWR	UWB Pilsen & CIRC CTU	Conceptual	<1.2% / 0.83	Spent VVER-400 fuel
Molten Salt Reactors (In total -1) (Generation-IV concept)						
Energy Well	8/20=40	MSR	Centrum vyzkumu Rez	Pre- Conceptual	<20% / 7	TRISO

Table A-12: SMRs and S&MRs from India (In total - 2)

Design	Output $MW_{el/th}$ =Th.Eff., %	Type	Designers	Status	Fuel Enrichment/ Cycle, years	Fuel Type
Land-based Water-cooled Reactors (In total - 2)						
AHWR- 300-LEU	304/920=33	PHWR	BARC	Conceptual	<5% (MOX) / Continuous	Th-U or Th- Pu, MOX
PHWR- 220	235/755=31.2	PHWR	NPCI Ltd.	16 Operational Units	<5% / Continuous	UO ₂

Table A-13: SMRs and S&MRs from Italy (In total - 2)

Design	Output $MW_{el/th}$ =Th.Eff., %	Type	Designers	Status	Fuel Enrichment/ Cycle, years	Fuel Type
Fast-Neutron-Spectrum Reactors (In total - 2) (Generation-IV concept)						
ALFRED	125/300=41.7	LFR	Ansaldo	Preliminary	N/A/ 5	MOX
ELFR	630/1500=42	LFR	Ansaldo	Conceptual	N/A/ 2.5	MOX

Table A-14: SMRs and S&MRs from Luxembourg (In total - 2)

Design	Output MW _{el/th} =Th.Eff., %	Type	Designers	Status	Fuel Enrichment/ Cycle, years	Fuel Type
Fast-Neutron-Spectrum Reactors (In total - 2) (Generation-IV concept)						
LFR- TL-X	5/15=33 10/30=33 20/60=33	LFR	Hydromine Nuclear Energy	Conceptual	19.8% / ≥8.33	LEU
LFR- AS-200	200/480=42	LFR		Preliminary	14.6%-20.4%-23.2% in Pu / 6.7 years for 5 batches	MOX

Table A-15: SMRs and S&MRs from Argentina (In total - 1)

Design	Output MW _{el/th} =Th.Eff., %	Type	Designers	Status	Fuel Enrichment/ Cycle, years	Fuel Type
Land-based Water-cooled Reactor (In total - 1)						
CAREM	30/100=30	PWR	CNEA	Construction	3.1%/1.2	UO ₂

Table A-16: SMRs and S&MRs from Brazil (In total - 1)

Design	Output MW _{el/th} =Th.Eff., %	Type	Designers	Status	Fuel Enrichment/ Cycle, years	Fuel Type
Land-based Water-cooled Reactor (In total - 1)						
FBNR	70/134=52.2	PWR	Federal University of Rio Grande do Sul	Conceptual	N/A/N/A	TRISO

Table A-17: SMRs and S&MRs from Indonesia (In total -1).

Design	Output MW _{el/th} =Th.Eff., %	Type	Designers	Status	Fuel Enrichment/ Cycle, years	Fuel Type
High-Temperature Gas-cooled Reactor (HTGR) (In total - 1) (Generation-IV concept)						
RDE/Micro- PeLUt	3/10=30	HTGR	BATAN	Preliminary	17% / On-line	Coated particle fuel

Table A-18: SMRs and S&MRs from Sweden (1 design)

Design	Output MW _{el/th} =Th.Eff., %	Type	Designers	Status	Fuel Enrichment/ Cycle, years	Fuel Type
Fast-Neutron-Spectrum Reactor (In total - 1) (Generation-IV concept)						
SEALER	3/8=38	Lead Cooled	LeadCold	Conceptual	19.75% / 27 full power years	UO ₂

Appendix B: Full Formulations of REFPROP v.10 Theoretical Models

B.1: Dimensionless Helmholtz Energy¹⁰

$$\phi^o(\delta, \tau) = \ln \delta + n_1^0 + n_2^0 \tau + n_3^0 \ln \tau + \sum_{i=4}^8 n_i^0 \ln [1 - e^{-\gamma_i^0 \tau}] \quad \text{B-1}$$

$$\begin{aligned} \phi^r(\delta, \tau) = & \sum_{i=1}^7 n_i \delta^{d_i} \tau^{t_i} + \sum_{i=8}^{51} n_i \delta^{d_i} \tau^{t_i} e^{-\delta c_i} \\ & + \sum_{i=52}^{54} n_i \delta^{d_i} \tau^{t_i} e^{-\alpha_i(\delta-\varepsilon_i)^2 - \beta_i(\tau-\gamma_i)^2} + \sum_{i=55}^{56} n_i \Delta^{b_i} \delta \psi \end{aligned} \quad \text{B-2}$$

$$\Delta = \theta^2 + B_i [(\delta - 1)^2]^{a_i} \quad \text{B-3}$$

$$\theta = (1 - \tau) + A_i [(\delta - 1)^2]^{\frac{1}{2\beta_i}} \quad \text{B-4}$$

$$\psi = e^{-C_i(\delta-1)^2 - D_i(\tau-1)^2} \quad \text{B-5}$$

Table B-1: Coefficients for Equations B-1.

i	n_i^0	γ_i^0	i	n_i^0	γ_i^0
1	-8.3204464837497	-	5	0.97315	3.53734222
2	6.6832105275932	-	6	1.27960	7.74073708
3	3.00632	-	7	0.96956	9.24437796
4	0.012436	1.28728967	8	0.24873	27.5075105

Table B-2: Coefficients for Equations B-2 – B-5.

i	c_i	d_i	t_i	n_i
1	-	1	-0.5	$0.12533547935523 \times 10^{-1}$
2	-	1	0.875	$0.78957634722828 \times 10^1$
3	-	1	1	$-0.87803203303561 \times 10^1$
4	-	2	0.5	0.31802509345418

¹⁰ All information contained within was presented in Wagner and Pruss (2002) but taken from IAPWS (2018)

i	c_i	d_i	t_i	n_i
5	-	2	0.75	-0.26145533859358
6	-	3	0.375	-0.78199751687981×10 ⁻²
7	-	4	1	0.88089493102134×10 ⁻²
8	1	1	4	-0.66856572307965
9	1	1	6	0.20433810950965
10	1	1	12	-0.66212605039687×10 ⁻⁴
11	1	2	1	-0.19232721156002
12	1	2	5	-0.25709043003438
13	1	3	4	0.16074868486251
14	1	4	2	-0.40092828925807×10 ⁻¹
15	1	4	13	0.39343422603254×10 ⁻⁶
16	1	5	9	-0.75941377088144×10 ⁻⁵
17	1	7	3	0.56250979351888 ×10 ⁻³
18	1	9	4	-0.15608652257135×10 ⁻⁴
19	1	10	11	0.11537996422951 × 10 ⁻⁸
20	1	11	4	0.36582165144204×10 ⁻⁶
21	1	13	13	-0.13251180074668×10 ⁻¹¹
22	1	15	1	-0.62639586912454×10 ⁻⁹
23	2	1	7	-0.10793600908932
24	2	2	1	-0.17611491008752×10 ⁻¹
25	2	2	9	0.22132295167546
26	2	2	10	-0.40247669763528
27	2	3	10	0.58983399985759
28	2	4	3	0.49969146990806×10 ⁻²
29	2	4	7	-0.31358700712549×10 ⁻¹
30	2	4	10	-0.74315929710341
31	2	5	10	0.47807329915480
32	2	6	6	0.20527940895948×10 ⁻¹
33	2	6	10	-0.13636435110343
34	2	7	10	0.14180634400617×10 ⁻¹
35	2	9	1	0.83326504880713×10 ⁻²
36	2	9	2	-0.29052336009585×10 ⁻¹
37	2	9	3	0.38615085574206×10 ⁻¹
38	2	9	4	-0.20393486513704×10 ⁻¹
39	2	9	8	-0.16554050063734×10 ⁻²
40	2	10	6	0.19955571979541×10 ⁻²
41	2	10	9	0.15870308324157×10 ⁻³
42	2	12	8	-0.16388568342530×10 ⁻⁴
43	3	3	16	0.43613615723811×10 ⁻¹
44	3	4	22	0.34994005463765×10 ⁻¹
45	3	4	23	-0.76788197844621×10 ⁻¹
46	3	5	23	0.22446277332006×10 ⁻¹
47	4	14	10	-0.62689710414685×10 ⁻⁴
48	6	3	50	-0.55711118565645×10 ⁻⁹

i	c_i	d_i	t_i	n_i				
49	6	6	44	-0.199905718354408				
50	6	6	46	0.31777497330738				
51	6	6	50	-0.11841182425981				
i	c_i	d_i	t_i	n_i	α_i	β_i	γ_i	ε_i
52	-	3	0	-0.31306260323435×10 ²	20	150	1.21	1
53	-	3	1	0.31546140237781×10 ²	20	150	1.21	1
54	-	3	4	-0.25213154341695×10 ⁴	20	250	1.25	1
i	a_i	b_i	B_i	n_i	C_i	D_i	A_i	β_i
55	3.5	0.85	0.2	-0.14874640856724	28	700	0.32	0.3
56	3.5	0.95	0.2	0.31806110878444	32	800	0.32	0.3

$$\phi_{\tau}^o = n_2^0 + \frac{n_3^0}{\tau} + \sum_{i=4}^8 n_i^0 \gamma_i^0 \left[\left(1 - e^{-\gamma_i^0 \tau}\right)^{-1} - 1 \right] \quad \text{B-6}$$

$$\begin{aligned} \phi_{\tau}^r = & \sum_{i=1}^7 n_i t_i \delta^{d_i} \tau^{t_i-1} + \sum_{i=8}^{51} n_i t_i \delta^{d_i} \tau^{t_i-1} e^{-\delta c_i} \\ & + \sum_{i=52}^{54} n_i \delta^{d_i} \tau^{t_i} e^{-\alpha_i(\delta-\varepsilon_i)^2 - \beta_i(\tau-\gamma_i)^2} \left[\frac{t_i}{\tau} - 2\beta_i(\tau - \gamma_i) \right] \\ & + \sum_{i=55}^{56} n_i \delta \left[\frac{\partial \Delta^{b_i}}{\partial \tau} \psi + \Delta^{b_i} \frac{\partial \psi}{\partial \tau} \right] \end{aligned} \quad \text{B-7}$$

$$\begin{aligned} \phi_{\delta}^r = & \sum_{i=1}^7 n_i d_i \delta^{d_i-1} \tau^{t_i} + \sum_{i=8}^{51} n_i e^{-\delta c_i} [\delta^{d_i-1} \tau^{t_i} (d_i - c_i \delta^{c_i})] \\ & + \sum_{i=52}^{54} n_i \delta^{d_i} \tau^{t_i} e^{-\alpha_i(\delta-\varepsilon_i)^2 - \beta_i(\tau-\gamma_i)^2} \left[\frac{d_i}{\delta} - 2\alpha_i(\delta - \varepsilon_i) \right] \\ & + \sum_{i=55}^{56} n_i \left[\frac{\partial \Delta^{b_i}}{\partial \delta} \delta \psi + \Delta^{b_i} \left(\psi + \delta \frac{\partial \psi}{\partial \delta} \right) \right] \end{aligned} \quad \text{B-8}$$

$$\phi_{\tau\tau}^o = -\frac{n_3^0}{\tau^2} - \sum_{i=4}^8 n_i^0 (\gamma_i^0)^2 e^{-\gamma_i^0 \tau} (1 - e^{-\gamma_i^0 \tau})^{-2} \quad \mathbf{B-9}$$

$$\begin{aligned} \phi_{\tau\tau}^r &= \sum_{i=1}^7 n_i t_i (t_i - 1) \delta^{d_i \tau t_i - 2} + \sum_{i=8}^{51} n_i t_i (t_i - 1) \delta^{d_i \tau t_i - 2} e^{-\delta^{c_i}} \\ &+ \sum_{i=52}^{54} n_i \delta^{d_i \tau t_i} e^{-\alpha_i (\delta - \varepsilon_i)^2 - \beta_i (\tau - \gamma_i)^2} \left[\left(\frac{t_i}{\tau} - 2\beta_i (\tau - \gamma_i) \right)^2 - \frac{t_i}{\tau^2} - 2\beta_i \right] \\ &+ \sum_{i=55}^{56} n_i \delta \left[\frac{\partial^2 \Delta^{b_i}}{\partial \tau^2} \psi + 2 \frac{\partial \Delta^{b_i}}{\partial \tau} \frac{\partial \psi}{\partial \tau} + \Delta^{b_i} \frac{\partial^2 \psi}{\partial \tau^2} \right] \end{aligned} \quad \mathbf{B-10}$$

$$\begin{aligned} \phi_{\delta\delta}^r &= \sum_{i=1}^7 n_i d_i (d_i - 1) \delta^{d_i - 2 \tau t_i} \\ &+ \sum_{i=8}^{51} n_i e^{-\delta^{c_i}} [\delta^{d_i - 2 \tau t_i} ((d_i - c_i \delta^{c_i})(d_i - 1 - c_i \delta^{c_i}) - c_i^2 \delta^{c_i})] \\ &+ \sum_{i=52}^{54} n_i \tau^{t_i} e^{-\alpha_i (\delta - \varepsilon_i)^2 - \beta_i (\tau - \gamma_i)^2} [-2\alpha_i \delta^{d_i} + 4\alpha_i^2 \delta^{d_i} (\delta - \varepsilon_i)^2 \\ &- 4d_i \alpha_i \delta^{d_i - 1} (\delta - \varepsilon_i) + d_i (d_i - 1) \delta^{d_i - 2}] \\ &+ \sum_{i=55}^{56} n_i \left[\frac{\partial^2 \Delta^{b_i}}{\partial \delta^2} \delta \psi + 2 \frac{\partial \Delta^{b_i}}{\partial \delta} \left(\psi + \delta \frac{\partial \psi}{\partial \delta} \right) + \Delta^{b_i} \left(2 \frac{\partial \psi}{\partial \delta} + \delta \frac{\partial^2 \psi}{\partial \delta^2} \right) \right] \end{aligned} \quad \mathbf{B-11}$$

$$\begin{aligned}
\phi_{\delta\tau}^r = & \sum_{i=1}^7 n_i d_i t_i \delta^{d_i-1} \tau^{t_i-1} + \sum_{i=8}^{51} n_i t_i e^{-\delta^{c_i}} [\delta^{d_i-1} \tau^{t_i-1} (d_i - c_i \delta^{c_i})] + \\
& \sum_{i=52}^{54} n_i \delta^{d_i} \tau^{t_i} e^{-\alpha_i(\delta-\varepsilon_i)^2 - \beta_i(\tau-\gamma_i)^2} \left[\frac{d_i}{\delta} - 2\alpha_i(\delta - \varepsilon_i) \right] \left[\frac{t_i}{\tau} - 2\beta_i(\tau - \gamma_i) \right] + \\
& \sum_{i=55}^{56} n_i \left[\frac{\partial^2 \Delta^{b_i}}{\partial \delta \partial \tau} \delta \psi + \delta \frac{\partial \Delta^{b_i}}{\partial \delta} \frac{\partial \psi}{\partial \tau} + \frac{\partial \Delta^{b_i}}{\partial \tau} \left(\psi + \delta \frac{\partial \psi}{\partial \delta} \right) + \Delta^{b_i} \left(\frac{\partial \psi}{\partial \tau} + \delta \frac{\partial^2 \psi}{\partial \delta \partial \tau} \right) \right]
\end{aligned} \tag{B-12}$$

B.2: Thermal Conductivity¹¹

$$\bar{\lambda}_0(\bar{T}) = \frac{\sqrt{\bar{T}}}{\sum_{k=0}^4 \frac{L_k}{\bar{T}^k}} \tag{B-13}$$

Table B-3: Values for L_k in Equation B-13.

k	L_k
0	2.443221×10^{-3}
1	1.323095×10^{-2}
2	6.770357×10^{-3}
3	-3.454586×10^{-3}
4	4.096266×10^{-4}

$$\bar{\lambda}_1(\bar{T}, \bar{\rho}) = \exp \left[\bar{\rho} \sum_{i=0}^4 \left(\left(\frac{1}{\bar{T}} - 1 \right)^i \sum_{j=0}^5 L_{ij} (\bar{\rho} - 1)^j \right) \right] \tag{B-14}$$

Table B-4: Values for L_{ij} in Equation B-14

j \ i	0	1	2	3	4	5
0	1.6039735 7	-0.6460135 23	0.111443906	0.102997357	-0.05041236 34	0.0060985925 8
1	2.3377184 2	-2.7884377 8	1.53616167	-0.4630455 12	0.083282701 9	-0.007192012 45
2	2.1965052 9	-4.5458078 5	3.55777244	-1.4094497 8	0.275418278	-0.020593881 6
3	-1.210137 8	1.60812989	-0.6211781 41	0.071637322 4	0	0
4	-2.720337 0	4.57586331	-3.1836924 5	1.1168348	-0.19268305	0.012913842

¹¹ All information contained within was presented in Huber et al. (2012) but was taken from IAPWS (2011).

$$\bar{\lambda}_2(\bar{T}, \bar{\rho}) = \Lambda \frac{\bar{\rho} c_p \bar{T}}{\bar{\mu} R} Z(y) \quad \text{B-15}$$

$$Z(y) = \frac{2}{\pi y} \left\{ [(1 - \kappa^{-1}) \tan^{-1} y + \kappa^{-1} y] - \left[1 - \exp\left(\frac{-1}{y^{-1} + \frac{y^2}{3\bar{\rho}^2}}\right) \right] \right\}$$

$$= 0, \quad y < 1.2 \times 10^{-7} \quad \text{B-16}$$

$$\kappa = \frac{c_p}{c_v} \quad \text{B-17}$$

$$y = \bar{q}_D \xi(\bar{T}, \bar{\rho}) \quad \text{B-18}$$

$$\xi(\bar{T}, \bar{\rho}) = \xi_0 \left(\frac{\Delta \bar{\chi}}{\Gamma_0} \right)^{\nu/\gamma} \quad \text{B-19}$$

$$\Delta \bar{\chi}(\bar{T}, \bar{\rho}) = \bar{\rho} \left[\zeta(\bar{T}, \bar{\rho}) - \zeta(\bar{T}_R, \bar{\rho}) \frac{\bar{T}_R}{\bar{T}} \right]$$

$$= 0, \quad \Delta \bar{\chi}(\bar{T}, \bar{\rho}) < 0 \quad \text{B-20}$$

$$\zeta = \left(\frac{\partial \bar{\rho}}{\partial \bar{p}} \right)_{\bar{T}} \quad \text{B-21}$$

Table B-5: Values for constants used in Equations B-15 – B-21.

Constant	Value
Λ	177.8514
\bar{q}_D^{-1}	0.40 nm

Constant	Value
ν	0.630
γ	1.239
ξ_0	0.13 nm
Γ_0	0.06
\bar{T}_R	1.5

B.3: Dynamic Viscosity¹²

$$\bar{\mu}_0(\bar{T}) = \frac{100\sqrt{\bar{T}}}{\sum_{i=0}^3 \frac{H_i}{\bar{T}^i}} \quad \text{B-22}$$

Table B-6: Values for H_i in Equation B-22.

i	H_i
0	1.67752
1	2.20462
2	0.6366564
3	-0.241605

$$\bar{\mu}_1(\bar{T}, \bar{\rho}) = \exp \left[\bar{\rho} \sum_{i=0}^5 \left(\left(\frac{1}{\bar{T}} - 1 \right)^i \sum_{j=0}^6 H_{ij} (\bar{\rho} - 1)^j \right) \right] \quad \text{B-23}$$

Table B-7: Values for H_{ij} coefficient in Equation B-23. Index combinations not listed are identically zero.

i	j	H_{ij}
0	0	5.20094×10^{-1}
1	0	8.50895×10^{-2}
2	0	-1.08374
3	0	-2.89555×10^{-1}
0	1	2.22531×10^{-1}
1	1	9.99115×10^{-1}
2	1	1.88797
3	1	1.26613
5	1	1.20573×10^{-1}
0	2	-2.81378×10^{-1}
1	2	-9.06851×10^{-1}
2	2	-7.72479×10^{-1}
3	2	-4.89837×10^{-1}
4	2	-2.57040×10^{-1}
0	3	1.61913×10^{-1}

¹² All information contained in this section was presented in Huber et al., (2009) but taken from IAPWS (2008).

i	j	H_{ij}
1	3	2.57399×10 ⁻¹
0	4	-3.25372×10 ⁻²
3	4	6.98452×10 ⁻²
4	5	8.72102×10 ⁻³
3	6	-4.35673×10 ⁻³
5	6	-5.93264×10 ⁻⁴

$$\bar{\mu}_2(\bar{T}, \bar{\rho}) = \exp(x_\mu Y) \quad \text{B-24}$$

$$Y = \frac{1}{5} q_c \xi (q_D \xi)^5 \left(1 - q_c \xi + (q_c \xi)^2 - \frac{765}{504} (q_D \xi)^2 \right), 0 \leq \xi \leq 0.3817016416 \text{ nm} \quad \text{B-25}$$

$$Y = \frac{1}{12} \sin 3\psi_D - \frac{1}{4q_c \xi} \sin 2\psi_D + \frac{1}{(q_c \xi)^2} \left[1 - \frac{5}{4} (q_c \xi)^2 \right] \sin \psi_D$$

$$- \frac{1}{(q_c \xi)^3} \left[1 - \frac{3}{2} (q_c \xi)^2 \right] \psi_D - |(q_c \xi)^2 - 1|^{\frac{3}{2}} L(w), \quad \text{B-26}$$

$$\xi > 0.3817016416 \text{ nm}$$

$$\psi_D = \cos^{-1} \left[(1 + (q_D \xi)^2)^{-1/2} \right] \quad \text{B-27}$$

$$L(w) = \ln \frac{1+w}{1-w}, q_c \xi > 1$$

$$= 2 \tan^{-1} |w|, q_c \xi < 1 \quad \text{B-28}$$

$$w = \left| \frac{q_c \xi - 1}{q_c \xi + 1} \right|^{1/2} \tan \left(\frac{\psi_D}{2} \right) \quad \text{B-29}$$

$$\xi(\bar{T}, \bar{\rho}) = \xi_0 \left(\frac{\Delta\bar{\chi}}{\Gamma_0} \right)^{\nu/\gamma} \quad \text{B-30}$$

$$\begin{aligned} \Delta\bar{\chi}(\bar{T}, \bar{\rho}) &= \bar{\rho} \left[\varsigma(\bar{T}, \bar{\rho}) - \varsigma(\bar{T}_R, \bar{\rho}) \frac{\bar{T}_R}{\bar{T}} \right] \\ &= 0, \quad \Delta\bar{\chi}(\bar{T}, \bar{\rho}) < 0 \end{aligned} \quad \text{B-31}$$

$$\varsigma = \left(\frac{\partial \bar{\rho}}{\partial \bar{p}} \right)_{\bar{T}} \quad \text{B-32}$$

Table B-8: Values for constants used in Equations B-15 – B-21.

Constant	Value
x_μ	0.068
q_C^{-1}	1.9 nm
q_D^{-1}	1.1 nm
ν	0.630
γ	1.239
ξ_0	0.13 nm
Γ_0	0.06
\bar{T}_R	1.5

Appendix C: Sample Python Code for Analysis of 1-m Supercritical Heat Transfer Dataset

```
"""
```

```
Created on Sun Jan 31 13:19:33 2021
```

```
@author: 100760198
```

```
"""
```

```
from numpy import zeros,loadtxt,savetxt
```

```
from math import pi
```

```
from CoolProp.CoolProp import PropsSI
```

```
#
```

```
=====
```

```
# Constants/Initial Values
```

```
#
```

```
=====
```

```
P=2.49e7 #MPa, Pipe pressure
```

```
G=201 #kg/m2-s, mass flux
```

```
D_i=0.01 #m, inner tube diameter
```

```
A_c=(pi/4)*(D_i)**2 #m2, cross-sectional area
```

```
m_dot=G*A_c #kg/s, mass flow rate
```

```
l=loadtxt('loc_NDG_1m_G_996_P_24_6.txt')/1000 #m, location of thermocouples
```

```
dx=zeros(21) #m, initial area for local pipe lengths
```

```
for i in range(20): #filling local pipe length array
```

```
    dx[0]=l[0]
```

```
dx[i+1]=l[i+1]-l[i]
```

```
h_b=loadtxt('h_b 1m_NDG G_201 P_24_9 q_374.txt') #kJ/kg, loading bulk enthalpy  
T_b=loadtxt('T_b 1m_NDG G_201 P_24_9 q_374.txt') #deg C, loading bulk Temperature  
q_loc=loadtxt('q_loc 1m_NDG G_201 P_24_9 q_374.txt')*1000 #W/m^2, local heat flux
```

```
k_b=zeros(21) #W/m-K, bulk thermal conductivity
```

```
u_b=zeros(21) #Pa-s, bulk dynamic viscosity
```

```
rho_b=zeros(21) #kg/m^3, density
```

```
Pr_b=zeros(21) #Prandtl number at bulk fluid
```

```
for j in range(len(T_b)): #filling empty property arrays
```

```
    k_b[j]=PropsSI('L', 'T',T_b[j]+273.15,'P',P,'REFPROP::Water')
```

```
    u_b[j]=PropsSI('V', 'T',T_b[j]+273.15,'P',P,'REFPROP::Water')
```

```
    rho_b[j]=PropsSI('D', 'T',T_b[j]+273.15,'P',P,'REFPROP::Water')
```

```
    Pr_b[j]=PropsSI('Prandtl', 'T',T_b[j]+273.15,'P',P,'REFPROP::Water')
```

```
#
```

```
=====
```

```
# Dittus-Boelter Correlation
```

```
#
```

```
=====
```

```
T_DB=zeros(21) #Wall Temperature, deg C, Dittus-Boelter
```

```
HTC_DB=zeros(21) #HTC, W/m^2-K, Dittus Boelter
```

```
for k in range(len(T_b)):
```

```
    Re_b=(G*D_i)/(u_b[k])
```

```
HTC_DB[k]=(k_b[k]/D_i)*(0.023)*(Re_b)**(0.8)*(Pr_b[k])**0.4)
```

```
T_DB[k]=(q_loc[k]/HTC_DB[k])+T_b[k]
```

```
#
```

```
=====
```

```
# Mokry et al. Correlation
```

```
#
```

```
=====
```

```
T_Mokry=zeros(21) #Wall Temperature, deg C, Mokry et al. Correlation
```

```
HTC_Mokry=zeros(21) #HTC, W/m^2-K, Mokry et al. Correlation
```

```
accuracy=0.001 #Defining target accuracy for iterative calculations, deg C
```

```
for m in range(len(T_b)):
```

```
    error=1.0 #Defining error threshold, deg C
```

```
    T_guess=T_b[m]+5 #Initializing initial temperature guesses; set @5 deg C above T_b
```

```
    while error>accuracy:
```

```
        h_w=PropsSI('H','T',T_guess+273.15,'P',P,'REFPROP::Water')
```

```
        rho_w=PropsSI('D','T',T_guess+273.15,'P',P,'REFPROP::Water')
```

```
        c_p=(h_w-h_b[m]*1000)/(T_guess-T_b[m])
```

```
        Pr__b=(c_p*u_b[m])/(k_b[m])
```

```
        Re__b=(G*D_i)/(u_b[m])
```

```
        HTC=[(k_b[m]/D_i)*(0.0061)*(Re__b)**(0.904)*
```

```
        (Pr__b)**(0.684)*(rho_w/rho_b[m])**0.564]
```

```

T_w=(q_loc[m]/HTC)+T_b[m]

error=abs(T_guess-T_w) #Find difference between calculated and guessed T
T_guess=T_w #If error target is not met, loop continues

else:
    HTC_Mokry[m]=HTC/1000 #If error target is met, value is saved in final data arrays
    T_Mokry[m]=T_w

#
=====
=====
# Gupta et al. Correlation
#
=====
=====

T_Gupta=zeros(21)
HTC_Gupta=zeros(21)
acc=0.3 #Target accuracy, deg C
check='yes' #Variable to keep 'while' loop functioning

for n in range(len(T_b)):
    T_guess=T_b[n]+5
    N=2500 #Number of initial iterative steps
    i=1
    while (check=='yes'):
        k_w=PropsSI('L', 'T',T_guess+273.15,'P',P,'REFPROP::Water')
        u_w=PropsSI('V', 'T',T_guess+273.15,'P',P,'REFPROP::Water')
        h_w=PropsSI('H', 'T',T_guess+273.15,'P',P,'REFPROP::Water')

```

```
rho_w=PropsSI('D','T',T_guess+273.15,'P',P,'REFPROP::Water')
```

```
c_p=(h_w-h_b[n]*1000)/(T_guess-T_b[n])
```

```
Pr__w=(c_p*u_w)/(k_w)
```

```
Re__w=(G*D_i)/(u_w)
```

```
HTC=[(k_w/D_i)*(0.0033)*(Re__w)**(0.941)*(Pr__w)**(0.764)*
```

```
(rho_w/rho_b[n])**0.156*(u_w/u_b[n])**0.398]
```

```
T_w=(q_loc[n]/HTC)+T_b[n]
```

```
if abs(T_w-T_guess)<acc: #If error target met within first set of iterations, values are added  
to the final data arrays
```

```
    HTC_Gupta[n]=HTC/1000
```

```
    T_Gupta[n]=T_w
```

```
    break
```

```
else: #If not, iteration continues
```

```
    T_guess=T_w
```

```
if i>N: #If iteration goes beyond defined set number of steps, accuracy is loosened
```

```
    acc=acc+0.05
```

```
if abs(T_w-T_guess)<acc: #If new accuracy met, value is added to final data array
```

```
    HTC_Gupta[n]=HTC/1000
```

```
    T_Gupta[n]=T_w
```

```
    break
```

```
else: #If not, accuracy is loosened once more and more iterative steps are added
```

acc=acc+0.01

N=N+1000

i+=1

savetxt('T_DB_NDG_G201_P_24_9 q_374 1m.txt', T_DB,fmt='%5f')

savetxt('HTC_DB_NDG_G201_P_24_9 q_374 1m.txt', HTC_DB/1000,fmt='%5f')

savetxt('T_Mokry_NDG_G201_P_24_9 q_374 1m.txt', T_Mokry,fmt='%5f')

savetxt('HTC_Mokry_NDG_G201_P_24_9 q_374 1m.txt', HTC_Mokry,fmt='%5f')

savetxt('T_Gupta_NDG_G201_P_24_9 q_374 1m.txt', T_Gupta,fmt='%5f')

savetxt('HTC_Gupta_NDG_G201_P_24_9 q_374 1m.txt', HTC_Gupta,fmt='%5f')

Appendix D: Sensitivity Analysis for SSR LUEC Parameters

In this section, the rest of the parameter variations that were performed on the *LUEC* calculation for the SSR are presented. While the chosen parameter was varied, all other parameters were held at the base-case level for consistency when comparing. All dollar figures are in 2007 USD. The data presented in the tables assume a 5% discount rate. Variation of the selected parameters at different discount rates are also included in the supplementary figures.

D.1: Plant Lifetime

Table D-1: Variation of SSR's *LUEC* due to plant lifetime.

G4ECONS Parameter	Levelized Annual Costs of Reactor	<i>LUEC</i> (\$/MW_{el}h)	Relative Change to Base Case (%)
Lifetime=10 years	Capital (First Core and <i>IDC</i> Inclusive)	111	+147
	Operations	19	0
	Fuel Cycle-Front	7	0
	Fuel Cycle-Back End	2	0
	D&D Sinking Fund	20	+1900
	Total:	159	+115
Lifetime=20 years	Capital (First Core and <i>IDC</i> Inclusive)	69	+53
	Operations	19	0
	Fuel Cycle-Front	7	0
	Fuel Cycle-Back End	2	0
	D&D Sinking Fund	8	+700
	Total:	105	+42
Lifetime=40 years	Capital (First Core and <i>IDC</i> Inclusive)	50	+11
	Operations	19	0
	Fuel Cycle-Front	7	0
	Fuel Cycle-Back End	2	0
	D&D Sinking Fund	2	+100
	Total:	80	+8
Lifetime=60 years	Capital (First Core and <i>IDC</i> Inclusive)	45	-
	Operations	19	-
	Fuel Cycle-Front	7	-

G4ECONS Parameter	Levelized Annual Costs of Reactor	LUEC (\$/MW_{el}h)	Relative Change to Base Case (%)
	Fuel Cycle-Back End	2	-
	D&D Sinking Fund	1	-
	Total:	74	/
Lifetime=80 years	Capital (First Core and <i>IDC</i> Inclusive)	44	-2
	Operations	19	0
	Fuel Cycle-Front	7	0
	Fuel Cycle-Back End	2	0
	D&D Sinking Fund	0.3	-70
	Total:	72.3	-2

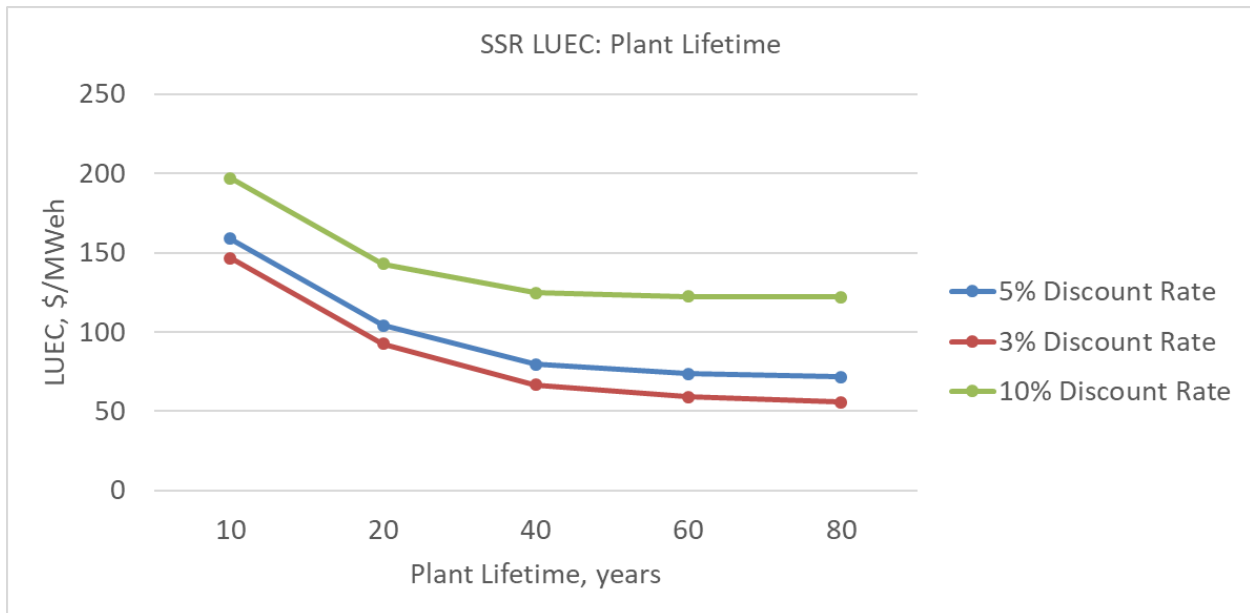


Figure D-1: Graphical representation of SSR’s LUEC variance due to plant lifetime.

D.2: Construction Time

Table D-2: Variation of SSR’s LUEC due to construction time.

G4ECONS Parameter	Levelized Annual Costs of Reactor	LUEC (\$/MW_{el}h)	Relative Change to Base Case (%)
Construction Time=3 years	Capital (First Core and <i>IDC</i> Inclusive)	44	-2
	Operations	19	0
	Fuel Cycle-Front	7	0

G4ECONS Parameter	Levelized Annual Costs of Reactor	<i>LUEC</i> (\$/MW_{eh})	Relative Change to Base Case (%)
	Fuel Cycle-Back End	2	0
	D&D Sinking Fund	1	0
	Total:	73	-1
Construction Time=4 years	Capital (First Core and <i>IDC</i> Inclusive)	45	-
	Operations	19	-
	Fuel Cycle-Front	7	-
	Fuel Cycle-Back End	2	-
	D&D Sinking Fund	1	-
	Total:	74	/
Construction Time=5 years	Capital (First Core and <i>IDC</i> Inclusive)	46	+2
	Operations	19	0
	Fuel Cycle-Front	7	0
	Fuel Cycle-Back End	2	0
	D&D Sinking Fund	1	0
	Total:	75	+1
Construction Time=6 years	Capital (First Core and <i>IDC</i> Inclusive)	48	+7
	Operations	19	0
	Fuel Cycle-Front	7	0
	Fuel Cycle-Back End	2	0
	D&D Sinking Fund	1	0
	Total:	77	+4
Construction Time=8 years	Capital (First Core and <i>IDC</i> Inclusive)	50	+11
	Operations	19	0
	Fuel Cycle-Front	7	0
	Fuel Cycle-Back End	2	0
	D&D Sinking Fund	1	0
	Total:	79	+7

G4ECONS Parameter	Levelized Annual Costs of Reactor	LUEC (\$/MWe_h)	Relative Change to Base Case (%)
Construction Time=10 years	Capital (First Core and <i>IDC</i> Inclusive)	53	+18
	Operations	19	0
	Fuel Cycle-Front	7	0
	Fuel Cycle-Back End	2	0
	D&D Sinking Fund	1	0
	Total:	82	+11

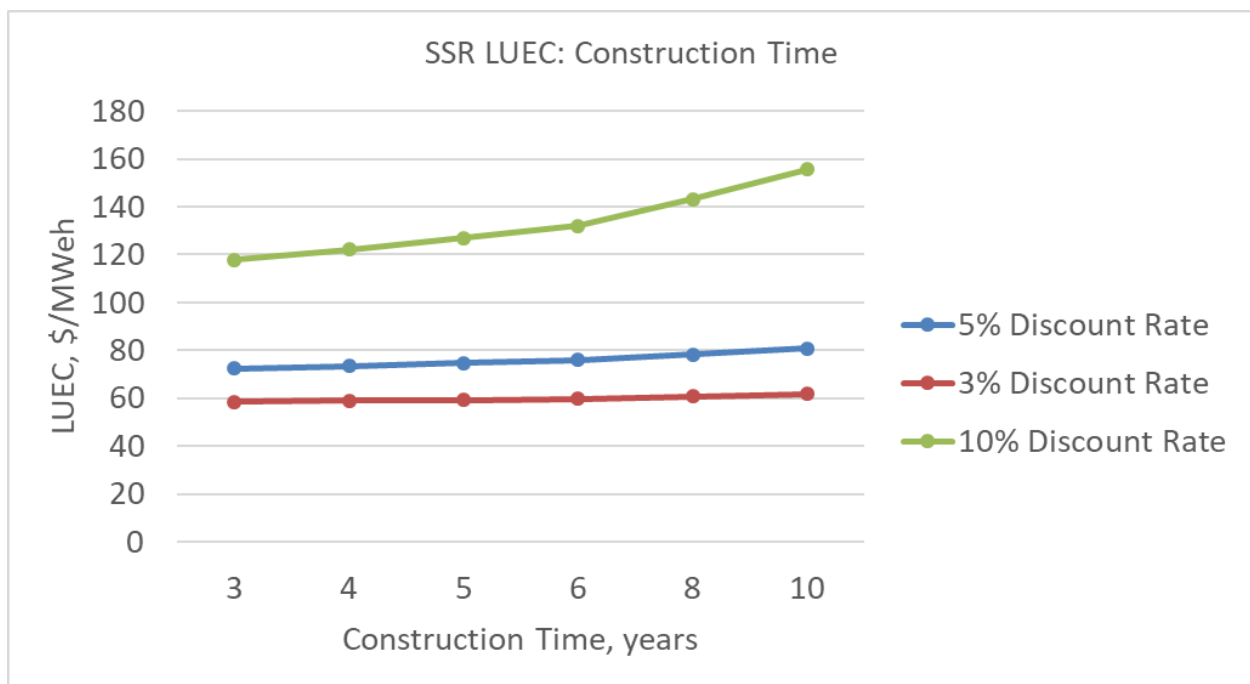


Figure D-2: Graphical representation of SSR’s LUEC variance due to construction period.

D.3: Plant Capacity Factor

Table D-3: Variation of SSR’s LUEC due to plant capacity factor.

G4ECONS Parameter	Levelized Annual Costs of Reactor	LUEC (\$/MWe_h)	Relative Change to Base Case (%)
Plant Capacity Factor=80%	Capital (First Core and <i>IDC</i> Inclusive)	54	+20
	Operations	22	+16
	Fuel Cycle-Front	7	0

G4ECONS Parameter	Levelized Annual Costs of Reactor	<i>LUEC</i> (\$/MWh)	Relative Change to Base Case (%)
	Fuel Cycle-Back End	2	0
	D&D Sinking Fund	1	0
	Total:	86	+16
Plant Capacity Factor=85%	Capital (First Core and <i>IDC</i> Inclusive)	51	+13
	Operations	21	+11
	Fuel Cycle-Front	7	0
	Fuel Cycle-Back End	2	0
	D&D Sinking Fund	1	0
	Total:	82	+11.0
Plant Capacity Factor=90%	Capital (First Core and <i>IDC</i> Inclusive)	48	+7
	Operations	20	+5
	Fuel Cycle-Front	7	0
	Fuel Cycle-Back End	2	0
	D&D Sinking Fund	1	0
	Total:	78	+5
Plant Capacity Factor=95%	Capital (First Core and <i>IDC</i> Inclusive)	45	-
	Operations	19	-
	Fuel Cycle-Front	7	-
	Fuel Cycle-Back End	2	-
	D&D Sinking Fund	1	-
	Total:	74	/
Plant Capacity Factor=99%	Capital (First Core and <i>IDC</i> Inclusive)	44	-2
	Operations	19	0
	Fuel Cycle-Front	7	0
	Fuel Cycle-Back End	2	0
	D&D Sinking Fund	1	0
	Total:	73	-1

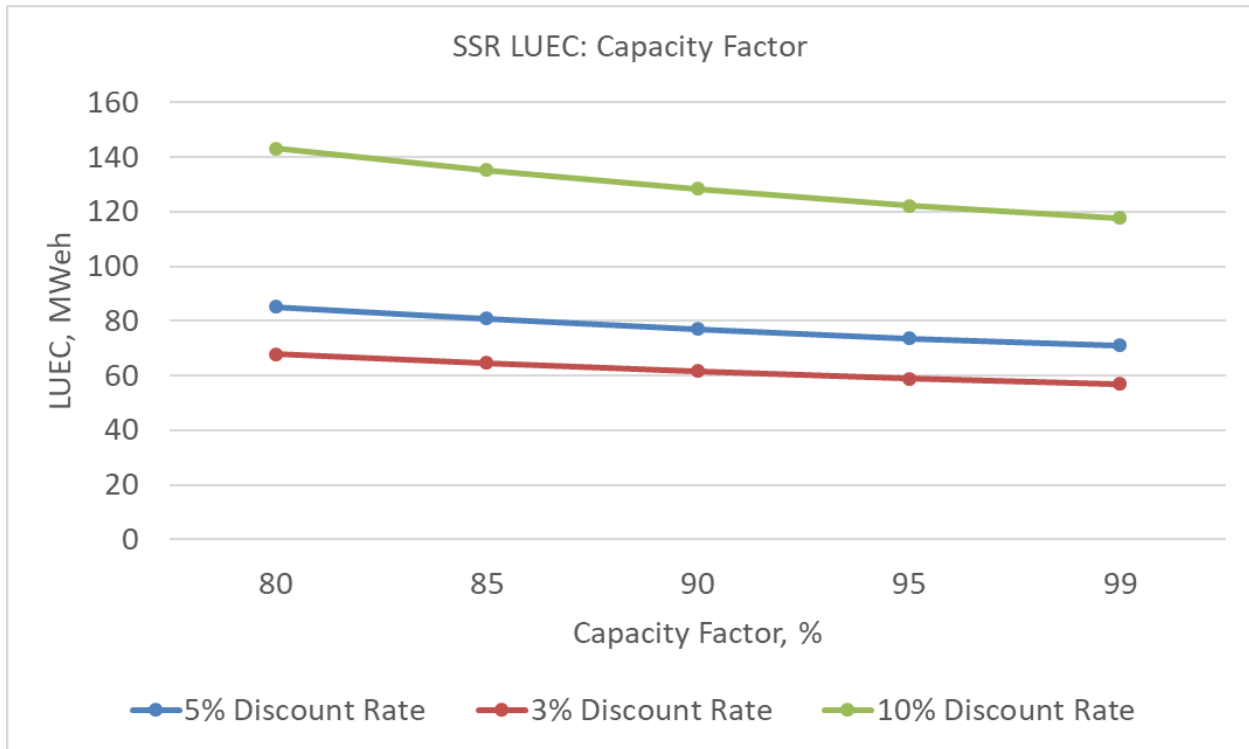


Figure D-3: Graphical representation of SSR’s LUEC variance due to capacity factor.

D.4: Natural Uranium Mining Prices¹³

Table D-4: Variation of SSR’s LUEC due to natural uranium mining costs.

G4ECONS Parameter	Levelized Annual Costs of Reactor	LUEC (\$/MWeh)	Relative Change to Base Case (%)
Natural U Mining Price=\$27.5/kgU	Capital (First Core and IDC Inclusive)	45	0
	Operations	19	0
	Fuel Cycle-Front	4	-43
	Fuel Cycle-Back End	2	0
	D&D Sinking Fund	1	0
	Total:	71	-4
Natural U Mining Price=\$55/kgU	Capital (First Core and IDC Inclusive)	45	0
	Operations	19	0
	Fuel Cycle-Front	4	-40

¹³ Limits for uranium mining prices were set based off data provided from the World Nuclear Association (2020c).

G4ECONS Parameter	Levelized Annual Costs of Reactor	<i>LUEC</i> (\$/MWe_h)	Relative Change to Base Case (%)
	Fuel Cycle-Back End	2	0
	D&D Sinking Fund	1	0
	Total:	71	-4
Natural U Mining Price=\$88/kg _U	Capital (First Core and <i>IDC</i> Inclusive)	45	0
	Operations	19	0
	Fuel Cycle-Front	5	-30
	Fuel Cycle-Back End	2	0
	D&D Sinking Fund	1	0
	Total:	72	-3
Natural U Mining Price=\$110/kg _U	Capital (First Core and <i>IDC</i> Inclusive)	45	0
	Operations	19	0
	Fuel Cycle-Front	5	-30
	Fuel Cycle-Back End	2	0
	D&D Sinking Fund	1	0
	Total:	72	3
Natural U Mining Price=\$165/kg _U	Capital (First Core and <i>IDC</i> Inclusive)	45	0
	Operations	19	0
	Fuel Cycle-Front	6	-14
	Fuel Cycle-Back End	2	0
	D&D Sinking Fund	1	0
	Total:	73	-1.0
Natural U Mining Price=\$208/kg _U	Capital (First Core and <i>IDC</i> Inclusive)	45	-
	Operations	19	-
	Fuel Cycle-Front	7	-
	Fuel Cycle-Back End	2	-

G4ECONS Parameter	Levelized Annual Costs of Reactor	<i>LUEC</i> (\$/MWe_h)	Relative Change to Base Case (%)
	D&D Sinking Fund	1	-
	Total:	74	/

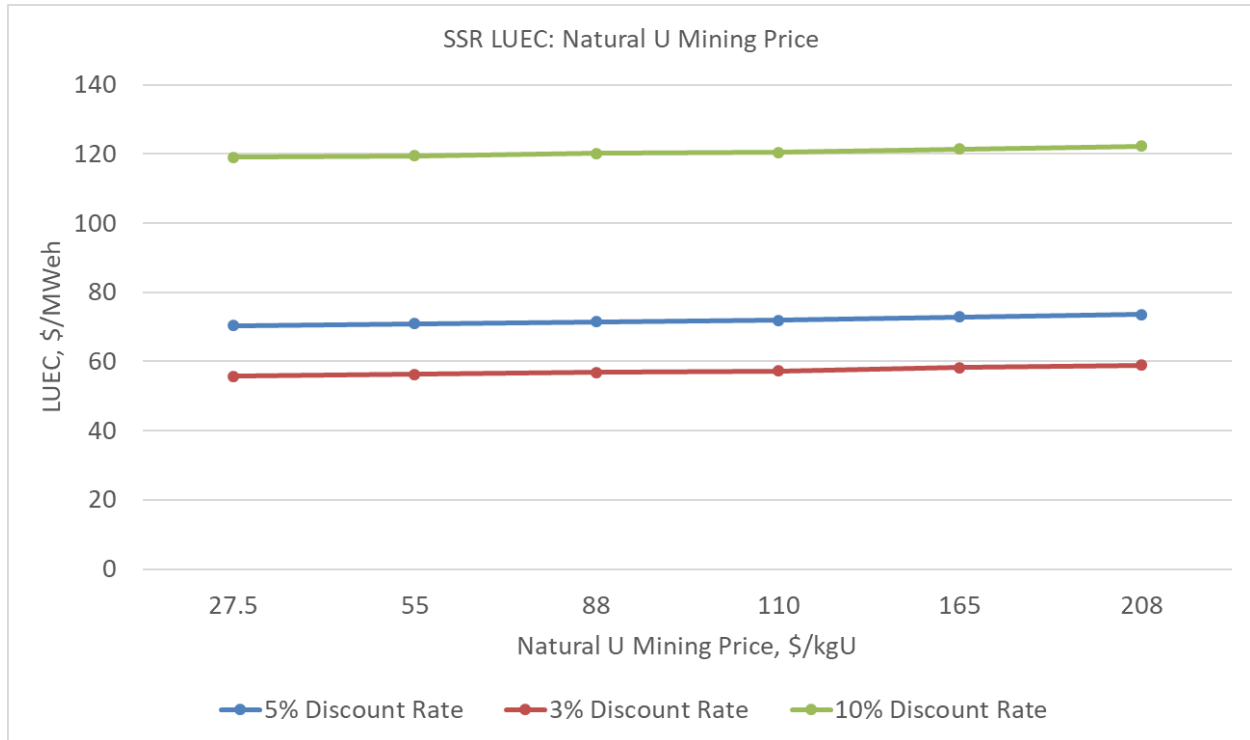


Figure D-4: Graphical representation of SSR’s LUEC variance due to natural uranium mining prices.

D.5: Fuel Enrichment Costs¹⁴

Table D-5: Variation of SSR’s *LUEC* due to fuel enrichment costs.

G4ECONS Parameter	Levelized Annual Costs of Reactor	<i>LUEC</i> (\$/MWe_h)	Relative Change to Base Case (%)
Fuel Enrichment Cost=\$76/SWU	Capital (First Core and <i>IDC</i> Inclusive)	45	0
	Operations	19	0
	Fuel Cycle-Front	6	-14
	Fuel Cycle-Back End	2	0

¹⁴ Limits for fuel enrichment costs were based off data from Ko and Gao (2012).

G4ECONS Parameter	Levelized Annual Costs of Reactor	<i>LUEC</i> (\$/MWh)	Relative Change to Base Case (%)
	D&D Sinking Fund	1	0
	Total:	73	-1
Fuel Enrichment Cost=\$130/SWU	Capital (First Core and <i>IDC</i> Inclusive)	45	-
	Operations	19	-
	Fuel Cycle-Front	7	-
	Fuel Cycle-Back End	2	-
	D&D Sinking Fund	1	-
	Total:	74	/
Fuel Enrichment Cost=\$148/SWU	Capital (First Core and <i>IDC</i> Inclusive)	45	0
	Operations	19	0
	Fuel Cycle-Front	7	0
	Fuel Cycle-Back End	2	0
	D&D Sinking Fund	1	0
	Total:	74	0
Fuel Enrichment Cost=\$171.5/SWU	Capital (First Core and <i>IDC</i> Inclusive)	45	0
	Operations	19	0
	Fuel Cycle-Front	8	+14
	Fuel Cycle-Back End	2	0
	D&D Sinking Fund	1	0
	Total:	75	+1



Figure D-5: Graphical representation of SSR’s LUEC variance due to uranium enrichment costs.

From the data above, it can be seen that natural uranium mining prices and fuel enrichment prices have little to no effect on the *LUEC* of the SSR when calculated with the G4ECONS software. Plant lifetime had the most acute effect on the *LUEC* value across all discount rates, especially noticeable at shorter lifespans. Construction time had relatively little effect on the *LUEC* with the exception of the 10% discount rate curve in Figure D-2. A longer construction period at a higher discount rate seemed to significantly increase the *LUEC* of the SSR. It should also be noted that the difference in magnitude between *LUECs* at the three discount rates did not greatly change. The distance between the curves, with the exception of Figure D-2, remained more or less constant across parameter variation. Essentially, the *LUEC* responded in the same

manner when a parameter was varied regardless of the set discount rate and no significant deviations were noted. Future work would entail analyzing different fuel cycle options and measuring the impact on the *LUEC* compared to the base case.

Appendix E: N. Dort-Goltz Publications and Conferences Attended

Papers in Refereed Journals

1. Pioro, I., Duffey, R.B., Kirillov, P.L., and Dort-Goltz, N., 2020. Current Status of Reactors Deployment and Small Modular Reactors Development in the World. *ASME J. NERS, Vol. 6, No. 4*, 24 pages. Free download from:
<https://asmedigitalcollection.asme.org/nuclearengineering/article/6/4/044001/1085654/Current-Status-of-Reactors-Deployment-and-Small>

Papers Published in Refereed Proceedings of International and National Conferences and Symposiums

1. Dort-Goltz, N., Burgener, J., Pioro, I., and McKellar, J., 2020. Specifics of Water-Cooled SMRs, Proceedings of 40th Annual Conference of the Canadian Nuclear Society and 44th Annual CNS/CNA Student Conference (virtual), May 31 - June 3, 6 pages.
2. Pioro, I., Dort-Goltz, N., and McKellar, J., 2020. Current Status of Nuclear Power in the World Including Latest Developments on SMRs, Proceedings of NENE-2020, Portorož, Slovenia, Sept. 7-10, Paper 409, 10 pages. Free download from:
http://www.rcp.ijs.si/bojan/NENE2020USB/pdf/NENE2020_0409.pdf.
3. Dort-Goltz, N., Pioro, I., and McKellar, J., 2021c. Specifics of Calculating Thermophysical Properties of Water in Critical Point Using NIST REFPROP Program, Proceedings of the 10th International Symposium on SCWRs (ISSCWR-10), Prague, the Czech Republic, March 15-18, 10 pages.
4. Dort-Goltz, N., Pioro, I., and McKellar, J., 2021b. Experimental Study on Heat Transfer to Upward Flow of Supercritical Water in a 1-M Vertical Bare Tube, Proceedings of 40th

Annual Conference of the Canadian Nuclear Society and 45th Annual CNS/CNA Student Conference (virtual), June 6th-9th, 6 pages. Master's Level Submission.

5. Burgener, J., Tsai, M., Dort-Goltz, N., Pioro, I., and McKellar, J., 2021. Study on Thermal Efficiency of SCWRs, Proceedings of the 40th Annual Conference of the Canadian Nuclear Society and 45th Annual CNS/CNA Student Conference (virtual), June 6-9, 6 pages. Master's Level Submission.
6. Dort-Goltz, N., Pioro, I., and McKellar, J., 2021a. Study on Deteriorated Heat Transfer in Upward Flow of Supercritical Water in a 1-M Vertical Bare Tube, Proceedings of 28th International Conference on Nuclear Engineering, Virtual Conference, August 4-6, 10 pages.

Conferences Attended

1. 40th Annual Conference of the Canadian Nuclear Society and 44th Annual CNS/CNA Student Conference (virtual), May 31-June 3, 2020.
2. 40th Annual Conference of the Canadian Nuclear Society and 45th Annual CNS/CNA Student Conference (virtual), June 6-9, 2021.
3. 28th International Conference on Nuclear Engineering, Virtual Conference, August 4-6, 2021.

Appendix F: Awards, Honours, and Accomplishments by N. Dort-Goltz

1. Recipient of the 2020 Jeffrey S. Boyce Engineering Award from the Faculty of Energy Systems and Nuclear Science and Faculty of Engineering and Applied Science, Ontario Tech University, December 11, Oshawa, Ontario, Canada.
2. Created and analyzed most comprehensive set of SMR concepts/designs from around the globe and presented the results in the Journal of Nuclear Engineering and Radiation Science (Pioro, ..., Dort-Goltz, 2020) and the 29th International Conference Nuclear Energy for New Europe (Pioro, Dort-Goltz, and McKellar, 2020).
3. First thorough investigation and analysis of the NIST REFPROP software for its calculation of the critical properties of water. It was found that the theoretical models used by REFPROP significantly overestimated the thermophysical properties of water at the critical point. Results presented at the 10th International Symposium of SCWRs and recommendations sent to NIST for adjustments regarding the methods of thermophysical property calculations (Dort-Goltz et al., 2021c).
4. First in-depth analysis of the experimental dataset obtained by Kirillov et al. with the 1-m, vertical bare tube test section cooled by the upward flow of supercritical water. This analysis showed that deteriorated heat transfer was present in almost all of the experimental tests but the deteriorated heat transfer regime was stable along the test section. It was also found that the severity of the onset of deteriorated heat transfer and entrance effects fluctuated throughout the experimental tests. These results were presented at the 40th Annual Conference of the Canadian Nuclear Society and 45th Annual CNS/CNA Student Conference (Dort-Goltz et al., 2021b) and was presented at the 28th International Conference on Nuclear Engineering (Dort-Goltz et al., 2021a).

5. Winner of the Best Student Presentation-North America award during ICONE-28 for the paper on DHT (Dort-Goltz et al., 2021a).

Appendix G: Copyright Permissions

Nikita Dort-Goltz <nikita.dortgoltz@ontariotechu.net>
to DarchiB ▾

Thu, Feb 18, 4:35 PM ☆ ↶

Dear Beth Darchi:

I am an MASC student of Professor I. Pioro and J. McKellar and, also, I am a co-author of the following paper:

Pioro, I., Duffey, R.B., Kirillov, P.L., and Dort-Goltz, N., 2020. Current Status of Reactors Deployment and Small Modular Reactors Development in the World, ASME Journal of Nuclear Engineering and Radiation Science, Vol. 6, No. 4, 24 pages. Free download from: <https://asmedigitalcollection.asme.org/nuclearengineering/article/6/4/044001/1085654/Current-Status-of-Reactors-Deployment-and-Small>.

I would like to ask for the ASME permission to use materials (figures, tables, text, etc.) from our paper in my MASC thesis!

Thank you in advance,

Regards,

--

Nikita Dort-Goltz
Graduate Student
Faculty of Energy Systems and Nuclear Science
Ontario Tech University

Beth Darchi <DarchiB@asme.org>
to me ▾

Mar 16, 2021, 8:30 AM ☆ ↶ ⋮

Dear Mr. Dort-Goltz,

It is our pleasure to grant you permission to use **all or any part of** the ASME paper "Current Status of Reactors Deployment and Small Modular Reactors Development in the World," by I. Pioro , R. B. Duffey , P. L. Kirillov , N. Dort-Goltz, ASME J of Nuclear Rad Sci. Oct 2020, 6(4), cited in your letter for inclusion in a thesis entitled Study on Heat Transfer to Supercritical Water in Application to SMRs to be published by Ontario Tech University (formerly University of Ontario Institute of Technology).

Permission is granted for the specific use as stated herein and does not permit further use of the materials without proper authorization. Proper attribution must be made to the author(s) of the materials. **Please note:** if any or all of the figures and/or Tables are of another source, permission should be granted from that outside source or include the reference of the original source. ASME does not grant permission for outside source material that may be referenced in the ASME works.

As is customary, we request that you ensure full acknowledgment of this material, the author(s), source and ASME as original publisher.

Many thanks for your interest in ASME publications.

Sincerely,

Beth Darchi
Publishing Administrator
ASME